

INVESTIGATION OF FRACTURE TOUGHNESS WITH FOUR POINT  
ASYMMETRIC BENDING ON RECTANGULAR ROCK SPECIMENS

A THESIS SUBMITTED TO  
THE GRADUATE SCHOOL OF APPLIED AND NATURAL SCIENCES  
OF  
MIDDLE EAST TECHNICAL UNIVERSITY

BY

UĞUR ALKAN

IN PARTIAL FULFILLMENT OF THE REQUIREMENTS  
FOR  
THE DEGREE OF MASTER OF SCIENCE  
IN  
MINING ENGINEERING

SEPTEMBER 2015



Approval of the thesis:

**INVESTIGATION OF FRACTURE TOUGHNESS WITH FOUR POINT  
ASYMMETRIC BENDING ON RECTANGULAR ROCK SPECIMENS**

submitted by **UĞUR ALKAN** in partial fulfillment of the requirements for the degree of **Master of Science in Mining Engineering Department, Middle East Technical University** by,

Prof. Dr. Gülbin Dural Ünver  
Dean, Graduate School of **Natural and Applied Science**

---

Prof. Dr. Ali İhsan Arol  
Head of Department, **Mining Engineering**

---

Prof. Dr. Levend Tutluoğlu  
Supervisor, **Mining Engineering Dept., METU**

---

**Examining Committee Members:**

Prof. Dr. Celal Karpuz  
Mining Engineering Dept., METU

---

Prof. Dr. Levend Tutluoğlu  
Mining Engineering Dept., METU

---

Assoc. Prof. Dr. Hakan Başarır  
Mining Engineering Dept., METU

---

Assoc. Prof. Dr. Hasan Öztürk  
Mining Engineering Dept., METU

---

Assoc. Prof. Dr. Mehmet Ali Hindistan  
Mining Engineering Dept., HU

---

**Date:** 07.09.2015

**I hereby declare that all information in this document has been obtained and presented in accordance with academic rules and ethical conduct. I also declare that, as required by these rules and conduct, I have fully cited and referenced all material and results that are not original to this work.**

Name, Last Name: Uğur Alkan

Signature:

## ABSTRACT

### INVESTIGATION OF FRACTURE TOUGHNESS WITH FOUR POINT BENDING LOADING ON RECTANGULAR ROCK SPECIMENS

Alkan, Uğur

M.S., Department of Mining Engineering

Supervisor: Prof. Dr. Levend Tutluoğlu

September 2015, 214 pages

In rock engineering applications inherent cracks and other type of impurities are seldom under the effect of loads acting along principal directions. Dominant loading states mostly consist of mixed mode type of loads. Mode I loading state has been studied by researchers for a long time. Therefore, common principles have been established for mode I loading state. Shear type (mode II) loading state is still an active subject to investigate in fracture mechanics. Although, numerous test methods have been suggested to determine the mode II fracture toughness  $K_{IIc}$  of a rock, common opinion for mode II loading state is not well-established yet.

Four-point asymmetric bending test specimen (FPAB) has a rectangular shaped geometry. Shear mode (mode II) fracture toughness investigations were conducted on rectangular shaped rock specimens under asymmetric bending loads. Tests were carried out under four-point asymmetric bending loads.

In order to assure generation of pure mode II stress intensity factor state for FPAB test geometry, numerical modeling with ABAQUS Finite Element Software was conducted.

Different sized rectangular shaped rock specimens were prepared to investigate size effect phenomena for FPAB test geometry. Numerical and experimental studies were conducted for three main beam depth groups having different notch lengths. The

generic FPAB test geometry which was 120 mm long and 50 mm thick consisted of three different beam depths 40-50-60 mm and included a preliminary single edge notch at the bottom center. Results of pure shear mode fracture toughness values from FPAB test geometry were compared to the ones from SNDB (Straight Notched Disk bending) method testing. The same rock type, namely Ankara Gölbaşı Andesite was used in both.

In the models, stress paths were created to analyze potential plastic regions or fracture process zones ahead of the preliminary notch. Von Mises plasticity in the vicinity of notch tip was examined along the potential crack propagation directions of mode I and mode II loading states. Stress paths were beginning from the notch tip and expanding to the outmost contour integral region. Stress paths for mode I and mode II stress intensity factor were compared. Boundary influence effect in rectangular shaped rock specimens under mode I and mode II loading states were compared.

Mode II fracture toughness value of Ankara Gölbaşı Andesite was found as  $K_{IIc} = 0.61 \text{ MPa}\sqrt{\text{m}}$  for FPAB test geometry. In comparison, mode II fracture toughness value of Ankara Gölbaşı Andesite was found as  $K_{IIc} = 0.62 \text{ MPa}\sqrt{\text{m}}$  for the tests with SNDB geometry.

Size of the beam specimens was changed by applying three different beam depths. Close results were achieved for mode II fracture toughness values for test geometries with different beam depths. No size effect was observed in shear mode fracture toughness values of tests with different beam depths of FPAB geometry.

Keywords: Rock fracture mechanics, mode II fracture toughness, mode II stress intensity factor, four-point asymmetric bending, FPAB, rectangular, beam shaped rock specimen.

## ÖZ

### DÖRTGEN KESİTLİ KAYA NUMUNELERİNİN ÇATLAK TOKLUĞUNUN DÖRT NOKTA ASİMETRİK EĞİLME DENEYİ İLE ARAŞTIRILMASI

Alkan, Uğur

Yüksek Lisans, Department of Mining Engineering

Tez Yöneticisi: Prof. Dr. Levent Tutluoğlu

Eylül 2015, 214 sayfa

Kaya mühendisliği uygulamalarında doğal çatlaklar ve diğer impürite unsurları nadiren asal gerilme gerilme düzlemleri üzrinden gelen gerilmelere maruzdur. Baskın yükleme durumları karışık mod tipindeki yüklerden oluşur. Mod I yükleme durumu araştırmacılar tarafından uzunca bir süredir çalışılmaktadır. Bu sebepten ötürü, yerleşik bir temel mod I yükleme durumu için geliştirilmiştir. Makaslama tipi (mod II) yükleme durumu ise hali hazırda kırılma mekaniği araştırmalarında güncel bir konudur. Bir çok sayıda test metodu önerilmesine rağmen kayalarda i mod II çatlak tokluğu tayini için ortak bir fikir birliği iyi bir şekilde oluşturulamamıştır.

Dört-nokta asimetrik eğme test numunesi dikdörtgen kesitli bir geometriye sahiptir. Makaslama modu (mod II) çatlak tokluğu araştırmaları dikdörtgen kesitli kaya numumeleri üzerine asimetrik eğme yükleri uygulanarak yürütülmüştür. Laboratuvar deneyleri de dört-nokta asimetrik eğme yükleri uygulanarak gerçekleştirilmiştir.

Dört-nokta asimetrik eğme numunesi üzerinde saf mod II gerilme şiddeti faktörü durumunu kesin bir şekilde sağlamak için ABAQUS Yazılımı ile numeric modelleme yöntemi kullanılmıştır.

Numune boyut etkisinin araştırılması için farklı boyutlardaki dört-nokta asimetric eğme kaya numuneleri hazırlanmıştır. Nümerik ve deneysel çalışmalar farklı çatlak boyları içeren üç farklı giriş derinliği grubu oluşturularak yürütülmüştür. 120 mm uzunluğunda ve 50 mm kalınlığında olan, 40-50 ve 60 mm olmak üzere üç farklı giriş derinliğine sahip genel dört-nokta asimetric eğme test geometrisi, alt taraf kenarından açılmış bir çatlak barındır. Dört-nokta asimetric eğme test numunesi için saf makaslama modu çatlak tokluğu sonuçları, düz çentikli Brezilyan diski numunesi sonuçlarıyla karşılaştırılmıştır. Bu iki farklı deney geometrisi için Ankara Andeziti olarak adlandırılmış aynı kaya tipi kullanılmıştır.

Modellerde, potansiyel plastik deformasyon bölgelerinin ve çatlak proses zonlarının analiz edilmesi için çatlakın ön kısmında gerilme izleri oluşturulmuştur. Mod I ve II yükleme durumlarında potansiyel çatlak ilerleme yönü doğrultusunda çatlak ucu civarındaki von Mises plastisite bölgeleri incelenmiştir. Bu gerilme izleri çatlak ucundan başlayarak en dış integrali konturuna doğru ilerleyen bir hat boyunca oluşturulmuştur. Mod I ve II gerilme şiddeti faktörü için oluşturulan bu iki gerilme izi birbirleriyle karşılaştırılmıştır. Dikdörtgen kesitli kaya numunelerinde numune sınırı etkisinin mod I ve mod II gerilme şiddeti faktörü üzerindeki etkileri karşılaştırılmıştır.

Dört-nokta asimetric eğme test geometrisi kullanılarak Ankara Andeziti için mod II çatlak tokluğu değeri  $K_{IIc} = 0.61 MPa\sqrt{m}$  olarak bulunmuştur. Aynı kaya tipi için düz çentikli Brezilyan diski test geometrisi kullanılarak yapılan deneyler de mod II çatlak tokluğu değeri  $K_{IIc} = 0.62 MPa\sqrt{m}$  olarak bulunmuştur.

Farklı boyutlardaki giriş tip numuneler, giriş derinliği ölçüleri değiştirilerek oluşturulmuştur. Farklı giriş derinliği ölçülerine sahip bu numuneler üzerinde yapılan mod II çatlak tokluğu deneyleri sonucu yakın çatlak tokluğu değerleri elde edilmiştir. Farklı giriş derinliğine sahip kaya numuneleri üzerinde yapılan deneyler sonucunda, dört-nokta asimetric eğme test geometrisi için makaslama modu çatlak tokluğu değerleri üzerinde boyut etkisinin olmadığı gözlemlenmiştir.

Anahtar Kelimeler: Kaya kırılma mekaniđi, mod II atlak tokluđu, mod II gerilme Őiddeti faktörü, dört-nokta asimetrik eđme, dikdörtgen kesitli kaya numuneleri, kiriş tipi kaya numuneleri.

## ACKNOWLEDGEMENTS

First of all, I would like to express my deep and sincere gratitude and appreciation to my supervisor, Prof. Dr. Levend Tutluođlu for his mentorship. His invaluable guidance, extensive knowledge, kind friendship and never ending confidence throughout the thesis study made this happen. I also present my special thanks to Prof. Dr. Celal Karpuz for his invaluable help and encouraging attitude towards the misfortune I have faced. I wish to express my thanks to Prof. Dr. Ali İhsan Arol for his embrace and invaluable help on the problems that I am confronted. I also wish to express my sincere appreciation to Assoc. Prof. Hakan Bařarır, Assoc. Prof. Dr. Hasan Öztürk, and Assoc. Prof. Dr. Mehmet Ali Hindistan for their valuable contributions and for serving on the M.Sc. thesis committee.

I present my special thanks to Tahsin Iřıksal for his help, guidance and joyful friendship during laboratory studies. I also thank to Hakan Uysal for his help during laboratory studies.

I must express my special thanks to my associates M.Sc Dođukan Güner, M.Sc. Ahmet Güneř Yardımcı, M.Sc. Onur Gölbařı for all their help and contributions. I would also like to thank my friends and colleagues; Assit. Prof. Dr. Mustafa Çırak, M.Sc. Deniz Tuncay, Selahattin Akdađ, M.Sc. Mahmut Camalan, M.Sc. Öznur Önel, Deniz Talan and Mahir Can Çetin for their support and motivation.

I owe my loving thanks to my parents Hüseyin Alkan and Nazmiye Alkan. Without their encouragement and understanding, it would have been impossible for me to finish this thesis.

Finally, I serve my deepest appreciation to Ayřegöl Rahvancı. Without her dedication and love, this thesis also would not have been accomplished like every other thing.

## TABLE OF CONTENTS

ABSTRACT.....	v
ÖZ .....	vii
ACKNOWLEDGEMENTS .....	x
TABLE OF CONTENTS .....	xi
LIST OF TABLES .....	xv
LIST OF FIGURES .....	xvii
LIST OF SYMBOLS AND ABBREVIATIONS .....	xxiii
CHAPTERS	
1. INTRODUCTION .....	1
1.1 General remarks .....	1
1.2 Historical development of fracture mechanics .....	3
1.3 Problem statement .....	9
1.4 Objective of the study.....	10
1.5 Methodology of the study.....	11
1.6 Sign convention of mechanical entities.....	13
1.7 Outline of the thesis.....	16
2. FUNDAMENTALS OF ROCK FRACTURE MECHANICS .....	19
2.1 Linear elastic fracture mechanics .....	21
2.1.1 Crack tip stresses.....	23
2.1.2 Typical geometries for mode I and mode II stress intensity factors ....	27
2.1.3 Fracture toughness .....	30
2.2 Elastic plastic fracture mechanics .....	31
2.2.1 Crack tip opening displacement.....	31

2.2.2	<i>J</i> -contour integral .....	32
2.3	Fracture mechanics in earth sciences practice .....	34
2.3.1	Hydraulic fracturing .....	34
2.3.2	Rock excavations.....	35
2.3.3	Rock slope stability engineering .....	39
2.3.4	Rock bursts .....	40
2.3.5	Application of fracture mechanics to the prediction of comminution behavior .....	42
2.4	Mode II fracture toughness testing methods.....	44
2.4.1	The punch-through test with confining pressure .....	44
2.4.2	Shear box test .....	47
2.4.3	Semi-circular bending test.....	51
2.4.4	Cracked straight through Brazilian disc .....	56
2.4.5	Straight notched disc bending test.....	62
3.	FOUR-POINT ASYMMETRIC BENDING TEST SPECIMEN.....	67
3.1	Four-point asymmetric bending test specimen .....	67
3.2	Development of FPAB test specimen.....	68
3.3	Symbols and geometric details of FPAB test specimen .....	69
3.4	Analytical methods for mode II fracture toughness $K_{IIc}$ calculation .....	73
4.	VERIFICATION STUDIES AND FINITE ELEMENT MODELING OF BEAM GEOMETRIES.....	79
4.1	Notations, definitions and terms used by ABAQUS in modeling works ....	80
4.1.1	Notation usage.....	80
4.1.2	Terms and definitions.....	81
4.2	Fracture mechanics computation techniques of ABAQUS .....	83

4.2.1	Seam crack .....	83
4.2.2	Crack front .....	85
4.2.3	Crack tip stress singularity calculation .....	86
4.3	Verification studies.....	87
4.3.1	Three-point bending plate verification problem .....	88
4.3.2	Pure-shear plate verification problem .....	94
4.4	Finite element modeling of beam geometries .....	101
4.4.1	Improvement studies of base numerical model of FPAB test specimen.. .....	102
4.4.2	Boundary conditions of numerical models .....	104
4.4.3	Mesh generation of FPAB specimen.....	108
4.4.4	Loading configuration investigation for pure mode II SIF state in FPAB models.....	110
4.4.5	Pure mode II SIF investigation for different beam depths and crack lengths .....	116
5.	PURE MODE II FRACTURE TOUGHNESS TESTING WITH FPAB GEOMETRY .....	125
5.1	Testing equipment utilized in experimental study .....	125
5.1.1	Milling machine .....	127
5.1.2	Diamond circular saw .....	127
5.1.3	Testing machine .....	129
5.2	Laboratory work for rock property determination.....	131
5.2.1	Static deformability test .....	131
5.2.2	Brazilian (Indirect Tensile) test.....	133
5.3	Fracture tests.....	135
5.3.1	Mode II fracture toughness testing work with FPAB test geometry..	136

6. RESULTS AND DISCUSSION .....	145
6.1 Stress analyses around the notch of FPAB testing geometry and other numerical works .....	146
6.1.1 Von Mises yield criterion .....	147
6.1.2 Mode I stress intensity factor investigations on FPB test geometry ..	149
6.1.3 Stress analyses for FPB and FPAB test geometries .....	151
6.2 Verification efforts for SNDB numerical study and justification of FPAB test results .....	156
6.2.1 Numerical modeling work for SNDB test geometry .....	156
6.2.2 Mode II fracture toughness determination with SNDB test geometry .....	159
7. CONCLUSIONS AND RECOMMENDATIONS .....	167
REFERENCES .....	170
APPENDICES .....	183
APPENDIX A: DIMENSIONLESS SHORT MOMENT ARM DISTANCE ANALYSIS .....	183
APPENDIX B: SPECIMEN PHOTOGRAPHS AFTER EXPERIMENTAL STUDY .....	196

## LIST OF TABLES

### TABLES

Table 2. 1 Fracture toughness values of some commonly used materials .....	30
Table 2. 2 Mode II fracture toughness results for shear box test .....	50
Table 2. 3 Mode II fracture toughness values of some rock types determined by SCB test geometry .....	56
Table 2. 4 Results mode I and mode II fracture toughness tests .....	58
Table 2. 5 Mode II fracture toughness values for some rock types determined by CSTBD test geometry .....	62
Table 2. 6 Mode II fracture toughness of some rocks determined by SNDB test geometry.....	65
Table 4. 1 Dimensions of three-point bending plate .....	90
Table 4. 2 Comparative results for three-point bending plate.....	94
Table 4. 3 Geometric dimensions and material properties of the .....	96
Table 4. 4 Modeling parameters of base FPAB model .....	103
Table 4. 5 Boundary conditions for FPAB test geometry .....	105
Table 4. 6 Various loading configurations applied to a specific specimen $W= 50$ mm and $a/W= 0.3$ for pure mode II SIF $K_{II}$ .....	110
Table 4. 7 Loading configurations and computed mode I and II SIF's for the.....	111
Table 4. 8 Dimensionless short moment arm values corresponding to dimensionless crack lengths.....	112
Table 4. 9 Pure mode II results for all beam depth groups .....	117
Table 4. 10 Dimensionless mode II SIF results for present work .....	121
Table 5. 1 Results of static deformability test.....	131
Table 5. 2 Results of Brazilian tests.....	134
Table 5. 3 FPAB test results for $W= 40$ mm.....	139
Table 5. 4 FPAB test results for $W= 50$ mm.....	140
Table 5. 5 FPAB test results for $W= 60$ mm.....	141
Table 6. 1 Geometric dimensions and material properties of FPB test.....	149

Table 6. 2 Von Mises stresses for mode I loading .....	152
Table 6. 3 Von Mises stresses for mode II loading .....	153
Table 6. 4 Geometric dimensions and material properties of SNDB.....	157
Table 6. 5 Comparative study for SNDB numerical model .....	158
Table 6. 6 Geometric dimensions and material properties of tested .....	160
Table 6. 7 Mode II fracture toughness values acquired from SNDB test geometry	161

## LIST OF FIGURES

### FIGURES

Figure 1. 1 Famous troopships (Liberty Ships) of World War II.....	4
Figure 1. 2 Focused on to the crack region of the ship .....	5
Figure 1. 3 Ripped off roof of Aloha's Aircraft .....	7
Figure 1. 4 Rivet arrangement of an aluminum sheet .....	7
Figure 1. 5 Rivet hole fracture .....	8
Figure 1. 6 Negative state of stress for sign convention of ABAQUS .....	14
Figure 1. 7 Positive state of stress for sign convention of ABAQUS .....	15
Figure 1. 8 Direction of crack opening and sign of mode I stress intensity factor ....	16
Figure 1. 9 : Direction of crack opening and sign of mode I stress intensity factor $K_{II}$ .....	16
Figure 2. 1 Crack displacement modes .....	21
Figure 2. 2 Stress concentration around a hole .....	22
Figure 2. 3 Strain energy release and new crack surfaces.....	23
Figure 2. 4 Crack tip stresses .....	24
Figure 2. 5 Three point bend specimen.....	27
Figure 2. 6 Center notched specimen mode .....	29
Figure 2. 7 Crack tip opening displacement method.....	32
Figure 2. 8 J- contour integral with two arbitrary contours .....	33
Figure 2. 9 Schematic demonstration of hydraulic fracturing.....	35
Figure 2. 10 Rock cutting mechanism.....	36
Figure 2. 11 Thrust force direction regarding positions of cracks .....	38
Figure 2. 12 Geometry of PTS/CP test specimen .....	45
Figure 2. 13 Loading procedure and test setup of PTS/CP test .....	46
Figure 2. 14 Experimental setup of Rao et al.'s shear box test .....	48
Figure 2. 15 Dimensional parameters of shear box test.....	49
Figure 2. 16 Geometry of SCB test specimen.....	51

Figure 2. 17 Kinematics and deformed shape of SCB test specimen .....	53
Figure 2. 18 SCB test specimen with inclined crack.....	55
Figure 2. 19 CTSBD test specimen geometry.....	57
Figure 2. 20 Analytical approach to calculate.....	59
Figure 2. 21 SNDB test specimen geometry .....	63
Figure 3. 1 FPAB test specimen dimensions.....	70
Figure 3. 2 Generic 4-point asymmetric loading test specimen.....	71
Figure 3. 3 Solid and wireframe forms of FPAB test specimen from different views .....	72
Figure 4. 1 Illustration of degree of freedoms and RPs in ABAQUS .....	81
Figure 4. 2 Terms utilized in ABAQUS.....	82
Figure 4. 3 Seam crack in two dimensional body .....	84
Figure 4. 4 Seam crack in three dimensional body .....	84
Figure 4. 5 Contour integral regions for two dimensional body .....	85
Figure 4. 6 Contour integral calculation in three-dimensional modelling .....	86
Figure 4. 7 Collapsed duplicated nodes in 2-dimensional space.....	87
Figure 4. 8 Collapsed duplicated nodes in 3-dimensional space.....	87
Figure 4. 9 Geometry of the three-point bending plate .....	90
Figure 4. 10 Loading point of three-point bending plate problem.....	91
Figure 4. 11 Boundary conditions of three-point bending plate problem .....	91
Figure 4. 12 Crack tip meshing .....	92
Figure 4. 13 Meshed domain.....	93
Figure 4. 14 Loading and boundary condition configuration of the pure shear.....	95
Figure 4. 15 Applied load and boundary conditions of the problem.....	98
Figure 4. 16 Whole body meshing of pure shear plate.....	99
Figure 4. 17 Crack tip meshing of pure shear plate .....	100
Figure 4. 18 Geometry of FPAB test specimen .....	102
Figure 4. 19 One of loading and supporting points configuration for FPAB specimen .....	104
Figure 4. 20 Boundary conditions 1 .....	106
Figure 4. 21 Kinematic coupling of reference points.....	107

Figure 4. 22 Boundary conditions of reference points .....	107
Figure 4. 23 Contour integral region and meshing .....	108
Figure 4. 24 Whole body meshing .....	109
Figure 4. 25 Crack tip meshing .....	109
Figure 4. 26 Fit function for loading configuration satisfies absolute .....	111
Figure 4. 27 Beam depth 50 mm fourth order polynomial fit function for $d/W$ vs $a/W$ .....	113
Figure 4. 28 Beam depth 40 mm fourth order polynomial fit function for $d/W$ vs $a/W$ .....	114
Figure 4. 29 Beam depth 40 mm fourth order polynomial fit.....	115
Figure 4. 30 Average $d/W$ vs $a/W$ relationship; all beam depths .....	115
Figure 4. 31 Pure mode II SIF vs $a/W$ results for all three beam depth groups .....	118
Figure 4. 32 Undeformed shape of FPAB test geometry .....	119
Figure 4. 33 Deformed shape of FPAB test geometry .....	119
Figure 4. 34 Calculated dimensionless mode II SIF versus crack length in this study .....	122
Figure 4. 35 Average dimensionless SIF and fourth order polynomial fit function fo all beam depth groups .....	123
Figure 5. 1 Flow chart for experimental study .....	126
Figure 5. 2 Milling machine.....	127
Figure 5. 3 Digital caliper adapted diamond.....	128
Figure 5. 4 MTS 815 Rock Testing Machine at a glance.....	130
Figure 5. 5 After static deformability test rock .....	132
Figure 5. 6 Stress-strain curve for Ankara Gölbaşı Andesite.....	133
Figure 5. 7 Brazilian discs before testing.....	133
Figure 5. 7 Installation of Brazilian test.....	134
Figure 5. 9 Brazilian discs after test.....	135
Figure 5. 10 Different notch lengths for beam depth group $W= 60$ mm .....	137
Figure 5. 11 Specimen labelling rule .....	137
Figure 5. 12 Setup of FPAB test and specimen view after test.....	138
Figure 5. 13 Calculation of fracture toughness values.....	142

Figure 5. 14 FPAB test specimen after testing .....	143
Figure 6. 1 Von Mises yield surface .....	148
Figure 6. 2 General geometry of FPB test specimen.....	150
Figure 6. 3 Deformed shape of FPB test geometry .....	150
Figure 6. 4 Stress path for mode I loading .....	151
Figure 6. 5 Stress path for mode II loading.....	152
Figure 6. 6 Boundary influence effect for mode II loading .....	154
Figure 6. 7 Boundary influence effect for mode I loading.....	154
Figure 6. 8 Von mises stresses around stress path for mode I and mode II.....	155
Figure 6. 9 SNDB test specimen geometry .....	157
Figure 6. 10 Deformed shape of SNDB model .....	158
Figure 6. 11 SNDB test specimens.....	159
Figure 6. 12 Installation of SNDB test geometry.....	160
Figure 6. 13 Tested SNDB specimens .....	162
Figure A. 1 Dimensionless short moment distance for $a/W= 0.15$ regarding pure shear SIF conditions .....	183
Figure A. 2 Dimensionless short moment distance for $a/W= 0.20$ regarding pure shear SIF conditions .....	184
Figure A. 3 Dimensionless short moment distance for $a/W= 0.25$ regarding pure shear SIF conditions .....	184
Figure A. 4 Dimensionless short moment distance for $a/W= 0.30$ regarding pure shear SIF conditions .....	185
Figure A. 5 Dimensionless short moment distance for $a/W= 0.35$ regarding pure shear SIF conditions .....	185
Figure A. 6 Dimensionless short moment distance for $a/W= 0.40$ regarding pure shear SIF conditions .....	186
Figure A. 7 Dimensionless short moment distance for $a/W= 0.50$ regarding pure shear SIF conditions .....	186
Figure A. 8 Dimensionless short moment distance for $a/W= 0.60$ regarding pure shear SIF conditions .....	187

Figure A. 9 Dimensionless short moment distance for $a/W= 0.15$ regarding pure shear SIF conditions.....	188
Figure A. 10 Dimensionless short moment distance for $a/W= 0.20$ regarding pure shear SIF conditions.....	188
Figure A. 11 Dimensionless short moment distance for $a/W= 0.25$ regarding pure shear SIF conditions.....	189
Figure A. 12 Dimensionless short moment distance for $a/W= 0.30$ regarding pure shear SIF conditions.....	189
Figure A. 13 Dimensionless short moment distance for $a/W= 0.35$ regarding pure shear SIF conditions.....	190
Figure A. 14 Dimensionless short moment distance for $a/W= 0.40$ regarding pure shear SIF conditions.....	190
Figure A. 15 Dimensionless short moment distance for $a/W= 0.50$ regarding pure shear SIF conditions.....	191
Figure A. 16 Dimensionless short moment distance for $a/W= 0.60$ regarding pure shear SIF conditions.....	191
Figure A. 17 Dimensionless short moment distance for $a/W= 0.15$ regarding pure shear SIF conditions.....	192
Figure A. 18 Dimensionless short moment distance for $a/W= 0.20$ regarding pure shear SIF conditions.....	192
Figure A. 19 Dimensionless short moment distance for $a/W= 0.25$ regarding pure shear SIF conditions.....	193
Figure A. 20 Dimensionless short moment distance for $a/W= 0.30$ regarding pure shear SIF conditions.....	193
Figure A. 21 Dimensionless short moment distance for $a/W= 0.35$ regarding pure shear SIF conditions.....	194
Figure A. 22 Dimensionless short moment distance for $a/W= 0.40$ regarding pure shear SIF conditions.....	194
Figure A. 23 Dimensionless short moment distance for $a/W= 0.50$ regarding pure shear SIF conditions.....	195

Figure A. 24 Dimensionless short moment distance for $a/W= 0.60$ regarding pure shear SIF conditions .....	195
Figure B. 1 $W= 40$ mm $a/W= 0.20$ specimens after test .....	196
Figure B. 2 $W= 40$ mm $a/W= 0.25$ specimens after test .....	197
Figure B. 3 $W= 40$ mm $a/W= 0.30$ specimens after test .....	198
Figure B. 4 $W= 40$ mm $a/W= 0.35$ specimens after test .....	199
Figure B. 5 $W= 40$ mm $a/W= 0.40$ specimens after test .....	200
Figure B. 6 $W= 40$ mm $a/W= 0.50$ specimens after test .....	201
Figure B. 7 $W= 50$ mm $a/W= 0.20$ specimens after test .....	202
Figure B. 8 $W= 50$ mm $a/W= 0.25$ specimens after test .....	203
Figure B. 9 $W= 50$ mm $a/W= 0.30$ specimens after test .....	204
Figure B. 10 $W= 50$ mm $a/W= 0.35$ specimens after test .....	205
Figure B. 11 $W= 50$ mm $a/W= 0.40$ specimens after test .....	206
Figure B. 12 $W= 50$ mm $a/W= 0.50$ specimens after test .....	207
Figure B. 13 $W= 50$ mm $a/W= 0.60$ specimens after test .....	208
Figure B. 14 $W= 60$ mm $a/W= 0.20$ specimens after test .....	209
Figure B. 15 $W= 60$ mm $a/W= 0.25$ specimens after test .....	210
Figure B. 16 $W= 60$ mm $a/W= 0.30$ specimens after test .....	211
Figure B. 17 $W= 60$ mm $a/W= 0.35$ specimens after test .....	212
Figure B. 18 $W= 60$ mm $a/W= 0.40$ specimens after test .....	213
Figure B. 19 $W= 60$ mm $a/W= 0.50$ specimens after test .....	214

## LIST OF SYMBOLS AND ABBREVIATIONS

$2D$  : Two Dimensional

$3D$  : Three Dimensional

$a$  : Crack Length

$B$  : Specimen Thickness

$C3D8R$  : Continuum Three Dimensional Eight Node with Reduced Integration

$CCNBD$  : Cracked Chevron-Notched Brazilian Disc

$CPE8$  : Continuum Plane Strain Eight Node

$CSTBD$  : Cracked Straight through Brazilian Disc

$d$ : Short Moment Arm Distance

$D$  : Specimen Diameter

$E$  : Young's Modulus

$G$  : Strain Energy Release Rate

$G_c$ : Critical Energy Release Rate

$H$  : Height

$ISRM$  : International Society for Rock Mechanics

$J$  : J-Integral

$J_2$  : Second deviatoric stress invariant

$K$  : Stress Intensity Factor

$k$ : Stiffness

$K_{Ic}$  : Mode I Fracture Toughness

$K_{IIc}$  : Mode II Fracture Toughness

$K_I$  : Stress Intensity Factor in Mode I

$K_{II}$  : Stress Intensity Factor in Mode II

$L$  : Long Moment Arm Distance

$LEFM$  : Linear Elastic Fracture Mechanics

$P_y$  : Applied Load

$P_{cr}$  : Critical Load

$PTS/CP$  : Punch Through Shear with Confining Pressure

$R$  : Specimen Radius

$S$  : Support Span

$S_{11}$  : Stress Component in  $x$  –direction

$S_{22}$  : Stress Component in  $y$  –direction

$S_{33}$  : Stress Component in  $z$  –direction

$S_{12}$  : Shear Stress Component in  $xy$  –direction

$S_{23}$  : Shear Stress Component in  $yz$  –direction

$S_{23}$  : Shear Stress Component in  $xz$  –direction

$SCB$  : Semi-Circular Specimen under Three-Point Bending

$SNDB$  : Straight-Notched Disc Specimen under Three-Point Bending

$UCS$  : Uniaxial Compressive Strength

$Y_I$  : Normalized Stress Intensity Factor in Mode I

$Y_{II}$  : Normalized stress intensity factor in Mode II

$\varepsilon$  : Strain

$\mu$  : Shear modulus

$\sigma$  : Stress

$\sigma_c$  : Uniaxial Compressive Strength

$\alpha$  :  $a/R$

$\tau$  : Shear stress

$\nu$  : Poisson's ratio

$\theta$  : Crack propagation angle

## **CHAPTER 1**

### **INTRODUCTION**

#### **1.1 General remarks**

No matter how flawless and homogeneous they look, objects which are produced from the materials found in nature and ready to be used in daily life, possess flaws and defects like cracks even in micro scale. These defects act as stress concentrators within the structure when they are subjected to loading. Stress concentrations cause the defect to propagate and next whole body fails due to overstressed field generation at vicinity of the crack tip. Fracture mechanics is a branch of mechanics and it is related to the investigation effects of micro and macro scale cracks and crack-like defects on material behavior. More specifically, it investigates crack initiation and propagation behaviors of loaded solid sections of materials. Fracture mechanics benefits from other disciplines of mechanics as supportive fields; like solid mechanics, continuum mechanics, theory of elasticity and theory of plasticity in order to define relations between cracks and responses of the material.

Following load applications, local stress concentrations at the tip of cracks in the object material might be in quite large scales. Dimensions of these stress concentration zones are geometrically in small scales compared to the dimension of the main object material. Stresses concentrated at the crack tip can be in magnitudes exceeding the yield strength of the material; but in global sense material can still be acting stable. However, due to these stress concentrations at the tip of the small cracks, undesired results can emerge for the material under a certain load. Normally, yielding behavior of a loaded material without having any cracks is described by the classical mechanical approaches. Classical mechanical approaches define the stress

distribution in the material based on the mechanical properties of the material. For instance, stresses for a linear elastic material exhibit proportional distribution in the material body with respect to the loading location. Maximum load that the material can resist is related to the maximum stress in the material. These stresses are proportionally distributed and their distribution in the material can be predicted easily by classical global stress analyses methods and strength of the material techniques. For a material including cracks, assessing the strength of the material based only on global strength parameters is not the right approach, since under the same load much higher stresses exist at the crack tips.

In order to assess the behavior of cracks, stress analysis at the tip of the crack is to be carried out by using fracture mechanics methods and parameters such as stress intensity factor and critical energy release rate defined by fracture mechanics principles. With the stress values obtained by these methods, it is possible to compute the crack driving force. This way, complete failure or fracture mechanism can be described completely for a material inherently possessing cracks. Safe designs can be conducted based on these evaluations.

In the past when fracture mechanics principles were not applied and designs were conducted based on global strength parameters, many catastrophic accidents occurred. The most important of them which probably led to the acceleration of fracture mechanics studies is the famous Titanic accident. In that era, similar accidents occurred due to the conventional design of the body with carbon steel which exhibits extremely brittle behavior under freezing temperatures without taking cracks into consideration.

In rock mechanics applications, such as rock breaking, fragmentation, cutting and crushing the main purpose is to produce cracks, thus, fracture mechanics discipline plays an important role in assessing the input energy needed and mechanical methods that is to supply the input energy.

In summary, any material which is thought to be flawless inherently possesses defects and impurities. Thus, any design should include design against negative effect of cracks. Especially for the materials like rock which holds cracks and discontinuities owing to its nature, design based on fracture mechanics principles is to be considered, in addition to the design in terms of global design parameters.

Rocks are naturally formed materials with inherent discontinuities. For rock mass classifications and strength estimations, rock mass quality indices like RMR, Q, and GSI are available. Behavior and effect of discontinuities in these quality indices are treated in the geological sense rather than mechanical and total quality rating is penalized. In the evaluation entries, no parameter based on fracture mechanics principles is used. Moreover, direct relationship defined by the fracture mechanics between the inputs for the operations like hydraulic fracturing, rock ripping, rock excavation, blasting and the loading conditions exists. For example, in ripping process, shear mode (mode II) stress state is directly involved in stress distribution at the crack tips.

In this study, theoretical and laboratory works were conducted for the determination of the material property mode II fracture toughness of andesite rock. Based on the principals of fracture mechanics, modeling work was conducted to estimate the related stress intensity factor (SIF). Rectangular beam shaped rock specimens were chosen in laboratory testing works. As a loading configuration, four-point asymmetric bending type of loading condition were chosen in order to create shear effect on the crack front.

## **1.2 Historical development of fracture mechanics**

The major development of fracture mechanics study, such in other scientific and technological advances was driven by World War II. In addition, natively, mankind always had encountered many severe fracture induced problems as long as there have been man-made structures. The problems faced before, when it is compared to

today's conditions, were relatively more harmless. Nowadays, humankind has inevitable desire in aerospace, nautical structures, civil and automotive industries to have compatible designs with long service life-time almost without any failure. Especially, the failures aroused from defects cause catastrophic results and also crack propagation causes permanent malfunction or long term break-downs. Therefore, today's technology needs more flawless materials. Thereby more flawless materials need to have lesser flaws in it, in other words micro-cracks or defects.

Fortunately, advances in fracture mechanics have compensated some of the potential dangers above-mentioned high-tech desires. Unfortunately, advances in fracture mechanics were achieved by the lessons learned from the accidents experienced before. In Figure 1.1 one of these accidents is illustrated.



Figure 1. 1 Famous troopships (Liberty Ships) of World War II (Adapted from <http://forum.worldwarwhips.com>)

The knowledge of fracture mechanics has achieved terrific improvement especially after some catastrophic disasters in the history. In World War II, some of the famous troopships of World War II known as Liberty Ships fleet has sunk in Alaska. Ten ships have completely broken down into two pieces (Figure 1.2). This accident took attention into welded assemblies of the ships. Because, Liberty Ships had a construction method which uses welded connections between steel sheets of the main-body while the old ones used to be constructed with riveted construction method. Researchers concluded the debate proposing the causes of the disaster by following three dominant factors:

- ❖ The welds involved flaws and cracks; they were produced by poor-quality labor.
- ❖ Most of the fractures initiated on the deck at square shaped sharp corners where there was stress accumulation.
- ❖ Construction material, the ships made of was poor quality steel which had underqualified mechanical properties.

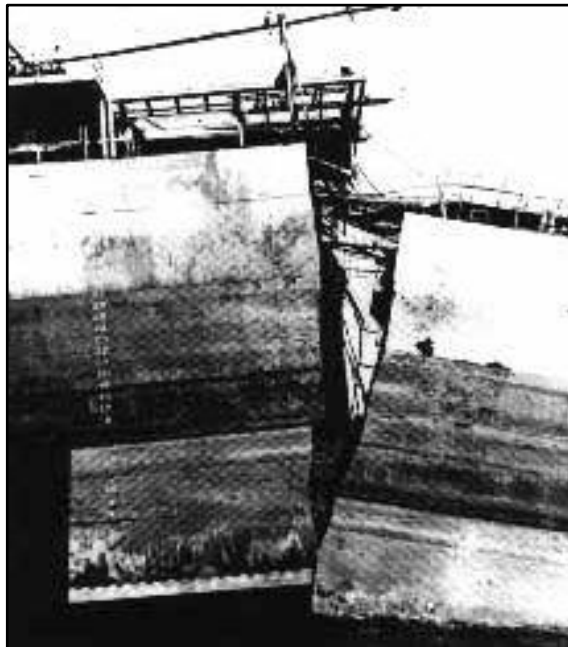


Figure 1. 2 Focused on to the crack region of the ship  
(Adapted from <http://forum.worldwarwhips.com>)

The steel, prime suspect of the accident, was questioned thoroughly by the investigators. Because, riveted ships had not experienced such issues while welded ones have problems with the same material. Riveting prevented the crack propagation across the steel panels. A welded deck which is composition of many welding joints showed behavior as if it was a single piece of metal. Therefore, this behavior made the whole metal sheet vulnerable with the contribution of man-made flaws to fracturing.

In order to overcome these fracture propagation problems and all other fracture issues, the researchers at Naval Research Laboratory U.S America have studied fractures in detail. They improved quality control standards and fracture mechanics study was born in this research center located Washington DC, during the decade following the World War II.

Another catastrophic disaster is the Comet plane disaster of civil aviation. Comet passenger jet aircrafts had made a breakthrough in commercial aviation in 1950's. However, after they serviced a few years a Comet exploded in the air unexpectedly; it shattered and all the cabin crew and passengers died instantly. Investigators have found that, aircraft's sharp edged rectangular window panes caused enormous stress accumulations in the vicinity of the frame corners and the material the aircraft was made of could not stand long flights over and over. Year after year Comet had become vulnerable to the internal cabin pressure so, one day in duty, it exploded for this reason. Thirty four years after the first Comet disaster; in April 28, 1988 the aircraft flight number 243 allied to Aloha Airlines was flying from Hilo Airport, Big Island to Honolulu International Airport. During flight due to the cabin pressure, roof of the aircraft was scraped off from the front side of the passenger cabin and caused crash-landing (Figure 1.3). Only one casualty was reported that was one of the cabin crew who was hurled out of the cabin by the reverse pressurization. Researchers from National Transportation Safety Board (NTSB) which is a federal foundation of USA have revealed that, rivet holes of the main-body having micro-fractures (Figure

1.5). These micro-cracks propagate through the body due to the cabin pressure and cause the aluminum sheet to disperse.



Figure 1. 3 Ripped off roof of Aloha's Aircraft (Adapted from National Geographic Channel documentary series “*Air Crash Investigation*” episode “*Hanging by Thread*”)

After this civil aviation accident, to prevent this rupturing failure arising from micro-fractures, special riveting design was applied to aircrafts. In case of any crack initiation within the hull, special designed rivet rows prevent all through propagation of the crack. Figure 1.4 this rivet array can be seen easily.

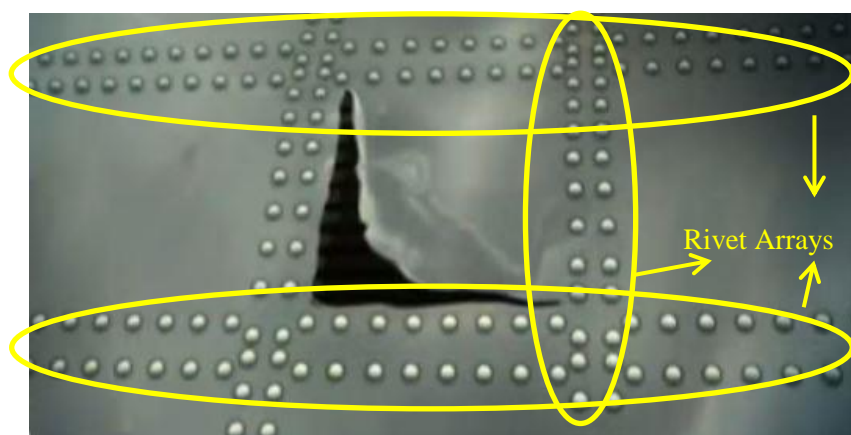


Figure 1. 4 Rivet arrangement of an aluminum sheet (Adapted from National Geographic Channel documentary series “*Air Crash Investigation*” episode “*Hanging by Thread*”)



Figure 1. 5 Rivet hole fracture (Adapted from National Geographic documentary series “*Air Crash Investigation*” episode “Hanging by Thread

All the causes of these undesired incidents were accomplished by the knowledge of fracture mechanics discipline. Fracture mechanics knowledge achieves progress with the investigation of researchers from many disciplines i.e. mechanical engineering, aerospace engineering, civil engineering and mining engineering.

From mining engineering point of view, material having in fracture problems is usually the rock material or various combinations of rocks in general. Mining structures, for example, mine shafts, production chambers, transportation galleries, slopes and etc. are developed through rock. In order to define the response of the rock to the man-made structures thoroughly, designers should consider both rock mechanics and fracture mechanics at the same time. As we know, rock have discontinuities inherently, those discontinuities govern the strength of the rock and stress redistribution behaviors when the rock is disturbed. In order to get comprehensive information about rock fracture mechanics, first, the basics of fracture mechanics should be understood properly.

The adaptation of toughness term used in fracture mechanics began with the study of Inglis (1913) about fractures and sharp edges. Inglis proposed that, defects or sharp edges within a plate may create stress concentrations many times of applied stress to the plate. He revealed defects that having smaller radius of curvature yields greater stress concentration. Then Griffith's works put the relation between strain energy and input energy for crack propagation (Griffith 192, 1924). He created the energy criterion for crack propagation and calculated the input energy to form new crack surfaces. Definition of parameter stated as fracture energy balance criterion  $G_c$  was made by Griffith. He revealed that  $G_c$  is proportional to  $\sqrt{a}$  which is the square root of initial crack length. Then, stress intensity factor "K" which is equal to  $\sigma \times \sqrt{a}$  approach was suggested.  $K$  was assigned to stress intensity factor term, and  $K_c$  was assigned to critical stress intensity factor or fracture toughness term. Crack tip stresses became mathematically identified by Westergaard's analytical solution (Westergaard, 1934).

### 1.3 Problem statement

Definition of mode II fracture toughness can be stated as, resistance of a crack to propagate due to acting in plane shear stress on it. Determination of mode II fracture toughness of rocks is a crucial work for rock mechanics applications such as hydraulic fracturing, rock cutting, and rock blasting. In addition, applications like nuclear waste disposal storage excavations and construction of storage sites in rock medium can benefit from rock fracture mechanics concepts. In geotechnical applications, rock medium is usually under the effect of compressive forces as a result of overburden stress. This increases the importance of shear mode crack formation and propagation under pure shear mode or under mixed mode involving compressive-shear mode over the crack surfaces.

Shear type mode II fracture toughness value of rocks is a useful parameter in rock breaking applications. In order to determine the mode I and mode II fracture toughness of a rock, certain methods have been suggested by ISRM. These are short

rod (SR), (Ouchterlony, 1988 and ISRM, 2014), chevron bend (CB), (Ouchterlony, 1988) and cracked chevron notched brazilian disc (CCNBD), (Shetty et al., 1985), semi-circular bending test (SCB) (Chong and Kuruppu, 1984), punch through shear with confining pressure (PTS/CP), (Backers, 2012) which is solely a mode II fracture toughness test. All these suggested methods are conducted on core based specimens. Especially, in determination of mode II fracture toughness of rocks, core based specimens have certain shortcomings. ISRM suggested punch through shear method for determination of mode II fracture toughness of rocks is only valid when the confining circumferential pressure is applied. Setting up this condition properly as proposed is practically rather difficult.

Beam shaped rock specimens eliminate mechanical shortcomings of core based specimens and difficulties of PTS/CP test specimen at the times in determination of mode II fracture toughness of rocks. The main problem associated with core based specimen geometries is that specimen size is limited to the core diameter and specimen shape is limited to circular sections. Applicability of FPAB test specimen and its performance on determining mode II fracture toughness  $K_{IIc}$  of rocks are challenging areas in rock fracture mechanics, since a well-developed mechanical background is available for beams. Geometrical parameters of the beam specimens can be changed easily for size effect and boundary influence issues. These aspects of beam shaped rock specimens should be investigated in detail by comparing results to those of the other core based testing.

#### **1.4 Objective of the study**

In the literature, there are limited investigations on FPAB test specimen. Ayatollohi and Aliha (2011) suggested geometric features of four-point asymmetric bending test. However, there was a drawback, suggested beam specimen was extremely long and thus practically hard to prepare. They suggested the dimensions of the beam as length ( $L$ ) 400 mm, width ( $W$ ) 40 mm and thickness ( $t$ ) 20 mm. He and Hutchinson (2000) proposed analytical expressions to find mode II stress intensity factor which

enables computation of mode II fracture toughness of a beam shaped specimen under four-point asymmetric bending type of loads. Analytical expressions proposed by He and Hutchinson for beams were constructed for infinitely thick beams under plane strain assumption. In reality, beam specimens have a finite thickness which requires 3D (three-dimensional) simulations and computations for a better accuracy in fracture toughness evaluations.

The main objective of this study is to determine mode II fracture toughness of rocks by performing four-point asymmetric bending (FPAB) test on beam shaped rock specimens. It covers specimen preparation phase with appropriate dimensions to generate the pure shear mode combinations for the beam and machined initial notch for shear mode fracture toughness testing of rocks.

Expanded objective of this study is to clarify and reveal appropriate geometrical features of the FPAB specimen to catch pure shear mode state at the preliminary notch tip. Figuring out loading and support points and their locations with respect to the crack plane is followed by the detailed objective related to the investigations of the stress fields at the crack tip regarding boundary influence effect and size effect of specimen.

## **1.5 Methodology of the study**

Methodology of this study is shortly structured by two parts which are numerical computation study and experimental study of four-point asymmetric loading test specimen. Numerical computation phase of this study actually was conducted before and after the laboratory testing phase. The first numerical computation study is performed to specify the loading configuration satisfying the pure shear state at the crack tip of the test specimen. This configuration consists of four asymmetric loading points which develop the shear type stress intensity factor effect on the crack plane. The second one was conducted after experimental work; acquired fracturing loads from experimental phase were implied to the corresponding numerical models and

then computation were conducted in order to find the shear type fracture toughness of the rock type, grey colored Ankara Gölbaşı Andesite.

Numerical modeling and computation studies were conducted utilizing Dassault Systemes' finite element package named ABAQUS v12. Software licensed by Middle East Technical University. Numerical models were created in three-dimensional space with six degree of freedoms assigned in every single node. Finite elements used in the numerical computation study selected as 8-noded 3-D stress elements which are hour-glass stress control enhanced. Crack tip stress singularity achieved by special finite elements called collapsed elements which were explained at Chapter 6 in detail. Validation of the numerical models was carried out by handling well-known fracture mechanics problems which are pure shear plate for mode II stress intensity factor and pure mode I stress intensity factor test specimen under three-point bending loading. Proper meshing was assured by mesh convergence studies applying different mesh amount and size.

Investigations about loading and support points and their locations and distances from crack plane were conducted.

In the experimental part of the thesis, grey colored Ankara Gölbaşı Andesite rock type is the choice due to its easily availability and its medium grained igneous texture. Test specimens are prepared as three main beam depth groups. For each group, different crack lengths are machined with varying notch length over beam depth ratios ( $a/W$ ) from 0.2 to 0.6.

In total, 64 specimens were prepared and tested. In testing work, servo-hydraulic MTS 815 stiff Rock Testing Machine was used. Fracture load readings were provided by the load cell which fits Turkish Standards Institute standards and certificated by Turkish Standards Institute (TSE). Experiments were conducted under displacement control by the software called MTS™ Series 793 Control Software

provided by MTS Company. Data acquisition is powered by MTS FlexTest 40 electronic controller console.

Finally, mode II fracture toughness values of grey colored Ankara Gölbaşı Andesite determined from four-point asymmetric bending (FPAB) test with specified geometric features were compared with straight notched disc bending (SNDB) test and discussions were made. Von-mises stress field were also analyzed in order to clarify behavior of mode II stress intensity factor of FPAB test specimen in terms of boundary influence effect and size effect.

## **1.6 Sign convention of mechanical entities**

In general mechanics study, positive orientation of stresses and displacements agrees with the positive direction of the related axes of coordinate systems. This means, compressive forces, stresses and displacements have negative sign while tensile ones have positive. On the other hand, in rock mechanics study opposite sign convention is utilized. Compressive forces, stresses and displacements are taken positive while tensile ones negative. In this study, sign convention of finite element code ABAQUS© were adapted which is same as general mechanics sign convention. ABAQUS© indicates the ordinary Cartesian coordinate system  $x, y, z$ ; as 1, 2, 3 respectively. In Figure 1.6 and 1.7, general tensor notation for ABAQUS and sign convention of the study can be seen easily.

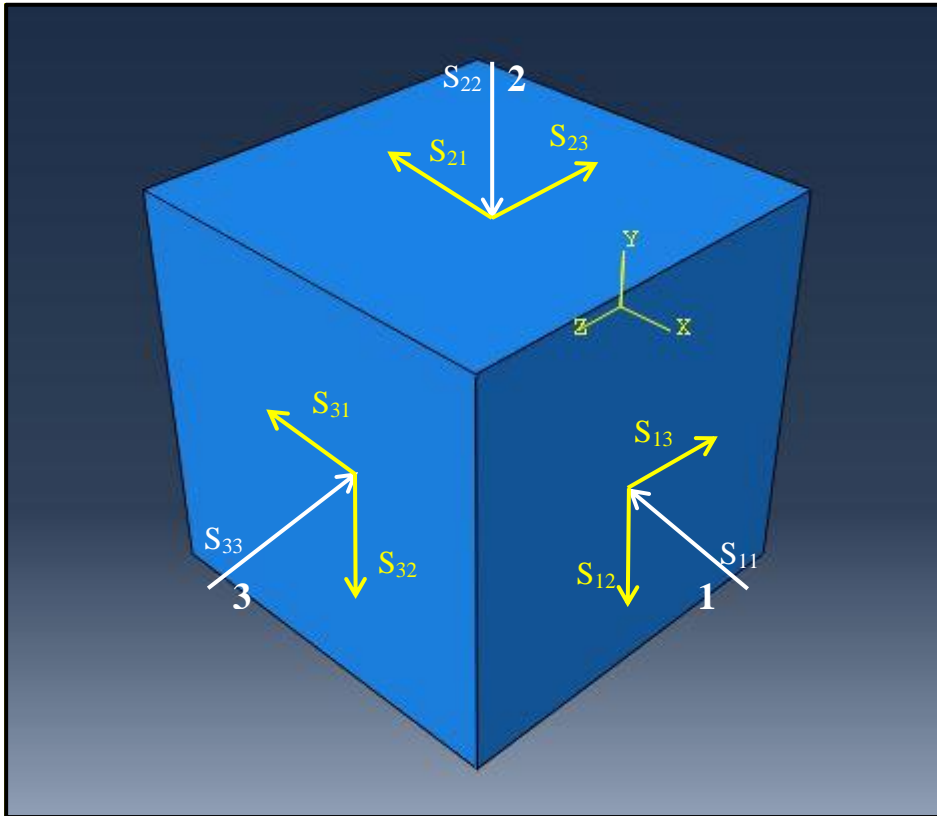


Figure 1. 6 Negative state of stress for sign convention of ABAQUS

As it is seen Figure 1.6, stress components of principle axes dictated as  $S_{12}$ ,  $S_{13}$ ,  $S_{21}$ ,  $S_{23}$ ,  $S_{31}$ , and  $S_{32}$ . This tensor notation corresponds to  $\tau_{12}$ ,  $\tau_{13}$ ,  $\tau_{21}$ ,  $\tau_{23}$ ,  $\tau_{31}$ , and  $\tau_{32}$  respectively. Principal axes x, y, and z correspond to 1, 2, and 3 respectively. All these principle directions and their components are in negative direction so, their signs are negative.

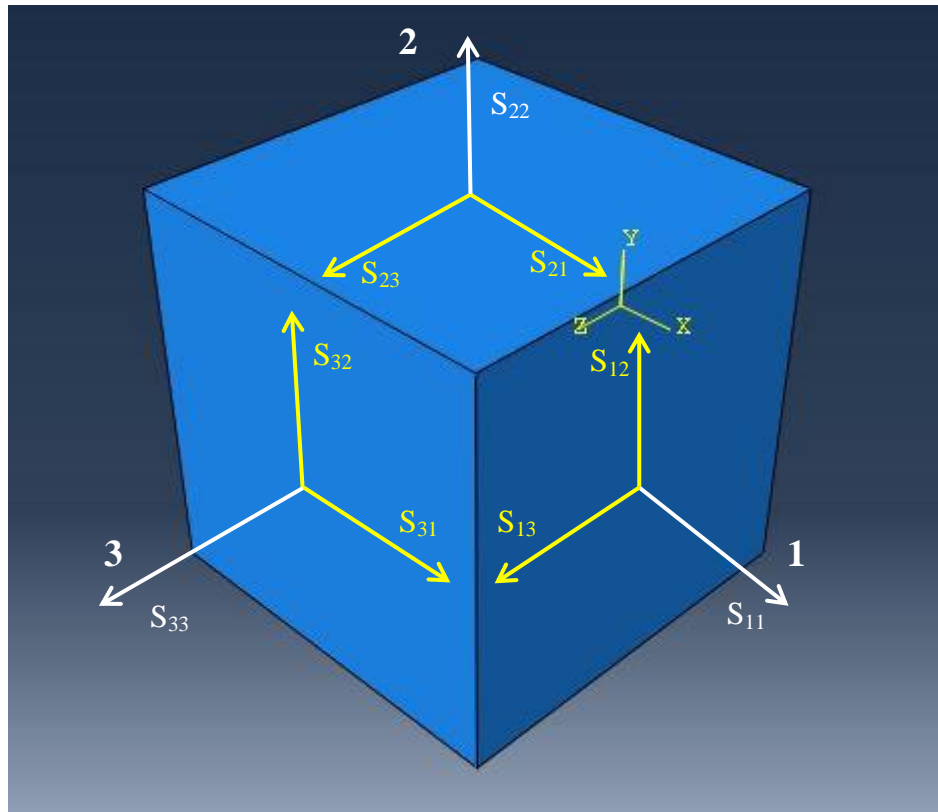


Figure 1. 7 Positive state of stress for sign convention of ABAQUS

Sign convention for stress intensity factor for mode I and mode II utilized in ABAQUS© is positive for  $K_I$  if crack tends to open, and negative if crack tends to close. Figure 1.8 shows the sign of mode I stress intensity factor  $K_I$ .  $K_{II}$  is negative when normal of zy plane pointing positive side of x-direction subjected to negative shear force ( $S_{12}$  or  $S_{21}$ ) when outward normal pointing positive direction of the out of plane. This definition is illustrated in the Figure 1.9.

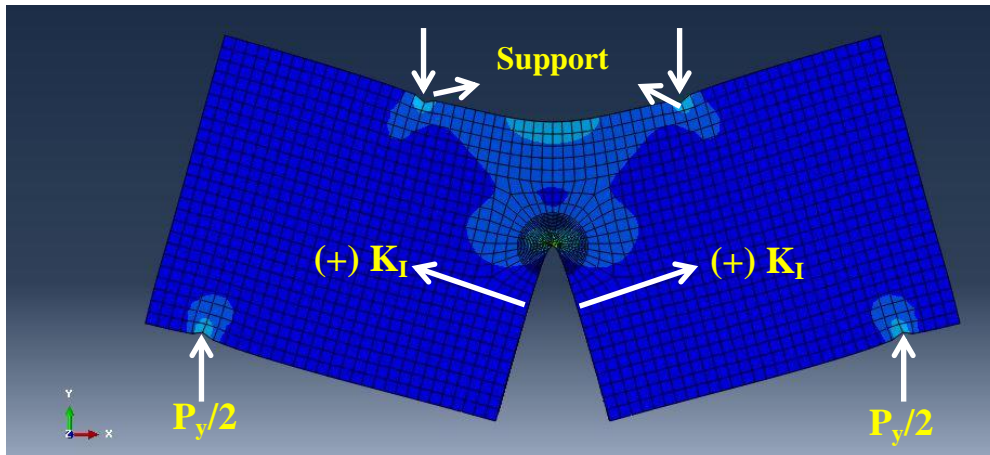


Figure 1. 8 Direction of crack opening and sign of mode I stress intensity factor  $K_I$  for FPAB test specimen

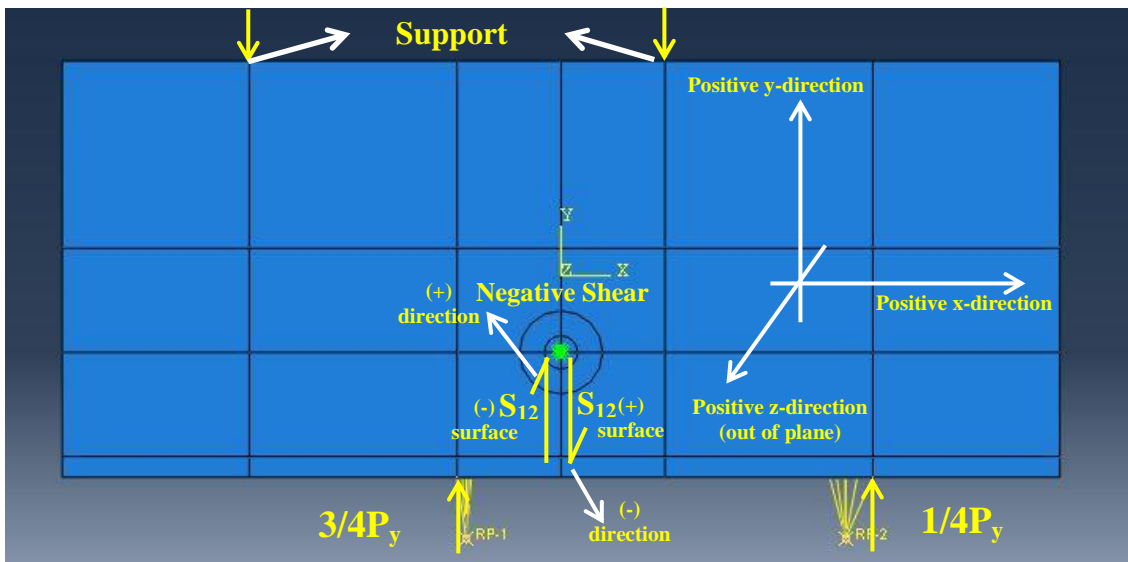


Figure 1. 9 : Direction of crack opening and sign of mode I stress intensity factor  $K_{II}$  for FPAB test specimen

### 1.7 Outline of the thesis

In Chapter 1, general remarks and a brief history of the fracture mechanics discipline are presented. In addition to this, problem statement and methodology of the thesis are given.

In Chapter 2, general background related to the theoretical development of fracture mechanics with formulas, definitions, and meaning of SIF concept, including well-known solutions (both mode I and II) for SIF's in plates and beams with references and literature review is presented. Application areas for rock fracture mechanics are reviewed. Utilization of rock fracture mechanics for some practices i.e. hydraulic fracturing, rock excavation and mine opening design etc. are reviewed with references from literature in chronological order. Importance of rock fracture mechanics in rock burst problems is given. Beam type specimen geometries for fracture testing are reviewed. Well-known three-point and four-point specimen geometries, solutions for SIF's for both core-based and rectangular sections, following the historical flow of related literature are given.

In Chapter 3, definitions of shear stress and bending moment are fulfilled and required mechanical prerequisites that satisfy pure shear effect on a deformable body are given. Four-point asymmetric bending (FPAB) test specimen is presented with its geometry and loading point configuration. Sketches for FPAB test specimen and  $K_{Ic}$  testing literature and analytical calculations are given.

In Chapter 4, modeling studies for stress intensity factor computation and utilized finite element code ABAQUS© and its structure are presented. Numerical verification problems are given. Boundary conditions, discretization and meshing of the FPAB test specimen are presented. Crack tip stress singularity issues and crack tip meshing with special finite elements are reviewed. Von Mises stress field contours and their meanings are presented for both  $K_I$  and  $K_{II}$  stress intensity factors. Results for numerical study conducted on mode II stress intensity factor with FPAB specimen are given.

In Chapter 5, experimental studies are presented. Test setup of four-point asymmetric bending (FPAB) test specimen is given. Testing machine and controller and their specifications are reviewed. Test procedures are also given. Results for mode II fracture toughness tests with FPAB test geometry are given.

In Chapter 6, stress analyzes for FPB and FPAB test geometries are given. Boundary influence effect and size effect phenomena are concluded. SNDB test specimen and its geometric features are given. Testing procedure and set-up for SNDB specimen are given. Numerical modeling study for SNDB test geometry is given. Accuracy level of numerical model of SNDB geometry is presented. Mode II fracture toughness values obtained from FPAB test and SNDB are compared.

In Chapter 7, conclusion of the thesis and recommendations for future works are presented .

## CHAPTER 2

### FUNDAMENTALS OF ROCK FRACTURE MECHANICS

The adaptation of toughness term used in fracture mechanics began with the study of Inglis (1913) about fractures and sharp edges. Inglis proposed that, defects or sharp edges within a plate may create stress concentrations many times of applied stress to the plate. He revealed defects that having smaller radius of curvature yields greater stress concentration. Then Griffith's works put the relation between strain energy and input energy for crack propagation (Griffith 1921 and 1924). He created the energy criterion for crack propagation and calculated the input energy to form new crack surfaces. Definition of parameter stated as fracture energy balance criteria  $G_c$  was made by Griffith. He revealed that  $G_c$  is proportional to  $\sqrt{a}$  which is the square root of initial crack length. Then, stress intensity factor "K" which is equal to  $\sigma \times \sqrt{a}$  approach was suggested.  $K$  was assigned to stress intensity factor term, and  $K_c$  was assigned to critical stress intensity factor or fracture toughness term. Crack tip stresses became mathematically identified by Westergaard's analytical solution (Westergaard, 1934).

Irwin (1957) introduced the crack tip failure modes regarding to principal stresses. He proposed mathematical relations of three failure modes as; mode I opening mode, mode II in plane sliding (shear mode), mode III out plane shear (tearing mode). He made the definition of critical energy release rate  $G_c$ . He proposed  $G_c$  as a material property and defined as critical energy input to create a new unit crack surface.

In 1960s crack tip plasticity investigations became concerned. Cottrell (1960) and Wells (1961) suggested crack tip opening displacement method as fracture criteria. Other approaches; "*Maximum Tangential Stress*" (Erdogan and Sih, 1963),

*“Maximum Energy Release Rate”* (Hussain and Pu, 1974) and *“Minimum Strain Energy Density”* (Sih, 1974) were proposed. Huge improvement was sustained by study of Rice (Rice, 1968). Rice generalized the crack tip plasticity issues suggesting a path independent line integral technique and proposed an analytical expression to calculate the both elastic and plastic energy around the crack tip. Because the calculations were based on stress invariants  $J_1$  and  $J_2$ , this technique is referred as  $J$ -Integral. Rice pioneered a new era for fracture mechanics study, and then elastic-plastic fracture mechanics studies became more reliable. After stress intensity factor (SIF) calculations became more reliable and easier, huge compendiums for SIF studies for different crack and specimen geometries were compiled by researchers (Tada et al., 1973; Rooke and Cartwright, 1976; Murakami et al., 1986).

Fracture mechanics is the science of cracked bodies. Cracks as stress concentrators are inherent impurities involved in materials or structures. Ordinary stress analysis is inadequate in specifying strength of cracked body because of stress concentration due to cracks. Stress intensity factor parameter proposed by fracture mechanics study enables to calculate amount of stress accumulated around a crack tip. This approach is quite acceptable compared to ordinary stress analysis techniques. In general, three different types of loading modes govern crack initiation and propagation. These are mode I, mode II and mode III. Mode I loading state is defined as opening mode because mode I loading condition compels the crack to open. Similarly, mode II is defined as sliding mode or in plane shear and finally, mode III is defined as tearing or out of plane shear. In Figure 2.1, three main crack displacement modes are illustrated.

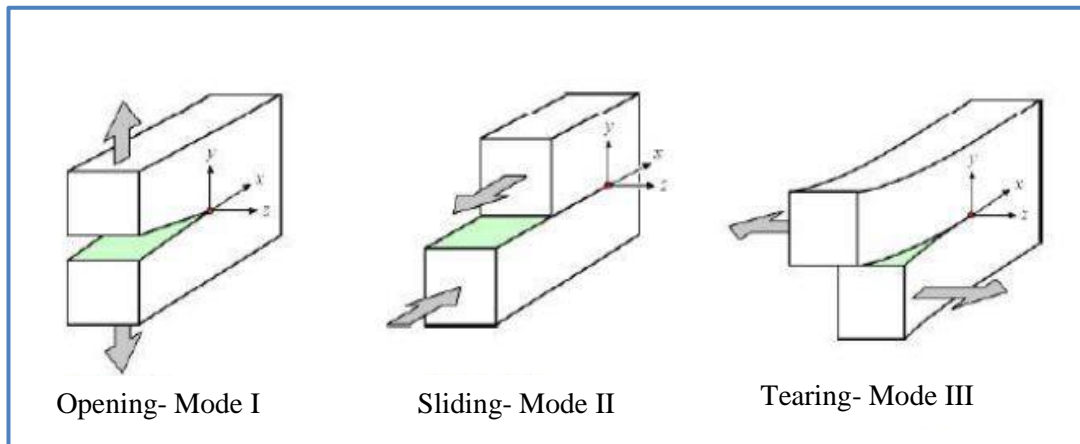


Figure 2. 1 Crack displacement modes

Fracture mechanics studies are divided into two main research groups: linear elastic fracture mechanics and elastic plastic fracture mechanics. In linear elastic fracture mechanics study, concerned structure or material is assumed to be linear elastic and isotropic while in elastic plastic fracture mechanics study nonlinearity and crack tip plasticity phenomenon are considered.

## 2.1 Linear elastic fracture mechanics

Definition of “*toughness*” began with the study of Inglis (1913). Inglis showed stress concentrations around a hole in a stressed domain. The amount of acting stress around the hole was considerably higher than the applied stress to the domain (Fischer-Cripss, 2007). In Figure 2.2, applied tensile stress and stress concentration around the hole can be seen.

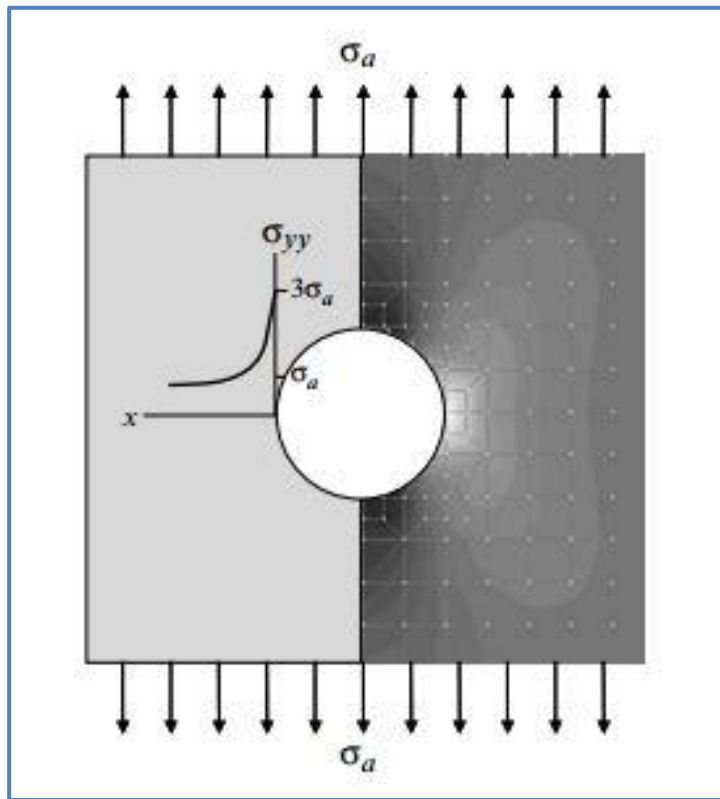


Figure 2. 2 Stress concentration around a hole (Adapted from Fischer-Cripps, 2007)

Inglis' study excluded one important parameter of cracked bodies. Excluded parameters were shape and size of the impurities. Griffith extended Inglis' study using elasticity theory. He combined strain energy knowledge with fracturing phenomenon. Griffith showed that when crack propagates it creates new surfaces and creating new surfaces requires energy. Therefore, creating new surfaces governed by the strain energy of the body. The balance between required energy input to create new crack surfaces and strain energy release was proposed as "*Energy Balance Criterion*" by Griffith (1921). An illustration is given in Figure 2.3 for energy balance criterion.

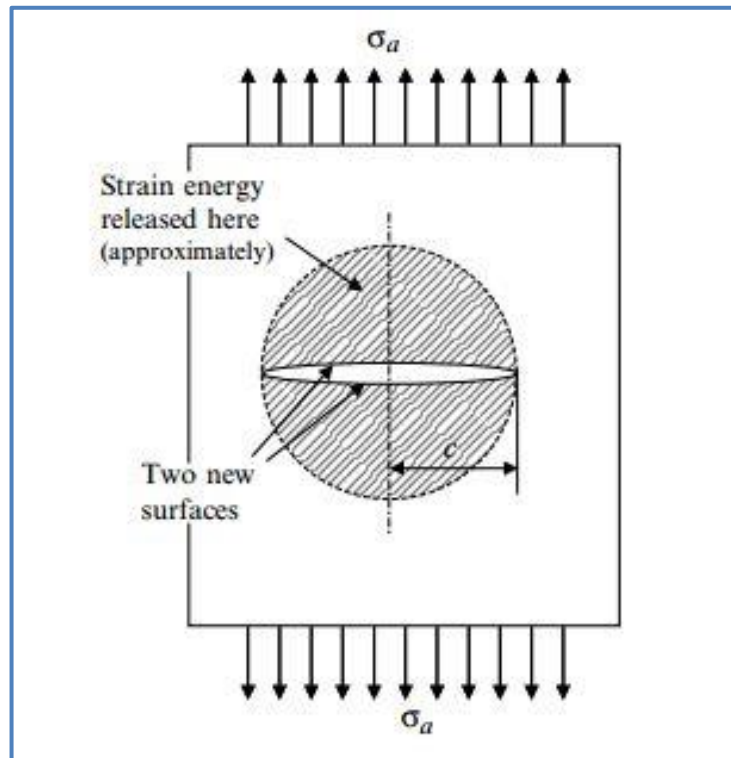


Figure 2. 3 Strain energy release and new crack surfaces  
(Adapted from Fischer-Cripss, 2007)

### 2.1.1 Crack tip stresses

Analytical expressions to calculate stresses and displacements around a crack tip (Figure 2.4) were proposed by Westergaard (1934) for mode I stress intensity factor. Then, the remaining analytical expressions for calculation of mode II and mode III crack tip stress and displacement were proposed by the study of Williams (1957). In the formulas below,  $K_I$ ,  $K_{II}$ , and  $K_{III}$  are stress intensity factors corresponding to the crack displacement modes defined before.

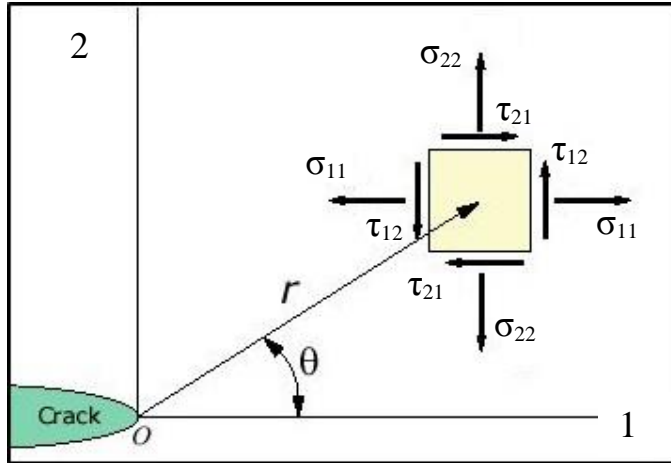


Figure 2. 4 Crack tip stresses

Singular stress field around a crack tip is proportional to inverse square root of distance “ $r$ ” from crack tip.

Analytical formulas for mode I crack tip stresses and displacement are;

Stress components;

$$\sigma_{11} = \frac{K_I}{\sqrt{2\pi r}} \times \cos \frac{\theta}{2} \times \left[ 1 - \sin \frac{\theta}{2} \times \sin \frac{3\theta}{2} \right] \quad (2.1)$$

$$\sigma_{22} = \frac{K_I}{\sqrt{2\pi r}} \times \cos \frac{\theta}{2} \times \left[ 1 + \sin \frac{\theta}{2} \times \sin \frac{3\theta}{2} \right] \quad (2.2)$$

$$\sigma_{33} = \begin{cases} 0 \text{ (Plane Stress)} \\ \nu \times (\sigma_{11} + \sigma_{22}) \text{ (Plane Strain)} \end{cases} \quad (2.3)$$

$$\tau_{12} = \frac{K_I}{\sqrt{2\pi r}} \times \cos \frac{\theta}{2} \times \sin \frac{\theta}{2} \times \cos \frac{3\theta}{2} \quad (2.4)$$

$$\tau_{13} = 0 \quad (2.5)$$

$$\tau_{23} = 0 \quad (2.6)$$

Displacements;

$$u_1 = \frac{K_I}{2\mu} \times \sqrt{\frac{r}{2\pi}} \times \cos \frac{\theta}{2} \left[ \kappa - 1 + 2 \times \sin^2 \frac{\theta}{2} \right] \quad (2.7)$$

$$u_2 = \frac{K_I}{2\mu} \times \sqrt{\frac{r}{2\pi}} \times \sin \frac{\theta}{2} \left[ \kappa + 1 - 2 \times \cos^2 \frac{\theta}{2} \right] \quad (2.8)$$

$$u_3 = 0 \quad (2.9)$$

$$\kappa = \begin{cases} \frac{3 - \nu}{1 + \nu} & (\text{Plane stress}) \\ 3 - 4\nu & (\text{Plane strain}) \end{cases} \quad (2.10)$$

Analytical formulas for mode II crack tip stresses and displacement are;

Stress components;

$$\sigma_{11} = -\frac{K_{II}}{\sqrt{2\pi r}} \times \sin \frac{\theta}{2} \times \left[ 2 + \cos \frac{\theta}{2} \times \cos \frac{3\theta}{2} \right] \quad (2.11)$$

$$\sigma_{22} = \frac{K_I}{\sqrt{2\pi r}} \times \sin \frac{\theta}{2} \times \cos \frac{\theta}{2} \times \cos \frac{3\theta}{2} \quad (2.12)$$

$$\sigma_{33} = \begin{cases} 0 & (\text{Plane Stress}) \\ \nu \times (\sigma_{11} + \sigma_{22}) & (\text{Plane Strain}) \end{cases} \quad (2.13)$$

$$\tau_{12} = \frac{K_{II}}{\sqrt{2\pi r}} \times \cos \frac{\theta}{2} \times \left[ 1 - \sin \frac{\theta}{2} \times \sin \frac{3\theta}{2} \right] \quad (2.14)$$

$$\tau_{13} = 0 \quad (2.15)$$

$$\tau_{23} = 0 \quad (2.16)$$

Displacements;

$$u_1 = \frac{K_{II}}{2\mu} \times \sqrt{\frac{r}{2\pi}} \times \sin \frac{\theta}{2} \left[ \kappa + 1 + 2 \times \sin^2 \frac{\theta}{2} \right] \quad (2.17)$$

$$u_2 = \frac{K_{II}}{2\mu} \times \sqrt{\frac{r}{2\pi}} \times \cos \frac{\theta}{2} \left[ \kappa - 1 - 2 \times \sin^2 \frac{\theta}{2} \right] \quad (2.18)$$

$$u_3 = 0 \quad (2.19)$$

Stress intensity factor defines the crack tip stress singularity. The magnitude of singular stress is referred as stress intensity factor and denoted as  $K$ . This factor is directly governed by amount of applied stress and crack length. Shape of the crack, geometry of stressed domain and boundary conditions of domain also have influence on stress intensity factor. Stress intensity factor solutions for some well-known loading and geometries are given in Figure 2.5 and 2.6. For beam type geometries and bending loading configurations, it is common to express stress intensity as following;

$$K = \sigma \times \sqrt{\pi \times a} \times f(a/W) \quad (2.20)$$

$$MPa\sqrt{m} = MPa \times \sqrt{(\pi \times m)} \times f(a / W)(dimensionless) \quad (2.21)$$

Where;

$K$ : Stress intensity factor

$\sigma$ : Applied stress to the domain

$a$ : Crack length

$f(a/W)$ : Correction function depending on crack length/beam depth ratio

It is important to note here that variations in material elastic properties like  $E$  and  $\nu$  do not effect SIF values, since these only depend on  $\sigma$  which is a function of loaded section geometrical parameters and applied loading, and on crack length  $a$ .

### 2.1.2 Typical geometries for mode I and mode II stress intensity factors

After mathematical expressions for SIFs and crack tip stresses derived, the researchers began to solve for SIFs of well-known geometries and specific loading types. Analytical solutions of mode I and mode II SIFs for beams and plates were given in “*The Stress Analysis of Cracks Handbook*” (Tada et al., 2000) and also in other compendiums. To give an idea about calculations of SIFs both mode I and II, typical geometries were given as follow;

*Three point bend beam for mode I SIF;*

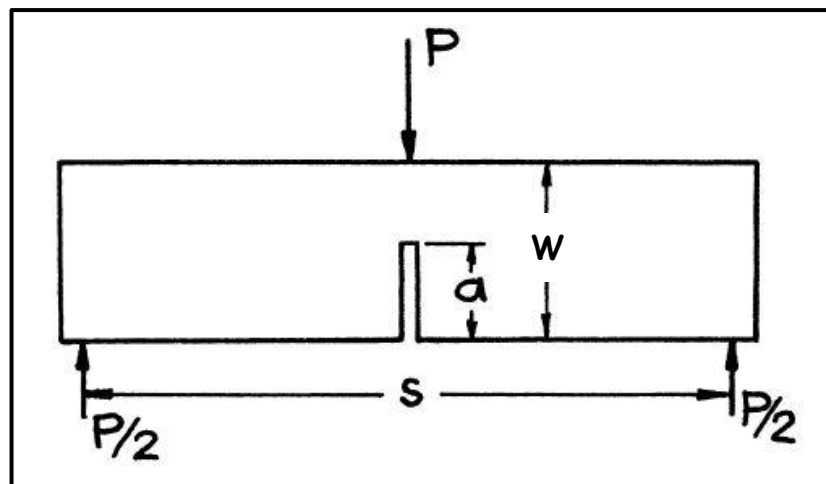


Figure 2. 5 Three point bend specimen (Adapted from Tada et al., 2000)

$$\sigma = \frac{6M}{b^2} \quad (2.22)$$

$$M = \frac{Ps}{4} \quad (2.23)$$

$$K_I = \sigma\sqrt{\pi a} F(a/W) \quad (2.24)$$

for  $s/W = 4$ ,

$$F(a/W) = \frac{1}{\sqrt{\pi}} \frac{1.99 - a/W (1 - a/W) (2.15 - 3.93(a/W) + 2.7(a/W)^2)}{1 + 2(a/W) (1 - (a/W))^{3/2}} \quad (2.25)$$

for  $s/W = 4$ ,

$$F(a/W) = 1.106 - 1.552(a/W) + 7.71(a/W)^2 - 13.53(a/W)^3 + 14.23(a/W)^4 \quad (2.26)$$

Where;

$\sigma$ : Effective stress on notch plane

$M$ : Bending moment

$P$ : Applied load

$s$ : Span length

$a$ : Notch length

$W$ : Beam depth

$F(a/W)$ : Geometric correction function

$K_I$ : Mode I SIF

$s/W$ : Geometric span ratio

*Center notched plate for mode II SIF;*

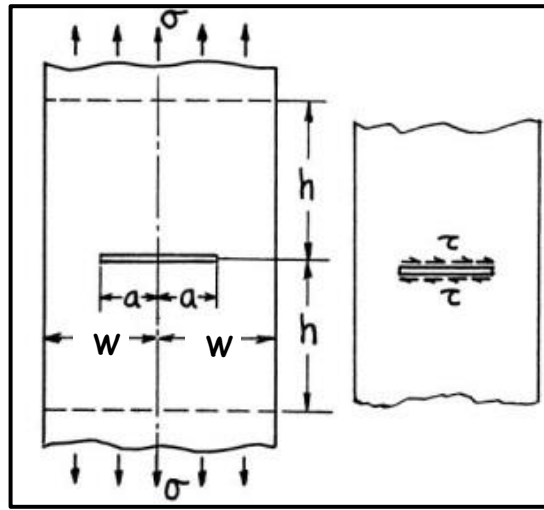


Figure 2. 6 Center notched specimen mode II SIF (Adapted from Tada et al., 2000)

$$K_{II} = \tau \sqrt{\pi a} F(a/W) \quad (2.27)$$

$$F(a/W) = \left\{ 1 - 0.025(a/W)^2 + 0.06(a/W)^4 \right\} \sqrt{\sec \frac{\pi a}{2W}} \quad (2.28)$$

Where;

$\tau$ : Effective shear stress on notch plane

$\sigma$ : Applied remote stress

$a$ : Notch Length

$W$ : Half plate depth

$h$ : Half plate height

$F(a/W)$ : Geometric correction function

$(a/W)$ : Dimensionless notch length

### 2.1.3 Fracture toughness

Fracture toughness is defined as critical form of stress intensity factor. Due to loading, stress intensity factor reaches a critical value, then, crack propagates. Stress based threshold for crack propagation is defined as fracture toughness and denoted as  $K_c$ . Fracture toughness as a material property is resistance of material to crack propagation (fracturing). Fracture toughness is directly governed by mechanical properties of material and geometry of the domain. To give an idea about the order of magnitude of fracture toughness of some commonly used materials, Table 2.1 is prepared from the literature listed in the table.

Table 2. 1 Fracture toughness values of some commonly used materials

Material Type	Material	Mode I Fracture Toughness $K_{Ic}$ MPa $\sqrt{m}$	Mode II Fracture Toughness $K_{IIc}$ MPa $\sqrt{m}$	Reference
Metals	Aluminum	14-28	-	ESDU 96013, 1996
	Steel	50	-	ESDU 83023, 1995
	Titanium alloy	44-66	-	Horiya and Kishi, 1994
Ceramics	Aluminum Oxide	3-5.3	$\approx 2$	Callister, 2007
	Silicon Nitride	7-8	$\approx 2$	Quinn et al., 1994
	Soda-Lime Glass	0.7	$\approx 0.4$	Callister, 2007
Rocks	Ankara Gölbaşı Andesite	1.12	0.61	Alkılıçgil, 2010 and Karakaş, 2011
	Gabbro	2.1	1.18	Het, 2014
	Marble	1.45	0.62	Alkılıçgil, 2010 and Karakaş, 2011
Concrete	Concrete C35	0.2-1.4	-	Callister, 2007

## 2.2 Elastic plastic fracture mechanics

Macroscopic stress applied to a structure or material (sometime called as remote stress) becomes infinite in the vicinity of crack tip as “ $r$ ” tends to “0”. In here “ $r$ ” is defined as distance from crack tip. As it is known, strength of a material is bounded by yielding stress and when the applied stress exceeds the yield stress, plastic deformation is occurred. The region near the crack tip which deformed plastically called as small scale yielding in fracture mechanics studies. Linear elastic formulations in this region are not valid. If this region is relatively too small, plasticity zones can be assumed as negligible and linear elastic fracture mechanics approaches can be utilized. However, if this region is not sufficiently small, instead of utilizing linear elastic fracture mechanics approaches, elastic plastic fracture mechanics approaches are employed. These approaches are “*crack tip opening displacement*” (CTOD) and “*J-contour integral*”.

### 2.2.1 Crack tip opening displacement

Wells (1961) showed that, as the initially sharp crack propagated, because of the plastic region around the crack tip it had transformed into blunted crack. He also revealed that, amount of blunting was proportional to toughness of the material. As the toughness of material increased, degree of blunting of initially sharp crack also increased. Therefore, a relationship between fracture toughness and degree of blunting of initially sharp crack was established mathematically by Wells. This approach is called as crack-tip opening displacement.

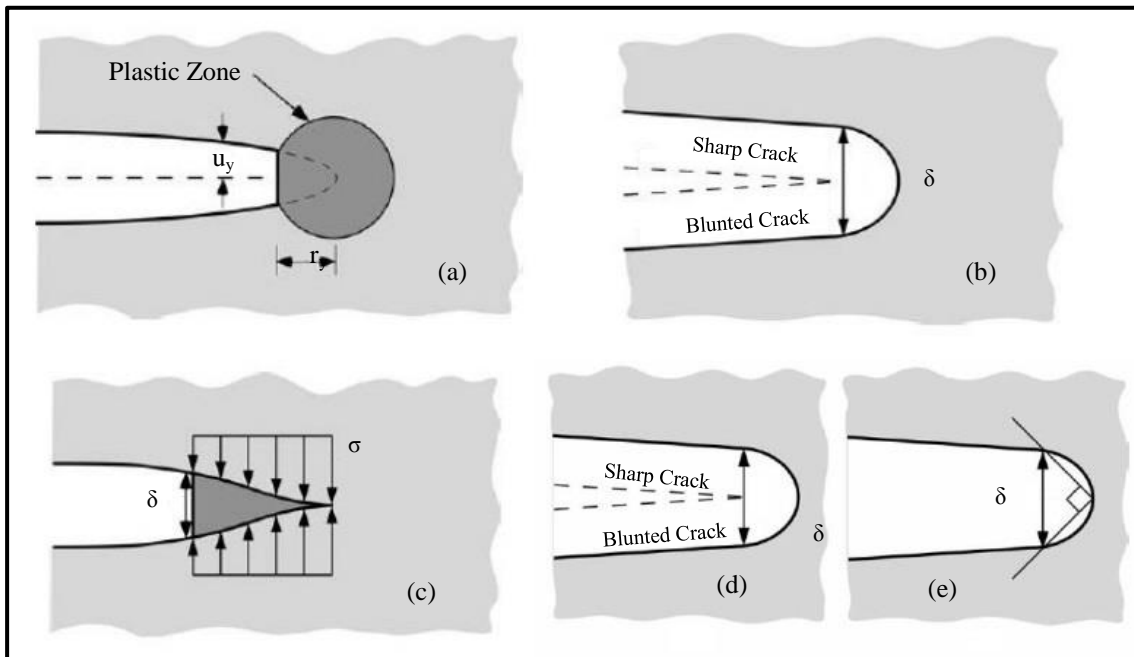


Figure 2. 7 Crack tip opening displacement method (Adapted from Anderson, 2005)

In Figure 2.7, crack tip opening displacement basics were given. a: plasticity zone near crack a tip and effective crack length, b: development of crack from sharp form to blunted form due to plasticity zone, c: calculation theory of crack tip opening displacement, d and e: best calculation technique for crack tip opening displacement (90 degree intercept lines radiated from crack tip).

### 2.2.2 *J*-contour integral

Rice (1968), proposed the *J*- contour integral to calculate the required input energy to create new crack surfaces. *J*- contour integral may be utilized for both linear elastic fracture mechanics and elastic plastic fracture mechanics. The theory of *J*-integral holds potential energy variation as the crack extends. This technique gives accurate results for the materials that obey plastic deformation mechanism. Mathematical expression is given as follows;

$$J = \int_{\Gamma} \left( W dy - T_i \frac{\partial u_i}{\partial x} d\Gamma \right) = \int_{\Gamma} \left( W n_1 - \sigma_{ij} \frac{\partial u_i}{\partial x} n_j \right) d\Gamma \quad (2.29)$$

Where;

$\Gamma$ : Arbitrary contour which begins from lower surface of the crack and extends to upper surface of the crack.

$n_j$ : Unit outward vector components which is normal to the arbitrary contour “ $\Gamma$ ”.

$T_i$ : Traction vector, product of  $\sigma_{ij}$  and  $n_j$  tensor notation in Cartesian coordinates

$$T_i = \sigma_{ij} n_j$$

$W$ : Strain energy density

$u_i$ : Components of displacement vectors

$d\Gamma$ : Differential arc length of contour  $\Gamma$  some books refer as “ $ds$ ”

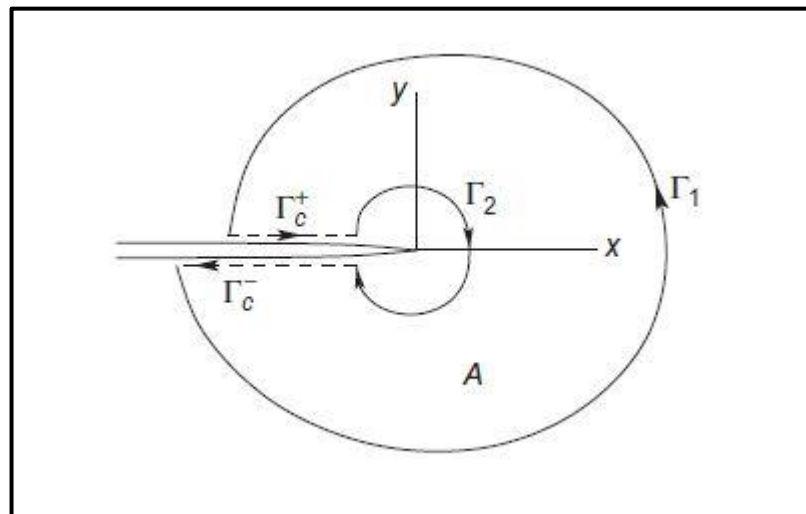


Figure 2. 8 J- contour integral with two arbitrary contours  
(Adapted from Sun and Jin, 2012)

## **2.3 Fracture mechanics in earth sciences practice**

Cracks and discontinuities are inherent for rocks. In applications dealing with rocks, such as rock excavations, tunneling, mining practices, hydraulic fracturing and rock slope stability studies, behavior of cracks and discontinuities should be identified properly. In general, fracture mechanics is utilized for defining fracturing process and to avoid fracturing by performing defect designs. In disciplines, such as; mechanical engineering, aerospace engineering and materials science, primary objective is to prevent the material of structural element or whole structure from fracturing. However, in rock fracture mechanics applications, the main idea here is to evaluate input energy for fracturing process. Because, in applications abovementioned, primarily task is to disintegrate the rock medium concerned.

### **2.3.1 Hydraulic fracturing**

Hydraulic fracturing (Figure 2.9) is a technique in which pressurized solution pumped into the rock formation to create fractures within the medium. This technique is utilized for oil extraction and production of special minerals in mining engineering. Boreholes are drilled into the rock medium and establishment of wells are configured as close loop. Fracturing resistance of rock is obtained from rock fracture mechanics studies. Input energy to create new fractures in rock medium is calculated and sufficient pressure is provided by pumps and the required amount of liquid for successful fracturing process is calculated. In hydraulic fracturing, both mode I and mode II crack opening modes are observed. However, during fracturing process, mode mixity effect is observed dominantly.

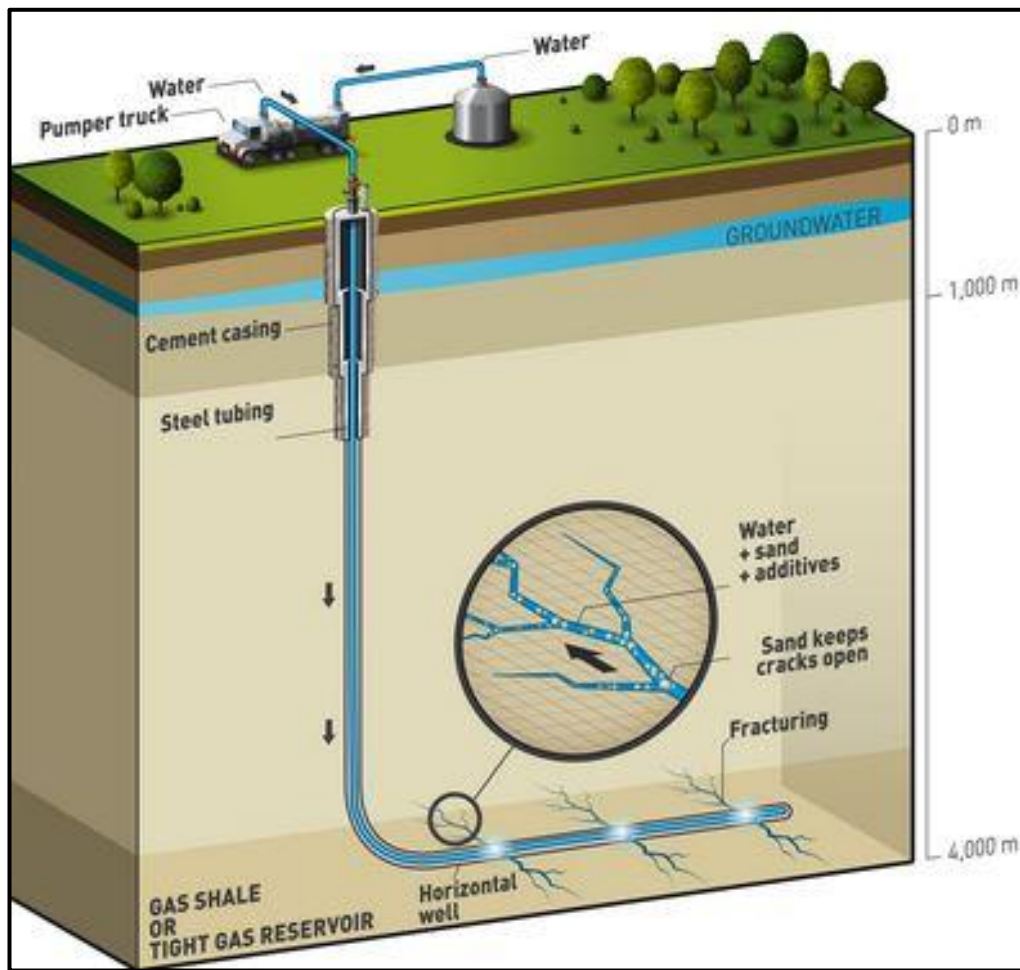


Figure 2. 9 Schematic demonstration of hydraulic fracturing (Adapted from <http://en.skifergas.dk/technical-guide/what-is-hydraulic-fracturing>)

### 2.3.2 Rock excavations

Rock excavations are conducted by blasting or using mechanical equipment. In rock blasting, energy provided by explosives is dissipated within rock medium and absorbed by crack tips. This energy is consumed to create new cracks. Thus, total breakage of rock medium is accomplished. This relation between fracture mechanics and rock mechanics is first proposed by Bienawski (1967).

Mechanical equipment utilized for rock excavations such as drag bits, hydraulic hammers, diggers and cutters create both compressive and shearing loads (Figure

2.10). Thus, both mode I and mode II loading on inherent cracks and discontinuities are applied. Grading equipment generates mode II effect while drag bits mode I. For an ordinary excavation both mode I and mode II and also mode mixity is observed. Well-known specimens applicability on rock excavations utilized in determination fracture toughness values of rocks were investigated by Xu (1993).

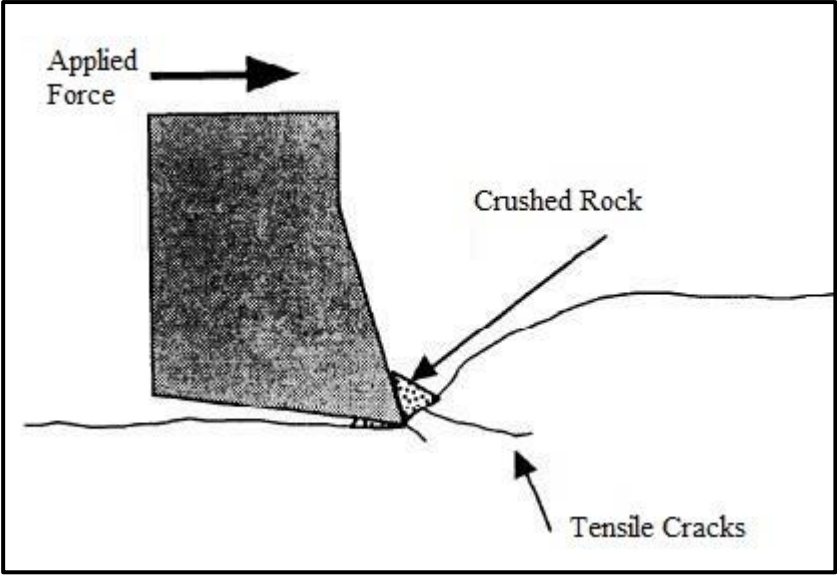


Figure 2. 10 Rock cutting mechanism (Adapted from Hood and Roxborough, 1992)

Relationship between rock excavation difficulties and fracture toughness values of rock investigated by a considerable number of researchers. Deliac (1986), proposed an expression for required amount of force to crush the rock. He referred this force as MPFC “mean peak cutting force”. Relation between MPFC and fracture toughness value of rock introduced as follows;

$$MPFC = C' \times K_{Ic} \times d^{3/2} \tag{2.30}$$

Where;

MPFC: Mean peak cutting force

C': Rock type coefficient

$K_{Ic}$ : Mode I fracture toughness value of rock

$d$ : Cutting depth

Similar to Deliac's study, another study to introduce the relationship between fracture toughness of rock and rock cutting mechanism was conducted by Guo (1990). Guo investigated the penetration rate of the excavation tool for five different rock types. Utilized rock types were sandstone, marble (fine grained and coarse grained), basalt and limestone. He showed that there was high correlation ( $R^2=0.90$ ) between fracture toughness values of these rocks and excavation difficulty degree. On the other hand, he proposed that, the only effective parameter for rock excavation mechanism was not fracture toughness but hardness of the rock also was an effective parameter. Relationship between penetration rate of the excavation tool and mode I fracture toughness of rock is given by following relationship;

$$\text{Penetration Rate of Excavation Tool} = 776.21 \times K_{Ic}^{-2.9109} \quad (2.31)$$

Another study was conducted by Zhou and Lin (2014). They investigated for the relation between brittle failure mechanism of rock and rock cutting process. The main purpose of the study was to introduce the whether size effect law exists for cut depth or not. They used beam type FPB (four-point bending) specimens to mimic the rock cutting process. Another reason utilizing FPB specimens was introduced as to investigate the size effect behavior of the rock. They observed size effect law for rock cutting process.

Another study for tunnel boring machine (TBM ) disc cutters and fracture toughness value of rock was conducted by Liu and Cao (2015). As it is known, TBM's are very efficient tools for rock excavation practices. TBM's are utilized for hard rock excavations if they are appropriate for rock medium characteristics and create fewer vibrations in comparison with blasting. The most effective usage of TBM's is provided by applying correct thrust to the excavation face. Optimum thrust depends on rock type and it is calculated by direct experimental methods. Liu and Cao

introduced relationship between the required thrust and fracture toughness of rock to cut and break the rock most effective way.

Another different aspect of this study is the given relationships for optimum cutting force to break the rock. They proposed two formulas both for mode I and mode II stress intensity factors regarding position of the crack. This assumption takes into account the layered rock mediums. Whether required input energy to break the rock is smaller regarding mode II loading than mode I loading conditions or not can be calculated by the given equations. Position of cracks regarded as median crack and lateral crack for mode I and mode II loading conditions respectively (Figure 2.11). Stress intensity factor for median crack is given as follows;

$$K_I = (\sigma_{t1}^* - \sigma)\sqrt{\pi(\sigma_{t1}^* - \sigma)}F \tag{2.32}$$

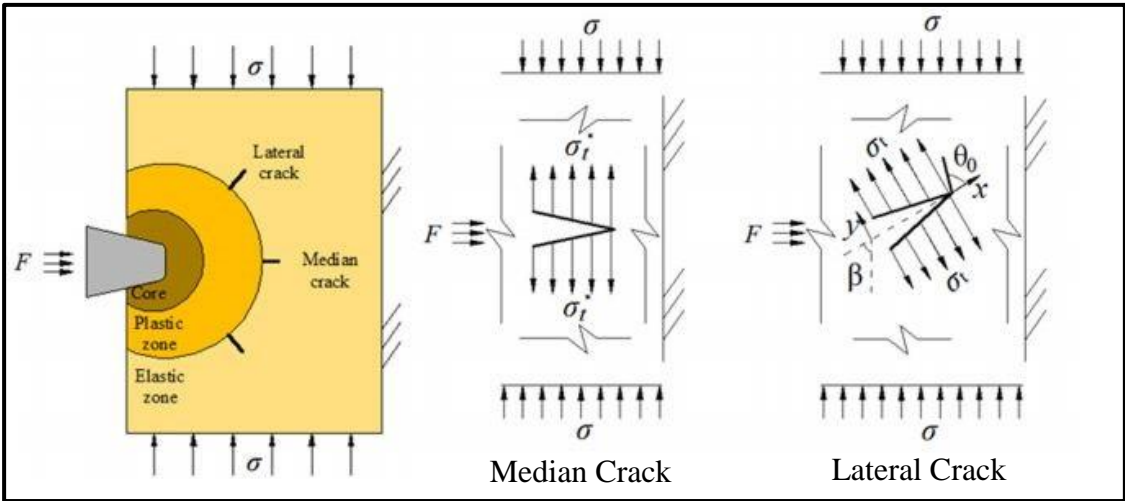


Figure 2. 11 Thrust force direction regarding positions of cracks (Adapted from Liu and Cao, 2015)

Where;

$K_I$ : Mode I stress intensity factor for median type crack

$\sigma_{t1}^*$ : Effective tensile stress on the crack plane

$\sigma$ : Remote stress (confining stress)

$F$ : Crack length constant

Position change of cracks creates different loading conditions. Lateral cracks will create mixed mode (mode I and mode II) loading conditions while median type cracks create mode I. They introduce following equations for such circumstances. In case of a lateral crack existence fracture angle  $\theta_0$  is given by;

$$\theta_0 = 2 \tan^{-1} \frac{\sqrt{1 + 8(K_{II} / K_I)^2} - 1}{4(K_{II} / K_I)} \quad (2.33)$$

They give mode I and mode II stress intensity factors as follow;

$$K_I = \sigma_t^{3/2} \sqrt{\pi} F \quad (2.34)$$

$$K_{II} = 0.5 \times \sigma [\sin 2\beta - f(1 - \cos 2\beta)] \sqrt{\pi a} \quad (2.35)$$

Where;

$K_I$ : Mode I stress intensity factor for lateral crack

$K_{II}$ : Mode II stress intensity factor for lateral crack

$\beta$ : Inclination of crack from vertical

$a$ : Crack length

$f$ : Friction coefficient of the crack

$\sigma_t$ : Maximum tensile stress

### 2.3.3 Rock slope stability engineering

Conventional rock slope engineering methods do not consider fracture mechanics parameters in determination of stability of rock slopes. These conventional methods assume the rock medium as a continuum. On the contrary, slope failures occur due to discontinuity surfaces of rock masses. A movement on these discontinuities initiates

from joints tips. Also, joint tips as stress concentrators may cause failures which are not able to detect with limit equilibrium methods. Limit equilibrium methods only consider kinematics of rock bodies and orientation of discontinuities.

Researchers have a common sense on that slope stability investigations excluding inherent impurities are not acceptable. So, especially in the last two decades, this topic has been investigated by the researchers. Chen and Wang (2004), analyzed stability of a rock slope subjected to dynamic loads with fracture mechanics parameters. Saouma (2010); reviewed some investigations which were made in the past.

#### **2.3.4 Rock bursts**

In the last three decades, mining activities are getting increasingly deeper in rock medium. As a result of this, rock bursts and coal bumps are begun to occur. Investigations (Zipf and Heasley, 1990, Heasley and Zelanko 1992, Maleki et al., 1995 and Innachione and Zelanko, 1995) showed that there is a direct relationship between rock bursts and energy release rate concept.

Firstly, energy release rate (ERR) concept as an indicator of coal bumps and rock bursts was proposed by Salamon (1963) and Cook (1965). These investigations were at deep hard rock mines in South Africa. This concept is shortly defined as, strain energy based rock burst phenomenon. Highly stressed rock in deeps tends to release its energy stored. This high stress causes strains within rock itself. Strain gaining characteristics of rock depend of its properties i.e. Young's modulus and Poisson's ratio. Strain energy concept has been used in mechanics for many years on the other hand, fracture based strain energy concept was built by fracture mechanics. As it is known from fracture mechanics knowledge, as the crack propagates energy release rate of the material increases and it tends to reach a critical value finally it causes to a catastrophic failure. This kind of failures worth many lives in mines. In order to

avoid casualties in deep hard rock mines fracture mechanics based strain energy release rate or energy storage rate concepts are crucial.

In underground mines, when a shaft or production opening is created, energy changes occur. First change is the work in physical meaning (potential energy) done by convergence of the back (roof) or deformation of opening surrounded by the rock mass. The second is the strain energy stored in rock medium. The sum of these two energies yields to total available energy. When mining operation advances this total energy is released by two ways. The first is strain energy increase and the second is dissipation by supports applied. As a matter of fact total dissipation energy can never be higher than total energy. This relationship is defined by following inequality;

$$W + U_m > U_c + W_s \quad (2.36)$$

Where;

$W$ : Potential energy of the system

$U_m$ : Strain energy stored in the rock mass

$U_c$ : Dissipated portion of strain energy stored in the rock mass

$W_s$ : Dissipated portion the energy by support pressure

From Equation 2.36 it is understood that, there is excess of energy. This energy should be dissipated somehow. Dissipation of this excess energy is occurred as kinetic energy (wave) if it is higher than strain energy stored in rock mass. Following equations introduce this relationship.

$$W_r = (W + U_m) - (U_c + W_s) > 0 \quad (2.37)$$

$$W_r \geq U_m > 0 \quad (2.38)$$

$$W_r = U_m + W_k \quad (2.39)$$

$$W_k = W - (U_c + W_s) \geq 0 \quad (2.40)$$

Where;

$W_r$ : Excess energy (the energy should be released)

$W_k$ : Kinetic energy

This kinetic energy is dissipated through new faces of advancing direction of the mine and crack and it damped by impurities located in rock mass. Therefore, local stress concentrations occur and it is concluded by rock bursts. Fracture toughness values of rock both for mode I and mode II are included in this phenomenon.

Energy changes can be assessed in terms fracture processes and fracture mechanics concepts. Energy release rate concept was utilized in fracture mechanics in study of Irwin (1957).  $G_c$  was introduced as fracture surface energy to create new cracks. This energy concept is given as follows for plane strain conditions,

$$G_c = \frac{K_c^2(1 - \nu^2)}{E} \quad (J/m^2) \quad (2.41)$$

In fracturing process  $G_c$  is a measure of energy input. Values for fracture surface energy can be assigned to the rock bursting medium by measuring  $K_{Ic}$  or  $K_{IIc}$  in tests, provided that linear elastic fracture mechanics assumptions are valid.

### **2.3.5 Application of fracture mechanics to the prediction of comminution behavior**

Not only researches for rock breakage in terms of rock excavations was conducted in literature but also comminution studies were placed. Bearman et al., (1997) studied the applicability of linear elastic fracture mechanics principles to predict comminution energy for rock particles. According to the study, mode I fracture

toughness  $K_{Ic}$  value of rocks can be predicted by performing Brazilian indirect tensile test and point load test. After,  $K_{Ic}$  value of rock sample was determined, they conducted a series of experiments. A correlation between drop weight parameters and  $K_{Ic}$  value of rock sample was observed. From these drop weight parameters they were able to predict the comminution energy. Finally, a comparative study was conducted utilizing bond mill and energy values obtained by drop weight tests. As a result of study they conducted, serious correlation between comminution energy and  $K_{Ic}$  value of rock was observed.

Donovan (2003) performed experimental study for optimum design of jaw crushers using rock fracture mechanics fundamentals. According to experiments, high correlated relationship was achieved between comminution energy and fracture toughness values of rocks particles. He introduced the following expression for jaw crusher parameters using fracture toughness values;

for  $1 \leq RR < 1.5$

$$P_c = \sum_i^j [-0.511 + 0.511RR_i]K_{Ic}C_i x_i + P_n \quad (2.42)$$

for  $RR \geq 1.5$

$$P_c = \sum_i^j [0.215RR_i^{0.428}]K_{Ic}C_i x_i + P_n \quad (2.43)$$

Where;

$P_c$ : Power consumption in Kw

$RR_i$ : Reduction ratio of particle size (subscript i denotes substantial fragmentation)

$K_{Ic}$ : Mode I fracture toughness ( $MPa\sqrt{m}$ )

$C_i$ : Breakage probability for particle size

$x_i$ : Mass flow for particle size (tons per hour)

$P_n$ : Idling power of the crusher

## **2.4 Mode II fracture toughness testing methods**

Laboratory testing of rocks are mostly conducted on core based specimens. The only reason of using core based specimens in laboratory experiments is that rock samples are originally extracted from boreholes. There is no other way to take rock samples from thousands of meters of deep rock formations with the available technology. As in ordinary laboratory experimental works of rocks, also in fracture toughness tests core based rock specimens are preferred.

International Society of Rock Mechanics (ISRM) suggests semi-circular bending test (SCB) for mode I fracture toughness determination and punch-through shear with confining pressure test (PTS/CP) for mode II fracture toughness determinations of rocks (ISRM, 2014).

Nevertheless, various experimental investigations for fracture toughness determination techniques of rocks for different specimen shapes and geometries have been conducted. To have an idea about those proposed testing methods for determination of fracture toughness of rocks the most important ones will be presented in this chapter.

### **2.4.1 The punch-through test with confining pressure**

Punch-through test with confining pressure is an improved form of study of Watkins, (1983). Watkins proposed this setup for cementitious soils and specimen prepared as cubic shaped for mode II fracture toughness determination. Then, Backers (2005), Backers et al., (2002a and 2002b) and Backers (2004) adapted to rock specimens to determine mode II fracture toughness. Backers (2004), changed the shape of specimen and configured this setup for core based rock specimens. In addition to these changes, Backers' setup enabled to apply confining pressure to the test specimen they proposed. Generic view of Backers' PTS/CP test specimen is illustrated in Figure 2.12.

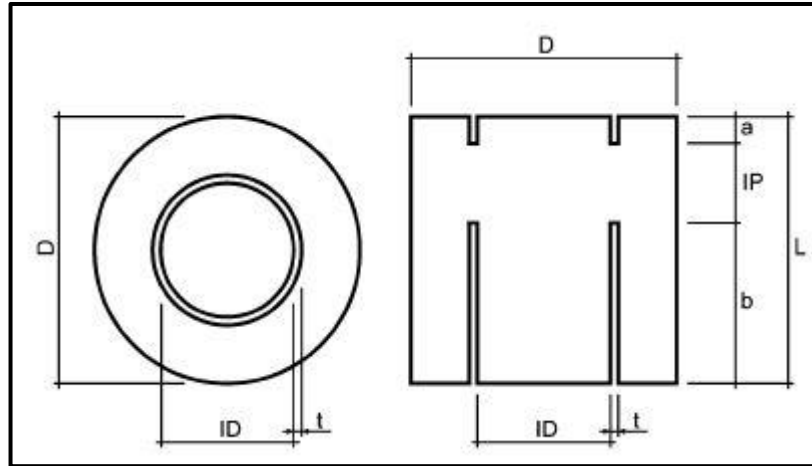


Figure 2. 12 Geometry of PTS/CP test specimen (Modified from ISRM, 2014)

Where;

D: Diameter of the test specimen

a: Notch length of upper end surface

b: Notch length of lower end surface

L: Length of the test specimen

t: Notch thickness

ID: Notch diameter

IP: Intact portion of the test specimen

Diameter and length of the PTS/CP test specimen are equal and notches are machined in circular shaped both end surfaces of the specimen. Both notches are concentrically aligned to each other. Instead for circular diamond saws, notches are generated by special machine which exhibit similarity with a core drill machine. The depth of circular notch machined upper end surface is  $0.1D$  and lower end surface is  $0.6D$ . Notches are machined with same the diameter which is  $0.5D$ .

Loading procedure of the test is relatively hard to perform. Specimen is placed on lower end surface onto support points (Figure 2.13). Coating membrane is suggested

to isolate the test specimen from confining pressure transmitting medium. Loading platen is placed to the upper end surface of the test specimen and it should be checked whether is aligned with support platen.

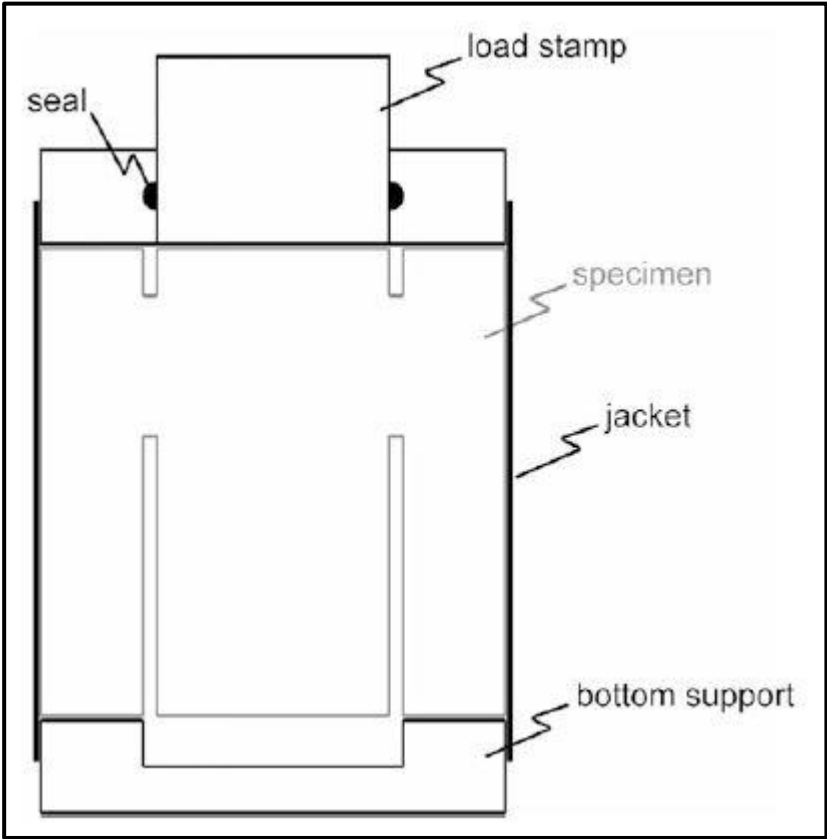


Figure 2. 13 Loading procedure and test setup of PTS/CP test specimen (Modified from ISRM, 2014)

Loading rate of experiment is suggested as 0.2 mm/min which is constant. Number of repeats of the test is suggested with a minimum of five specimens.

Mode II fracture toughness calculations are done by the proposed formula below (ISRM, 2014).

$$K_{IIc} = 7.74 \times 10^{-2} \times F_{max} \tag{2.44}$$

$$F_{max} = -1.80 \times 10^{-3} \times P_c \quad (2.45)$$

Where;

$K_{IIc}$ : Mode II fracture toughness in  $\text{MPa}\sqrt{\text{m}}$

$F_{max}$ : Fracturing load in kN

$P_c$ : Confining pressure in MPa

Backers declares that given formula above is only valid for the specimen  $L=D= 50$  mm,  $ID= 25$  mm,  $a= 25$ mm and  $b= 30$  mm.

### 2.4.2 Shear box test

Shear box test for determination of mode II fracture toughness of rocks was first proposed by Rao et al., (2003). They claim that maximum mode I stress intensity factor  $K_{I_{max}}$ , is always higher in terms of magnitude than maximum mode II stress intensity factor  $K_{II_{max}}$  under pure shear, pure tensile and shearing by compression and tensile loading conditions. On the contrary, brittle materials i.e. rocks, have smaller mode I fracture toughness  $K_{Ic}$  in comparison with mode II fracture toughness  $K_{IIc}$ . Therefore they claim, in experimental studies conducted with ordinary mixed mode tests maximum mode I stress intensity factor reaches  $K_{I_{max}}$  mode I fracture toughness  $K_{Ic}$  before maximum mode II stress intensity factor  $K_{II_{max}}$  reaches mode II fracture toughness  $K_{IIc}$ . Because of this reason they argue; mode II fracture toughness tests conducted on specimens that have mechanical loading configuration except for pure shearing always measure for  $K_{Ic}$  instead of  $K_{IIc}$ . For this reason, Rao proposed the shear box test for mode II fracture determination of rocks.

Both numerical and experimental studies were conducted in the study. Rao et al., (2003) utilized a finite element program to compute stress intensity factor named ALGOR FEA 3D. Experiments were conducted on three main strength groups from high to low of rock samples which are granite, marble and sandstone respectively. However, strength results of these three rock types are not in their order given by Rao. Strength order tabulated as from higher one to lower, marble, sandstone and granite respectively.

General form of a test specimen is cubic and the experimental setup of shear box test is given in Figure 2.14. Specimen can be configured both as single edge notched and double edge notched. Size effect and boundary influence effects were investigated by changing notch length and thickness of the test specimen.

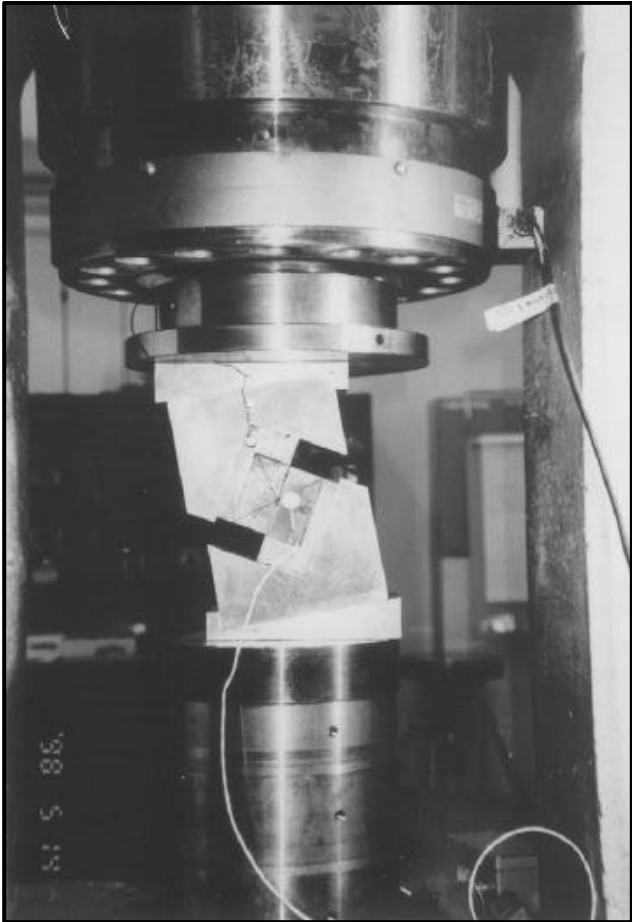


Figure 2. 14 Experimental setup of Rao et al.'s shear box test (Adapted from Rao et al., 2003)

Axial loading creates shear effect on the specimen due to beveled platens which are oriented to create shearing effect. Inclination of the platens and other dimensional parameters are given in Figure 2.15.

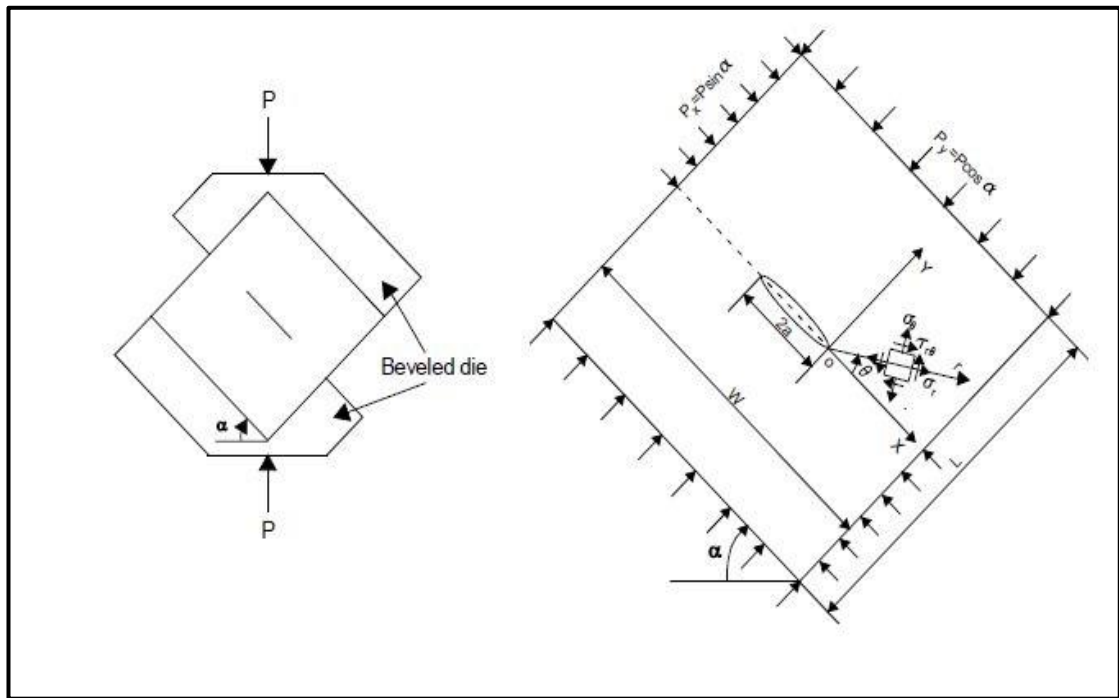


Figure 2. 15 Dimensional parameters of shear box test (Adapted from Rao et al., 2003)

Where;

$\alpha$ : Inclination of beveled platens

$P$ : Load

$W$ : Depth of the specimen

$L$ : Length of the specimen

$a$ : Notch length

Rao et al., (2003) give the following equations for pure mode II stress intensity factor calculations;

$$K_{II} = \frac{Q_e}{B\sqrt{W}} \times f(a/W) \text{ (for single edge notched specimen)} \quad (2.46)$$

$$K_{II} = \frac{Q_e}{B\sqrt{W}} \times f(2a/W) \text{ (for double edge notched specimen)} \quad (2.47)$$

$$F \times m^{-3/2} = \frac{F}{m \times m^{1/2}} \text{ (So, } P \text{ load is not distributed load)} \quad (2.48)$$

$$f(a/W) = \frac{2.138 - 5.2(a/W) + 6.674(a/W)^2 - 3.331(a/W)^3}{\sqrt{1 - (a/W)}} \quad (2.49)$$

$$f(2a/W) = 1.780 + 3.095(2a/W) - 10.559(2a/W)^2 + 8.167(2a/W)^3 \quad (2.50)$$

$$Q_e = P \times (\sin \alpha - \tan \phi \cos \alpha) \quad (2.51)$$

Where;

$K_{II}$ : Mode II stress intensity factor

$Q_e$ : Effective shear load

$B$ : Thickness of the specimen

$W$ : Width of the specimen

$f(a/W)$ : Geometric function for single edge notched specimen

$f(2a/W)$ : Geometric function for double edge notched specimen

$P$ : Applied load (concentrated load)

$\phi$ : Internal friction angle (in degrees)

$\alpha$ : Inclination of beveled platen (in degrees)

Pure mode II fracture toughness of tested rock types were given by Rao et al., (2003) as tabulated in Table 2.2.

Table 2. 2 Mode II fracture toughness results for shear box test (Rao et al.,2003)

Rock Type	$K_{IIc}$ MPa $\sqrt{m}$	$K_{IIc}/K_{Ic}$
Marble	6.1	Not given
Sandstone	5.0	Not given
Granite	4.9	2.6

### 2.4.3 Semi-circular bending test

Semi-circular bending test (SCB) is a suggested test method of ISRM (ISRM, 2014) for mode I fracture toughness determination. This specimen was presented by the study of Chong and Kuruppu (1984). Geometry of specimen is illustrated in Figure 2.16. Chong, who is inventor of SCB test specimen, summarizes advantages of SCB test specimen as follow;

- ❖ Requires very little machining of notch
- ❖ Easy experiment setup
- ❖ Enables compressive loading (previous tests are arranged as tensile loading)
- ❖ Appropriate for brittle materials i.e. rocks, ceramics, concrete etc. which are weak in tension
- ❖ Appropriate for size effect
- ❖ Enables easier data acquisition

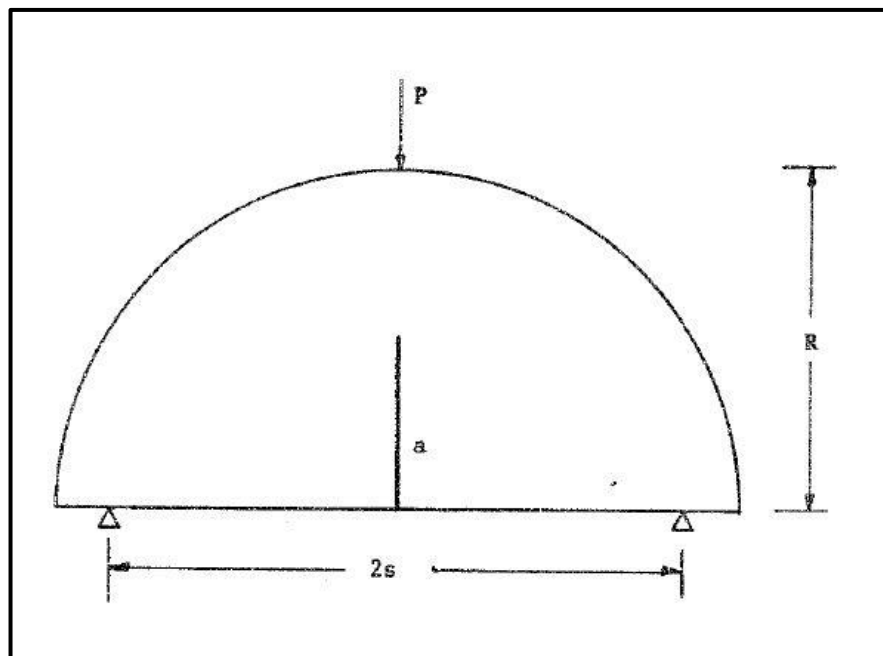


Figure 2. 16 Geometry of SCB test specimen (Adapted from Chong and Kuruppu, 1984)

Chong defines the parameters of SCB test specimen as follow;

$a$ : Notch length

$l$ : Half gage length between knife edges

$q$ : Load line displacement

$r$ : Rotational factor

$R$ : Radius of SCB test specimen

$s$ : Half span

$v$ : Crack mouth opening between knife edges

$x$ : Vertical distance between load point and supports

$z$ : Thickness of knife edges

$\theta$ : Half angle of rotation

$\alpha$ : An angle constant

Kinematics of SCB test specimen and calculation deformed shape factors were also given by Chong and Kuruppu (1984). Schematic view of deformed shape of SCB test specimen with its kinematics illustrated in Figure 2.17.

Crack mouth opening between knife edges were given as;

$$v = \Delta v + 2l = 2[r(R - a) + a + z] \frac{\sin(\alpha + \theta)}{\cos \alpha} \quad (2.52)$$

Where;

$$\tan \alpha = \frac{l}{r(R - a) + a + z} \quad (2.53)$$

Here;  $\Delta v$  is crack mouth opening displacement. Center of rotation is defined at a distance  $r(R - a)$  from crack tip.

Vertical displacement between load point and support points of deformed shape was given as;

$$x = P'Q + QT - KT = (1 - r)(R - a) + [r(R - a) + a + z] \frac{\cos \alpha + \theta}{\cos \alpha} \quad (2.54)$$

$$-[(s - l) \sin \theta + z \cos \theta] \quad (2.55)$$

Load line displacement was given as;

$$q = PP' = R - x \quad (2.56)$$

Rotation angle was given as;

$$\theta = \sin^{-1} \left\{ \frac{(\Delta v + 2l) \cos \alpha}{2[r(R - a) + a + z]} \right\} - \alpha \quad (2.57)$$

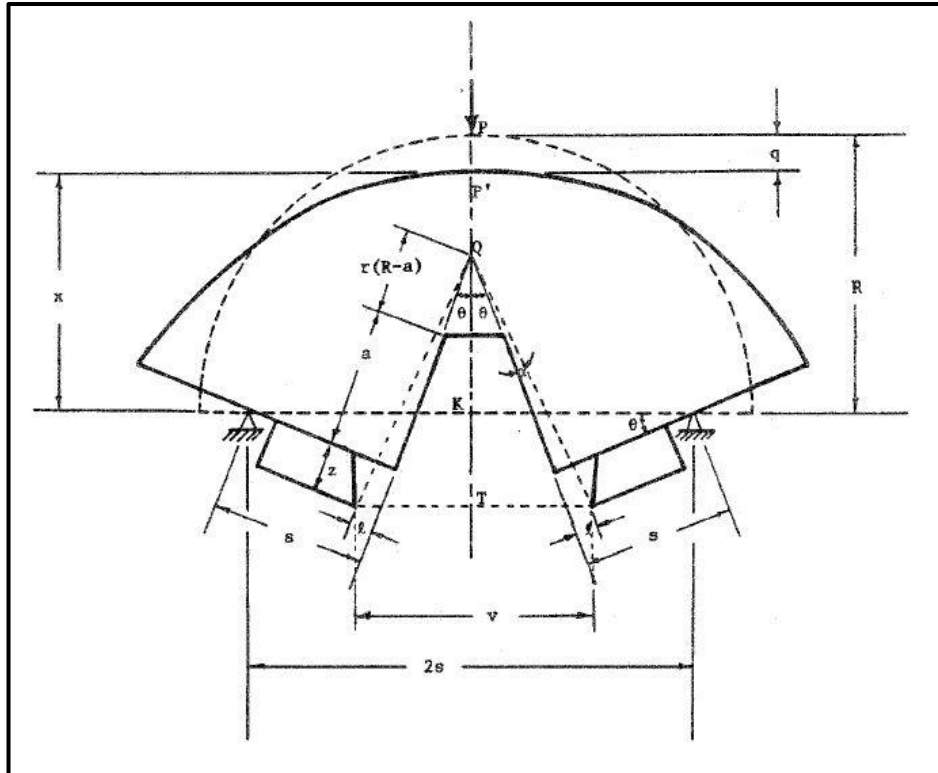


Figure 2. 17 Kinematics and deformed shape of SCB test specimen (Adapted from Chong and Kuruppu, 1984)

Whittaker et al., (1992) suggested that crack inclination for pure mode II stress intensity factor calculation as  $63^\circ$ .

Lim et al., (1993) conducted numerical computations for a wide range of specimen geometries utilizing ABAQUS finite element software as a computation tool. As a result of the numerical computations on stress intensity factors for possible specimen geometries of SCB test specimen analytical expressions were derived for mode I fracture toughness determination. Their work covered numerical computation of SCB test specimens for different crack length/radius ( $a/r$ ) ratios from 0.1 to 0.8, notch angles from  $0^\circ$  to  $75^\circ$  and span length/radius ( $2S/r$ ) ratios. From the results of these computations, the following expression was proposed in terms of mode I normalized stress intensity factor. In Figure 2.18, SCB test specimen with inclined crack can be seen.

$$Y_I = \frac{K_I}{\sigma_0 \sqrt{\pi a}} \quad (2.58)$$

Where;

$Y_I$ : Dimensionless stress intensity factor for mode I

$K_I$ : Stress intensity factor for mode I

$a$ : Notch length

$$\sigma_0 = \frac{P}{2rt}$$

$P$ : Applied load (concentrated load)

$r$ : Radius of test specimen

$t$ : Thickness of test specimen

Lim et al., (1994) conducted for this time for various geometric parameters of SCB test specimen. SCB specimens were prepared for three different radiuses which are 55, 95, 144 mm and a range of specimen thickness which are from 11.9 to 43.9 mm. Combination of results of these two studies were concluded as SCB is an appropriate test specimen for mode I fracture toughness experiments (Figure 2.18).

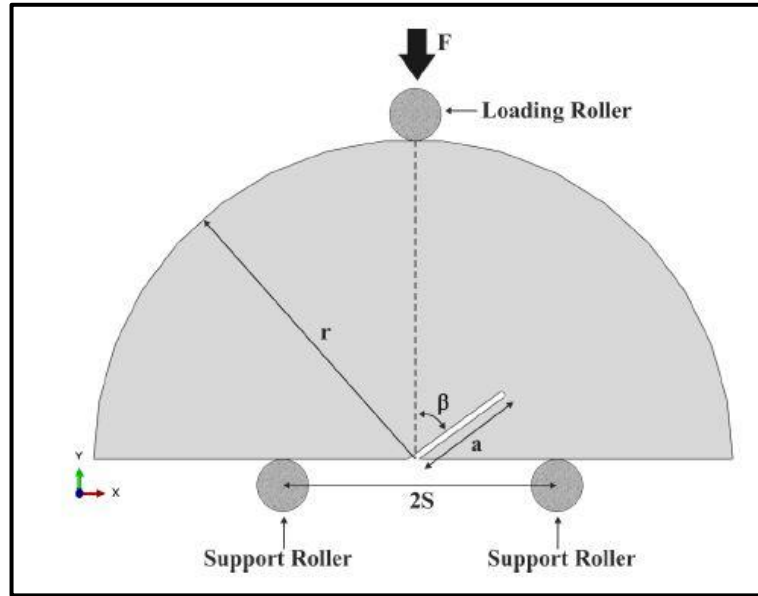


Figure 2. 18 SCB test specimen with inclined crack (Adapted from Het, 2014)

More investigations on SCB test specimen were conducted by the researchers. Ayatollahi et al., (2006) performed mode I and mode II tests on PMMA and concluded by a contradiction on analytical and experimental results of mode II stress intensity factors. Ayatollahi and Aliha (2007) compared the results of SCB and CSTBD experiments for mode I, mode II and mixed mode I-II fracture toughness determination. This study revealed that CSTBD test specimen causes high amount of stress singularity due to its sharp crack compared to SCB specimen. Aliha and Ayatollahi (2011) performed mixed mode I-II fracture toughness tests to introduce whole range from pure  $K_I$  to pure  $K_{II}$ . As a result, the ratio of  $K_{IIc}/K_{Ic}$  was found as 0.4. Tutluoglu and Keles (2011) reported limited numerical results for the ranges  $0.4 \leq \beta \leq 0.6$  and  $0.5 \leq s/2R \leq 0.8$ .

Table 2.3, mode II fracture toughness of some rock types determined by SCB test geometry were listed.

Table 2. 3 Mode II fracture toughness values of some rock types determined by SCB test geometry

<b>Rock Type</b>	<b>Mode II Fracture Toughness MPa<math>\sqrt{m}</math></b>	<b>Reference</b>
Ankara Gölbaşı Andesite	0.43	Karakaş, 2011
Marble	0.46	Karakaş, 2011
Gabbro	0.92	Het, 2014

#### **2.4.4 Cracked straight through Brazilian disc**

Ayatollahi and Sistaninia (2011) declare that, cracked straight through Brazilian disc test specimen is a cored based specimen that allows diametrical compressive loading and a relatively easy test setup. Raw rock samples extracted from core drills are convenient for preparing CSTBD test geometry and require very little adjustment. CTSBD test specimen involves centered notch and orientation of the notch enables capability of different modes of crack initiation and propagation. Changing notch orientation with respect to diametrical loading points enables a wide range of stress intensity factors from pure mode I to pure mode II. These advantages make CTSBD test geometry ideal specimen for experimental program of mode I, mode II and mixed mode I-II fracture toughness determination of rocks. In Figure 2.19 CSTBD test specimen geometry can be seen.

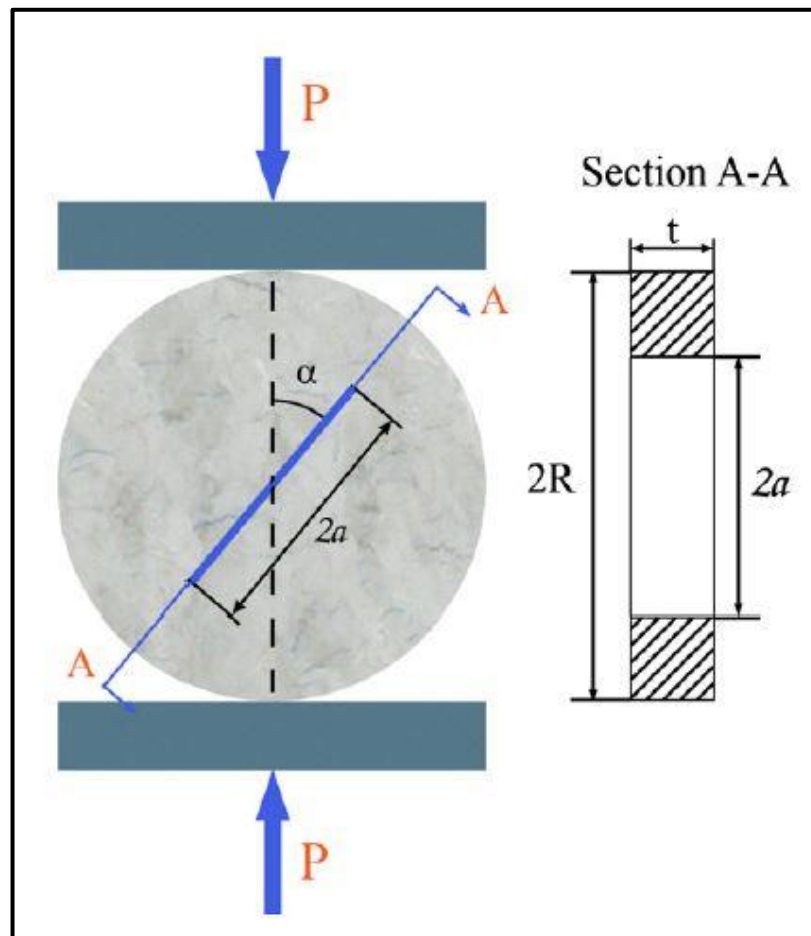


Figure 2. 19 CTSBD test specimen geometry

Where;

$P$ : Applied load

$\alpha$ : Orientation of notch relative to diametrical loading plane

$a$ : Half crack length

CTSBD test geometry was pioneered by Libatskii and Kovichick (1967) in determination of mode I fracture toughness of glasses. Awaji and Sato (1978), again declared that, CSTBD test specimen is appropriate test specimen for mode I and mode II also mixed mode I-II fracture toughness determination by changing notch orientation. In the study, they utilized marble, graphite and plaster and isotropy of the materials were checked (Table 2.4). Except for marble, sharp central notches were

machined with thin circular saw of 0.2 mm thickness and 13 mm diameter in the CTSBD specimens. Notches of marble specimens were machined by another cutter which was originally utilized for dental uses. Thickness of slit was 0.6 mm for marble specimen. Dimensionless notch length ( $a/R$ ) notch length/disk diameter was kept to be approximately 0.5. As a numerical computation tool, to calculate the stresses around crack tips and boundaries of loading points, boundary collocation method and boundary dislocation methods were utilized. Hertzian contact stresses were considered in order to specify effective external boundary loading on the outer boundary. Stress intensity factor calculations were considered as sum of three superposition stages (Figure 2.20) as listed below;

- ❖ Circular region loaded by diametrical forces which are concentrated loads, (Figure 2.20a)
- ❖ Distributed loading effect subjected to notch surface, (Figure 2.20b)
- ❖ Crack regions where assigned boundary stresses on (Figure 2.20c)

Table 2. 4 Results mode I and mode II fracture toughness tests (Awaji and Sato, 1978)

<b>Tested Material</b>	$K_{Ic}$ (MPa $\sqrt{m}$ )	$K_{IIc}$ (MPa $\sqrt{m}$ )	$K_{IIc} / K_{Ic}$
<b>Marble</b>	0.93	1.05	1.13
<b>Plaster</b>	0.13	1.09	1.16
<b>Graphite</b>	0.94	0.15	1.14

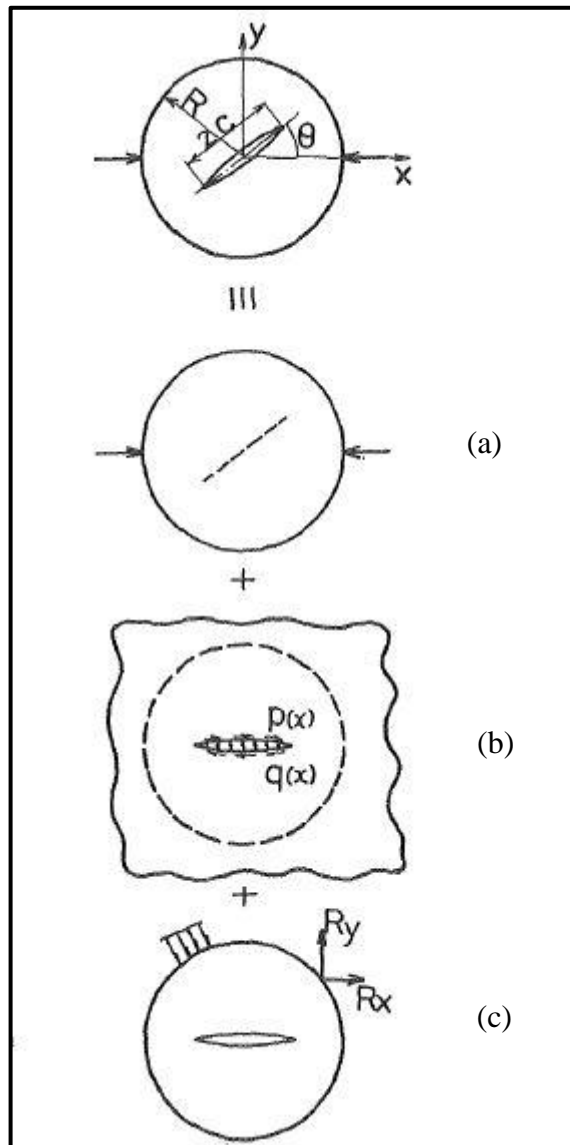


Figure 2. 20 Analytical approach to calculate stress intensity factors for CSTBD test (Adapted from Atkinson et al., 1986)

Limited numerical results for stress intensity factors were achieved by following studies. Atkinson, 1982 conducted a series of mode I and mode II fracture toughness experiments on PMMA. Dimensionless stress intensity factors were reported and as a conclusion analytical equations were proposed for CTSBD test with some shortcomings. Reported dimensionless stress intensity factors and analytical equations were valid only specimens having dimensionless notch length  $a/R \leq 0.3$ .

Where;

$a$ : Notch length

$R$ : Radius of the disk

Shetty et al., (1986) utilized CTSBD test specimen to determine mixed mode behaviors of ceramics. According to conducted mixed mode I-II experiments on ceramics, CSTBD test specimen geometry was found reliable for full range of stress intensity factors from pure mode I to pure mode II. CSTBD test specimen reported as an appropriate method for fracture toughness determination including mixed mode I-II conditions.

However, numerical results for CTSBD test geometry were still lacking. Only numerical results of stress intensity factors for CSTBD test specimen had been proposed by the study of Atkinson et al., (1986) up to that time. Fowell and Xu (1993) reported new polynomial fit functions for both modes I and II dimensionless stress intensity factor determination. In the study, it was also reported that notch angle provides for pure mode II conditions. Apart from equation proposed by Atkinson et al., (1993), Fowell and Xu, (1993) was valid for almost full range of dimensionless crack lengths from  $a/R = 0.05$  to  $a/R = 0.95$  ( $\alpha = a/R$ ).

$$\begin{aligned} Y_I(\alpha) = & 0.0354 + 2.0394\alpha - 7.0356\alpha^2 + 12.8154\alpha^3 + 8.4111\alpha^4 - 30.7417\alpha^5 \\ & - 29.4959\alpha^6 + 62.9739\alpha^7 + 66.5439\alpha^8 - 82.1339\alpha^9 - 73.6742\alpha^{10} \\ & + 73.8466\alpha^{11} \end{aligned} \quad (2.59)$$

$$\begin{aligned} Y_{II}(\alpha) = & 0.06462 + 2.8956\alpha - 6.8663\alpha^2 + 9.8566\alpha^3 - 0.4455\alpha^4 - 1.0494\alpha^5 \\ & - 13.2492\alpha^6 + 9.0783\alpha^7 - 10.7354\alpha^8 + 28.4775\alpha^9 - 6.3197\alpha^{10} + 10.6626\alpha^{11} \\ & - 10.0268\alpha^{12} - 34.2997\alpha^{13} + 1.7292\alpha^{14} + 25.2216\alpha^{15} \end{aligned} \quad (2.60)$$

$$\begin{aligned} \theta_{II} = & 30.4406 - 4.6734\alpha - 17.6741\alpha^2 - 9.6827\alpha^3 + 3.9819\alpha^4 + 12.9163\alpha^5 \\ & - 13.3222\alpha^6 + 12.8001\alpha^7 - 13.1239\alpha^8 \end{aligned} \quad (2.61)$$

In addition, an equation for the relation between stress intensity factor and dimensionless stress intensity factor was also reported.

$$K_{IIc} = \frac{P_{cr}}{B \times \sqrt{R}} Y_{II} \quad (2.62)$$

Where,

$P_{cr}$ : Fracturing load

$Y_I$ : Mode I dimensionless stress intensity factor

$Y_{II}$ : Mode II dimensionless stress intensity factor

$K_{IIc}$ : Mode II fracture toughness

$\alpha$ :  $a/R$

$a$ : Notch length

$R$ : Radius of the disc

$B$ : Thickness of the disc

Another study for examination of mixed mode behaviors of a kind of sandstone, Krishman et al., (1998) found that critical notch inclination for pure mode II reported as  $\theta = 29^\circ$ . Temperature effects under confining pressure on CSTBD test specimen for modes I and II were investigated by Al-Shaeya et al., (2000). Ayatollahi and Torabi (2010) conducted numerical computations for CSTBD test specimen in order to determine effect of blunt notches on mode I and mode II fracture toughness values of PMMA and soda-glass. Aliha et al., (2012) compared the results of mode I and mode II fracture toughness values acquired from a series of experiments on CSTBD and SCB test specimens. SCB test specimen was reported as giving overestimated results for fracture toughness values of same materials in comparison with CSTBD test specimen.

In Table 2.5, mode II fracture toughness of some rock types determined by CSTBD test geometry were listed.

Table 2. 5 Mode II fracture toughness values for some rock types determined by CSTBD test geometry

<b>Rock Type</b>	<b>Mode II Fracture Toughness MPa<math>\sqrt{m}</math></b>	<b>Reference</b>
Ankara Gölbaşı Andesite	0.99	Karakaş, 2011
Marble	0.86	Karakaş, 2011
Gabbro	1.76	Het, 2014

#### 2.4.5 Straight notched disc bending test

Straight notched disc bending test first introduced by Tutluoglu and Keles (2011) to determine mode I fracture toughness values of brittle materials i.e. rocks, ceramics, glass etc. Introduced test specimen mainly was a cylindrical plate which is Brazilian disc shaped, having a single straight edge notch and subjected to three point bending (Figure 2.21). They conducted a series of experiments for two different rock types Ankara Gölbaşı Andesite and Marble. Shortly they listed advantages of this test specimen as follows;

- ❖ Easy test specimen preparation
- ❖ Easy experimental setup
- ❖ Appropriate for size effect changes
- ❖ Stiff test specimen geometry
- ❖ Little fracture process zone respect to other disc specimens

In the study, great variety of three dimensional numerical computations were conducted for stress intensity factor calculations only mode I. Numerical study was performed by utilizing commercial finite element package ABAQUS software. In numerical study, diameter of the test specimen was kept constant at 75 mm. Other changed geometrical parameters were given in dimensionless form regarding radius of the test specimen. These parameters were given as; dimensionless span length

( $S/R$ ) between 0.5-0.8, dimensionless notch length ( $a/t$ ) between 0.1-0.9, and dimensionless specimen thickness ( $t/R$ ) between 0.5-3.0. Geometric parameter of SNDB test specimen can be seen in the following figure.

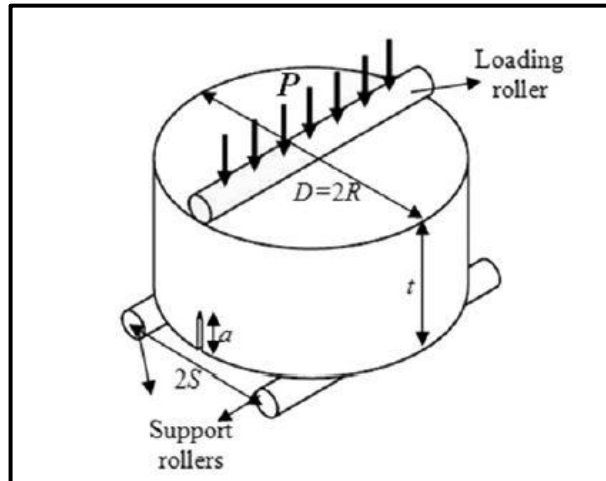


Figure 2. 21 SNDB test specimen geometry  
(Adapted from Tutluoglu and Keles, 2011)

Where;

$S$ : Half span length

$R$ : Radius of the test specimen

$D$ : Diameter of the test specimen

$a$ : Notch length

$t$ : Thickness of the test specimen

$P$ : Applied load (concentrated load)

As a result of study Tutluoglu and Keles (2011) reported two types of fit functions. The first one was a linear fit function and the second was a fifth order polynomial. The first linear fit function was constructed relation between dimensionless mode I stress intensity factor  $Y_I$  and  $S/R$ .

$$Y_I = m \left( \frac{S}{R} \right) + n \quad (2.63)$$

Introduced linear fit function is only valid for specific  $a/t$  ratio corresponding dimensionless specimen thickness  $t/R$ . For this reason,  $Y_I$  fit functions for each  $a/t$  ratio regarding  $t/R$  were tabulated in their study specifically.

A fifth order polynomial fit function provided a relation between mode I stress intensity factor  $Y_I$  and  $t/R$  as:

$$Y_I = C_1 \left(\frac{t}{R}\right)^5 + C_2 \left(\frac{t}{R}\right)^4 + C_3 \left(\frac{t}{R}\right)^3 + C_4 \left(\frac{t}{R}\right)^2 + C_5 \left(\frac{t}{R}\right) + C_6 \quad (2.64)$$

This fifth order polynomial fit function was reported to be valid for specific  $a/t$  ratios.  $C$  values vary from -414 to 369.  $Y_I$  fit functions for each  $a/t$  ratio regarding  $S/R$  were given in their study:

Normalization equations for SNDB test specimen was given as follows;

$$Y_I = \frac{K_I}{\sigma_0 \sqrt{\pi a}} \quad (2.65)$$

$$\sigma_0 = \frac{P}{2Dt} \quad (2.66)$$

Where;

$Y_I$ : Mode I dimensionless stress intensity factor

$K_I$ : Mode I stress intensity factor

$\sigma_0$ : Effective tensile stress on notch plane

$P$ : Applied load (concentrated load)

$D$ : Diameter of the test specimen

$t$ : Thickness of the test specimen

$a$ : Notch length

Mode II stress intensity factor and fracture toughness determination studies were conducted by Karakaş (2011). Likewise, study of Tutluoglu and Keles (2011), fifth order polynomial fit functions for SNDB test specimen proposed to determine mode II fracture toughness of rocks. Normalization equation for SNDB test specimen to determine mode II fracture toughness value was given as follows;

$$Y_{II} = \frac{K_{II}}{\sigma_0 \sqrt{\pi a}} \quad (2.67)$$

$$\sigma_0 = \frac{P}{2Dt} \quad (2.68)$$

Where;

$Y_{II}$ : Mode II dimensionless stress intensity factor

$K_{II}$ : Mode II stress intensity factor

$\sigma_0$ : Effective tensile stress on notch plane

$P$ : Applied load (concentrated load)

$D$ : Diameter of the test specimen

$t$ : Thickness of the test specimen

$a$ : Notch length

In Table 2.6 mode II fracture toughness of some rock types determined by SNDB test geometry were listed.

Table 2. 6 Mode II fracture toughness of some rocks determined by SNDB test geometry

Rock Type	Mode II Fracture Toughness MPa√m	Reference
Ankara Gölbaşı Andesite	0.61	Karakaş (2011)
Marble	0.62	Karakaş (2011)
Gabbro	1.18	Het (2014)



## CHAPTER 3

### FOUR-POINT ASYMMETRIC BENDING TEST SPECIMEN

Major purpose of this study is to estimate the pure shear fracture toughness mode II of an edge notched beam shaped rock specimen. For mode II stress intensity factor computations of FPAB test, analytical, semi-analytical, and numerical modeling results from the previous work is summarized. Geometry of FPAB test specimen is illustrated with some sketches.

#### 3.1 Four-point asymmetric bending test specimen

General geometry of the test specimen is selected as a beam. Beams are well-known structural elements in engineering analysis. In previous studies of structural analysis investigations, numerous loading conditions have been tested on beams and considerable experiences have been gained in Civil Engineering, Mechanical Engineering and also Mining Engineering disciplines. These experiences enable accurate computation of structural parameters for beams under different loading configurations. The other advantage of using beam type specimen is that stresses and deflections in beams are directly proportional to the applied loads. This condition requires that the action of the applied loads must not be affected by the change in shape of the beam due to bending (Timoshenko and Gere, 2013). These advantages of beams are main reasons on selecting rectangular beam as base test specimen geometry.

### 3.2 Development of FPAB test specimen

Four-point asymmetric bending (FPAB) test specimen was first proposed by Arrea and Ingraffea (1982). This work was concentrated on determining shear type fracture energy and mixed mode (mode I and mode II) fracturing parameters of concrete. Bazant and Pfeiffer's (1986) work was on size effect on fracturing behavior of concrete using FPAB specimen. Barr and Derradj (1990) used double edge notched FPAB specimen to investigate size effects in shear failure. Martin and Davidson (1999) conducted mode II fracture toughness determination studies for laminated materials referring beam theory. They stated, there was a direct relationship between delamination and flexure amount for beams under loading. They defined flexure amount around crack by using beam theory formulations than mode II fracture toughness estimations for laminated materials.

Fett, (1998) conducted a series of both mode I and mode II fracture toughness determination studies utilizing FPAB test geometry. He and Hutchinson (2000) proposed new analytical formulas to estimate mode I and mode II SIF's for FPAB. With FPAB Yoshihara (2008) conducted mode II fracture toughness determination of wood. Aliha, et al., (2009) using marble specimens, a series of mode II fracture toughness experiments were performed. The main purpose of the study is determination of correct short moment arm distance that satisfies pure mode II brittle fracture. They prepared beam specimens with different dimensionless short moment arm distance  $d/W= 0.025, 0.1, 0.2, 0.3, 0.4, 0.5, 0.75$  and 1. They stated, to provide pure shear effect on crack plane  $d/W$  ratio should be greater than 0.5.

Ayatollahi et al., (2012), investigated to determine optimum short and long moment arm distances to create pure mode II loading conditions on the crack plane for v-notched FPAB specimen. They proposed long moment arm distance should be three times greater than short moment arm distance ( $L/d=3$ ) to satisfy pure shear effect on the crack plane. They used 120 mm long beam with 24 mm beam depth. They also claimed that dimensionless crack length ( $a/W$ ) should be greater than 0.3 for pure

mode II loading. Ayatollahi and Aliha, 2011 defined  $T$ -stresses around crack tip. They claimed, for small short moment arm distances (the ratio of short moment arm distance and beam depth)  $d/W < 0.5$  considerable  $T$ -stresses observed and this yields significant mode I deformation on the crack plane.

Krishnan and Xu, 2011 investigated shear mode testing conditions for short beams. In the study, two different beam depth groups were created as  $W= 19.1$  and  $30.5$  mm. Short moment arm and long moment arm distances for each beam were set as  $20$  and  $40$  mm, respectively. Thicknesses of beams were kept constant at  $5.4$  mm. Total lengths of beams were chosen as  $152.2$  and  $122$  mm, respectively. All beams were made of polycarbonate and polymethyl methacrylate (PMMA). As a result of this study it is stated that, pure mode II loading conditions can be provided also for short beams.

### **3.3 Symbols and geometric details of FPAB test specimen**

(FPAB) test specimen consists of two loading points and two support points which are configured asymmetrically. Arbitrary configurations of these points do not yield pure shear conditions on crack plane every time. Creating pure shear effect on crack plane is satisfied by structural analysis techniques using “*Equilibrium of shear stress*” concept. This condition requires that total bending moment along axis parallel to crack plane must be equal to zero. Loading was applied from bottom flat surface of the specimen in the numerical and experimental works. Therefore, rollers located on upper flat surface of the specimen became support points for this kind of loading configuration (Figure 3.1).

In the literature, abbreviations of specimen dimensions and parameters, such as; beam depth and beam thickness do not agree each other. In this study, these dimensions and parameters are adopted from the beam theory and they are;

W: Beam depth  
B: Beam thickness  
d: short moment arm  
L: Long moment arm  
a: Crack length  
F: Concentrated load

Units of parameters like beam depth, beam thickness, crack length, short and long moment arm are in meters and applied load is in Newtons in order to get stress intensity factor in  $\text{MPa}\sqrt{\text{m}}$  unit.

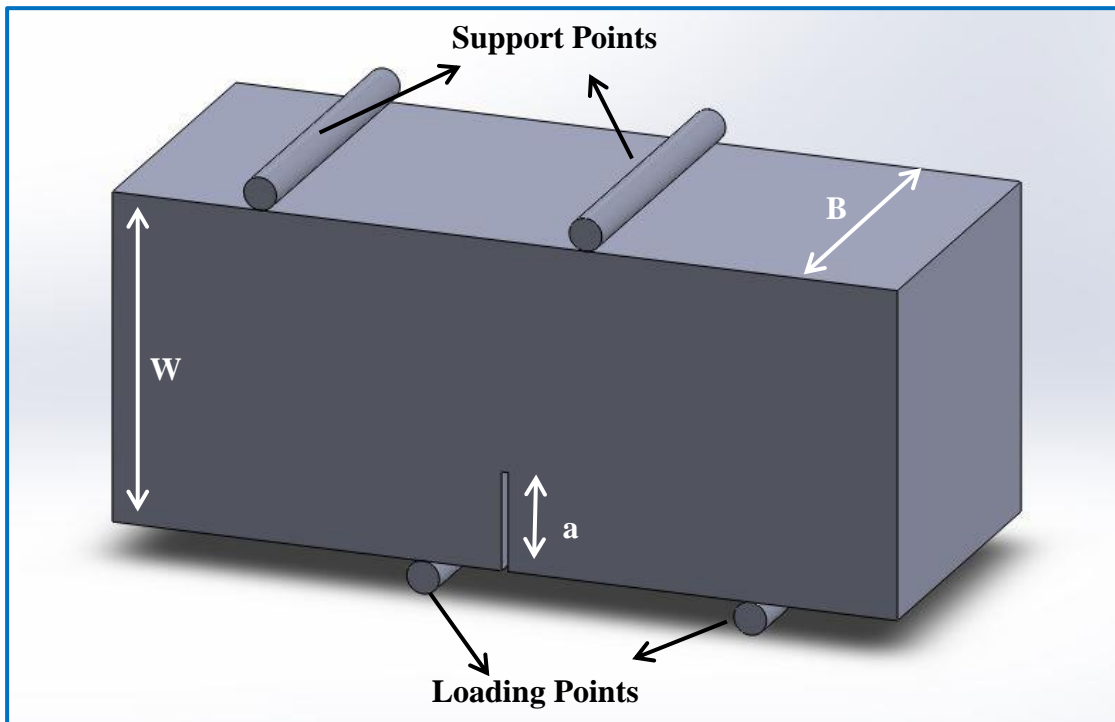


Figure 3. 1 FPAB test specimen dimensions

Pure shear conditions were satisfied by applying  $L=3d$  configuration of asymmetric loads. A Unit load of 1 N were applied to the loading points and it was proportioned as three quarters of  $F$  for short moment arm and one quarter of  $F$  for long moment arm to create zero total bending moment on the crack plane.

For different beam depths and crack lengths pure shear conditions were satisfied by changing loading configuration of asymmetric loads.

For both numerical models and test samples, FPAB test specimens were prepared at three-main beam depth groups which were 40-50 and 60 mm. Each beam depth group included cracks of different lengths. Crack lengths were normalized as crack length over beam depth which is  $a/W$ . Stress intensity factors for numerical models and fracture toughness values for pure shear mode were analyzed in terms of normalized crack lengths.

Loading and support points and other dimensional entities were illustrated in detail on 2D section of specimen in Figure 3.2

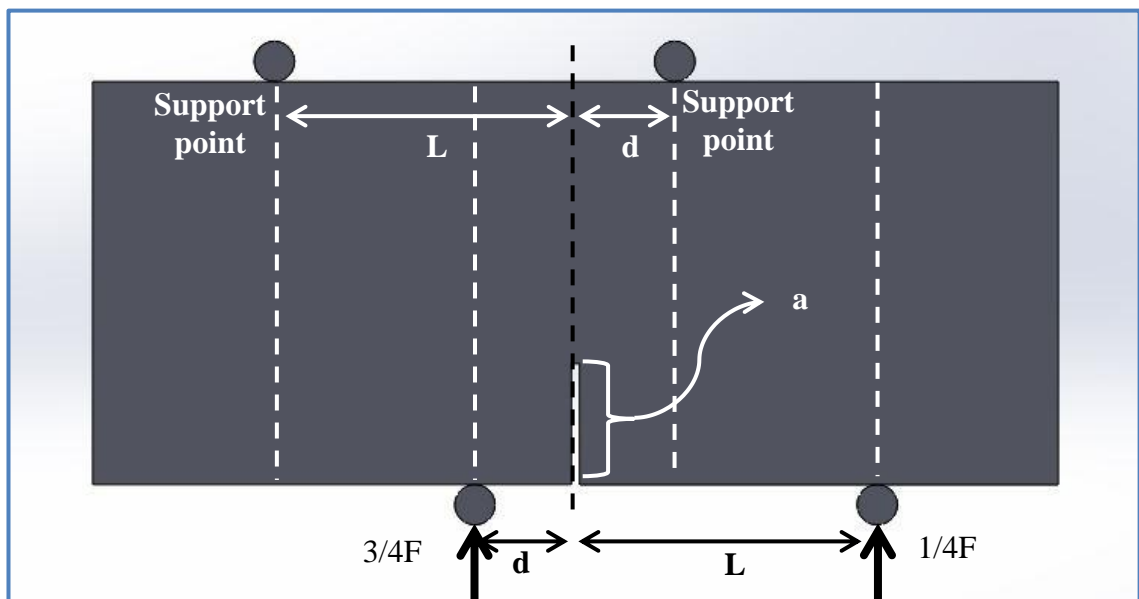


Figure 3. 2 Generic 4-point asymmetric loading test specimen

Different views of four-point asymmetric bending specimen geometries for both solid and wireframe forms are given in Figure 3.3.

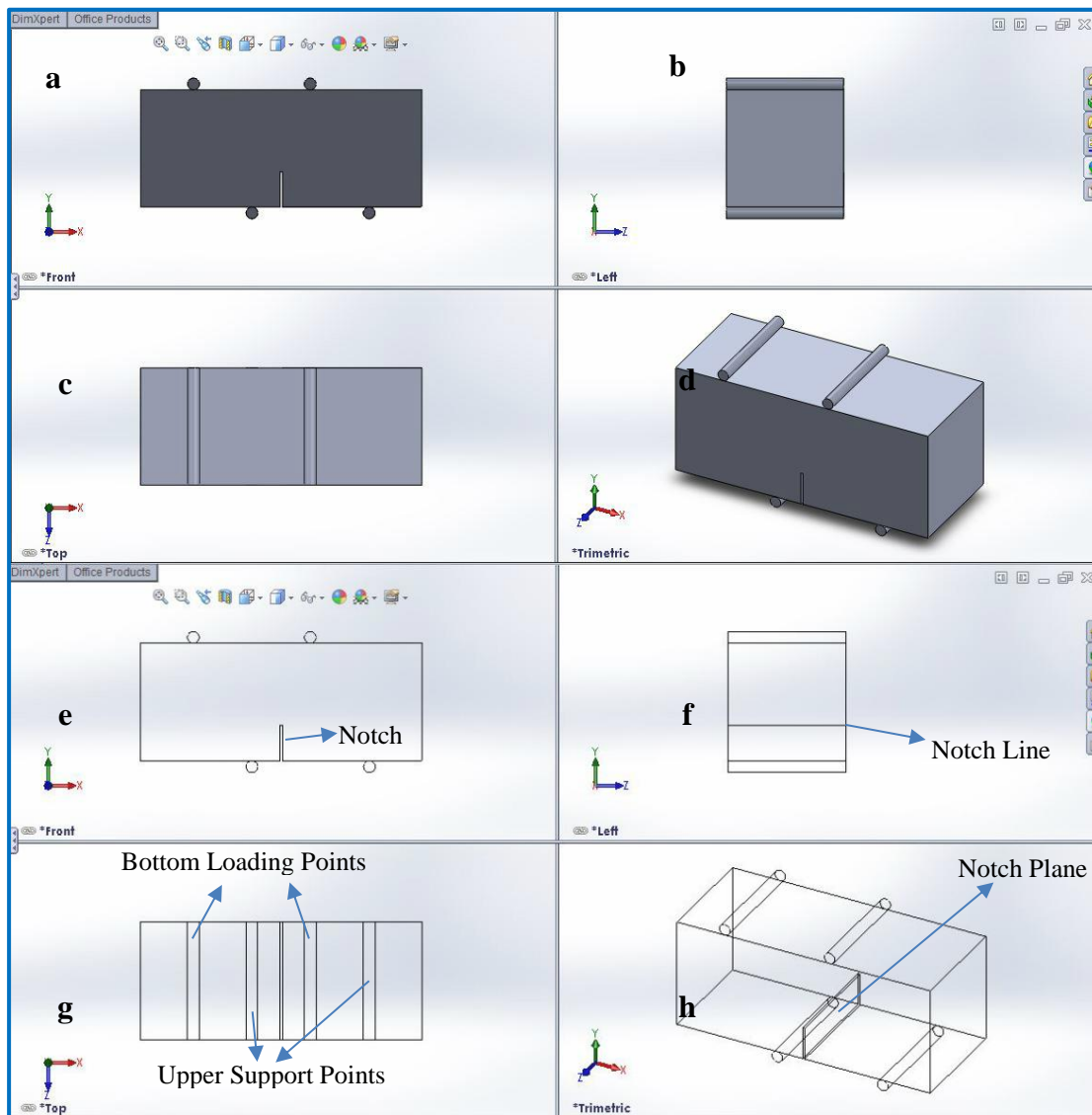


Figure 3.3 Solid and wireframe forms of FPAB test specimen from different views

Machined notch creates a line and a plane within the specimen. This line is referred as notch line for 3-dimensional view, (Figure 3.3f). Similarly, the plane along which notch lies is referred as notch plane (Figure 3.3h).

Here, to avoid confusion, terms “*notch*” and “*crack*” should be clarified. In fracture mechanics, crack refers to inherent impurities of materials or structures; on the other hand notches refer to artificial cracks which are machined deliberately in a specimen. These definitions had been become a need because of experimental studies of

fracture mechanics investigations. In order to observe crack propagation precisely notches are generated for intact specimens rather than utilizing arbitrarily cracked specimens. To make distinction over materials that generated human-made cracks from contain cracks inherently; “*notch*” and “*crack*” terms were derived by investigators.

### 3.4 Analytical methods for mode II fracture toughness $K_{IIc}$ calculation

Stress intensity factor is given in three main modes and they are: mode I, mode II and mode III. These modes are governed by the stresses acting from principal planes of a given state of stress on the crack plane. Fracture toughness is the form of a stress intensity factor that reaches a critical value under loading of a cracked body. As stress intensity factor reaches this critical value, crack cannot stand the stresses around crack tip and it propagates. Stress intensity factor is defined as;

$$K_I = \sigma_{xx} \times \sqrt{\pi a} \times Y_I(a/W) \text{ for mode I (opening mode)} \quad (3.1)$$

$$K_{II} = \tau_{xy} \times \sqrt{\pi a} \times Y_{II}(a/W) \text{ for mode II (in-plane shear mode)} \quad (3.2)$$

$$K_{III} = \tau_{zx} \times \sqrt{\pi a} \times Y_{III}(a/W) \text{ for mode II (out of plane shear mode)} \quad (3.3)$$

$K_I$ : Mode I stress intensity factor

$K_{II}$ : Mode II stress intensity factor

$K_{III}$ : Mode III stress intensity factor

$\sigma_{xx}$ : Normal stress

$\tau_{xy}$ : In plane shear stress

$\tau_{zx}$ : Out of plane shear stress

$Y_I(a/W)$ : Crack length function for mode I

$Y_{II}(a/W)$ : Crack length function for mode II

$Y_{III}(a/W)$ : Crack length functions for mode III

Crack length functions can be stated as correction functions for geometric differences of test specimen's thicknesses with different crack lengths. Therefore, it is given in the dimensionless form of  $(a/W)$  which is the ration of crack length to depth of the beam specimen.

Dimensionless form of mode I and mode II stress intensity factors which are  $Y_I$  and  $Y_{II}$  for FPAB test specimen has been investigated by the researchers and there are two well-developed solutions for calculation of them.

The first one was proposed by Fett (1998) who defined the dimensionless form of mode I and mode II stress intensity factor for FPAB specimen as;

$$K_I = \frac{F}{B \times W} \times \left(1 - \frac{d}{L}\right) \times Y_I \times \sqrt{\pi a} \quad (3.4)$$

$$K_{II} = \frac{F}{B \times W} \times \left(1 - \frac{d}{L}\right) \times Y_{II} \times \sqrt{\pi a} \quad (3.5)$$

So; dimensionless mode I and mode II stress intensity factors proposed by Fett was given by;

$$Y_I = \frac{K_I \times B \times W \times L}{F \times (L - d)} \times \frac{1}{\sqrt{\pi a}} \quad (3.6)$$

$$Y_{II} = \frac{K_{II} \times B \times W \times L}{F \times (L - d)} \times \frac{1}{\sqrt{\pi a}} \quad (3.7)$$

Here;

$K_I$ : Mode I stress intensity factor

$K_{II}$ : Mode II stress intensity factor

$Y_I$ : Dimensionless mode I stress intensity factor

$Y_{II}$ : Dimensionless mode II stress intensity factor

$F$ : Concentrated load

$B$ : Beam thickness

$W$ : Beam depth

$L$ : Long moment arm

$d$ : Short moment arm

$a$ : Crack length

The second noticeable solution was proposed by He and Hutchinson (2000) in which the dimensionless form of mode I and II stress intensity factors for FPAB specimen was;

$$Y_I = \frac{K_{II} \times \sqrt{W}}{Q} \times \frac{1}{\sqrt{\pi a}} \quad (3.8)$$

$$Y_{II} = \frac{K_I \times W^2}{6cQ} \times \frac{(1 - a/W)^{1/2}}{(a/W)^{3/2}} \quad (3.9)$$

$$K_I = \frac{6cQ}{W^2} \sqrt{\pi a} \times F_I(a/W) \quad (3.10)$$

$$F_I(a/W) = 1.122 - 1.121(a/W) + 3.740(a/W)^2 + 3.873(a/W)^3 - 19.05(a/W)^4 + 22.55(a/W)^5 \text{ for } (a/W) \leq 0.7 \quad (3.11)$$

$$K_{II} = \frac{Q}{\sqrt{W}} \times \frac{(a/W)^{3/2}}{(1 - a/W)^{1/2}} \times F_{II}(a/W) \quad (3.12)$$

for  $0 \leq (a/W) \leq 1$

$$Q = P \times \frac{(L - d)}{(L + d)} \quad (3.13)$$

$$F_{II}(a/W) = 7.264 - 9.37 \times (a/W) + 2.74 \times (a/W)^2$$

$$+1.87 \times (a/W)^3 - 1.04 \times (a/W)^4 \quad (3.14)$$

So; dimensionless form of mode I and II stress factors according to He and Hutchinson is defined by;

In here;

$K_I$ : Mode I stress intensity factor

$K_{II}$ : Mode II stress intensity factor

$Q$ : Shear force acting on crack plane

$P$ : Distributed load (on beam thickness)

$d$ : Short moment arm

$L$ : Long moment arm

$a$ : Crack length

$c$ : Distance between notch and symmetry plane of the specimen

$W$ : Beam depth

$F_I(a/W)$ : Crack length correction function

$Y_I$ : Dimensionless mode I stress intensity factor

$F_{II}(a/W)$ : Crack length correction function proposed by He and Hutchinson

$Y_{II}$ : Dimensionless mode II stress intensity factor

In order to derive these semi-analytical expressions to calculate mode I and mode II stress intensity factors, numerical computation studies are performed. From numerical computations geometric correction functions are derived for different dimensionless notch lengths ( $a/W$ ). Apparently, these functions are derived in terms of geometric changes in initial notch length “ $a$ ” or beam depth “ $W$ ”. This approach enables test conductors to define stress intensity factors independent from dimensional differences of possible test specimens. Likewise, both study expressed above utilized similar numerical computation studies. Stress intensity factors were calculated for different initial notch lengths then highly correlated polynomial fit functions derived for these two parameters (SIF vs  $a/W$ ). This relationship defines

SIF change over geometric changes and can be used for geometric correction factor. Remaining part of the given functions are depend on dimensional changes. In order to give dimensionless form of SIFs dimensional parameters are cancelled with SIF. Generated new value is given as dimensional stress intensity factor.

Dimensionless stress intensity factors for different geometries are given in two ways. The first way is to give definitive mathematical expressions like He and Hutchinson (2000). The second way is to give specific values for each geometric configuration like Fett (1998).



## CHAPTER 4

### VERIFICATION STUDIES AND FINITE ELEMENT MODELING OF BEAM GEOMETRIES

Many of engineering problems are defined by partial differential equations and exact solution of these equations for complex shaped domains is quite difficult and sometimes impossible. For this reason, numerical computations of stress intensity factors were carried out by adopting finite element method.

The finite element method is a mathematical tool that enables to solve these complex partial differential equations approximately with high accuracy. The main theory of finite element method is to divide the domain into finite elements. These elements are connected by nodes and approximate values for partial differential equations are achieved from these nodes. To achieve high convergence for solutions of these partial differential equations thousands of meshes should be generated. Computers can solve for node variables assigned to partial differential equations by programming a task for them. As number of nodes are increased in the model, accuracy of the solution tends to get higher convergence levels, but meanwhile, the computation time increases as well. Computing time is not only increased by number of nodes used, but also affected by the quality of the code (programming task) imposed to the computer (Davies A. J., 2011). So, to discard the disadvantageous effects of poor-structured finite element codes, some commercial packages have been introduced to users i.e. ANSYS, NASTRAN, LS-DYNA, ABAQUS etc. In this study, numerical computations are conducted utilizing ABAQUS commercial finite element package v12.

## 4.1 Notations, definitions and terms used by ABAQUS in modeling works

As it is known, notation of mechanics may vary from text to texts and notation should be established before giving explanations. Likewise, finite element codes may utilize different notations for specific mechanical entities i.e. stress displacement and boundary condition etc. In order to prevent misunderstanding, notation of these terms is given. Other definitions and terms used in ABAQUS are given again to avoid lack of explanation in context.

### 4.1.1 Notation usage

ABAQUS denotes six degrees of freedom which are displacements with respect to  $x, y, z$  as  $u_1, u_2, u_3$ , and rotations  $ur_1, ur_2, ur_3$  about  $x, y, z$  axes. Stresses and strains are given in tensor notation as;

$$[\sigma_{ij}] = \begin{bmatrix} \sigma_{11} & \sigma_{12} & \sigma_{13} \\ \sigma_{21} & \sigma_{22} & \sigma_{23} \\ \sigma_{31} & \sigma_{32} & \sigma_{33} \end{bmatrix} = \begin{bmatrix} S_{11} & S_{12} & S_{13} \\ S_{21} & S_{22} & S_{23} \\ S_{31} & S_{32} & S_{33} \end{bmatrix} \text{ (ABAQUS Notation)} \quad (4.1)$$

$$[\varepsilon_{ij}] = \begin{bmatrix} \varepsilon_{11} & \varepsilon_{12} & \varepsilon_{13} \\ \varepsilon_{21} & \varepsilon_{22} & \varepsilon_{23} \\ \varepsilon_{31} & \varepsilon_{32} & \varepsilon_{33} \end{bmatrix} = \begin{bmatrix} e_{11} & e_{12} & e_{13} \\ e_{21} & e_{22} & e_{23} \\ e_{31} & e_{32} & e_{33} \end{bmatrix} \text{ (ABAQUS Notation)} \quad (4.2)$$

Following Figure 4.1 illustrates degree of freedoms and reference points (RP) utilized in ABAQUS Software.

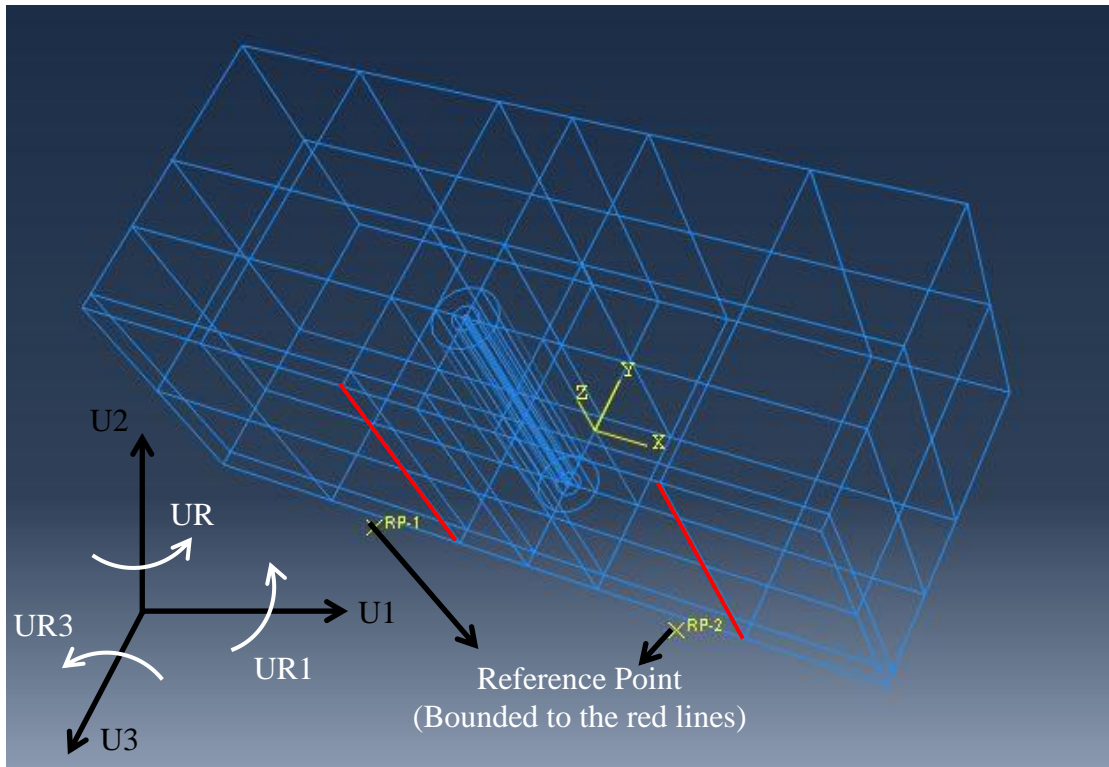


Figure 4. 1 Illustration of degree of freedoms and RPs in ABAQUS

Stress intensity factors and crack propagation direction notations of ABAQUS code are:  $K_I$ : Mode I stress intensity factor

$K_{II}$ : Mode II stress intensity factor

$K_{III}$ : Mode III stress intensity factor

CPD: Crack propagation direction

#### 4.1.2 Terms and definitions

ABAQUS software utilizes some special terms that used in finite element modelling procedure itself. Only the ones utilized in this study are explained and they are; seeding, partitioning, crack line, cell, face, reference point.

Seeding term is used for setting number of nodes per surface, edge or vertex. It is used for generating desired mesh density and geometry for whole body.

Partitioning term is used for dividing operation of bodies. It is used to form predefined parts to generate special mesh elements within the main body. It is also used to determine queries for stress and displacement readings. Successful partitioning leads to generate perfect meshes generation for part especially in the vicinity of cracks.

Face term is used for partitioned two-dimensional closed surfaces. Faces can be labelled and can be used for multiple purposes. Cell term is used for partitioned three-dimensional closed volumes. Again cells can be labelled and used for multiple purposes i.e. assigning different material properties, mesh types and boundary conditions. Reference point is used for created arbitrary points non-dimensionally. Reference point is used to create distributed loads and boundary conditions can be assigned to it. It is an unbounded element and it is not a part of a main body. It is excluded by assembly. It transmits every single imposed mechanical effect to desired point, line or part of the domain. It may be assumed as a source of mechanical effect for coupled node, surface or cell. All these mentioned terms are illustrated in Figure 4.2.

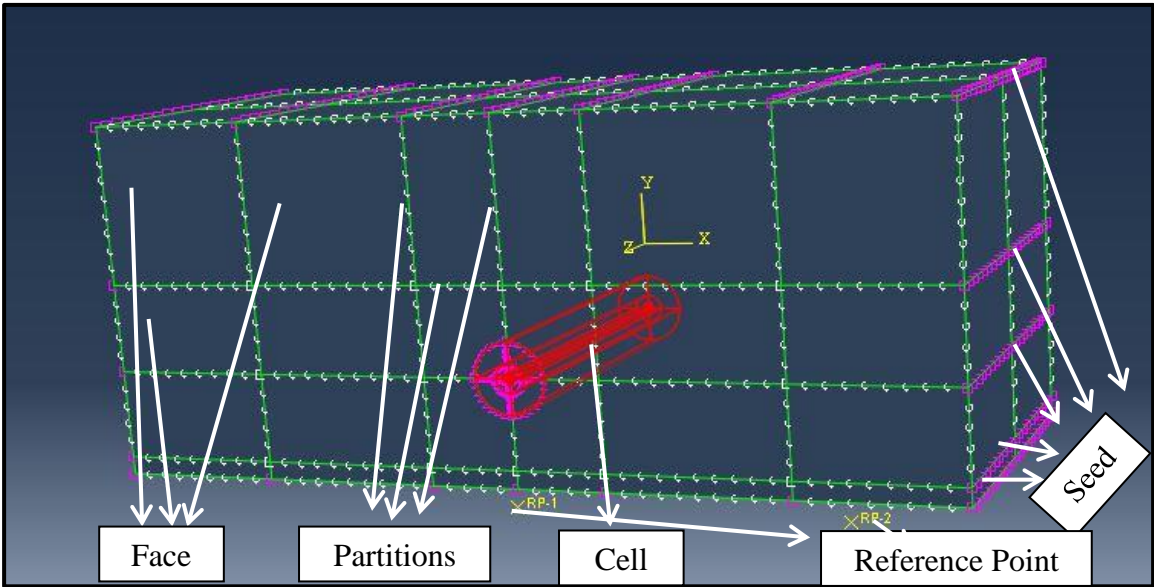


Figure 4. 2 Terms utilized in ABAQUS

## 4.2 Fracture mechanics computation techniques of ABAQUS

Fracture mechanics is the science of stress concentrators. Stress concentration (stress accumulation around a point) is resulted by the effect of far field stress acting on stress concentrators (cracks, notches, sharp edges). Around these points, stresses become infinite and create singularity. Singular stress is the key idea here and it should be evaluated precisely. It is known that for linear elastic brittle materials, stress state around crack tip has square root singularity. ABAQUS software offers special finite elements in order to compute singular stresses around a crack tip.

Crack modeling is achieved by utilizing two methods in ABAQUS. The first method is employing “*seam crack*” and the second method is creating the notch by modelling. Het (2014) introduced that, there is no considerable difference between results of seam crack and blunted notches. Achieved difference is around 1%. So, for ease of modeling seam cracks are appropriate method for fracture mechanics computations.

After seam crack is defined, crack tip and first contour of crack tip are defined. In order to evaluate J-integrals for each finite element, predefined contour region should be created. Finally, “*q-vector*” determination is performed. “*q-vector*” is a unit vector for virtual crack extension direction.

### 4.2.1 Seam crack

In the simplest form seam is a virtual edge or a face with zero thickness that has ability of separation. Geometry of a seam changes upon the finite element model created in two dimensional (line shaped) or three dimensional space (face shaped). Seam divides the body as two corresponding surfaces where the seam is located and it is closed before loading. However, it has capability of separate with no resistance during loading. ABAQUS sets lap-jointed duplicate nodes throughout the seam. The

seam has to be embedded within a solid part of a three-dimensional domain as a plane. After the seam is defined, following crack modeling procedures can be performed. In Figure 4.3 and Figure 4.4 seam crack is illustrated in both two and three dimensional spaces.

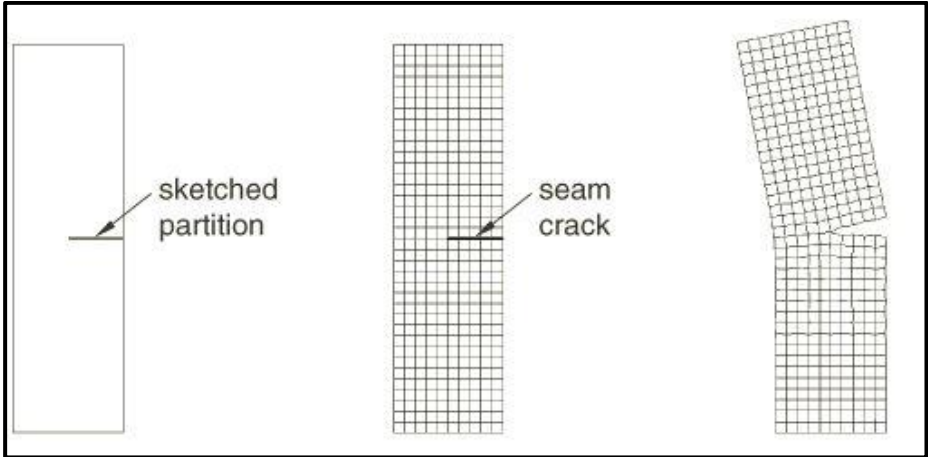


Figure 4. 3 Seam crack in two dimensional body (ABAQUS User Documentation, 2012)

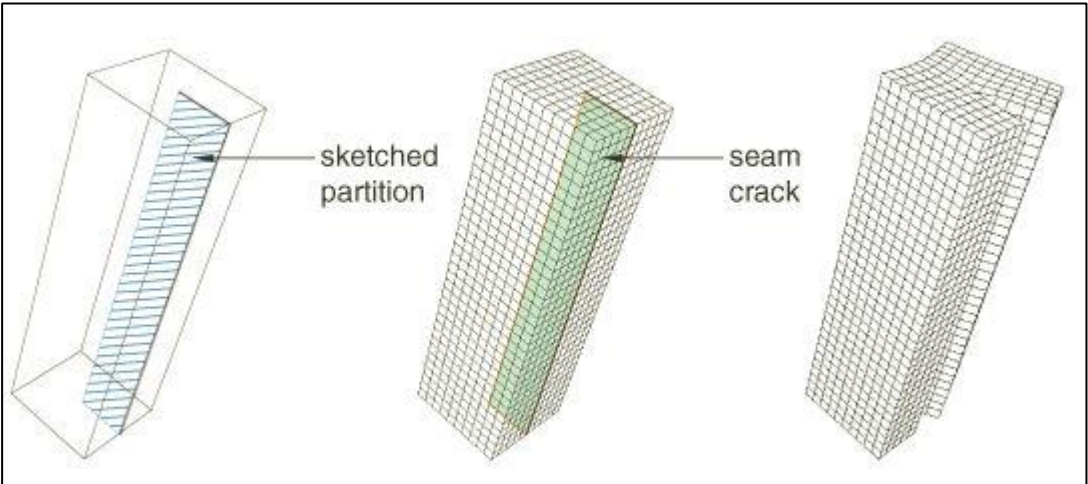


Figure 4. 4 Seam crack in three dimensional body (ABAQUS Documentation, 2012)

Defining the seam is the first part of the crack modelling procedure. This step is followed by defining the crack itself. In this study crack definition and its calculation is conducted by using J-contour integral technique.

## 4.2.2 Crack front

The area surrounding the crack tip till the first contour integral circle is defined as a crack front. Crack front is utilized to evaluate singular stresses of the first contour integral. Evaluation is performed by calculating J-integral for each contour. Accuracy level of contour integral calculations depends on size of contours created. In the Figure 4.5 contour integral regions are illustrated.

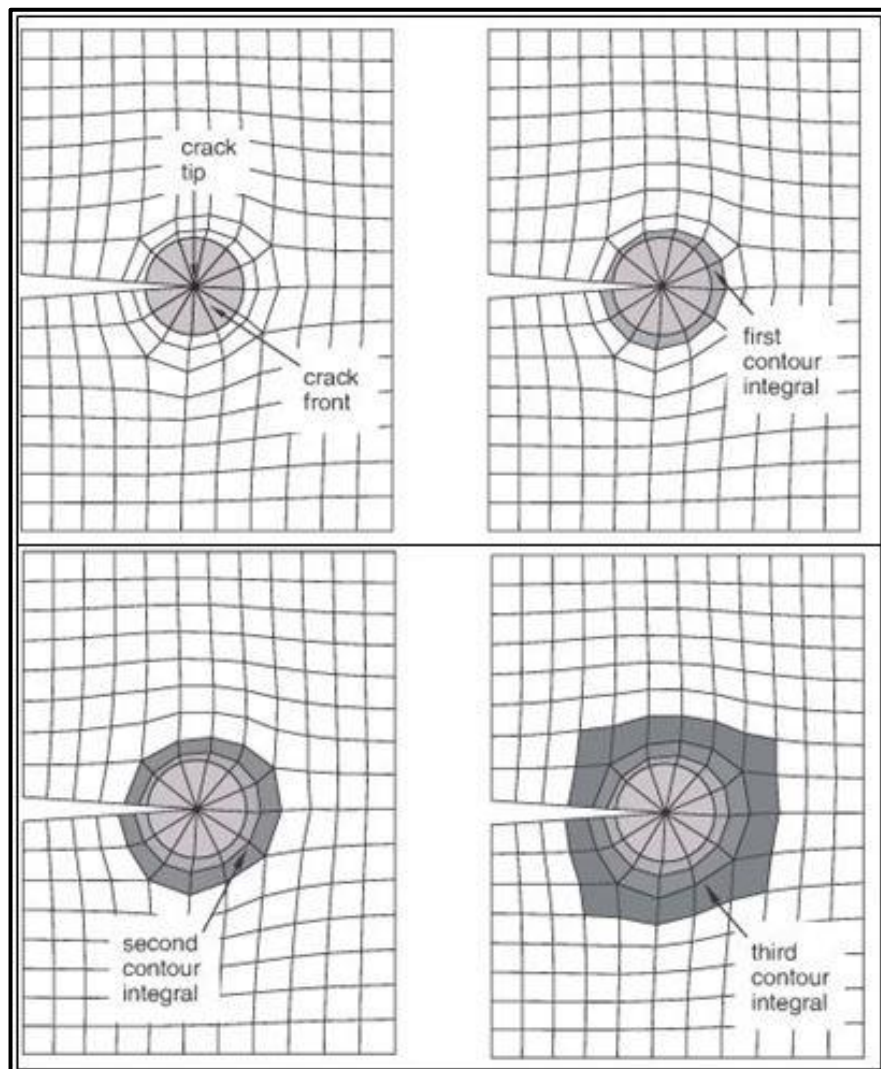


Figure 4. 5 Contour integral regions for two dimensional body (ABAQUS Documentation, 2012)

In three-dimensional finite element modelling, contour integral calculation extends through the crack line. This means, in addition to calculations made expanding from the first contour integral to the outer contours; calculations are repeated for each node located on the crack line in a row. In the Figure 4.6 crack front and contour integral regions in three-dimensional body is illustrated (ABAQUS, 2006).

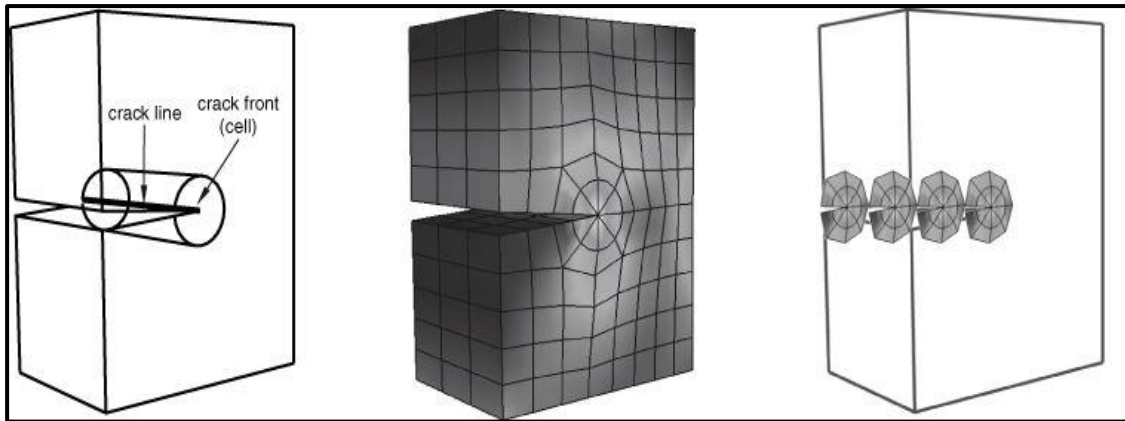


Figure 4. 6 Contour integral calculation in three-dimensional modelling (ABAQUS Documentation, 2012)

### 4.2.3 Crack tip stress singularity calculation

Materials include crack inherently and cracks create singularity in terms of strain field at the crack tip. In order to improve the precision of contour integrals small-strain analysis should be conducted. In order to satisfy the small-strain analysis conditions, special meshing styles should be utilized.

Creating crack tip singularity improves the precision of the calculation of the J-integral. Thus, at the vicinity of the crack tip, stresses and strains are calculated more accurately. If it is assumed that “r” is the distance from crack tip ABAQUS offers singularity form for a small-strain analysis in linear elastic medium as  $\epsilon \propto r^{-1/2}$ .

Numerically, crack tip singularity is provided by collapsed elements. Collapsed elements are the crucial part of the crack tip meshing procedure. A quadrilateral

element is degraded to a triangular element by combining the edge nodes of quadrilateral element to a single node. Therefore, a triangular element is generated. In Figure 4.7 degraded mesh element is illustrated.

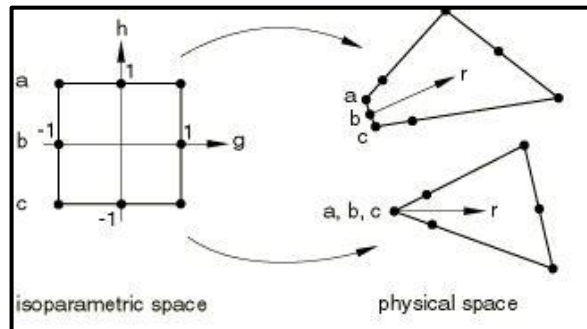


Figure 4. 7 Collapsed duplicated nodes in 2-dimensional elements (ABAQUS Documentation, 2012)

Similarly, in three-dimensional space a hexahedral element degrades into a wedge element. Three-dimensional collapsed element is illustrated in Figure 4.8.

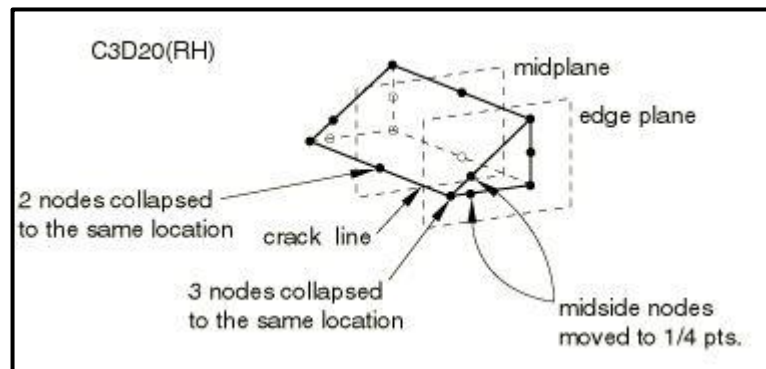


Figure 4. 8 Collapsed duplicated nodes in 3-dimensional elements(ABAQUS Documentation, 2012)

### 4.3 Verification studies

In order to illustrate user skills in FEM modelling and capabilities of numerical approximation of fracture mechanics code ABAQUS software, two verification problems are modeled and analyzed. First one of the verification problems is the

three-point bending plate problem. The second one is the pure shear plate problem. Both verification problems have analytical solutions for mode I and mode II stress intensity factors. SIF results calculated with analytical expressions and numerical results computed by ABAQUS software are compared below.

#### 4.3.1 Three-point bending plate verification problem

Numerical verification of the three-point bending plate problem performed comparing with its analytical solution given by Srawley (1976), and Tada et al., (2000). Verification study was divided into two parts. First, analytical solutions of the problem are given, then numerical computations efforts are compared with available solutions in the literature.

##### *Analytical Solution*

Srawley (1976), proposed a polynomial expression in order to improve the calculation of the stress intensity factor to define plane strain fracture toughness of materials. Previously proposed mathematical expressions for stress intensity factor calculation of plates subjected to bending type of loads have errors for which having dimensionless crack length  $a/W$  less than 0.45 or greater than 0.55. While declared range of ratios sufficient for the purpose of crack growth they are not suitable for cases that have the ratio of  $a/W$  range from 0 to 1. In order to achieve this restriction, Srawley proposed the expression below.

$$\frac{KB\sqrt{W}}{P} = \frac{3\left(\frac{S}{W}\right)\sqrt{\alpha}[1.99 - \alpha(1 - \alpha)(2.15 - 3.93\alpha + 2.7\alpha^2)]}{2(1 + 2\alpha)(1 - \alpha)^{3/2}} \quad (4.3)$$

For  $0 \leq \alpha = a/W \leq 1$  and where;

$K$ : Stress intensity factor

$B$ = Thickness

$W$ = Width

$a$ = Crack length

$S = \text{Span}$

Apart from this, Tada et al., (2000), by giving a reference to Srawley (1976), explains the same problem as follows,

$$\sigma = \frac{6M}{W^2} \quad (4.4)$$

$$\sigma = \frac{6M}{W^2} \quad (4.5)$$

$$M = \frac{PS}{4} \quad (4.6)$$

$$KI = \sigma\sqrt{\pi a} \times F\left(\frac{a}{W}\right) \quad (4.7)$$

$$F\left(\frac{a}{W}\right) = \frac{1}{\sqrt{\pi}} \times \frac{1.99 - \frac{a}{W} \left(1 - \frac{a}{W}\right) \left(2.15 - 3.93 \frac{a}{W} + 2.7 \left(\frac{a}{W}\right)^2\right)}{\left(1 + 2 \frac{a}{W}\right) \left(1 - \frac{a}{W}\right)^{3/2}} \quad (4.8)$$

Using Srawley's and Tada's formulations for mode I stress intensity factor  $K_I$  calculation for three-point bending plate was evaluated as  $1159.43 \text{ Pa}\sqrt{m}$  and  $1160 \text{ Pa}\sqrt{m}$  respectively.

### ***Numerical Solution***

Numerical model of three-point bending plate problem was constructed by given dimensions in the Table 4.1. Dimensions and geometry illustration is given in Figure 4.9.

Table 4. 1 Dimensions of three-point bending plate

Dimension	Value (mm)
Plate Length (x-direction)	75
Plate Depth (y-direction)	15
Plate Thickness (z-direction)	75

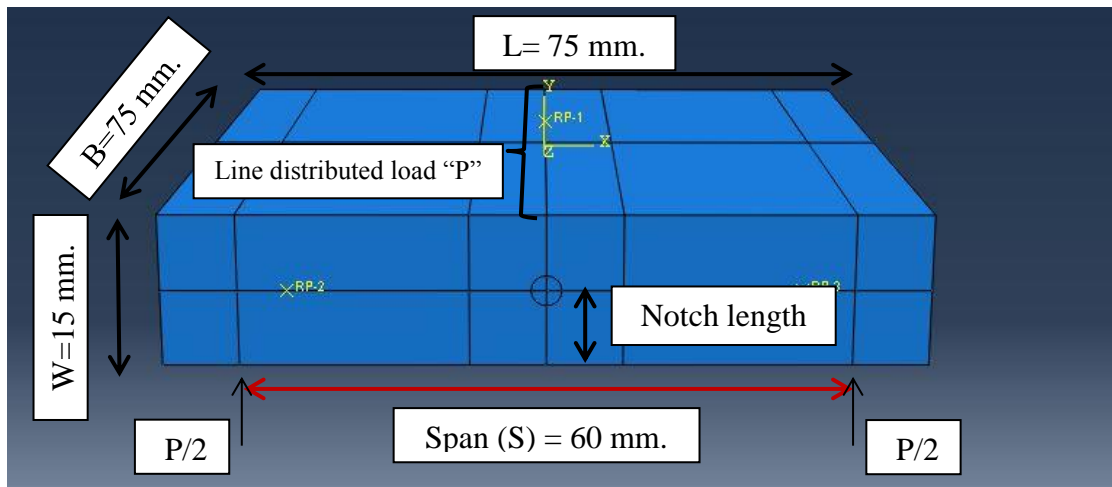


Figure 4. 9 Geometry of the three-point bending plate

Properties used in modeling andesite plate were adopted from Het (2014) as elastic modulus of  $E=12.35$  GPa and Poisson's Ratio of  $\nu=0.15$ . After material properties were assigned to the body, boundary conditions were to be defined properly.

Since it is a bending problem, there is a loading application point at the top reference point and there are two supporting points at the bottom boundary. In order to provide bending conditions, those three points have to be configured properly. Applied boundary conditions for support points are imposed as fixed displacement as  $u_2=0$ , and  $u_3=0$ , and fixed rotations as  $u_{r1}=0$ , and  $u_{r2}=0$ . They are free to move in x direction and to rotate out of plane. In Figure 4.10 loading point and in Figure 4.11 boundary conditions of the domain can be seen.

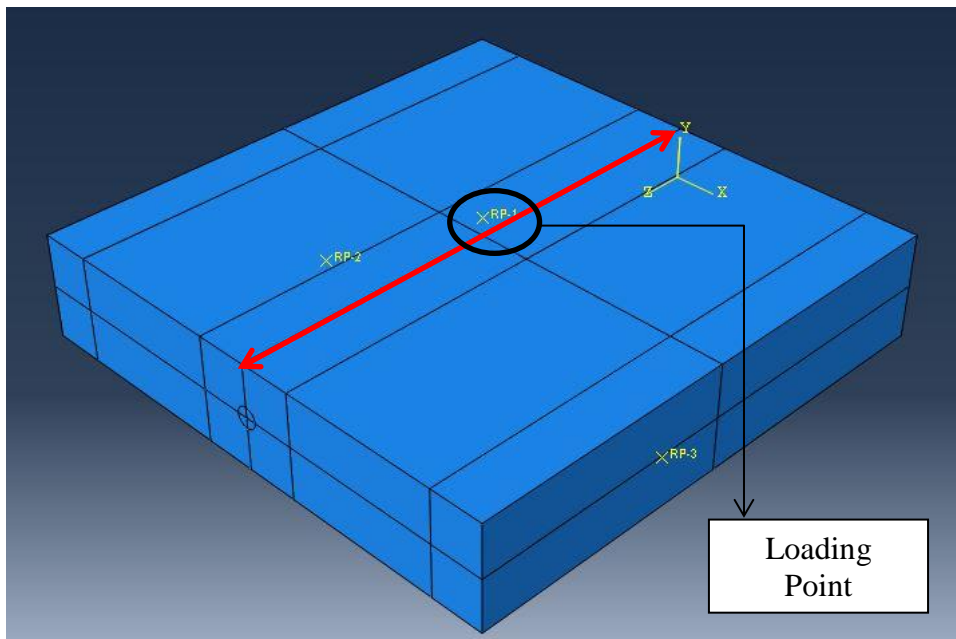


Figure 4. 10 Loading point of three-point bending plate problem

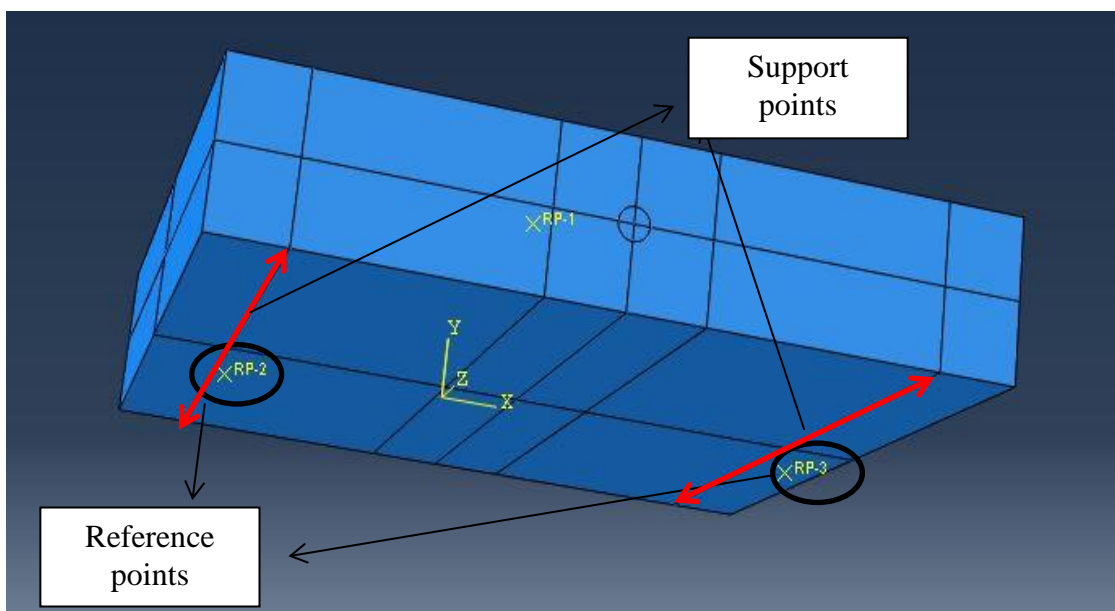


Figure 4. 11 Boundary conditions of three-point bending plate problem

After boundary conditions are defined next step is dividing the domain into finite elements. Meshing process is the crucial part of the numerical modeling. User

experience on meshing process affects the quality of meshes and finally numerical computations results. Crack tip meshing procedure requires extra care. Because of stress singularity, ABAQUS strongly suggests utilizing sweep mesh around crack tip which radially expands through the first contour. Number of lines radiated from crack tip is another accuracy issue. Suggested number of lines radiated from crack tip by ABAQUS is between 8 and 36. In order to have an idea about this, Het (2014) conducted mesh convergence study and showed that full accuracy was satisfied by dividing the crack tip into 32 lines. In the Figure 4.12, utilized meshing style can be seen easily.

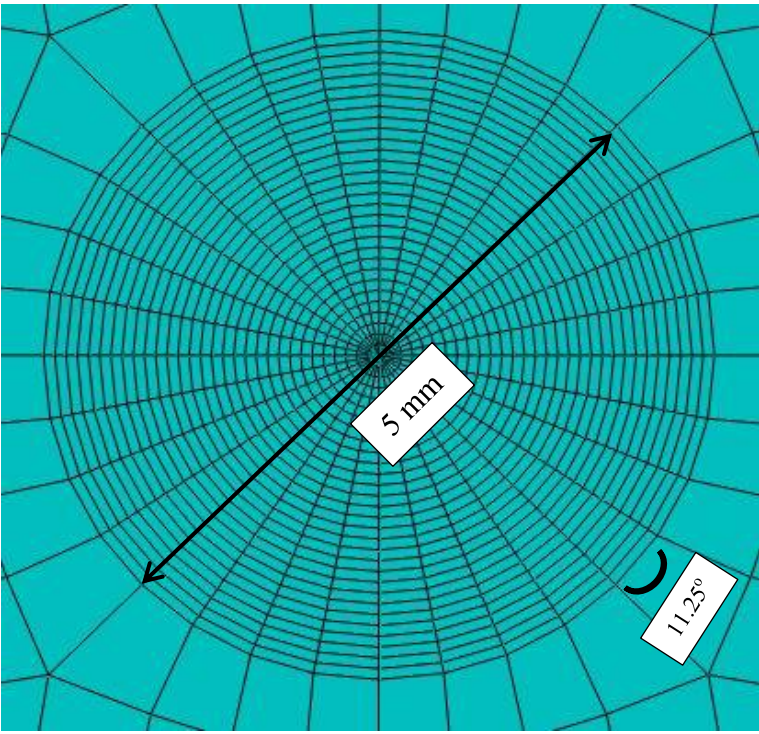


Figure 4. 12 Crack tip meshing

For this pure opening mode problem for which  $K_{II}$  is theoretically zero, numerically computed  $K_{II}$  has to be close to zero. In order to obtain high accuracy results in terms of  $K_I$  and  $K_{II}$ , fine meshing procedure was performed. Around 80000 finite elements were generated in total and nearly 50000 of them were structured in the vicinity of

contour integrals. Remaining finite elements were located on other parts of the domain. In Figure 4.13, whole body meshing can be seen in different views.

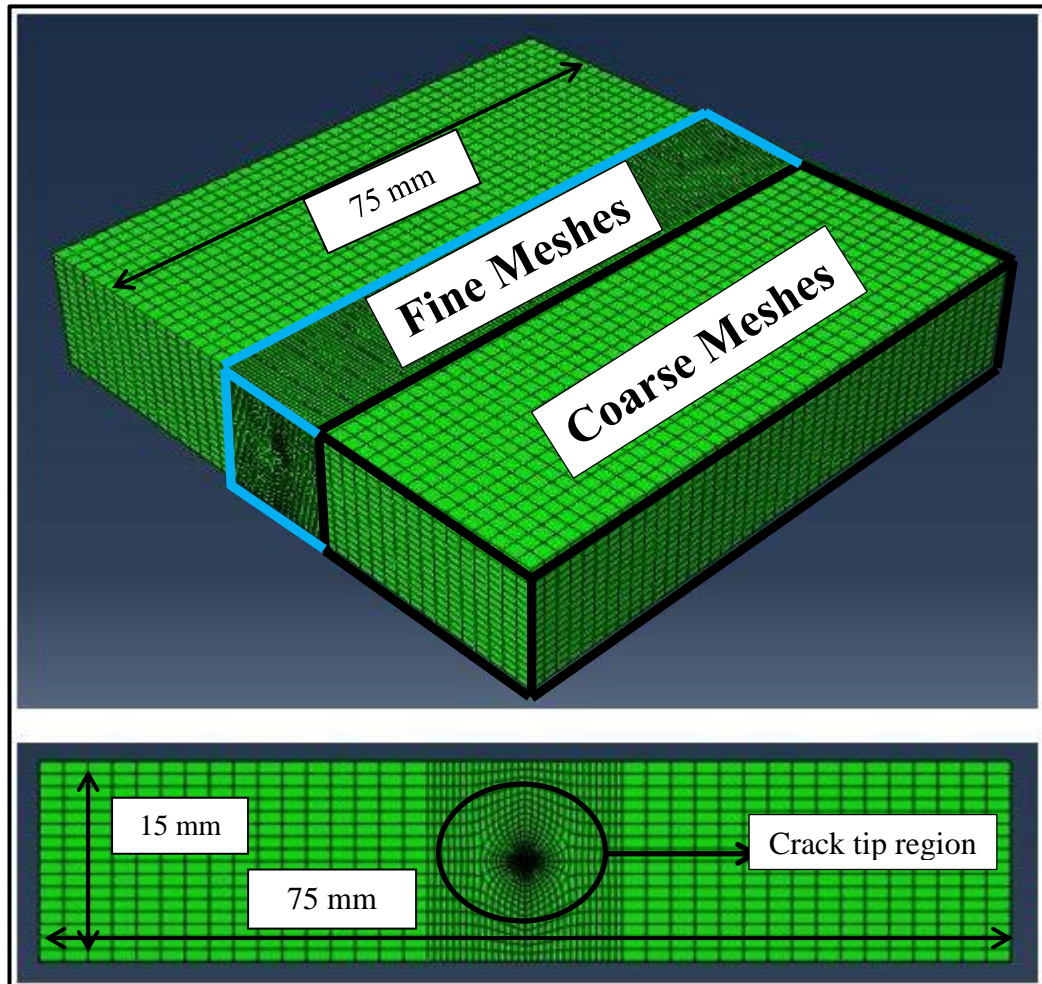


Figure 4. 13 Meshed domain

Finite elements were generated by C3D8R type structured elements. ABAQUS defines these elements as 3D stress brick elements which have 8 vertex nodes.

As a result of numerical computation, good agreement with analytical solution of the three-point bending problem was achieved. Mode I  $K_I$  and mode II  $K_{II}$  stress intensity factors were computed as  $1154.8 \text{ Pa}\sqrt{m}$  and  $7.3 \times 10^{-8} \text{ Pa}\sqrt{m}$ , respectively. Mode II stress intensity factor  $K_{II}$  was approximately zero as expected. Therefore, pure

bending conditions were satisfied. Both results of analytical solutions and numerical solution of the pure bending plate problem were listed in Table 4.2 below.

Table 4. 2 Comparative results for three-point bending plate

<b>Problem</b>	$K_I$ (Pa $\sqrt{m}$ )	$K_{II}$ (Pa $\sqrt{m}$ )	<b>Difference (%)</b>
<b>Srawley (1972)</b> <b>(2D Plane Strain)</b>	1159.43	0	-
<b>Tada et al., (2000)</b> <b>(2D Plane Strain)</b>	1160.00	0	-
<b>Numerical Result</b> <b>(3D Modeling)</b>	1154.80	$7.30 \times 10^{-8}$	0.4

3D numerical modeling  $K_{II}$  value is a little bit lower than 2D plane strain analytical values since in 3D modeling beam can expand in the out of plane direction freely as opposed to the solutions based on plane strain assumption. These results and agreements with solutions of Srawley (1976) and Tada (2000) show that numerical modeling of the problem is robust.

**4.3.2 Pure-shear plate verification problem**

Pure-shear plate can be defined as: a plate having a central embedded crack which is subjected to a shear traction on the upper surface. In Figure 4.14 applied surface shear stress and boundary conditions are illustrated.

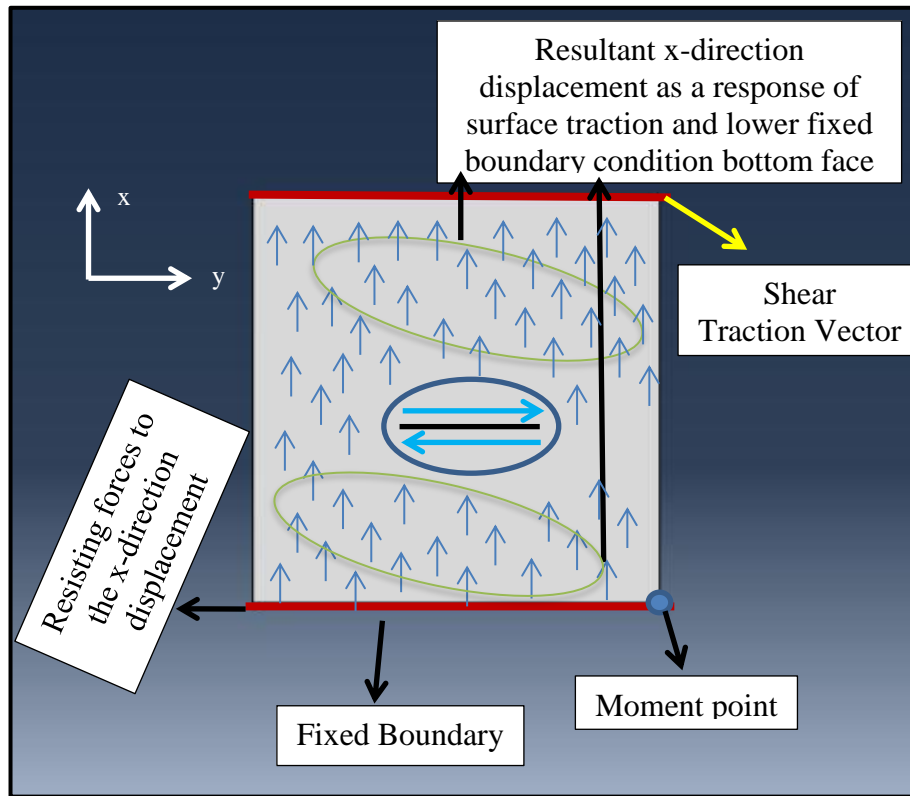


Figure 4. 14 Loading and boundary condition configuration of the pure shear plate problem

### *Analytical Solution*

On a 400 mm square plate having a 20 mm crack mode II loading conditions are imposed by applying 1 MPa surface shear traction at the upper boundary. Mode I and mode II stress intensity factors,  $K_I$  and  $K_{II}$  are calculated analytically by following formulas:

$$K_I = \sigma\sqrt{\pi a} \quad (4.9)$$

$$K_{II} = \tau\sqrt{\pi a} \quad (4.10)$$

For an only unit 1 MPa shear stress applied to upper boundary of the plate, stress intensity factor for mode I;

$$K_I = \sigma\sqrt{\pi a} = 0 \times \sqrt{\pi \times 0.01} = 0 \text{ MPa}\sqrt{\text{m}} \quad (4.11)$$

Since applied normal stress  $\sigma=0$ , and SIF for mode II;

$$K_{II} = \tau\sqrt{\pi a} = 1 \times \sqrt{\pi \times 0.01} = 0.177 \text{ MPa}\sqrt{\text{m}} \quad (4.12)$$

### *Numerical Solution*

The pure shear plate problem was modeled as a plane strain problem in two-dimensional space and assumed as linear elastic. Mechanical properties of the plate are used as Elastic Modulus of  $E = 200$  MPa, and Poisson's Ratio of  $\nu = 0.3$ . Out of plane thickness is 1600 mm long. This a plane strain problem; this dimension is there and significant only for computation of stress at the loaded boundary. In Following Table 4.3 geometric dimensions and material properties are listed.

Table 4. 3 Geometric dimensions and material properties of the problem

<b>Parameter</b>	<b>Value</b>
<b>Elastic Modulus (E)</b>	200 MPa
<b>Poisson's Ratio (<math>\nu</math>)</b>	0.3
<b>Height (2H)</b>	400 mm
<b>Width (2W)</b>	400 mm
<b>Plane Strain Thickness</b>	1600 mm
<b>Crack Length (2a)</b>	20 mm
<b>Surface Traction Amount</b>	1 MPa

Material properties of the previous beam problem and verification problem here are different and one may question these differences. At this point, in order to compare given solutions of these two well-known fracture mechanics problems no changes were made in properties used by previous researchers like Het (2014). In fact,

another study conducted by Het (2014) to investigate the effect of elastic properties on SIF's showed that no effect of varying  $E$  and  $\nu$  was observed. So, for better visualization of deformed shape of plate in checking the results, a rather low value of stiffness as  $E=200$  MPa was chosen to be input to the model.

In order to create 1 MPa shear stress on the upper surface of the plate, required load application was calculated from equation 4.13.

Edge of square plate = 400 mm.

Plane Strain Thickness= 1600 mm.

$$400 \text{ mm} \times 1600 \text{ mm} = 640,000 \text{ mm}^2.$$

$$\sigma = \frac{\text{Force}}{\text{Area}} \quad (4.13)$$

So,

$$1 \text{ MPa} = \frac{\text{Force}}{640,000 \text{ mm}^2} \quad (4.14)$$

$$\text{Force} = 640,000 \text{ N}.$$

In the Figure 4.15 loading and boundary conditions of the model can be seen.

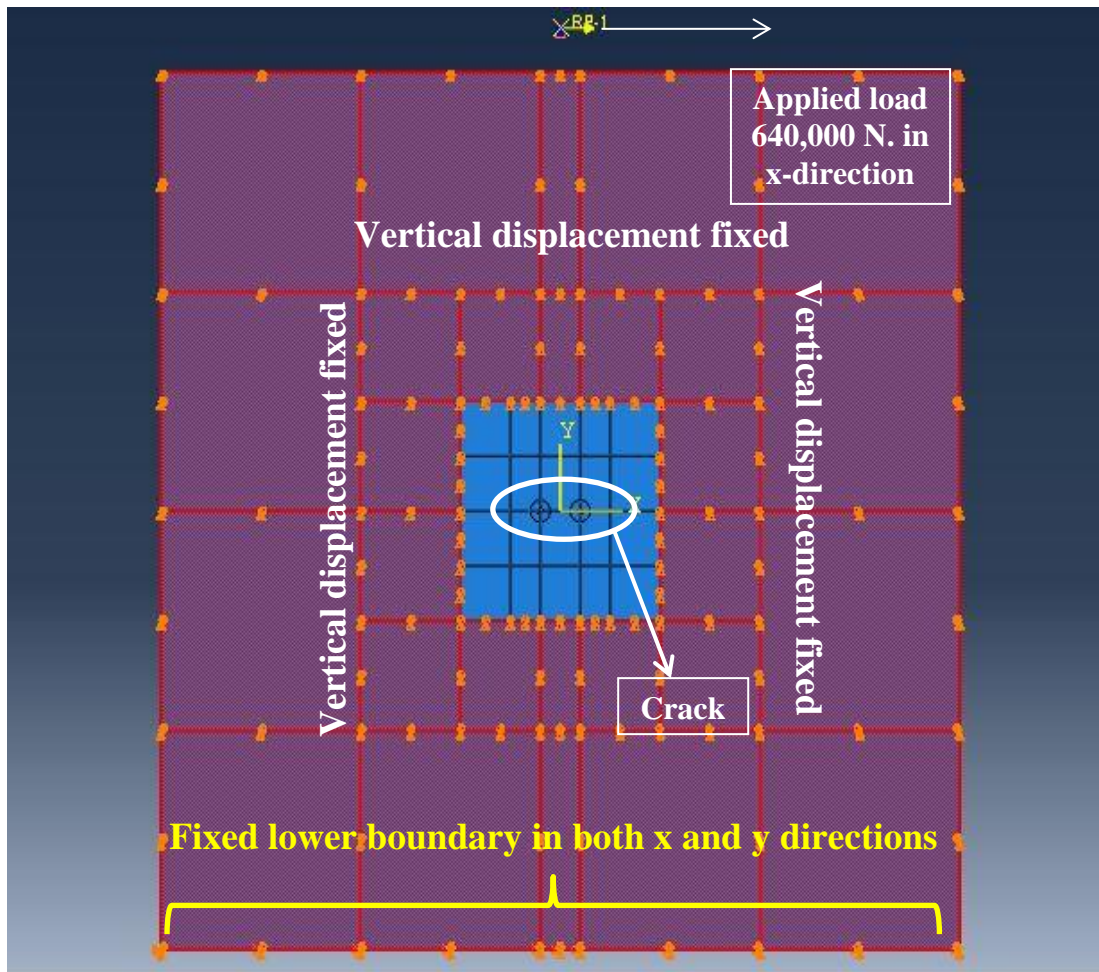


Figure 4. 15 Applied load and boundary conditions of the problem

In the three-point bending plate problem crack an edge crack, so there was only one crack tip inside the plate. In this problem because of the embedded crack, there are two crack tips naturally. Meshing was imposed by taking these effects into consideration. In the model, around 8000 eight-node plane strain CPE8R elements were utilized. Mesh concentration was structured in detail at the crack region again. In Figure 4.16 meshed form of whole body and crack region can be seen.

A seam crack with zero thickness was embedded to the center of the plate. ABAQUS constructs duplicate nodes on the seam and those duplicate nodes enable the crack to have ability of separation.

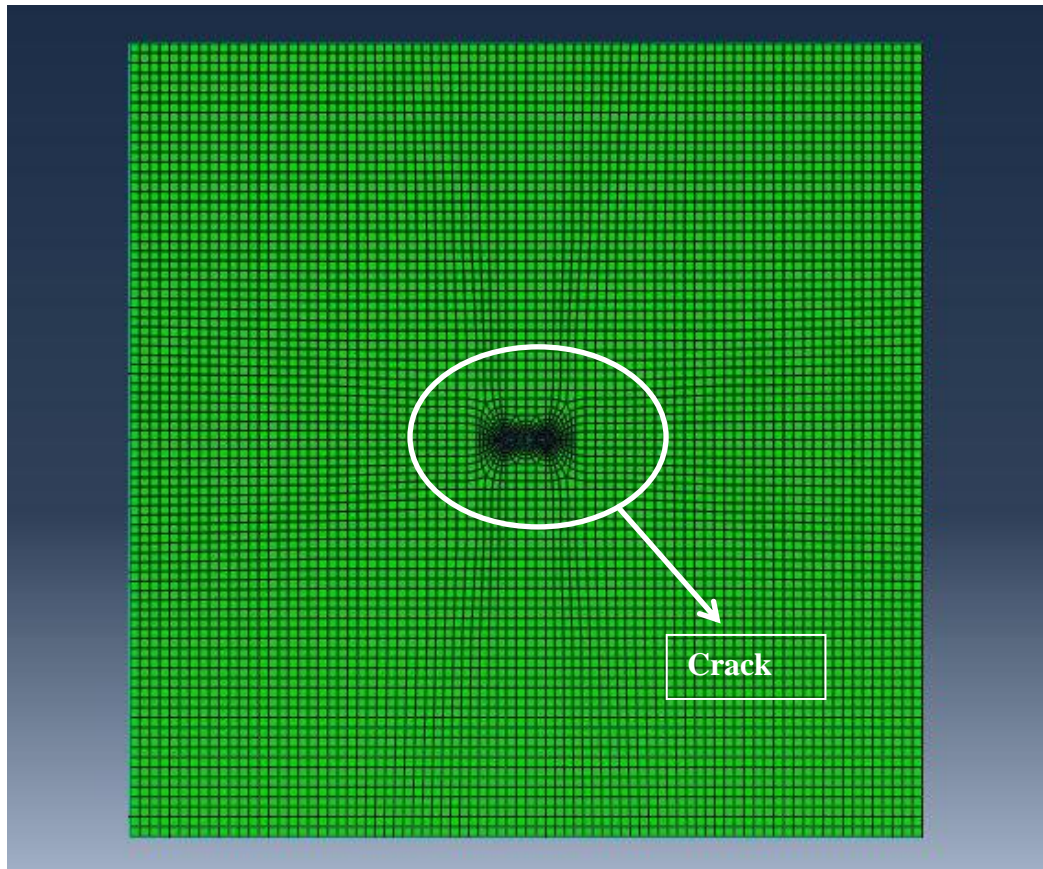


Figure 4. 16 Whole body meshing of pure shear plate

Fracture toughness is a material property. Stress intensity factor is in the form of  $K = \sigma\sqrt{\pi a}$  for plates under pure shear. So, in general crack propagation occurs when  $\sigma$  is equal to critical value  $\sigma_c$  or when crack is equal to critical length. This means,  $\sigma$  might be lower critical value but crack length might be long and ensures propagation.

In the formulation of crack tip stress field only  $\sigma$  and crack length are involved with constant stiffness. Thus, Young's modulus and Poisson's ratio do not effect stress intensity computations. In Figure 4.17 crack tip meshing style can be seen.

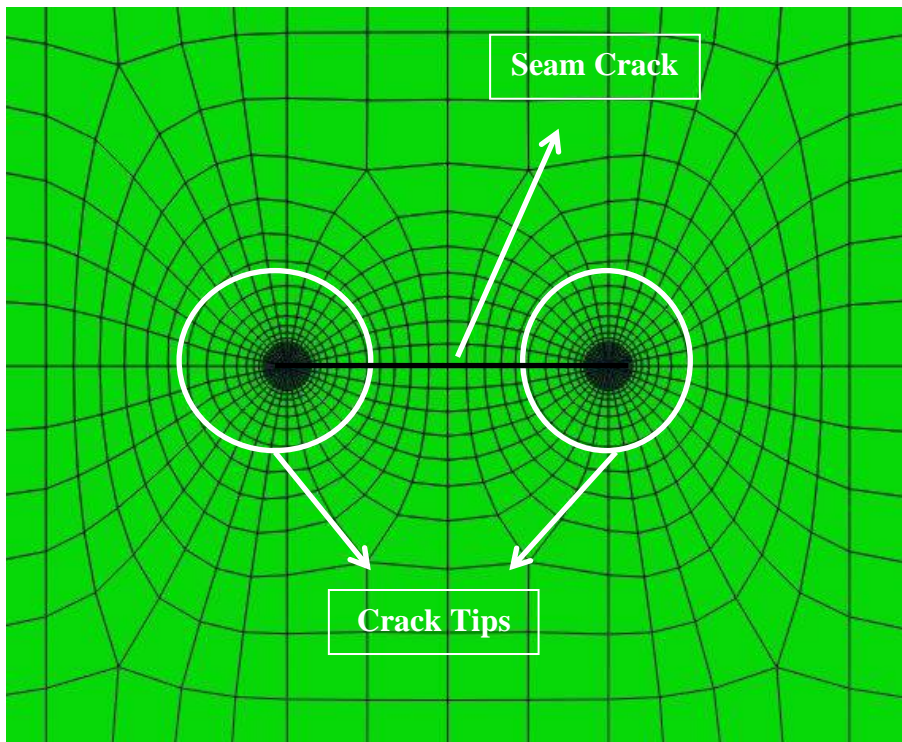


Figure 4. 17 Crack tip meshing of pure shear plate

Results extracted from the numerical computation of the pure-shear plate problem were very close to the results of analytical solutions. Numerical computation result for mode I stress intensity factor  $K_I$  was obtained as “0”. Mode II stress intensity factor  $K_{II}$  was  $0.175 \text{ MPa}\sqrt{\text{m}}$  compared to the analytical result of  $0.177 \text{ MPa}\sqrt{\text{m}}$ . The error between numerical computation and analytical calculation was around 0.2%.

Based on the results of verification work, it can be safely stated that modeling procedures, crack tip handling, and SIF computations are expected to yield sufficiently accurate results in SIF computations for modeling of FPAB specimen geometries in the following sections.

In order to get accurate results for SIF computations optimum number of contour integrals were decided as 19 contours. Optimum spacing between two succeeding

contours was 0.25 mm. Diameter of the outmost contour integral was set as 5 mm around the crack tip.

#### **4.4 Finite element modeling of beam geometries**

This chapter covers all the efforts creating numerical models of FPAB (four-point asymmetric bending), FPB (four point bending), and SNDB (straight notched disc bending) test specimen geometries.

Principal investigations concentrated on FPAB specimen geometry to investigate characteristics of pure mode II loading conditions and stress intensity factors. First, base numerical model was created for FPAB specimen, then stress redistribution and stress intensity factor parameters were investigated for different beam depths and crack lengths. FPAB test specimen models were constructed for three main beam depth groups. Then, behavior of models of each beam depth group was analyzed with eight different notch lengths. Entire specimen geometry and boundary load configurations were varied and adjusted to catch the right combinations generating pure mode II loading conditions at the crack tip.

FPB test specimen was modeled to have an idea about size of the crack tip plasticity zone under mode I loading for a beam type geometry under four point bending load similar to FBAB geometry. Purpose was to compare extent of fracture process zone (FPZ) for FPAB and FPB geometries under the same load intensity and similar boundary conditions.

Numerical model for SNDB test specimen was created to obtain the pure mode II SIF for a different geometry. A number of pure mode II tests were planned to be conducted with SNDB geometry.  $K_{IIc}$  result of SNDB tests was planned to be compared to mode II fracture toughness values of FPAB tests.

Numerical studies were conducted by utilizing Dassault Systemes' finite element code named ABAQUS<sup>®</sup> v.12 which mentioned in Chapter 6. Overall 120 numerical models were created to compute mode II stress intensity factor with FPAB specimen. In Figure 4.18 general geometry of FPAB specimen for mode II type of loading is illustrated.

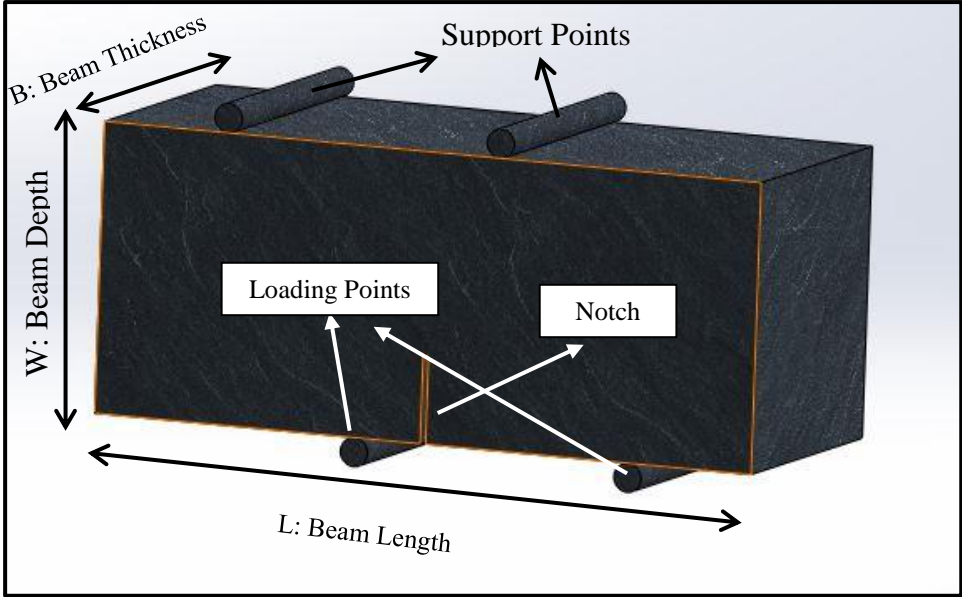


Figure 4. 18 Geometry of FPAB test specimen

**4.4.1 Improvement studies of base numerical model of FPAB test specimen**

In order to create reliable and robust numerical model of FPAB test specimen several trial numerical models were created. These numerical models were generated for one model geometry at first.

Beam length or in other words span of specimen was constrained by platen size of compression test machine in the laboratory. So, beam length was configured as 120 mm in first place. Then, in order to create well-shaped geometry, beam depth of the specimen was set as 50 mm and beam thickness as well. Initial notch length was preferred as 15 mm ( $a/W=0.3$ ) in order to avoid possible boundary influence effects

(Bazant and Pfeiffer 1986). After base specimen geometry was structured, location selection and configuration studies for load and support points were performed to create pure shear effect on the crack plane. To do this, first 2D (plane strain) numerical models were created. Plane stress thickness of the numerical model was implied as 50 mm. Then, bottom loading points were subjected to a unit load of 1 N in total and support locations were varied to create pure shear effect on the crack plane.

In the literature there are such investigations (Bazant and Pfeiffer, 1986; Suresh et.al., 1990; Ayatollahi et. al., 2012) that were aimed at creating pure shear effect on the crack plane for FPAB test specimen. Therefore, to create zero bending moment on the crack plane unit load partially was divided and applied to the loading points. For each loading point a part of the unit load was applied proportional to their distances to the crack plane.

2D plane strain numerical models showed that, the best configuration is obtained for  $L=3d$ . For the specimen having  $L=120$  mm,  $W=50$  mm  $B=50$  mm and  $a=15$  mm, pure shear mode II stress intensity factor was satisfied when  $d=12.5$  mm and  $L= 37.5$  mm.

Table 4. 4 Modeling parameters of base FPAB model

<b>Parameters</b>	<b>Values</b>
Length	120 mm
Depth (W)	50 mm
Thickness (B)	50 mm
Short moment arm distance (d)	12.5 mm
Long moment arm distance (L)	37.5 mm
Notch length (a)	15 mm
Young's Modulus	12.3 GPa
Poisson's Ratio	0.12
Load (short moment arm)	0.75
Load (long moment arm)	0.15

In Figure 4.19 loading and support points that satisfy the pure shear conditions on the crack plane are shown. Material properties ( $E$  and  $\nu$ ) for Ankara Gölbaşı Andesite are extracted from laboratory tests. In Table 4.4 modeling parameters of base FPAB model are listed.

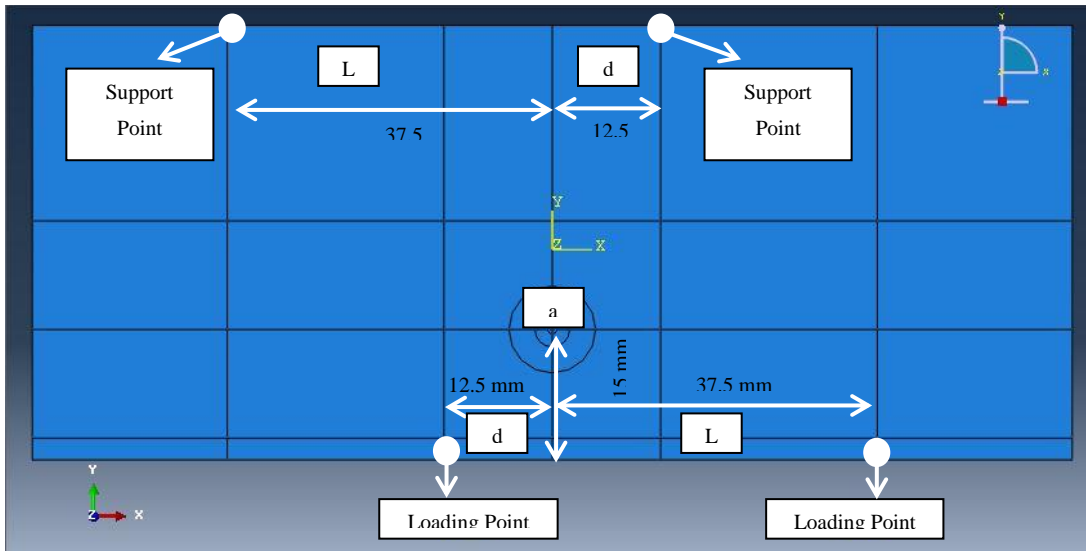


Figure 4. 19 One of loading and supporting points configuration for FPAB specimen

After locations of loading and support points were determined from 2D models, 3D numerical models were created for more realistic simulation of the beam as a plate with finite thickness as used in test samples. 3D numerical models are more sensitive to boundary conditions than 2D numerical models. Therefore, defining boundary conditions are crucial for 3D dimensional numerical analysis. In the following section, development of boundary conditions of FPAB test specimen will be explained.

#### 4.4.2 Boundary conditions of numerical models

Essential boundary conditions are one of the most critical parameters in numerical modeling studies. Finite element method uses to make approximations to compute the stresses, bending moments and the other mechanical entities on given body and

uses differential equations. These differential equations are in form of boundary value problems. Shortly it can be said that, essential boundary conditions in Finite Element Analysis are the initial values of the differentiated entities. Then, essential boundary conditions are implied to the numerical model. So, all the approximations are made by using these essential boundary conditions. Therefore, to have an idea of correct essential boundary conditions, several trial computations have to be conducted and their results must be mechanically examined to achieve accurate solutions.

After all these trials the most reliable numerical model that accurately approximated real-life behavior of the test specimen were selected as the modeling technique of this beam or plate problem.

For upper support points along entire thickness of the beam were ( $u_2$  and  $u_3$ ) fixed against displacement in  $-y$  and  $-z$  directions. For right and left flat sides of the beam all planar surfaces were fixed against rotation about  $-z$  axis. For loading points along entire thickness of the beam except for  $-y$  direction ( $u_2$ ) all degree of freedoms fixed ( $u_1, u_3, u_{r1}, u_{r2}, u_{r3}$ ). Boundary conditions identified as ideal for FPAB specimen geometry are shown in Figure 4.20 and Figure 4.21. In Table 4.5 boundary conditions for FPAB specimen geometry are listed.

Table 4. 5 Boundary conditions for FPAB test geometry

<b>Boundary Condition</b>	<b>Implied Geometric Entity</b>	<b>Fixed DOF</b>
B.C. 1	Reference point 1 (loading line)	$u_1, u_3, u_{r1}, u_{r2}, u_{r3}$
B.C. 2	Reference point 2 (loading line)	$u_1, u_3, u_{r1}, u_{r2}, u_{r3}$
B.C. 3	Support points of short moment arm	$u_2, u_3$
B.C. 4	Support points of long moment arm	$u_2, u_3$
B.C. 5	Right flat side	$u_{r3}$
B.C. 6	Left flat side	$u_{r3}$

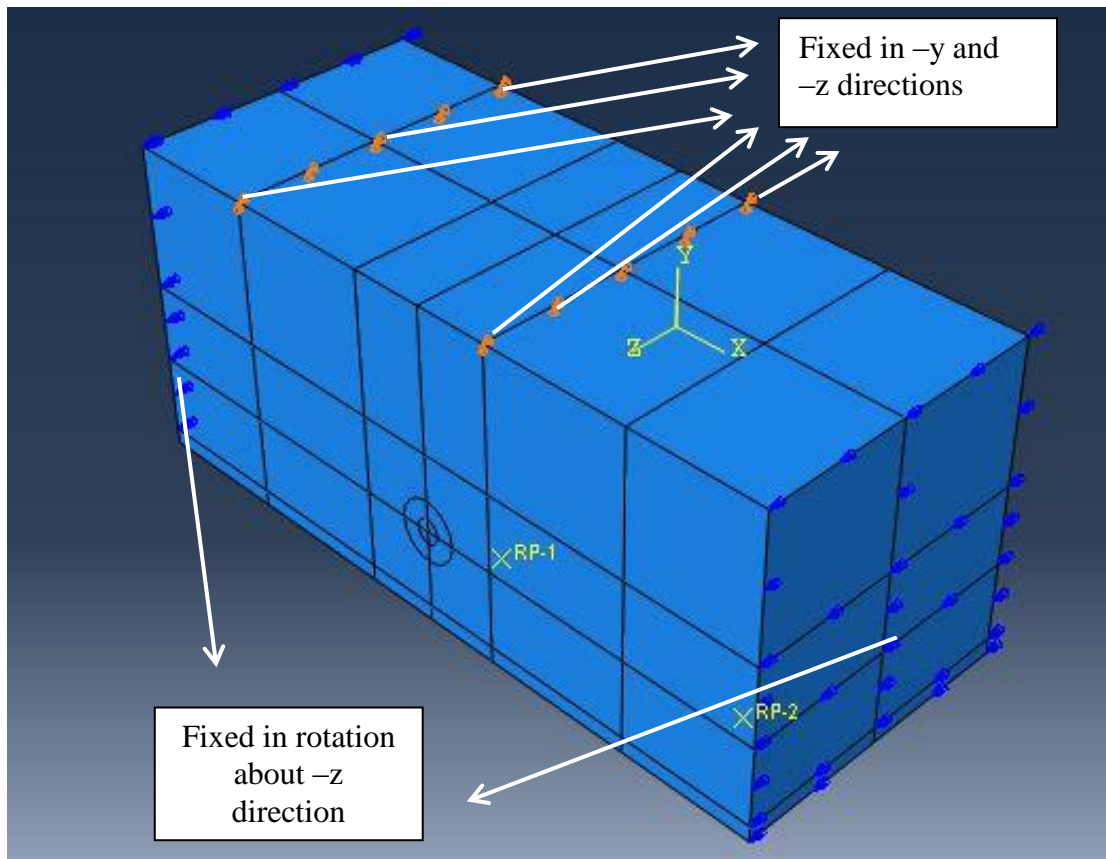


Figure 4. 20 Boundary conditions 1

Reference Points are special entities that offered by ABAQUS<sup>®</sup> software. Unit load was applied through Reference Points to the related loading points. They were utilized for converting the concentrated load into distributed load. Reference Points were bounded by kinematic coupling method to related points. Kinematic coupling creates links between Reference Points and influenced node regions which are selected by user. In Figure 4.21 these kinematic coupling links are illustrated Kinematic coupling method enables the control of selection which degree of freedom of the selected nodal surface will be affected by implied conditions. In our case these implied conditions are two concentrated loads which are distributed to the two lines that lie on the bottom flat surface of beam. Implied boundary conditions of Reference Points are shown in Figure 4.22.

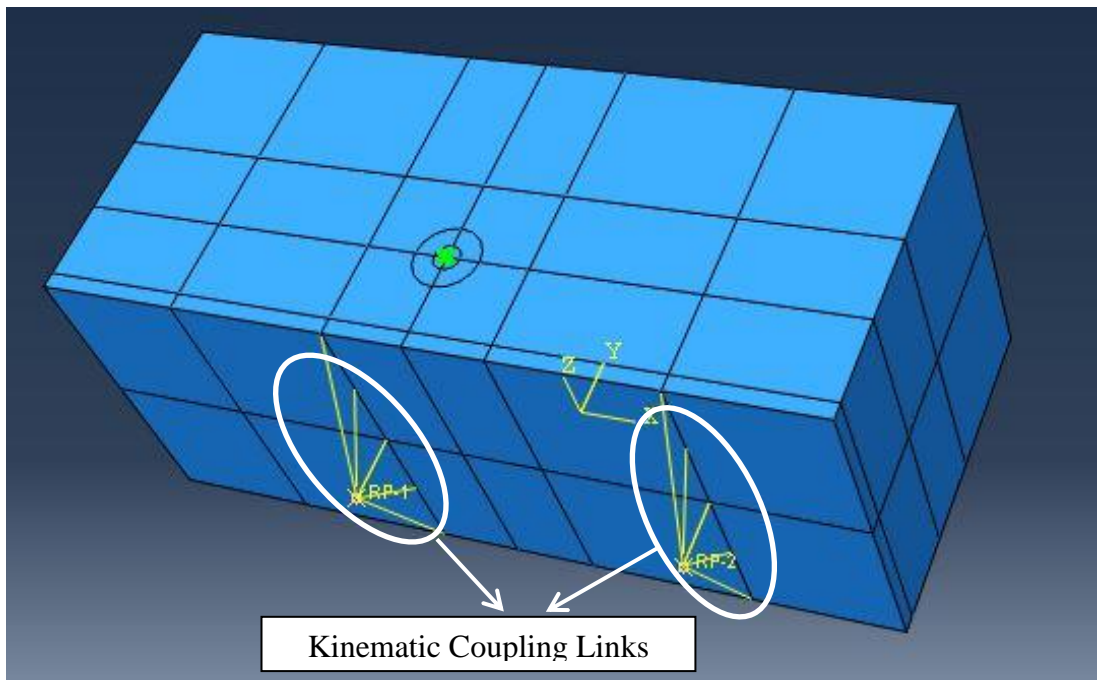


Figure 4. 21 Kinematic coupling of reference points

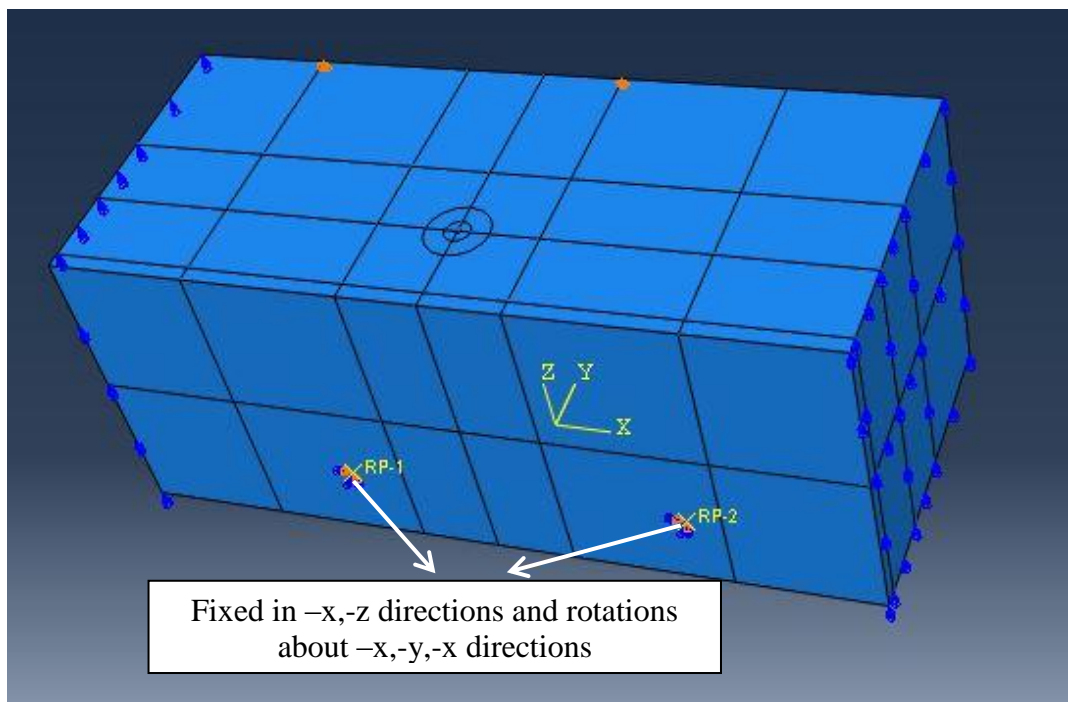


Figure 4. 22 Boundary conditions of reference points

### 4.4.3 Mesh generation of FPAB specimen

Meshing process of numerical modeling work is the most important part of finite element analysis. Wang et al., (1977) employed singularity elements, in order to compute singular stresses around crack tip. Crack tip possesses  $\sigma \propto \frac{1}{\sqrt{r}}$  type singularity. Likewise, in this study, to compute crack tip stress singularity the same singularity element offered by ABAQUS element library was employed.

Another important point on meshing process in crack problems is size of the contour integral region. Improper contour integral regions which are excessively large or small may lead acquiring inaccurate results for SIFs. ABAQUS suggests certain techniques for size of contour integral region. These techniques are related to the length of the crack. Following these suggestions, size of the outmost contour integral region was set as 5 mm (Figure 4.23). The innermost contour integral region (first contour integral region) was set as 0.5 mm. So, 19 contour integrals were achieved and this number was stated as appropriate number of contours in the integral region (ABAQUS User's Manual, 2012). All numerical models were created with the same contour integral region properties in terms of size and number. This consistency and stability enabled justifiable comparisons of size of potential plastic zones and von-mises stresses around crack tip for different models.

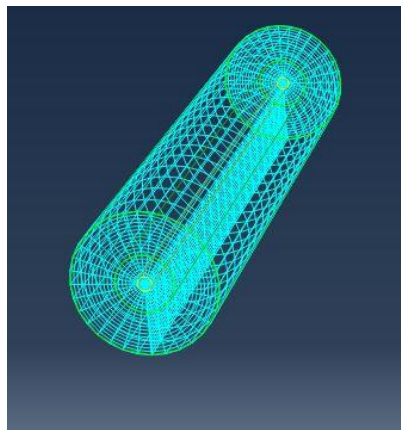


Figure 4. 23 Contour integral region and meshing

Remaining parts of the FPAB test specimen were built by utilizing structured C3D8R brick elements. Element density of the numerical model was set as approximately 80000. In Figure 4.24 and 4.25 crack tip meshing and whole body meshing of FPAB test specimen are illustrated.

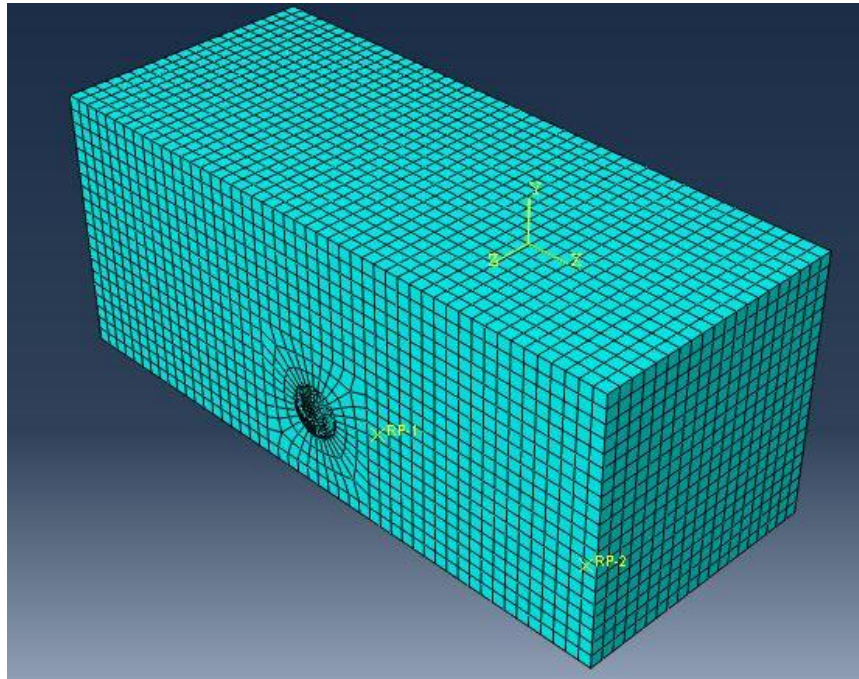


Figure 4. 24 Whole body meshing

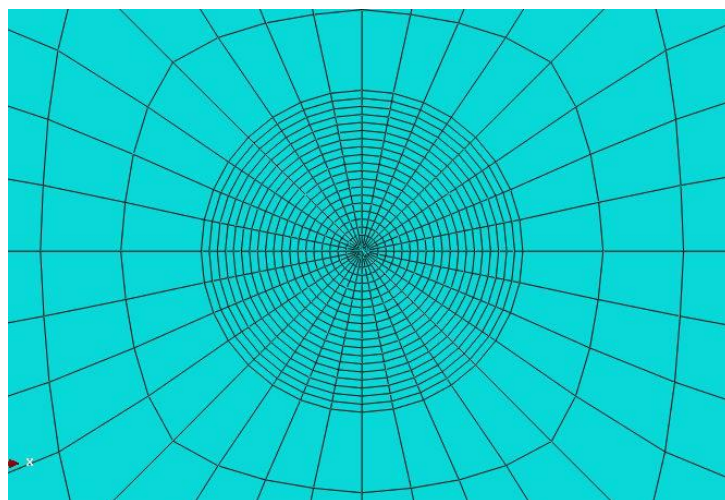


Figure 4. 25 Crack tip meshing

#### 4.4.4 Loading configuration investigation for pure mode II SIF state in FPAB models

The pure shear mode II configuration of each beam depth group was investigated for different crack lengths (notch length/ beam depth)  $a/W=0.15, 0.20, 0.25, 0.30, 0.35, 0.40, 0.50$  and  $0.60$ . In order to find the proper loading configuration, five different loading configurations were employed for each crack length. In Table 4.6 applied loading configurations for the specimen having beam depth 50 mm, 0.3 dimensionless notch length (in dimensional form 15 mm) were listed.

Table 4. 6 Various loading configurations applied to a specific specimen  $W= 50$  mm and  $a/W= 0.3$  for pure mode II SIF  $K_{II}$

Beam Length (mm)	Beam Depth (mm)	Beam Thickness (mm)	Notch Length (mm)	Dimensionless Notch Length	Short Moment Arm (d) (mm)	Long Moment Arm (L) (mm)
					11.5	34.5
					12.0	36.0
120	50	50	15	0.3	<b>12.5</b>	<b>37.5</b>
					13.0	39.0
					13.5	40.5

For described specimen geometry, loading configuration with  $d= 12.5$  mm and  $L= 37.5$  mm yielded almost pure mode II SIF condition on the crack plane. In table 4.7,  $K_I$  and  $K_{II}$  results for the concerned specimen were listed.

Using these results, actual loading configuration that makes mode I SIF absolutely “zero” (pure shear) was calculated. Linear fit in Figure 4.26 gives optimum value of “ $d$ ” distance that makes mode I SIF absolute “zero”.

Table 4. 7 Loading configurations and computed mode I and II SIF's for the specimen  $W=50$  mm and  $a/W=0.3$

<b>d (mm)</b>	<b>L (m)</b>	<b><math>K_I</math> Pa<math>\sqrt{m}</math></b>	<b><math>K_{II}</math> Pa<math>\sqrt{m}</math></b>	<b><math>K_I/K_{II}</math> (%)</b>
11.5	34.5	-2.26	-49.07	4.62
12.0	36.0	-1.31	-48.47	2.64
<b>12.5</b>	<b>37.5</b>	<b>-0.38</b>	<b>-47.68</b>	<b>0.78</b>
13.0	39.0	0.48	-42.02	-1.19
13.5	40.5	1.32	-43.93	-3.02

In this case “ $d$ ” distance that satisfies pure shear conditions on the notch plane is evaluated as 12.72 mm. In modeling work the reason for choosing  $d=12.5$  mm instead of exact value of short moment arm is due the accuracy of machining the initial notch to the beam specimen in experimental work of fracture toughness investigations. Locating the loading rollers in real life to such a number like  $d=12.72$  mm is not possible. Half millimeters of sensitivity is the limit point of experimental study.

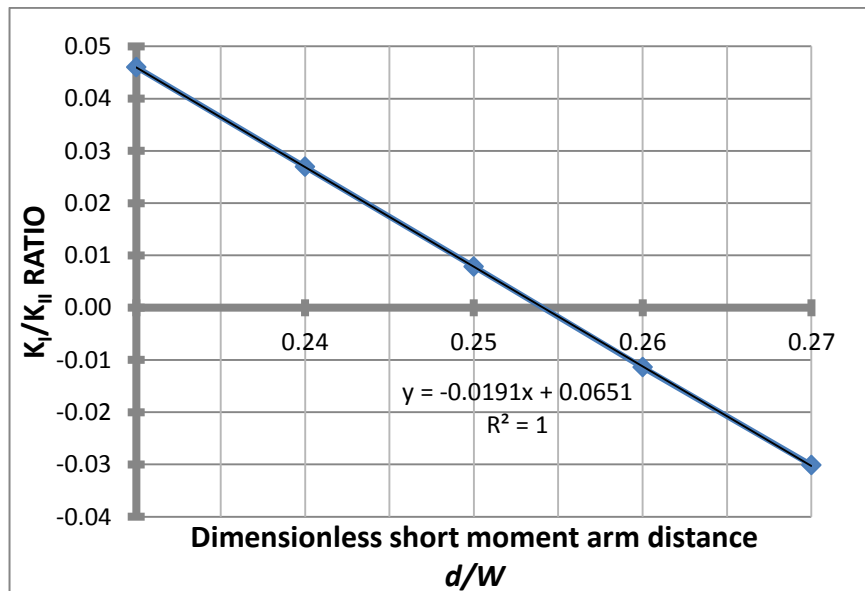


Figure 4. 26 Fit function for loading configuration satisfies absolute Pure mode II SIF effect

This computation process was applied to the all crack lengths  $a/W=0.15, 0.20, 0.25, 0.30, 0.35, 0.40, 0.50$  and  $0.60$  for the specimen  $W=50$  mm. In table 4.8, dimensionless short moment arm “ $d/W$ ” values corresponding dimensionless crack lengths  $a/W$  were listed. Remaining charts for dimensionless short moment arm and  $K_I/K_{II}$  ratios were given in APPENDIX A.

Table 4. 8 Dimensionless short moment arm values corresponding to dimensionless crack lengths

<b>Dimensionless crack length (<math>a/W</math>)</b>	<b>Dimensionless short moment arm (<math>d/W</math>)</b>
0.15	0.21
0.20	0.23
0.25	0.25
0.30	0.25
0.35	0.24
0.40	0.23
0.50	0.18
0.60	0.14

As a result, fourth order polynomial fit function (Figure 4.27) was derived for  $d/W$  and  $a/W$  values. This result apparently shows the relationship between moment arms and crack lengths. This also indicates that required bending moment on the initial notch for crack propagation regarding pure mode II conditions is independent from beam depth.

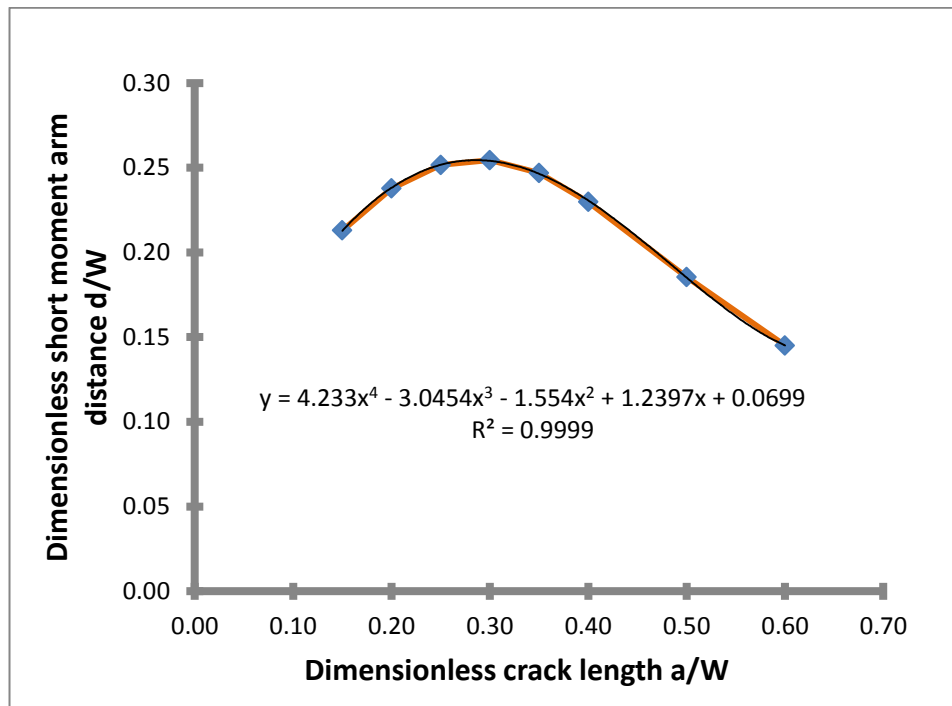


Figure 4. 27 Beam depth 50 mm fourth order polynomial fit function for  $d/W$  vs  $a/W$  FPAB specimens for  $W=40$  and  $60$  mm, similar results for dimensionless short moment arm distance versus dimensionless crack lengths  $a/W=0.15, 0.20, 0.25, 0.30, 0.35, 0.40, 0.50$  and  $0.60$  were established. Graphical results for these relationships are illustrated in following Figures 4.28 and 4.29.

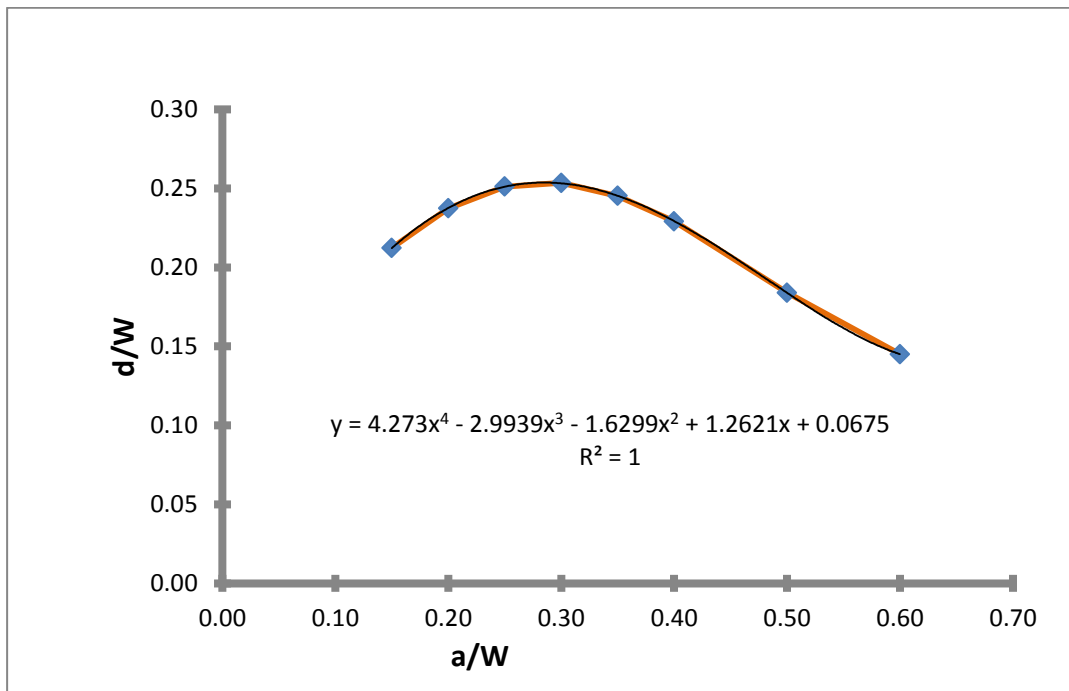


Figure 4. 28 Beam depth 40 mm fourth order polynomial fit function for  $d/W$  vs  $a/W$

Dimensionless short moment arm distance ( $d/W$ ) first shows an increasing trend up to relative crack length ( $a/W$ ) around 0.3, then decreases following a fourth order polynomial form.

The critical  $d/W$  values ensuring pure shear condition is measured in terms of  $K_I/K_{II}$  ratio, (ratio should be zero, for pure shear condition).

Values other than the optimum  $d/W$  cause development of opening mode and non-zero mode I stress intensity factor on the crack plane. In this case pure shear condition fails.

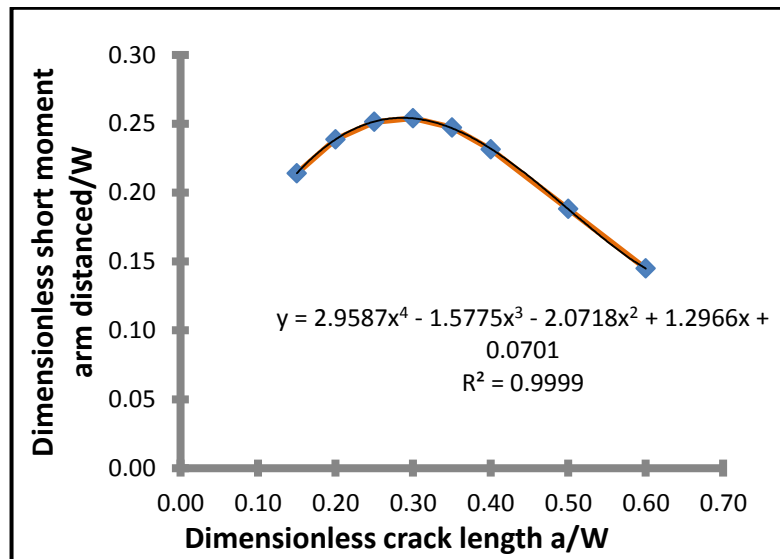


Figure 4. 29 Beam depth 40 mm fourth order polynomial fit function for  $d/W$  vs  $a/W$

Relationship between  $d/W$  and  $a/W$  was represented quite accurately in the same fourth order polynomial for all beam depth groups. Combining all beam depths in a single plot and functional form, dimensionless short moment arm distances ( $d/W$ ) were averaged in terms of corresponding dimensionless notch lengths ( $a/W$ ) and plotted in Figure 4.30.

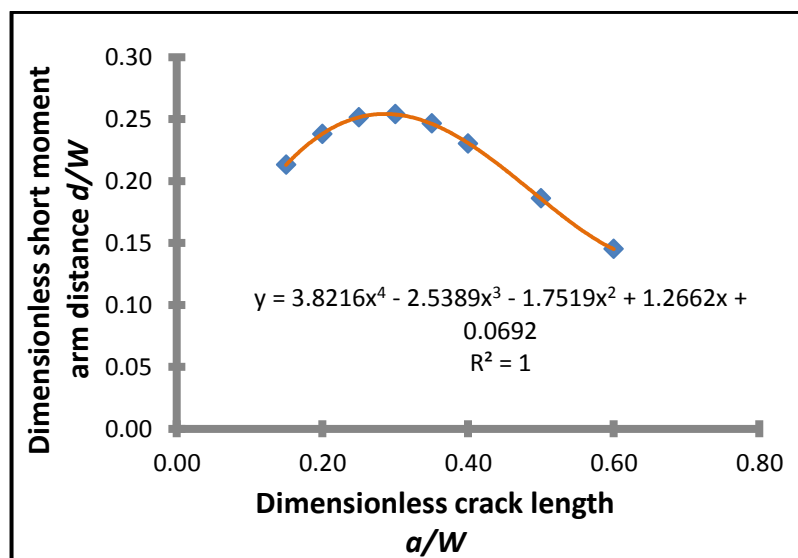


Figure 4. 30 Average  $d/W$  vs  $a/W$  relationship; all beam depths were combined

For  $d/W$  vs  $a/W$  relationship, a fourth order polynomial fit function produced quite accurate ( $R^2=1$ ) results in estimating correct short moment arm distance to create pure shear state on the notch plane. New parametric equation is proposed for optimum  $d/W$  value for pure mode II conditions as;

$$\begin{aligned} d/W = & 3.8216(a/W)^4 - 2.5389(a/W)^3 - 1.7519(a/W)^2 \\ & + 1.2662(a/W) + 0.0692 \end{aligned} \quad (4.15)$$

These findings are not sufficient to declare for FPAB testing geometry that there is no size effect and boundary influence effect on mode II SIF. These are strong indications of FPAB testing geometry is free from size and boundary effects. Therefore, SIF investigations and stress analyses should be conducted. In this study stress analyses were conducted in terms of von-mises yield criterion.

#### **4.4.5 Pure mode II SIF investigation for different beam depths and crack lengths**

Numerical models of pure mode II stress intensity factors for each beam depth group and dimensionless crack lengths were created. For three beam depth groups  $W= 40, 50$  and  $60$  mm and dimensionless crack lengths  $a/W=0.15, 0.20, 0.25, 0.30, 0.35, 0.40, 0.50$  and  $0.60$  geometries were modeled. In all, 24 loading configurations were obtained that satisfy pure mode II conditions. Pure mode II results for these geometries are listed in Table 4.9. All Mode I stress intensity factors of computed specimen geometries were approximately “0”.

Table 4. 9 Pure mode II results for all beam depth groups

<b>Beam Depth Group (mm)</b>	<b>Dimensionless Crack Length (a/W)</b>	<b>Dimensionless Short Moment arm Distance (d/W)</b>	<b>Short Moment Arm Distance (mm)</b>	<b>Pure Mode II SIF (Pa√m)</b>
<b>40</b>	0.15	0.2125	8.5	26.98
	0.20	0.2375	9.5	35.18
	0.25	0.2500	10.0	44.06
	0.30	0.2500	10.0	53.30
	0.35	0.2500	10.0	60.81
	0.40	0.2250	9.0	68.05
	0.50	0.1875	7.5	76.99
	0.60	0.1375	5.5	81.04
<b>50</b>	0.15	0.2100	10.5	24.46
	0.20	0.2400	12.0	31.26
	0.25	0.2500	12.5	39.63
	0.30	0.2500	12.5	47.68
	0.35	0.2500	12.5	54.59
	0.40	0.2300	11.5	60.92
	0.50	0.1800	9.0	68.38
	0.60	0.1400	7.0	73.18
<b>60</b>	0.15	0.2167	13.0	21.56
	0.20	0.2417	14.5	28.60
	0.25	0.2500	15.0	36.36
	0.30	0.2500	15.0	43.75
	0.35	0.2500	15.0	49.80
	0.40	0.2333	14.0	55.77
	0.50	0.1833	11.0	62.90
	0.60	0.1417	8.5	67.32

In order to see the relation between pure mode II SIF and different notch lengths, graphical illustration of dimensionless notch length  $a/W$  versus pure mode II SIF plots were created. Finally, graphical study showed that there was a regular functional relationship between pure mode II SIF and dimensionless crack length  $a/W$ . In Figure 4.31 relationships between pure mode II SIF and dimensionless crack length for all three beam depth groups are illustrated.

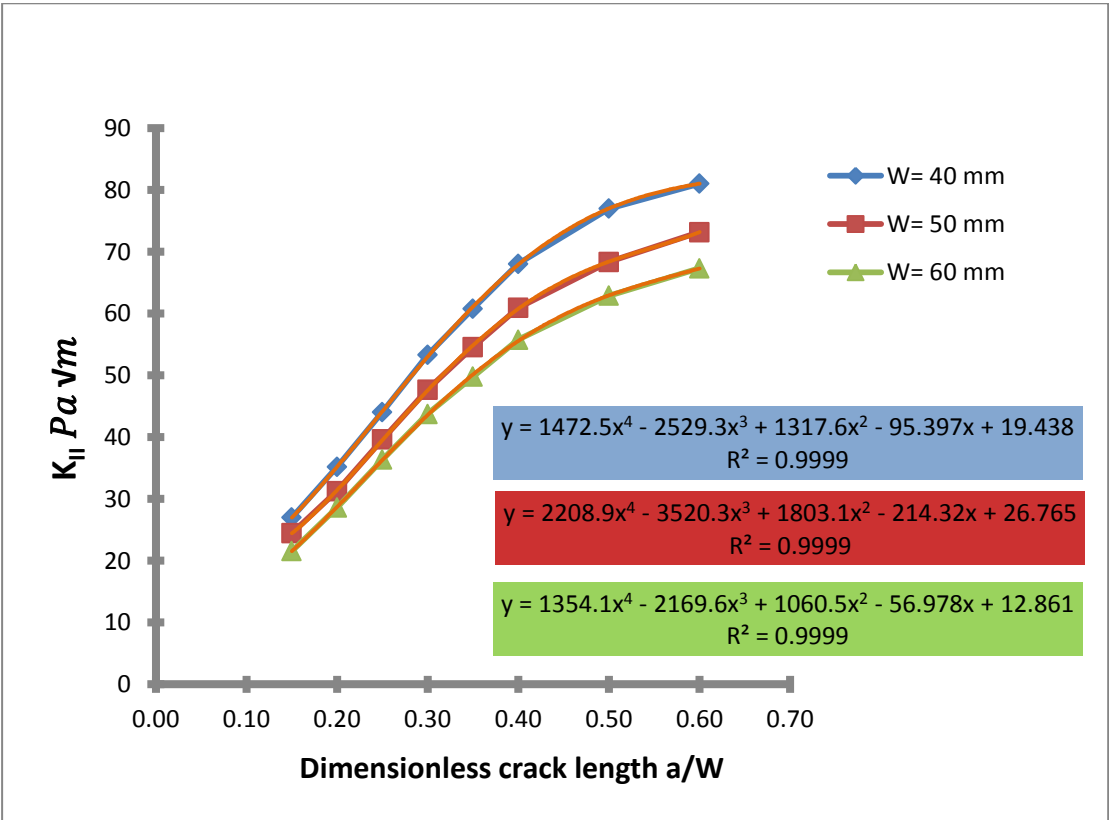


Figure 4. 31 Pure mode II SIF vs  $a/W$  results for all three beam depth groups

Deformed and undeformed shapes of FPAB test specimen geometry are illustrated in Figure 4.32. As it is can be seen in the Figure 4.33, crack tip is under effects of shear stresses obviously.

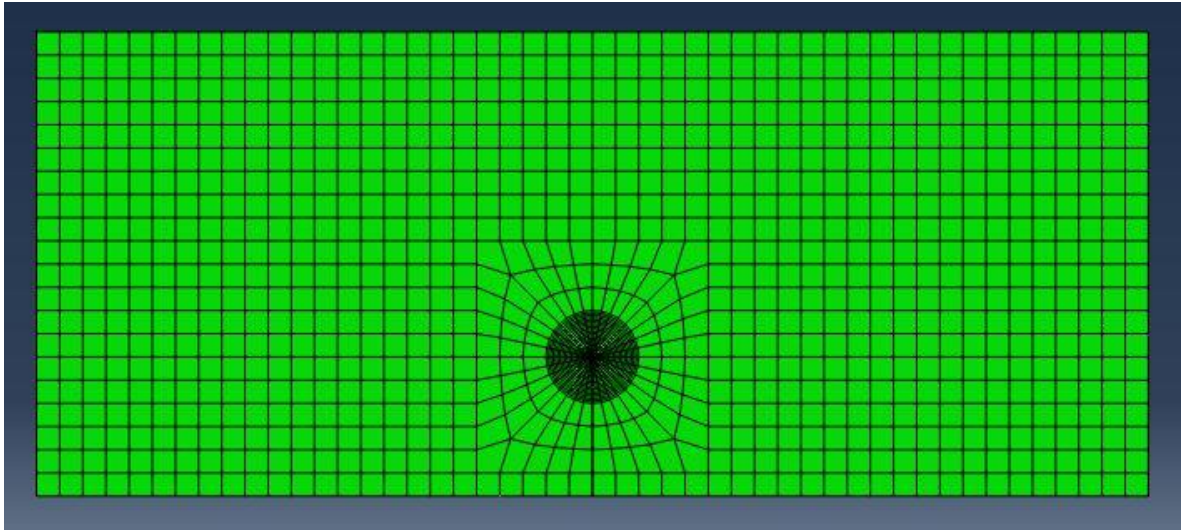


Figure 4. 32 Undeformed shape of FPAB test geometry

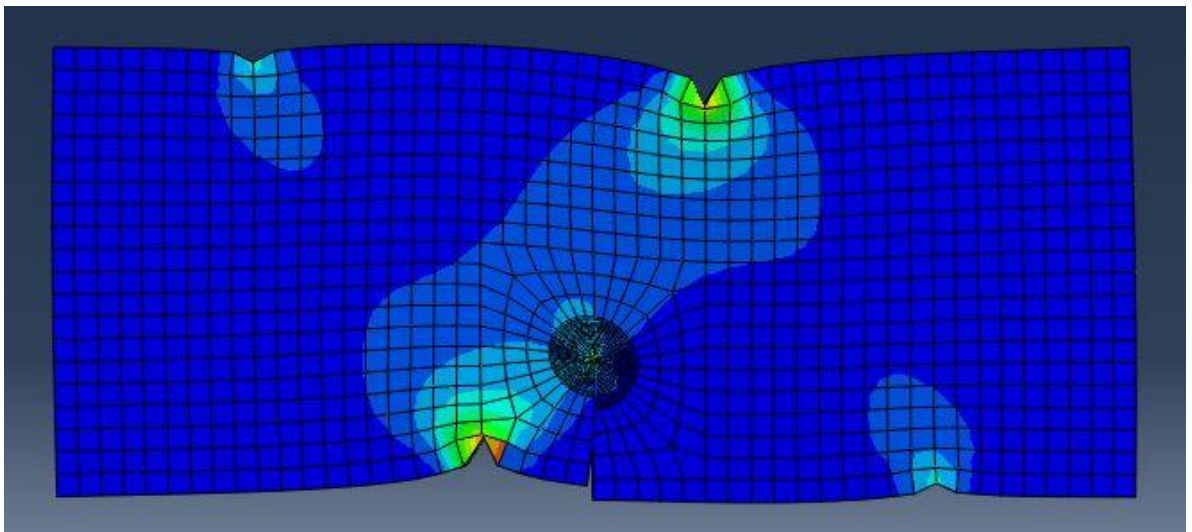


Figure 4. 33 Deformed shape of FPAB test geometry

Dimensionless stress intensity factors both mode I and mode II were achieved by using following equations (4.16 and 4.17); the same equations were also given by Fett (1998);

$$K_I = \frac{F}{BW} \left(1 - \frac{d}{L}\right) Y_I \sqrt{\pi a} \quad (4.16)$$

$$K_{II} = \frac{F}{BW} \left(1 - \frac{d}{L}\right) Y_{II} \sqrt{\pi a} \quad (4.17)$$

$$Y_I = \frac{K_I BW}{F \sqrt{\pi a}} \left(\frac{L}{L-d}\right) \quad (4.18)$$

$$Y_{II} = \frac{K_{II} BW}{F \sqrt{\pi a}} \left(\frac{L}{L-d}\right) \quad (4.19)$$

Other researchers He and Hutchinson (2000) were proposed new equations for calculation of dimensionless stress intensity factor both mode I and II. Proposed new equations were as follow;

$$K_I = \frac{6cQ}{\sqrt{W^2}} \sqrt{\pi a} Y_I(a/W) \quad (4.20)$$

$$Y_I = \sqrt{\frac{2W}{\pi a} \tan \frac{\pi a}{2W} \frac{0.923 + 0.199 \left(1 - \sin \frac{\pi a}{2W}\right)^2}{\cos \frac{\pi a}{2W}}} \quad (4.21)$$

for;  $0 \leq \frac{a}{W} \leq 1$

$$K_{II} = \frac{Q}{\sqrt{W}} \frac{(a/W)^{3/2}}{(1 - a/W)^{1/2}} Y_{II}(a/W) \quad (4.22)$$

$$Q = P \left(L - \frac{d}{L + d}\right) \quad (4.23)$$

Utilizing these two expressions mode II dimensionless stress intensity factors  $Y_{II}$  values were calculated. In table 4.10 calculated pure mode dimensionless II stress intensity factors  $Y_{II}$  were listed.

Table 4. 10 Dimensionless mode II SIF results for present work

<b>Beam Depth Group (mm)</b>	<b>Dimensionless Crack Length (a/W)</b>	<b>Pure mode II SIF (Pa√m)</b>	<b>Dimensionless SIF <math>Y_{II}</math> present work</b>
<b>40</b>	0.15	26.98	0.59
	0.20	35.18	0.67
	0.25	44.06	0.75
	0.30	53.30	0.82
	0.35	60.81	0.87
	0.40	68.05	0.91
	0.50	76.99	0.92
	0.60	81.04	0.89
<b>50</b>	0.15	24.46	0.60
	0.20	31.26	0.66
	0.25	39.63	0.75
	0.30	47.68	0.82
	0.35	54.59	0.87
	0.40	60.92	0.91
	0.50	68.38	0.91
	0.60	73.18	0.90
<b>60</b>	0.15	21.56	0.58
	0.20	28.60	0.66
	0.25	36.36	0.75
	0.30	43.75	0.83
	0.35	49.80	0.87
	0.40	55.77	0.91
	0.50	62.90	0.92
	0.60	67.32	0.90

In Fett’s study there is no information about FPAB test specimen for such geometries which are conducted throughout this study. In addition to this, no mathematical expressions were proposed for geometric functions of FPAB specimen in Fett (1998). As a result of SIF study conducted here, fourth order polynomial fit functions were derived for three main beam depth groups by using the same formula of dimensionless SIFs given in Fett 1998 (Figure 4.34). Difference between dimensionless values of mode II SIFs of He-Hutchinson (2000) and Fett (1998) is explained by utilization of different geometric parameters involved in expressions for dimensionless stress intensity functions.

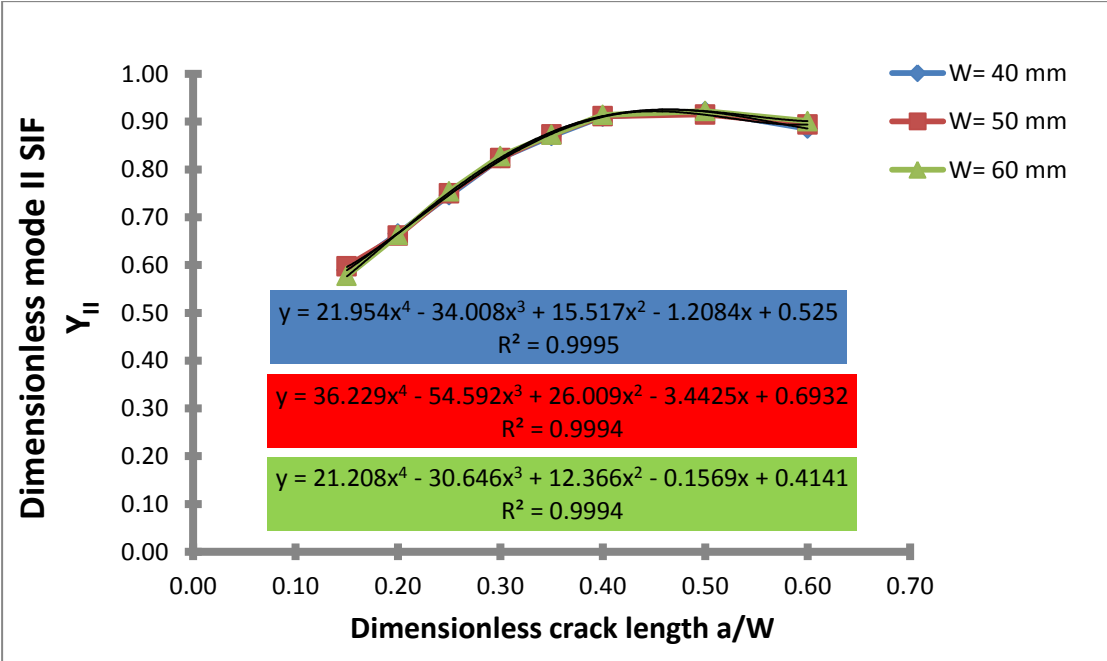


Figure 4. 34 Calculated dimensionless mode II SIF versus crack length in this study

It is observed that the same curved behaviour dominate the  $Y_{II}$  versus  $a/W$  trend and this trend can be represented by a fourth order functional form in sufficient accuracy.

In order to propose single polynomial fit function, dimensionless SIF values were averaged individually. In figure 4.35 graphical illustration of average dimensionless SIF values and fourth order polynomial fit function were given.

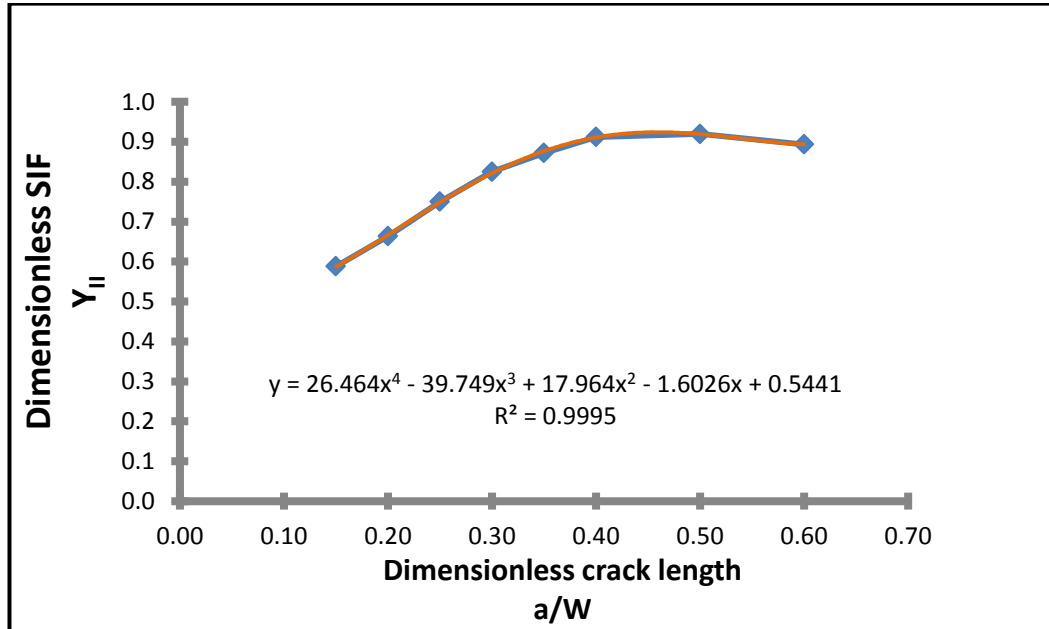


Figure 4. 35 Average dimensionless SIF and fourth order polynomial fit function for all beam depth groups

As a result, in order to calculate mode II stress intensity factor for FPAB test specimen following equations were proposed;

$$K_{II} = \frac{F}{BW} \left(1 - \frac{d}{L}\right) Y_{II} \sqrt{\pi a} \quad (4.24)$$

$$Y_{II} = 26.464 \left(\frac{a}{W}\right)^4 - 39.749 \left(\frac{a}{W}\right)^3 + 17.964 \left(\frac{a}{W}\right)^2 - 1.6026 \left(\frac{a}{W}\right) + 0.5441 \quad (4.25)$$

In literature, analytical and semi-analytical solutions for SIF computation are in the form of fourth order polynomial (Tada et al., 2000 and Srawley 1976). So, in this

study following general trend in fracture mechanics investigations on beam type geometries, mode II SIF estimation equations are given as fourth order polynomial powers of  $a/W$ .

## CHAPTER 5

### PURE MODE II FRACTURE TOUGHNESS TESTING WITH FPAB GEOMETRY

Experimental studies were conducted on grey colored Ankara Gölbaşı Andesite rock type. In order to evaluate mechanical properties of grey colored Ankara Gölbaşı Andesite, static deformability and Indirect Tensile (Brazilian) tests were performed. From these tests, Young's Modulus (E) and Poisson's Ratio ( $\nu$ ) values were obtained and they were used for input parameters of numerical models. Uniaxial compressive strength of the rock was acquired from static deformability test. Three static deformability tests on core samples of andesite were tested. Six Brazilian test disc samples were tested to evaluate indirect tensile strength. Static deformability and Brazilian tests were performed according to ISRM standards. Fracture toughness tests were carried out on beam specimens under asymmetric four point bending loads. Results were analyzed to evaluate mode II fracture toughness tests conducted on FPAB test specimen. Experimental work was performed in Rock Mechanics Laboratory of Department of Mining Engineering at Middle East Technical University.

#### **5.1 Testing equipment utilized in experimental study**

Experimental study is necessary to determine the rock parameters such as Elastic Modulus, Poisson's Ratio and Uniaxial Compressive Strength (UCS). Obviously, laboratory tests provide important inputs for rock engineering designs and modeling. Therefore, determination capabilities and measurement sensitivity of these inputs have strong influence on designs and modeling. Laboratory tests should be

conducted with extra care. In the following Figure 5.1 laboratory testing phases were given in form of flow chart.

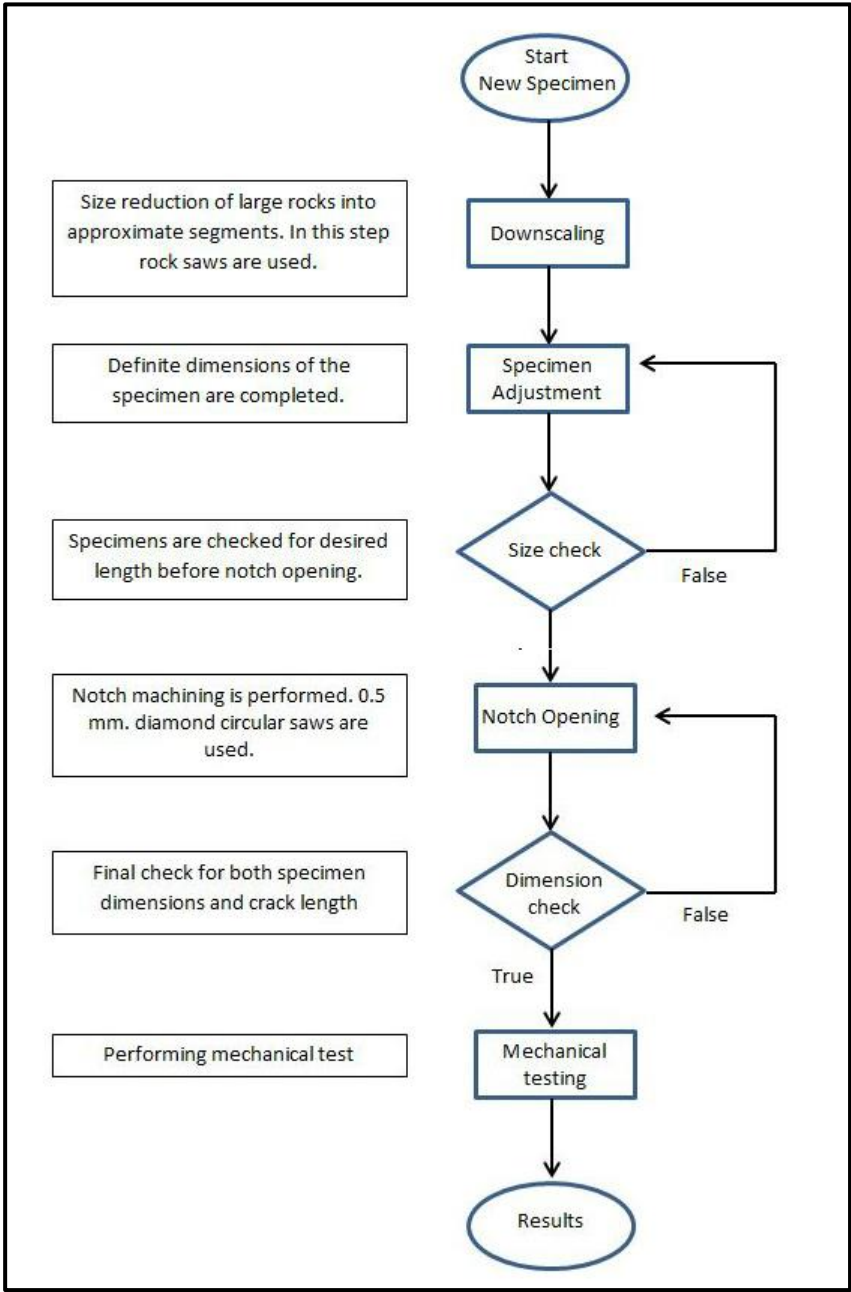


Figure 5. 1 Flow chart for experimental study

Rock fracture tests are more sensitive to specimen dimensions and shape in comparison with ordinary rock mechanics tests. In order to avoid probable unwanted irregularities and undesired results attention should be given from specimen preparation phase to final mechanical testing phase. In this study, experimental works were conducted with special procedure and step by step.

### **5.1.1 Milling machine**

Milling machine was utilized for creating flat surfaces of FPAB test specimen (Figure 5.2). Mode II fracture toughness testing of FPAB specimen is highly sensitive to any angular irregularities on these flat surfaces. Flat surfaces were created by using diamond impregnated milling cutter. Irregularities on flat surfaces achieved with maximum 0.1 mm error.



Figure 5. 2 Milling machine

### **5.1.2 Diamond circular saw**

Diamond circular saw was utilized for notch opening works. Both notches of FPAB and SNDB test specimens were machined using diamond impregnated 0.5 mm thick

circular saws (Figure 5.3). Notch depth calibration was performed utilizing digital caliper.

Notch thicknesses of prepared specimens were between 0.9-1.2 mm. Notch thickness error in machining was around 0.3 mm. Reason of notch thickness deviation in machining may be justified by grain size of rock type and buckling of thin circular saw .

There is an error about  $\pm 0.3$  mm in machining the preliminary notch along the desired direction. So, a ten millimeter length notch can be around 9.9 mm or 10.2 mm which corresponds to 3% error in machining the correct 10 mm length. For longer notches ranging from 20 to 30 mm percentage error obviously decreases. With the equipment used, physically, it is not possible to insert preliminary notches better than this accuracy range.



Figure 5. 3 Digital caliper adapted diamond circular saw

### 5.1.3 Testing machine

MTS 815 Rock Testing Machine is known as one of the most reliable testing machines in such usages compressive strength tests, deformability tests and fracture tests of rocks. The machine mainly consists of highly rigid load frame with fixed crossheads, single-ended actuator, servo-hydraulic service manifold, directional valve and hydraulic power unit (pump), under the control of digital controller. Servo-hydraulic service manifold and servo-controlled directional valve provides definite control on the actuator of the machine. Displacement of the actuator is measured and controlled with LVDT and differential pressure transducer ( $\Delta P$ ) attached to the stroke and transmits a signal to the servo in order to define its location by local coordinates of the machine. Therefore, according to the feedback signal received, the servo calculates the hydraulic fluid requirement to provide the constant pressure on the actuator which is 21 MPa all the time. This means the machine serves under stable pressurized conditions and provides sufficient hydraulic power to compress rock samples with intended loading rates.

Frame of the machine is structured as cross-head and the cross-head is highly rigid up to 3750 kN and its stiffness is  $9 \times 10^9$  N/m. Data acquisition system and controller unit of the machine is located in same box named FlexTest 40. FlexTest 40 controller unit consists of four channels which are connected to servo-hydraulic service manifold, differential pressure transducer, internal linear variable differential transformer, extensional and circumferential extensometers and the load-cell. FlexTest40 controller unit allows the actuator to move by means of displacement controlled, force controlled or extensometer controlled. Controller unit also allows data acquisition up to 4096 Hz for four channels in total. In mechanical property identification tests and fracture toughness tests data acquisition frequency was set from all channels as 8 Hz. Force readings were achieved by externally adapted MTS 500kN  $\pm$  0.25 load-cell which is calibrated by Turkish Standards Institution and certificated as Class 0.5. In Figure 5.4 general working principle of MTS machine is illustrated.

Extensional and circumferential extensometer readings were executed with same data acquisition system from allocated channel of the unit with frequency of 8 Hz.

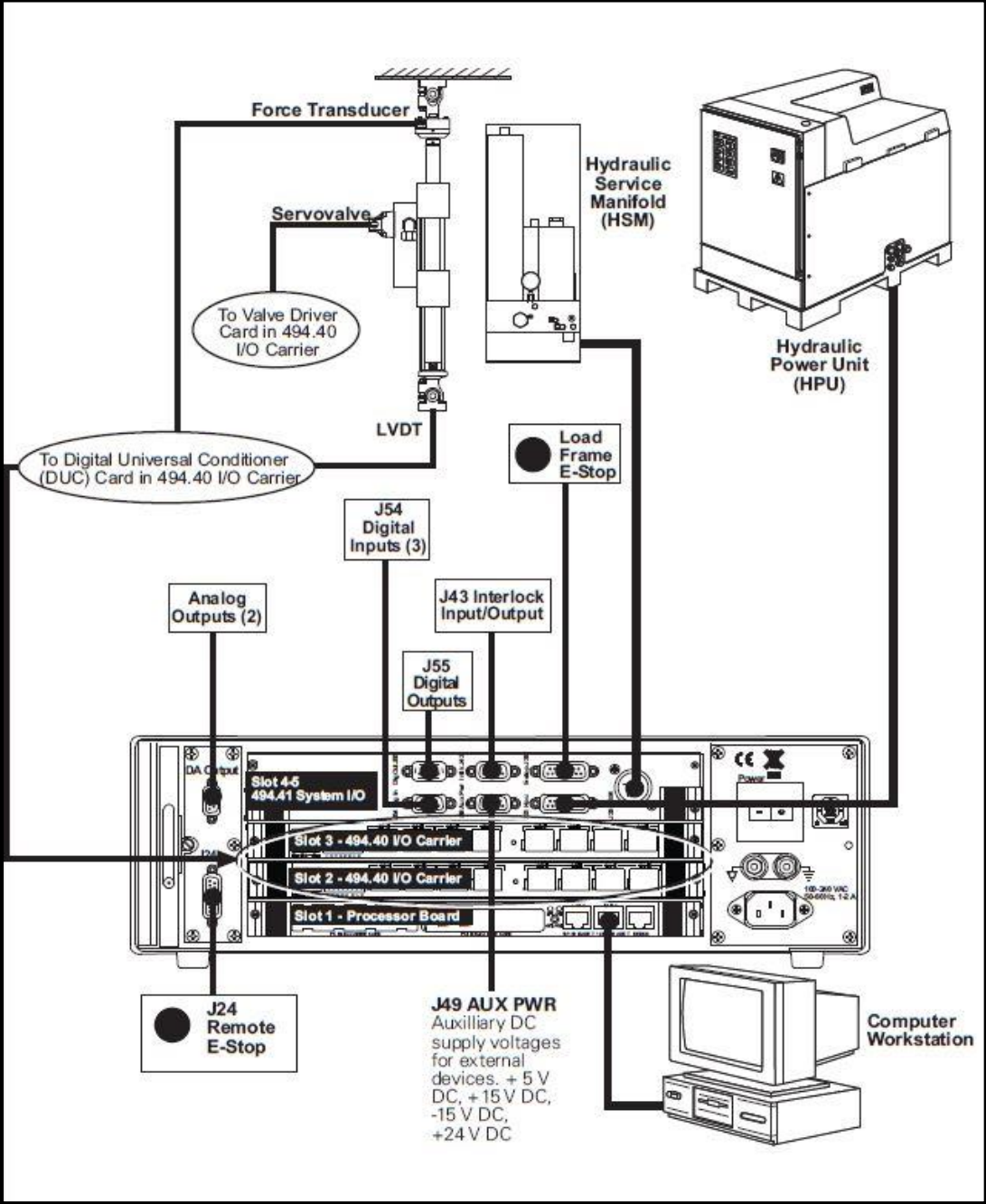


Figure 5. 4 MTS 815 Rock Testing Machine at a glance

## 5.2 Laboratory work for rock property determination

Mechanical and physical property determination tests were conducted according to ISRM standards. Static deformability and Brazilian tests were performed using MTS Rock Testing Machine. In order to determine Young's modulus and Poisson's ratio of Ankara Gölbaşı Andesite, 3 NX size core specimens were prepared. Tensile strength determination was conducted by performing Brazilian (Indirect Tensile) test. For Brazilian test 6 disc specimens were prepared.

### 5.2.1 Static deformability test

Three NX type core samples were prepared to determine Young's Modulus and Poisson's Ratio of Ankara Gölbaşı Andesite rock (Figure 5.5). Static deformability tests were conducted utilizing MTS 815 Rock Testing Machine. Axial and circumferential deformations were measured by using extensometers called clip-on gages. Dual MTS series 632.94F-20 model axial extensometers that have 10 mm expansion capacity were utilized to measure axial deformation and single EPSILON circumferential extensometer was utilized to measure circumferential deformation of tested rock sample. Results of unit weight, static deformability, and strength tests are tabulated in Table 5.1.

Table 5. 1 Results of static deformability test

<b>Specimen Code</b>	<b>Length (mm)</b>	<b>Diameter (mm)</b>	<b>Density (gr/cm<sup>3</sup>)</b>	<b>UCS (MPa)</b>	<b>Elastic Modulus (GPa)</b>	<b>Poisson's Ratio</b>
A.SD.1	120.63	55.00	2.15	57.68	11.60	0.12
A.SD.2	120.70	54.94	2.15	58.43	12.43	0.11
A.SD.3	121.19	54.98	2.14	59.72	12.82	0.12
Average	120.84	54.97	2.15	58.61	12.28	0.12
± STD	± 0.25	± 0.025	± 0.005	± 0.84	± 0.51	± 0.05

Data acquisition was executed utilizing MTS Flextest40 controller and data acquisition box. During tests, load rate was kept constant rate 0.003 mm/s and data acquisition frequency was 8Hz.



Figure 5. 5 After static deformability test rock core samples

According to static deformability tests conducted a typical stress strain curve for Ankara Gölbaşı Andesite is given in Figure 5.6.

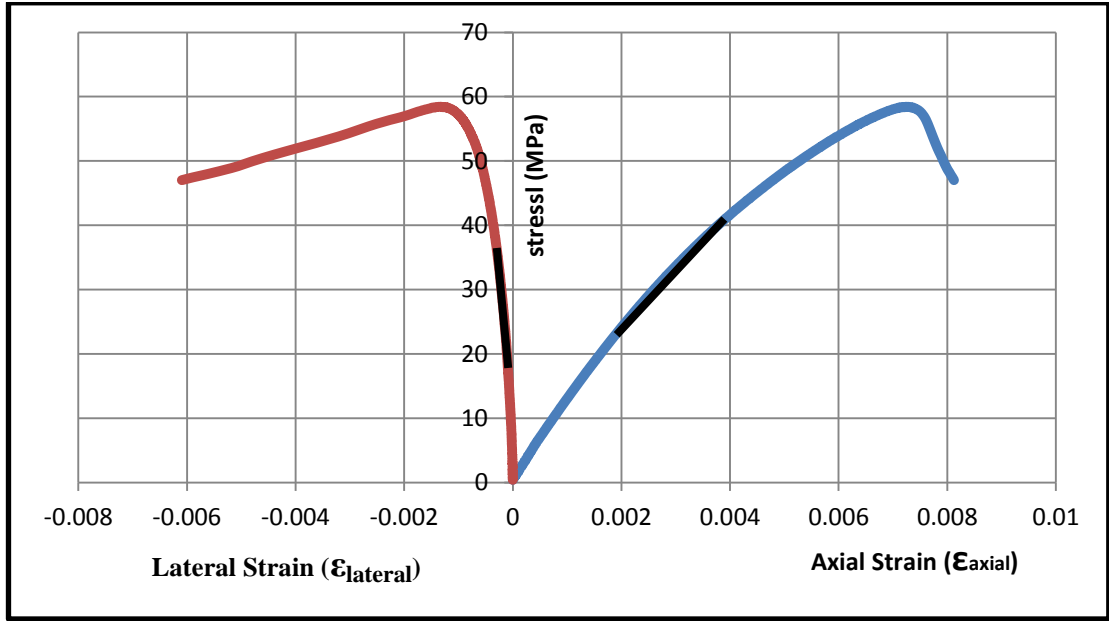


Figure 5. 6 Stress-strain curve for Ankara Gölbaşı Andesite

### 5.2.2 Brazilian (Indirect Tensile) test

In order to determine tensile strength of Ankara Gölbaşı Andesite Brazilian tests were performed on six discs (Figure 5.7). During tests load rate was kept constant 0.003 mm/s (Figure 5.8). Result of Brazilian tests were tabulated in Table 5.2



Figure 5. 7 Brazilian discs before testing

Table 5. 2 Results of Brazilian tests

<b>Specimen Code</b>	<b>Thickness (mm)</b>	<b>Diameter (mm)</b>	<b>Density (gr/cm<sup>3</sup>)</b>	<b>Failure Load (kgf)</b>	<b>Tensile Strength (MPa)</b>
A.BT.1	31.86	55.01	2.09	2015.64	3.59
A.BT.2	30.85	54.99	2.09	1655.84	3.05
A.BT.3	31.00	54.98	2.09	1742.72	3.19
A.BT.4	31.37	54.98	2.09	2040.11	3.69
A.BT.5	34.08	55.00	2.04	2055.16	3.42
A.BT.6	32.00	54.99	2.09	1852.54	3.29
Average	31.86	54.99	2.08	1893.67	3.37
± STD	± 1.08	± 0.01	± 0.02	± 154.62	± 0.22



Figure 5. 8 Installation of Brazilian test

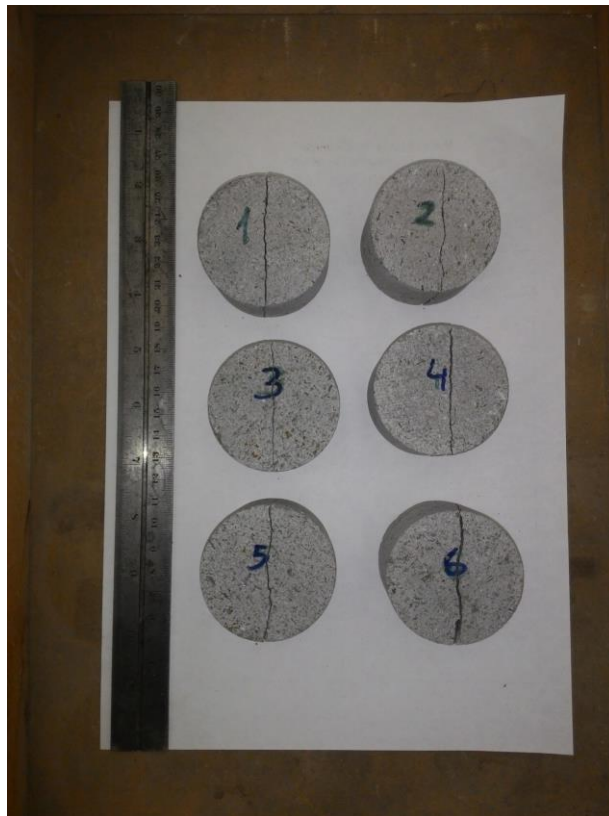


Figure 5. 9 Brazilian discs after test

### 5.3 Fracture tests

Although computers and simulation codes are very helpful in computing, they are not able to find out material properties. For instance, in fracture mechanics, complicated specimen geometries with arbitrary cracks may be computed in terms of SIFs, CPDs or energy utilizing finite element analysis. However, failure load cannot be determined by using finite element method. Input parameters should be provided to these simulation codes all time. They use these input parameters to solve problems. Therefore, laboratory works should be performed to determine material properties or other input parameters. Likewise, in this study, although SIFs can be determined by utilizing FEM code (ABAQUS), determination of fracture toughness values were performed by conducting experiments on rock specimens.

Fracture testing study was performed again same servo-hydraulic testing machine MTS 815. Data acquisition was performed utilizing FlexTest40 controller box and software support MTS series 793 testing software. Data acquisition frequency was set 8 Hz for each channel.

### **5.3.1 Mode II fracture toughness testing work with FPAB test geometry**

In fracture tests with FPAB geometry three main beam depth groups  $W= 40, 50,$  and  $60$  mm were decided to be tested. For beam depth groups of  $W=40$  and  $60$  mm, six different notch lengths expressed in dimensionless form as  $a/W= 0.20, 0.25, 0.30, 0.35, 0.40$  and  $0.50$  were machined. For beam depth group of  $W= 50$  specimens were prepared for seven different crack lengths  $a/W= 0.20, 0.25, 0.30, 0.35, 0.40, 0.50$  and  $0.60$ .

FPAB test geometries were created properly to satisfy pure mode II conditions for all beam depth groups and associated crack lengths. All beam specimen dimensions as beam length and thickness except beam depth were kept constant. Preliminary starter notches were machined as straight edge notches with  $\beta = 0^\circ$  from vertical loading axis. In Figure 5.10 FPAB specimens with different notch lengths are illustrated.



Figure 5. 10 Different notch lengths for beam depth group  $W= 60$  mm

From large blocks of Ankara Golbasi Andesite, rectangular rock beam specimens were carefully machined to final shape and dimensions utilizing milling and grinding apparatus in the lab. Rock samples were labeled in order to conduct the experiments and organize the results conveniently. Labelling rule is illustrated in Figure 5.11.

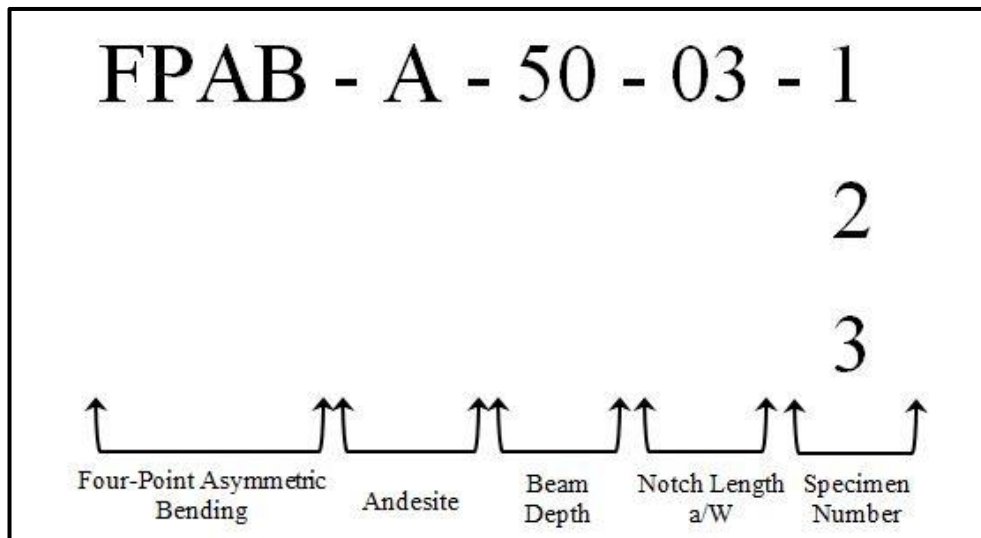


Figure 5. 11 Specimen labelling rule

During fracture toughness tests with FPAB geometry, rollers of 8 mm diameter were utilized to apply bending loads. Installation of FPAB test and view of fractured specimen after test can be seen in Figure 5.12

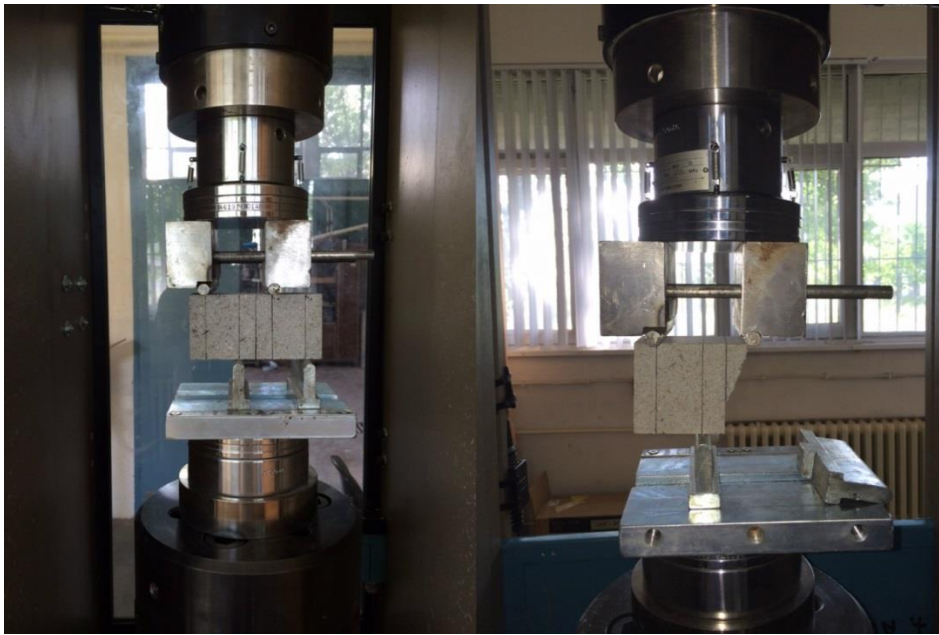


Figure 5. 12 Setup of FPAB test and specimen view after test

From experimental study, fracture loads were recorded. Fracture Loads were used in order to calculate pure mode II fracture toughness value of Ankara Andesite. Fracture load levels were synchronized with computed mode II stress intensity factors by ABAQUS. Models that were initially constructed by applying unit 1 N loads were updated with actual load values obtained from the testing. For all beam depth groups of  $W=40$ , 50 and 60mm, calculated pure mode II fracture toughness values were given in graphical form in Tables 5.3, 5.4 and 5.5, respectively.

Table 5. 3 FPAB test results for W= 40 mm

<b>Specimen Code</b>	<b>Fracture Load (kN)</b>	<b>Pure Mode II Fracture Toughness <math>K_{IIc}</math> MPa<math>\sqrt{m}</math></b>
FPAB-A-40-020-1	16.58	0.58
FPAB-A-40-020-2	26.38	0.93
FPAB-A-40-020-3	23.28	0.82
FPAB-A-40-025-1	9.28	0.41
FPAB-A-40-025-2	11.49	0.51
FPAB-A-40-025-3	8.02	0.35
FPAB-A-40-025-4	9.56	0.42
FPAB-A-40-030-1	19.01	1.01
FPAB-A-40-030-2	8.52	0.45
FPAB-A-40-030-3	13.79	0.74
FPAB-A-40-030-4	9.95	0.53
FPAB-A-40-035-1	6.98	0.42
FPAB-A-40-030-2	8.64	0.53
FPAB-A-40-030-3	10.08	0.69
FPAB-A-40-030-4	6.85	0.42
FPAB-A-40-040-1	7.10	0.48
FPAB-A-40-040-2	14.44	0.98
FPAB-A-40-040-3	9.85	0.67
FPAB-A-40-040-4	10.12	0.69
FPAB-A-40-050-1	10.00	0.77
FPAB-A-40-050-2	7.34	0.57
FPAB-A-40-050-3	7.08	0.55
Average $\pm$ STD	11.56 $\pm$ 5.24	0.62 $\pm$ 0.19

Table 5. 4 FPAB test results for W= 50 mm

<b>Specimen Code</b>	<b>Fracture Load (kN)</b>	<b>Pure Mode II Fracture Toughness <math>K_{IIC}</math> MPa<math>\sqrt{m}</math></b>
FPAB-A-50-020-1	23.40	0.73
FPAB-A-50-020-2	26.50	0.83
FPAB-A-50-020-3	17.24	0.54
FPAB-A-50-025-1	17.30	0.69
FPAB-A-50-025-2	10.73	0.43
FPAB-A-50-025-3	10.67	0.42
FPAB-A-50-030-1	23.45	1.12
FPAB-A-50-030-2	10.49	0.50
FPAB-A-50-030-3	12.37	0.59
FPAB-A-50-030-4	10.04	0.48
FPAB-A-50-035-1	7.30	0.40
FPAB-A-50-030-2	6.87	0.38
FPAB-A-50-030-3	9.98	0.55
FPAB-A-50-030-4	10.06	0.55
FPAB-A-50-040-1	7.98	0.49
FPAB-A-50-040-2	6.45	0.39
FPAB-A-50-040-3	6.60	0.40
FPAB-A-50-040-4	9.56	0.58
FPAB-A-50-050-1	8.33	0.57
FPAB-A-50-050-2	6.58	0.45
FPAB-A-50-050-3	7.68	0.53
FPAB-A-50-060-1	13.40	0.98
FPAB-A-50-060-2	12.30	0.90
FPAB-A-50-060-3	5.33	0.39
Average $\pm$ STD	11.69 $\pm$ 5.70	0.58 $\pm$ 0.20

Table 5. 5 FPAB test results for W= 60 mm

<b>Specimen Code</b>	<b>Fracture Load (kN)</b>	<b>Pure Mode II Fracture Toughness <math>K_{IIc}</math> MPa<math>\sqrt{m}</math></b>
FPAB-A-60-020-1	36.17	1.03
FPAB-A-60-020-2	28.85	0.83
FPAB-A-60-020-3	13.79	0.39
FPAB-A-60-025-1	19.94	0.73
FPAB-A-60-025-2	15.30	0.56
FPAB-A-60-025-3	13.12	0.48
FPAB-A-60-030-1	8.64	0.38
FPAB-A-60-030-2	16.24	0.71
FPAB-A-60-030-3	9.30	0.41
FPAB-A-60-035-1	8.02	0.40
FPAB-A-60-030-2	10.00	0.50
FPAB-A-60-030-3	7.44	0.37
FPAB-A-60-040-1	13.08	0.73
FPAB-A-60-040-2	13.24	0.74
FPAB-A-60-040-3	19.78	1.10
FPAB-A-60-050-1	10.12	0.64
FPAB-A-60-050-2	9.52	0.60
FPAB-A-60-050-3	8.38	0.56
Average $\pm$ STD	14.50 $\pm$ 7.44	0.62 $\pm$ 0.21

Calculation of mode II fracture toughness values was conducted by ABAQUS Software. Fracture loads obtained from experimental study were utilized as input to ABAQUS Software. Fracture loads were divided proportional to short moment arm and long moment arm distances. In Figure 5.13 input windows for fracture loads are illustrated.

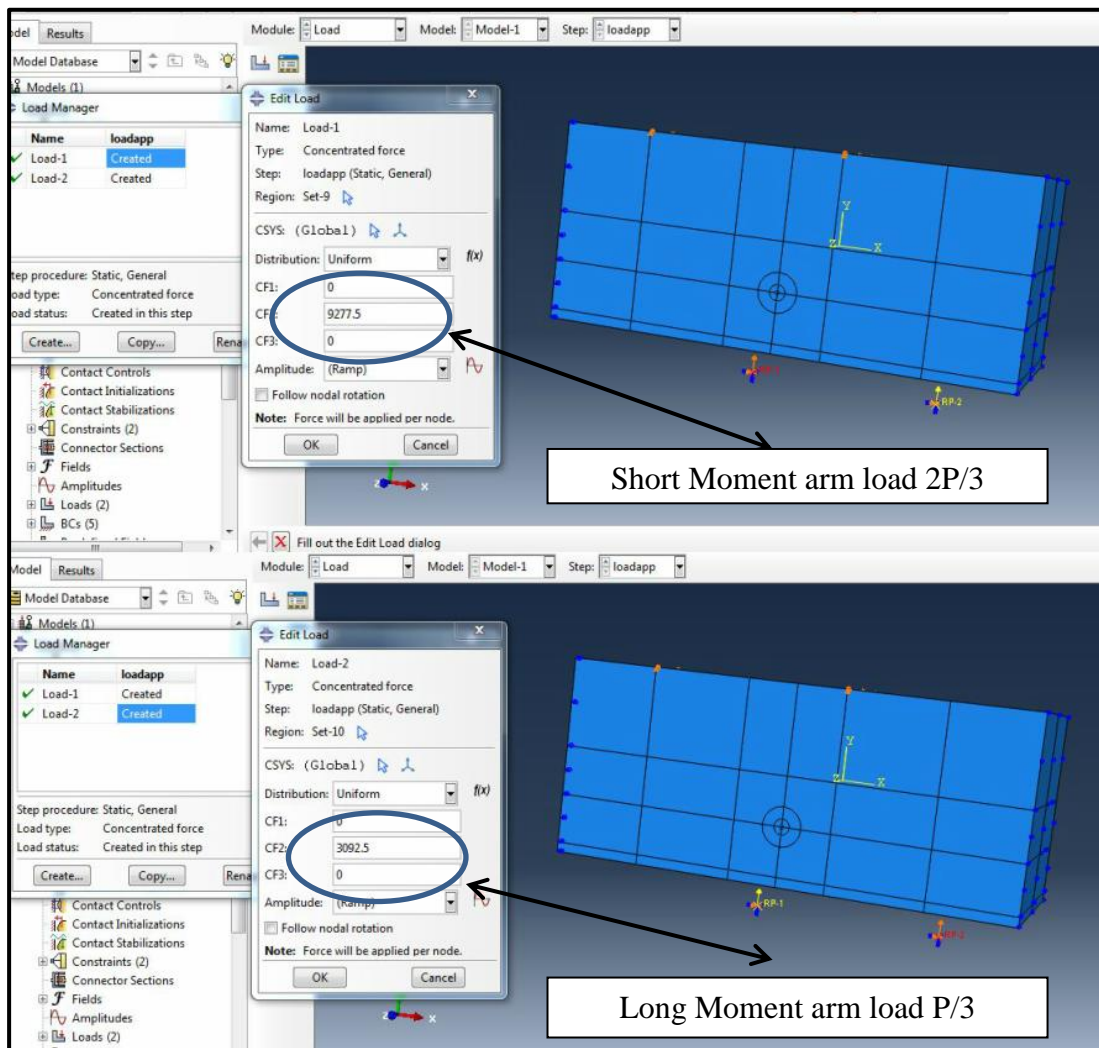


Figure 5. 13 Calculation of fracture toughness values

As it is shown in results of experimental study, average pure mode II fracture toughness values of Ankara Gölbaşı Andesite are very close for different beam depths. This result indicates that there is no size effect for mode II fracture toughness with FPAB testing geometry. Finally, average pure mode II fracture toughness  $K_{IIc}$  of Ankara Gölbaşı Andesite can be declared as  $0.61 \text{ MPa}\sqrt{\text{m}}$ .

In Figure 5.14 typical FPAB test specimen after fracturing can be seen. Similar views of tested specimens are illustrated in APPENDIX B. In order to compare pure mode

II fracture toughness values acquired from FPAB specimen, SNDB testing geometry was used. Comparative study for fracture testing studies was introduced in Chapter 6.



Figure 5. 14 FPAB test specimen after testing



## CHAPTER 6

### RESULTS AND DISCUSSION

Previously, rock fracture mechanics investigations have been mostly performed under mode I loading state. In the literature, more data is available for size effect and boundary influence phenomena for mode I loading state in comparison with mode II loading state. First Bazant, showed the global energy release leading to a simple size effect law in 1983 and 1984. Then, justification of this law was made by a number of studies of the researcher (Bazant and Pfeiffer, 1987, Bazant and Kazemi, 1990a, b, and Bazant et al., 1995). Aliha et al., (2010) studied crack trajectory deviation for different sized SCB and CSTBD specimens. Ayatollahi and Akbardoost (2012) proposed a new approach for size effect law on quasi-brittle materials. They employed maximum tangential stress criterion adapting higher order Williams expansion. Kumar and Barai (2012), introduced size effect phenomenon for rectangular beam shaped specimens under mode I loading state. Although mode II fracture toughness determination studies have been conducted for rectangular shaped rock specimens, sufficient data is not available about boundary influence effect and size effect for beam type specimens.

Results of numerical studies and laboratory experimental work indicated that size and boundary influence effects were not observed for mode II loading state on rectangular shaped rock specimens. Finally, it was concluded that increasing the beam size by increasing the beam depth had no influence in terms so called size effect on mode II fracture toughness. In order to comparatively analyze boundary influence effect, stress analysis studies were conducted for numerical models of FPAB test geometry under both mode I and mode II loading states. Stress analyzes

were conducted by adapting von Mises yield criterion around the crack tip in the models.

According to results of laboratory tests conducted on different sized FPAB specimens, no size effect was observed. Almost the same mode II fracture toughness values for beam depth groups of 40, 50 and 60 mm were acquired as 0.62, 0.58 and 0.62 MPa $\sqrt{m}$ , respectively. Overall fracture toughness value for mode II loading state was obtained as 0.61 MPa $\sqrt{m}$  for Ankara Gölbaşı Andesite. In order to justify the mode II fracture toughness values acquired by utilizing FPAB test geometry SNDB testing results was employed. Close results between FPAB and SNDB geometries were achieved for Ankara Gölbaşı Andesite in terms of mode II fracture toughness.

### **6.1 Stress analyses around the notch of FPAB testing geometry and other numerical works**

As reported in Chapter 5, almost the same dimensionless short moment arm distances were obtained to reach pure mode II state at the crack tip for different beam depths. This finding was attributed to the same bending moment requirement to reach critical stress state for mode II crack propagation of the different sized specimens.

In order to clarify this point, stress analyses were conducted both FPB (four-point bending) and FPAB (four-point asymmetric bending) test geometries. FBP test geometry was modeled in order to acquire mode I stress intensity factor behavior of rectangular shaped rock specimens. Stress analyses were conducted by examining von Mises stresses for a specific path which extended with crack propagation angle (around 70 degrees) from the notch tip to the outmost contour integral.

Von Mises stress is a measure of potential plasticity zones of stressed domains. Examination of this stress prescribed paths around crack for both mode I and mode II loading conditions yields indications about the size of plasticity zones and boundary influence effects.

In order to justify the results of  $K_{IIc}$  acquired from FPAB test geometry SNDB test geometry modeling and related experimental work were conducted. Justification study by the modeling and comparison of mode II fracture toughness values for FPAB and SNDB test geometries were presented in Section 6.2.

### 6.1.1 Von Mises yield criterion

Results of numerical computations are available in form of stress contour map. ABAQUS presents stress contour maps and including von Mises stress. Von Mises stress contour maps are dependent on second deviator stress invariant. Intensity of the von Mises stress contour maps indicate relative size of potential plasticity zones around cracks.

Von Mises yield criterion was first proposed in 1904 by Huber. Then, in 1913 the same criterion was formulated and well-organized by Von Mises (1913). Von Mises yield criterion is also called “*Maximum Distortion Energy Criterion*”. The theory states that, if the distortion energy of a material is smaller than maximum distortion energy that the material can stand no yielding occurs. Von misses yield function is given as follows;

$$f(J_2) = \sqrt{J_2} - k = 0 \quad (6.1)$$

or;

$$f(J_2) = J_2 - k^2 = 0 \quad (6.2)$$

In here;

$f(J_2)$ : Von Mises yield function

$J_2$ : Second deviatoric stress invariant

$k$ : yielding stress value of a material in pure shear conditions

Investigations made showed that yielding stress is  $\sqrt{3}$  times higher than maximum shear stress. Therefore, von Mises stress is redefined as;

$$\sigma_v = \sqrt{3J_2} \quad (6.3)$$

And von Mises yield function became;

$$f(J_2) = \sqrt{3J_2} - \sigma_y = 0 = \sigma_v - \sigma_y = 0 \quad (6.4)$$

If this function is reoperated substituting  $J_2$  in terms of the principle stresses it gives;

$$(\sigma_1 - \sigma_2)^2 + (\sigma_2 - \sigma_3)^2 + (\sigma_1 - \sigma_3)^2 = 2\sigma_y^2 \quad (6.5)$$

or in tensor notation;

$$(\sigma_{11} - \sigma_{22})^2 + (\sigma_{22} - \sigma_{33})^2 + (\sigma_{11} - \sigma_{33})^2 + 6(\sigma_{12} + \sigma_{23} + \sigma_{13}) = 2\sigma_y^2 \quad (6.6)$$

This equation finally yields to a cylindrical yield surface (Figure 6.1).

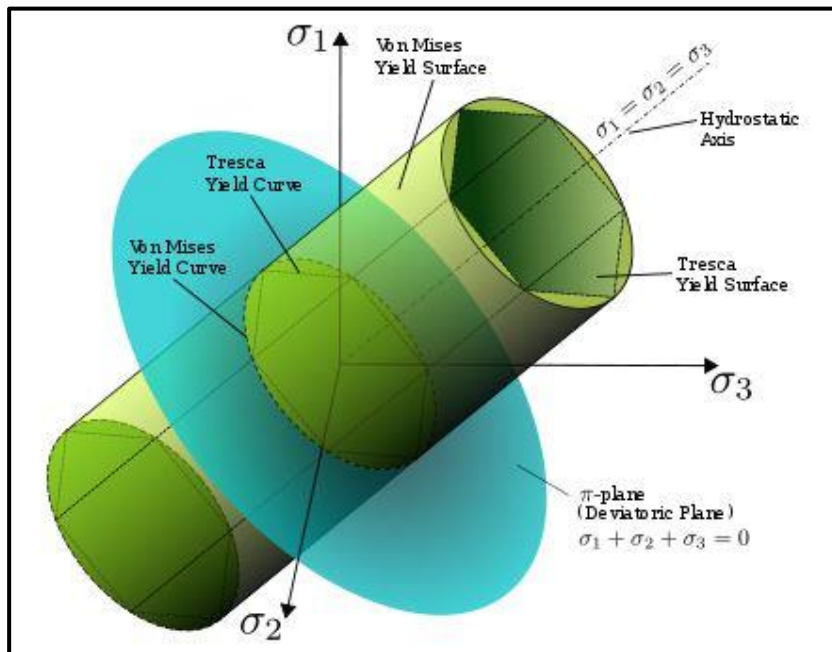


Figure 6. 1 Von Mises yield surface

In summary, von Mises yield criterion indicates that, if the second deviatoric stress invariant  $J_2$  reaches critical value material begins to yield. Therefore,  $J_2$  indicates plasticity zone in stress contour maps in other words von Mises stresses. Stress and plasticity analyses of this study are done in terms of this yielding criterion.

### 6.1.2 Mode I stress intensity factor investigations on FPB test geometry

A FPB testing geometry for mode I stress intensity factor investigation was modeled. Dimensionless crack length  $a/W$  of the numerical model was selected as 0.6 (Figure 6.2). Because of dimensionless crack length  $a/W= 0.6$  this geometry becomes the most probable geometry for boundary influence effect. Modeling geometries and material properties for FPB test geometry were given in Table 6.1.

Table 6. 1 Geometric dimensions and material properties of FPB test geometry

<b>Property</b>	<b>Value</b>
Beam Length	120 mm
Beam Depth	50 mm
Beam Thickness	50 mm
Crack Length	30 mm
E (Young's Modulus)	12300 MPa
$\nu$ (Poisson's Ratio)	0.12
Short Span	50 mm
Long Span	100 mm
Load	-1 N

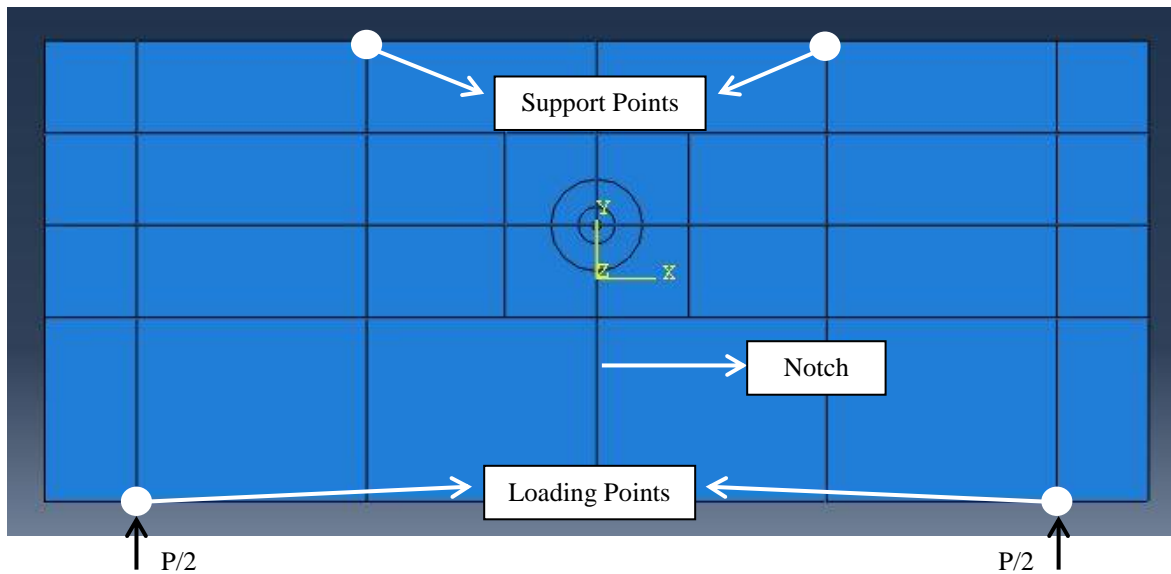


Figure 6. 2 General geometry of FPB test specimen

Numerical computation was conducted using around 58000 brick elements. Deformed shape of the numerical model is illustrated in Figure 6.3.

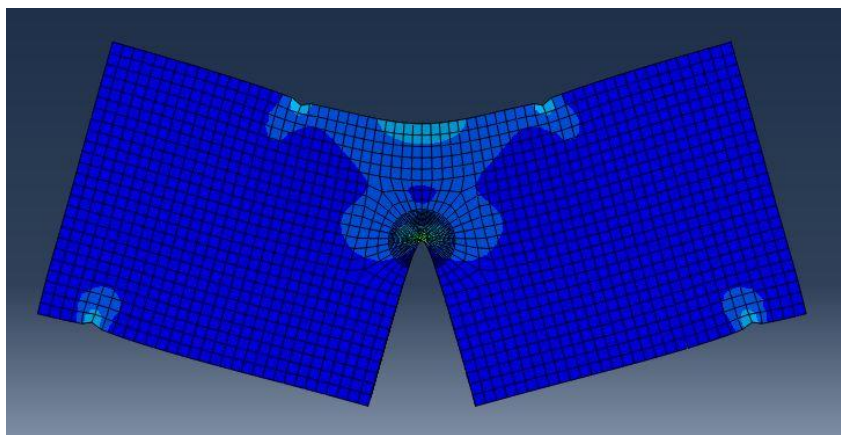


Figure 6. 3 Deformed shape of FPB test geometry

As a result of numerical computation mode I mode II stress intensity factors obtained as  $K_I= 355.8 \text{ Pa}\sqrt{\text{m}}$ ,  $K_{II}= 0.001 \text{ Pa}\sqrt{\text{m}}$  respectively, and CPD (crack propagation direction) =  $0^\circ$ .

### 6.1.3 Stress analyses for FPB and FPAB test geometries

Von Mises stresses were examined around prescribed path which extended through crack propagation direction of FPB and FPAB test specimens. These paths begin from notch tip and reach to the outmost contour integral region. In all, 21 points were examined for each geometry. Distance between two points was selected as 0.25 mm which was the same length for successive contour integral regions. Total length of these two paths was 5 mm long from notch tip. As described before crack propagation angle or direction is an output of the modeling work. Direction of these paths trails along CPD of each loading mode. For mode I loading (FPB test geometry) vertical angle equals to “0” while for mode II loading (FPAB test geometry) equals to about 70 degrees. In Figures 6.4 and 6.5 stress paths for mode I and mode II loading conditions are illustrated respectively.

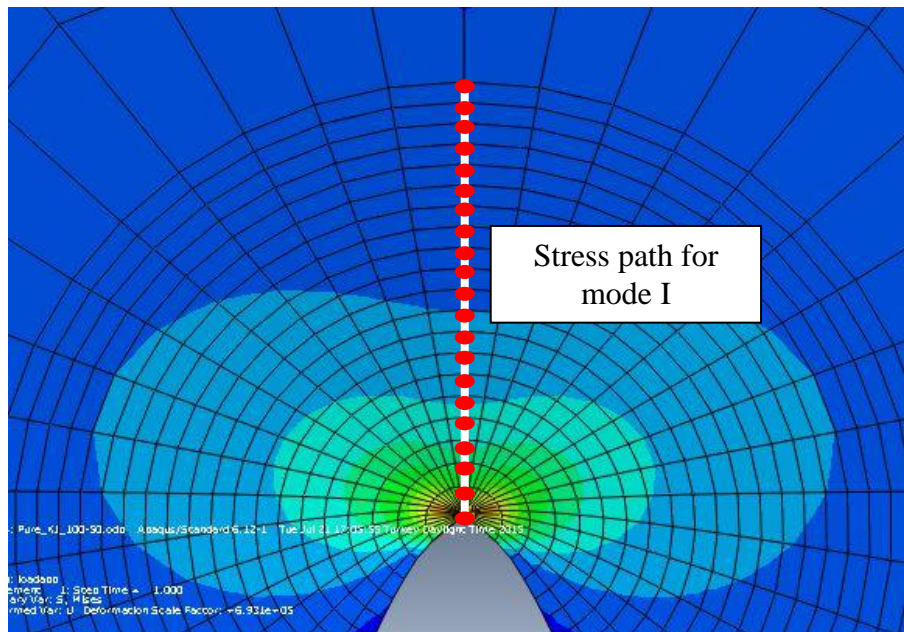


Figure 6. 4 Stress path for mode I loading

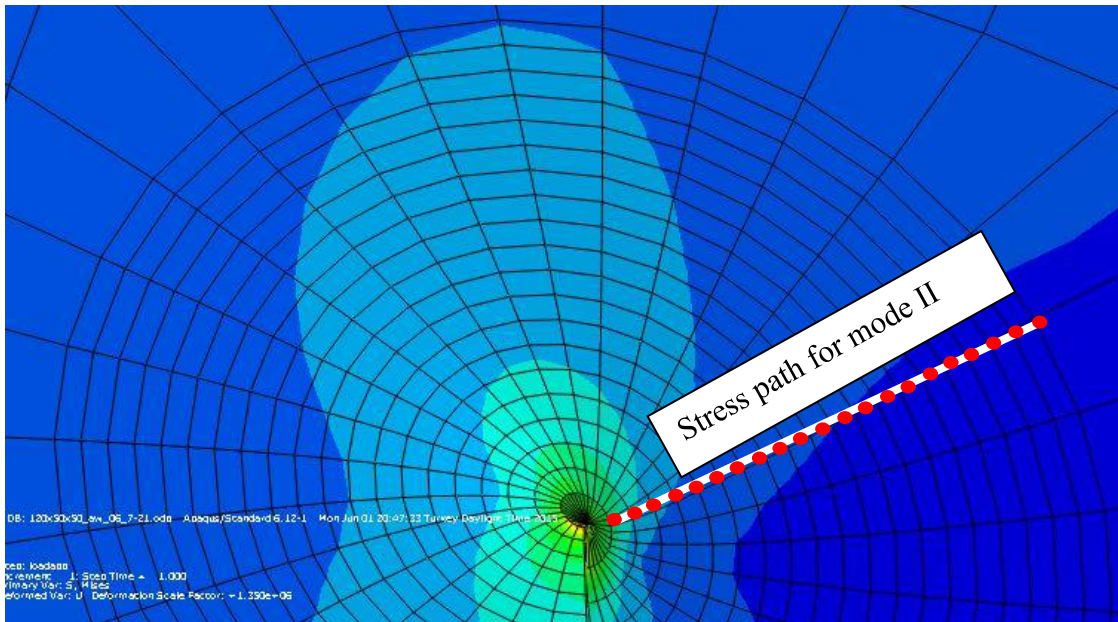


Figure 6. 5 Stress path for mode II loading

As it is shown in Figures 6.4 and 6.5, red dots are probes for von Mises stress analysis. Probe values in terms of von Mises stress for both mode I and mode II loading type are listed in Table 6.2 and Table 6.3 respectively.

Table 6. 2 Von Mises stresses for mode I loading

Distance from Crack Tip (mm)	von Mises stress values (Pa) Mode I	Distance from Crack Tip (mm)	von Mises stress values (Pa) Mode I
0	9559.86	2.75	1739.11
0.25	5933.57	3.00	1631.50
0.50	4459.25	3.25	1536.09
0.75	3729.04	3.50	1451.14
1.00	3226.97	3.75	1375.31
1.25	2862.40	4.00	1307.56
1.50	2581.18	4.25	1247.02
1.75	2353.10	4.50	1193.02
2.00	2162.93	4.75	1143.90
2.25	2001.07	5.00	1060.54
2.50	1861.26		

Table 6. 3 Von Mises stresses for mode II loading

<b>Distance from Crack Tip (mm)</b>	<b>Von-mises stress values (Pa) Mode II</b>	<b>Distance from Crack Tip (mm)</b>	<b>Von-mises stress values (Pa) Mode II</b>
0	4177.94	2.75	1359.37
0.25	2813.98	3.00	1316.82
0.50	2559.91	3.25	1278.66
0.75	2206.01	3.50	1244.03
1.00	1976.56	3.75	1212.32
1.25	1816.89	4.00	1183.03
1.50	1697.43	4.25	1155.83
1.75	1603.45	4.50	1130.54
2.00	1526.79	4.75	1106.95
2.25	1462.50	5.00	1062.62
2.50	1407.42		

Von Mises stress field was redesigned in terms of stress values obtained from stress analysis. These probe values were acquired from the contour map presented by ABAQUS. Once more again, it was observed that for mode II loading state boundary influence effect in FPAB test geometry (Figure 6.6) was negligible. FPAB test specimen contour map was limited to 1000 Pa and 1100 Pa respectively for the specimen having dimensionless notch length of  $a/W= 0.6$ . While, contour map was limited to 1100 Pa, no contact was observed between von Mises stress field and upper boundary within the specified range. Then, limitation was applied as 1000 Pa; von Mises stresses did not reach the upper boundary at all. (See table 6.3)

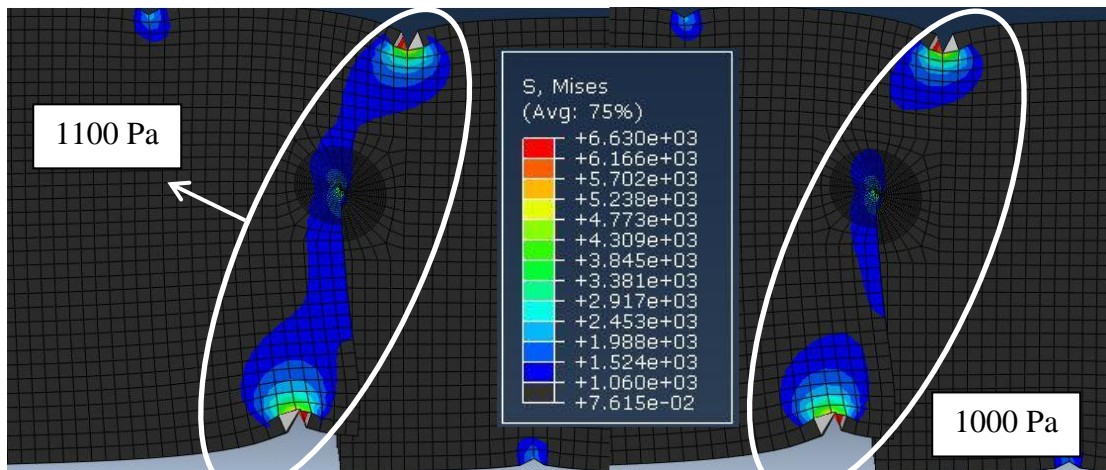


Figure 6.6 Boundary influence effect for mode II loading

The same examination was conducted for mode I loading condition as well. Similar probe value ranges were applied to limit the stress contour map of pure mode I SIF test specimen (FPB). It was observed that von Mises stress contour map showed an intensive distribution of potential yielding zones and intensive boundary influence effect, (Figure 6.7).

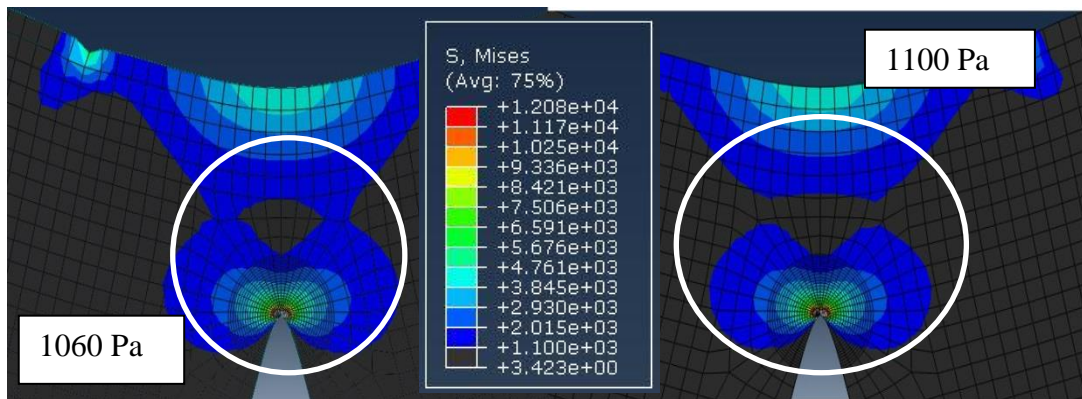


Figure 6.7 Boundary influence effect for mode I loading

In order to examine more effectively, these probe values were illustrated graphically. In the following Figure 6.8 Von-mises stress values for both mode I and mode II loading were plotted.

Stress distribution analysis at the crack tip of four-point bend test specimen geometries under opening and shear mode was conducted. By assigning stress paths at the vicinity of crack tip stress distributions and von Mises stresses were compared. It was found that, crack tip under mode I had a higher potential to develop plastic zones at the crack tip.

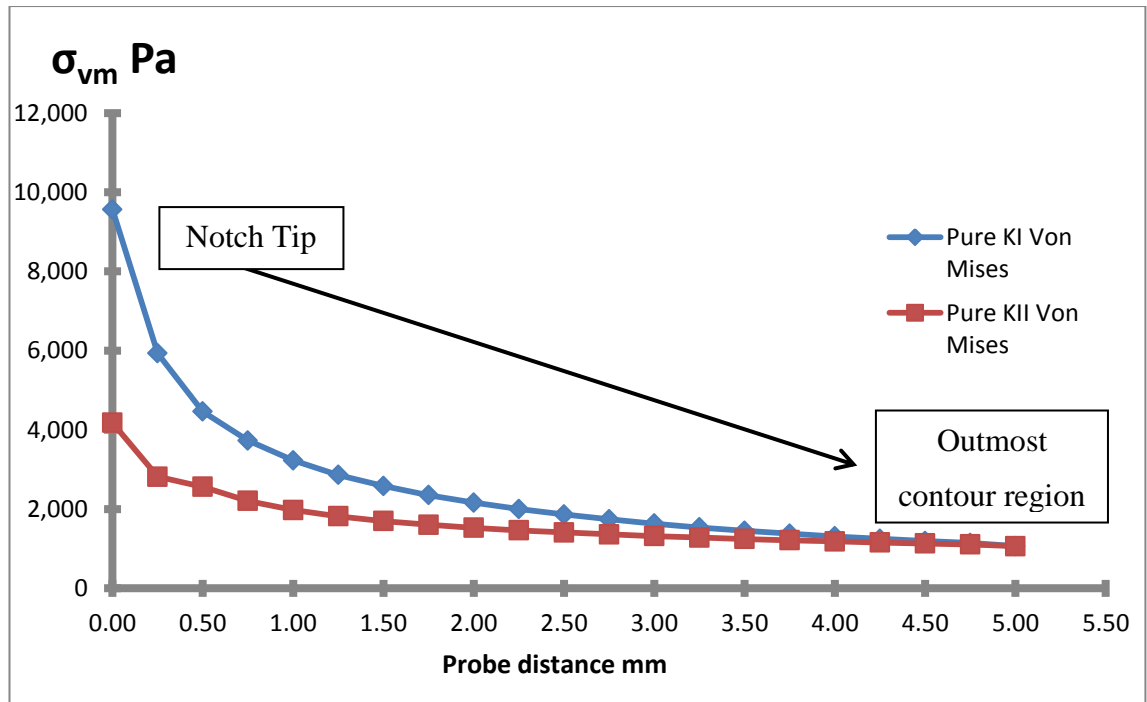


Figure 6. 8 Von mises stresses around stress path for mode I and mode II

The reason of having no size effect for mode II fracture toughness in FPAB tests was explained based on the argument of having smaller plastic zones and FPZ's at the crack tip.

Beam type specimens are associated with high plastic zones/FPZ zones under opening mode loading conditions. For mode II loading state, size of the potential plastic zone compared in terms von Mises stress is about 2.5 times less than mode I model section almost up to a crack front extent of 3.5 mm, even for elastic models of analyses. If such stress analyses were carried out with elastic-plastic modeling work,

it would be expected to have higher difference between sizes of crack tip plasticity zones of beam specimens of  $K_{Ic}$  and  $K_{IIc}$  testing work. Considering that crack length used in stress comparison is about 30 mm in both models, existence of a potentially plastic zone of about 3.5 mm ahead of the crack tip reflects the significance of plastic zone dimension and effected dimension is expected to be more than 10% in comparison of extent of FPZ for opening and shear loading states.

## **6.2 Verification efforts for SNDB numerical study and justification of FPAB test results**

SNDB (straight notched disc bending) test geometry was modeled to justify mode II fracture toughness values obtained from FPAB test geometry. Experimental study of the FPAB test geometry was given in Chapter 8. In order to compare the mode II fracture toughness values obtained from FPAB test specimen, comparative study was conducted. This comparison was performed by using SNDB test geometry. In this section, first, numerical verification for SNDB modeling work was introduced then; mode II fracture toughness values obtained from using these two different testing methods were compared.

### **6.2.1 Numerical modeling work for SNDB test geometry**

Pure shear geometry for SNDB test geometry adopted from Het (2014). In order to prove accuracy level of the modeled SNDB geometry, numerical computation results were compared with the ones given by Het (2014). Instead of giving all details of numerical computation techniques of SNDB test geometry, only comparative study was introduced. Geometric dimensions and material properties for SNDB test geometry were given in Table 6.4.

Table 6. 4 Geometric dimensions and material properties of SNDB model

Property	Value
Disc Diameter (D)	100 mm
Disc Radius (R)	50 mm
Disc Thickness (B)	50 mm
Notch Length (a)	25 mm
Notch Angle <i>vertical</i> ( $\beta$ )	50°
Load (P)	-1 N
Span Length (S)	60 mm
Elastic Modulus (E)	18144 MPa
Poisson's Ratio ( $\nu$ )	0.15

SNDB test specimen can be seen in Figure 6.9.

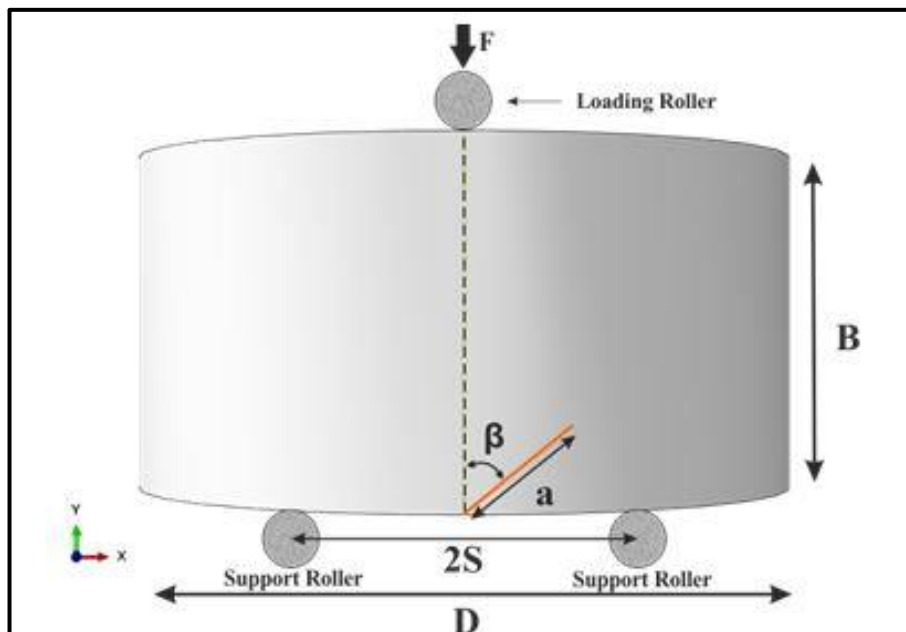


Figure 6. 9 SNDB test specimen geometry

Numerical model was created by employing around 100000 brick elements. Obtained results and comparison with Het’s work are in Table 6.5.

Table 6. 5 Comparative study for SNDB numerical model

Parameters	Present Model	Het’s Model	Difference %
Mode I SIF ( $K_I$ )	2.05 Pa√m	2.00 Pa√m	%2.50
Mode II SIF ( $K_{II}$ )	28.30 Pa√m	28.02 Pa√m	%0.99

Mode I stress intensity factor difference between present work modeling and Het’s modeling work was around 2.5%. On the other hand, difference in mode II stress intensity factor values of these two modeling works was around 1%. As a result of this comparative study, acceptable resemblance between computed SIFs were believed to be achieved.

For a mechanical checking, deformed shape of SNDB model is illustrated in Figure 6.10.

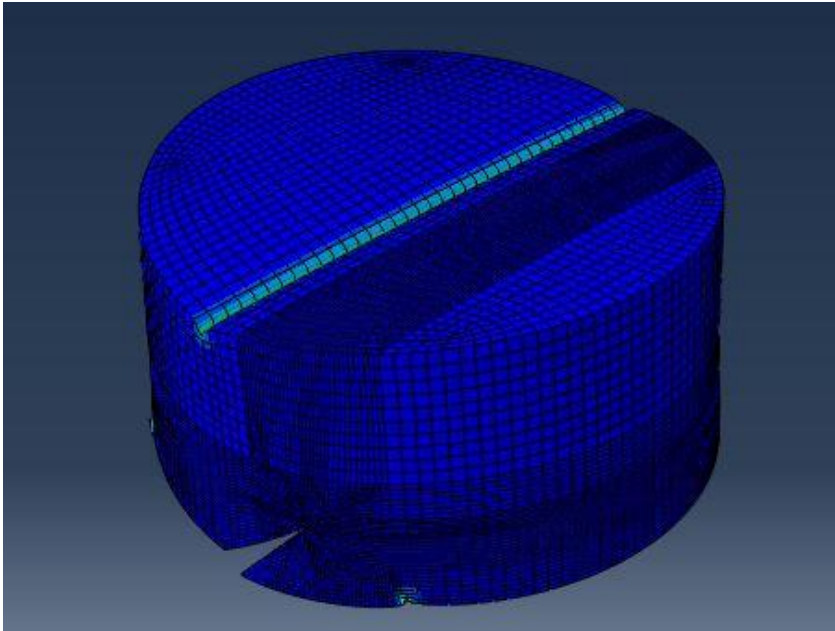


Figure 6. 10 Deformed shape of SNDB model

### 6.2.2 Mode II fracture toughness determination with SNDB test geometry

SNDB (straight notched disc bending) test geometry is a core based specimen and firstly introduced by Tutluoglu and Keles (2011). SNDB geometry is highly recommended testing geometry for mode II fracture toughness determination of beam type rock core specimen geometries.

For pure mode II fracture toughness testing study, in total three SNDB specimens were prepared. In Figure 6.11, SNDB test specimens are illustrated.



Figure 6. 11 SNDB test specimens

For testing of SNDB test specimen, similar testing procedure as in FPAB testing work was employed. Pure mode II SIF condition and appropriate geometry for SNDB test specimen were provided by previous researchers (Het, 2014). This appropriate geometrical organization of SNDB specimen geometry is summarized in Table 6.6.

Table 6. 6 Geometric dimensions and material properties of tested SNDB test geometry

Property	Value
Diameter (D)	100 mm
Thickness (B)	50 mm
Notch Length ( $a_n$ )	25 mm
Span (2S)	60 mm
Notch Inclination ( $\beta$ )	51°
Elastic Modulus (E)	12.3 GPa
Poisson's Ratio ( $\nu$ )	0.12
Dimensionless Span Length (S/R)	0.6
Dimensionless Notch Length (a/R)	0.5



Figure 6. 12 Installation of SNDB test geometry

With SNDB test geometry for determination of pure mode II fracture toughness of Ankara Gölbaşı Andesite, results were close to the ones that were obtained by FPAB tests. Experimental study conducted on SNDB test geometry resulted in an average mode II fracture toughness for pure shear state as  $K_{IIc} = 0.62 \text{ MPa}\sqrt{\text{m}}$ . Mode II fracture toughness values of tested specimens were calculated by using the fracturing load values of experimental work in ABAQUS software models. In the following table, results of pure mode II fracture toughness experiments for SNDB test geometry were listed.

Table 6. 7 Mode II fracture toughness values acquired from SNDB test geometry

<b>Specimen Number</b>	<b>Fracture Load (kN)</b>	<b>Pure Mode II Fracture Toughness <math>K_{IIc}</math> (MPa<math>\sqrt{\text{m}}</math>)</b>
SNDB 1	22.9	0.64
SNDB 2	22.7	0.63
SNDB 3	21.3	0.59
<b>Average <math>\pm</math> STD</b>	<b>22.3 <math>\pm</math> 0.71</b>	<b>0.62 <math>\pm</math> 0.02</b>

Obtained pure mode II fracture toughness  $K_{IIc}$  with FPAB specimen approximately equals to  $0.61 \pm 0.20 \text{ MPa}\sqrt{\text{m}}$ .

Obtained pure mode II fracture toughness  $K_{IIc}$  with SNDB specimen approximately equals to  $0.62 \pm 0.02 \text{ MPa}\sqrt{\text{m}}$ .

*Difference (%)*

$$= \frac{\text{Computed } K_{IIc} \text{ with SNDB} - \text{Computed } K_{IIc} \text{ with FPAB}}{\text{Computed } K_{IIc} \text{ with FPAB}} \times 100$$

$$\text{Difference } (\%) = \frac{0.62 - 0.61}{0.61} \times 100 = \%1.62$$

As a result of comparative study, a good agreement between mode II fracture toughness  $K_{IIc}$  values of FPAB and SNDB tests was achieved with approximately 1.62% difference.

In Figure 6.13 SNDB test specimens after experimental study are illustrated.



Figure 6. 13 Tested SNDB specimens

Beam shaped rectangular rock specimens subjected to four-point asymmetric bending loading were investigated for mode II fracture toughness  $K_{IIc}$  testing. In all, over 120 finite element models were created for three main different beam depth groups with different notch lengths. Beam thickness was kept constant and 64 laboratory tests were conducted. In tests, grey colored Ankara Gölbaşı Andesite rock was used. As input to numerical models, mechanical properties of grey colored

Ankara Gölbaşı Andesite were used. Average mode II fracture toughness value acquired from all four-point asymmetric bending (FPAB) tests was found as  $0.61 \pm 0.20 \text{ MPa}\sqrt{\text{m}}$ .

This work made a contribution in using rectangular beams of short dimensions instead of using very long large sized beam geometries previous works

Pure mode II fracture toughness of Ankara Gölbaşı Andesite obtained from four-point asymmetric bending test work was compared to the result of SNDB test work using the same rock type. Previous mode II fracture toughness results of andesite rock of Karakaş, (Karakaş, 2011) obtained by straight notched disc bending (SNDB) test for was used to compare the results of FPAB testing of this work. From SNDB tests, pure mode II fracture toughness was reported as  $0.62 \text{ MPa}\sqrt{\text{m}}$  by Karakaş, 2011. Results with these two different bending type test configurations showed a good agreement.

Beam depth was found to have no effect on the mode fracture toughness results of FPAB tests. As beam depth three entries with 40, 50, and 60 mm were implemented in modeling and testing work. Numerical computations showed that, as the beam depth of test specimen increases the mode II stress intensity factor value decreases. However, stress intensity factor illustrates no change when mode II stress intensity factor is presented in dimensionless form as normalized with geometrical dimensions of crack and beam. A fourth order polynomial fit function produces quite accurate results for  $Y_{II}$  which is the dimensionless form of  $K_{II}$ .

No size effect on mode II fracture toughness was observed from the data acquired by laboratory tests. Size effect on beam type specimens under opening mode was proven in previous work both theoretically and experimentally.

In order to explain the reasons why no size effect existed in the results, stress distribution analysis at the crack tip of four-point bend test specimen geometries

under opening and shear mode was conducted. By assigning stress paths at the vicinity of crack tip, stress distributions and von Mises plasticity indicator stresses were compared. The reason of having no size effect for mode II fracture toughness FPAB test was attributed having smaller von Mises plasticity and FPZ at the crack tip.

Another reason for having no size effect and boundary influence issue is explained by the position of short moment arm “ $d$ ” parameter of the loading point configuration along the beam specimen. Direct relationship was observed between parameter called as dimensionless short moment arm distance  $d/W$  and bending moment amount to ensure pure mode II state on crack plane. For specimens having small beam depth, positions of short moment arm “ $d$ ” were observed to be relatively closer to the crack plane compared to the other beam depth groups.

In other words, the ratio of short moment arm distance and beam depth ( $d/W$ ) were the same for all three beam depth groups for related crack lengths expressed as  $a/W$ . This phenomenon was attributed to the critical amount of bending moment requirement for crack initiation ensuring mode II loading state in rectangular shaped rock specimens. Finally, it was concluded as, the critical value for bending moment should be the same on the crack plane to ensure pure mode II state for different beam depths.

Similar results were observed individually for each specimen groups having the same beam depths. To satisfy the pure mode II state at the crack for each beam depth group, there was an optimum value of short moment arm  $d$ .

As crack length increases optimum value of short moment arm  $d$  initially increases, reaches a peak, and then decreases again. This trend is found to be described by a fourth order functional form using a “ $d$ ” value other than the optimum causes development of opening mode and non-zero mode I stress intensity factor on the crack plane. In this case pure shear condition fails.

Experimental work results showed that crack depth/beam depth ratio ( $a/W$ ) had no effect on mode II fracture toughness value. No boundary influence issue was observed for FPAB test specimen geometries with varying beam depths. This finding was tried to be explained by studying Von-Mises stress field between the crack tip and beam loading points. For beam depth groups having 40-50-60 mm depths, mode II fracture toughness values were computed as  $0.62\pm 0.19$ ,  $0.59\pm 0.20$  and  $0.62\pm 0.21$ ,  $\text{MPa}\sqrt{\text{m}}$  respectively. This indicated that increasing the beam size by increasing the beam depth had no influence in terms so called size effect on mode II fracture toughness.



## CHAPTER 7

### CONCLUSIONS AND RECOMMENDATIONS

The conclusions extracted from this study can be listed as;

- ❖ Four-Point Asymmetric Bending test is an accurate way to determine the mode II fracture toughness of rocks. The theory behind this test specimen geometry aims to produce zero absolute bending moment (sum of the reciprocal bending moments) on the crack plane. This condition is satisfied by the asymmetrically placed loading and support points. Nevertheless, location of loading and support points should be identified properly by precise modeling work.
- ❖ Configuration of loading and support points that satisfy pure mode II conditions can be easily set using structural analysis techniques. Areas of shear force and bending moment diagrams clearly show the response of test specimen to corresponding changes.
- ❖ Four-point asymmetric bending (FPAB) test specimen has flexibility advantages for dimension changes of the geometry with no drastic deviations of the boundary conditions.
- ❖ Zero absolute bending moment which causes pure shear effect on the crack plane can be easily satisfied by changing the locations of loading and support points.

- ❖ Short moment arm “ $d$ ” should be located sufficiently far from the crack plane to avoid opening mode and non-zero  $K_I$  effect. Excessive proximity of “ $d$ ” to the crack plane compromises existence of pure mode II stress state and causes generation of non-zero mode I stress intensity factor  $K_I$  with opening effect.
- ❖ Four-point asymmetric bending test configuration is also proven to be convenient for shorter beam lengths adopted in this study, compared to the previous work with beams extremely long spans.

The recommendations for future work can be listed as;

- ❖ In this work,  $L/d=3$  is used in all beam geometries. Different position configurations of loading and support points should be investigated in detail. For example it is suggested to include geometries with  $2 \leq L/d \leq 3$ .
- ❖ For the same geometric dimensions of test specimen, different positioning of loading and support points that satisfy pure mode II conditions should be investigated.
- ❖ The effect of beam thickness ( $B$ ) on pure mode II fracture toughness should be investigated.
- ❖ For different positioning of loading and support points and different beam thicknesses boundary influence and size effects should be examined by studying Von-Mises stress fields between crack tip and loading points/support points.
- ❖ Von-Mises stress field around crack tip and loading points should be investigated seriously with plastic models. Von-Mises stress field for mode I stress intensity factor  $K_I$  covers broader area on the specimen compared to the same stress field created by mode II stress intensity factor  $K_{II}$ .

- ❖ Rock type utilized for four-point asymmetric bending (FPAB) test should consist of fine grained material. Coarse grains within the rock matrix may lead crack to propagate through improper paths. This issue causes undesirable fracturing of the test specimen and effects validity of the test results.
- ❖ Specimen preparation process should be considered carefully. Results of laboratory tests are very sensitive to the any angular deviations on the flat surfaces of the test specimen. Corresponding surfaces should be totally parallel to each other. Errors on flatness and parallelism of the corresponding surfaces cause torsional and twisting effects on crack plane. This leads to undesirable crack propagation and fracturing mechanism.
- ❖ Rocks tested under compression fails by forming major shear mode cracks at maximum load. Thus, it is recommended to investigate existence of any possible relationship between unconfined and confined strength values and mode fracture toughness values of rock units of different origin.
- ❖ Loading rate of test procedure should allow the proper stress redistribution on the crack plane and of the test specimen itself. Excessively high or low loading rates may cause to develop instant overload on the crack plane or on stress fields.
- ❖ Loading rate of test procedure should be within the limits of 8 to 2 microns per seconds. In this study it is set as 3 microns per second.

## REFERENCES

ABAQUS Analysis User's Manual, Version 6.12 Documentation.

ABAQUS/CAE User's Manual, Version 6.12 Documentation.

ABAQUS, Inc., "*Modeling Fracture and Failure with ABAQUS*", 2006.

Al-Shayea, N.A., Khan, K. and Abduljawwad, S.N., "*Effects of Confining Pressure and Temperature on Mixed-Mode (I-II) Fracture Toughness of A Limestone Rock*", Int. J. Rock. Mech. & Min. Sci., Vol.37, pp. 629 – 643, 2000.

Alkılıçgil, Ç., "*Development of Specimen Geometries For Mode I Fracture Toughness Testing with Disc Type Rock Specimen*", PhD. Thesis, METU, Ankara, 172p., 2010.

Aliha, M.R.M., Ayatollahi, M.R. and Kharazai, B., "*Mode II Brittle Fracture Assessment Using ASFPB Specimen*", Int. J. Fract., DOI 10.1007/s10704-009-9402-z, vol.159 pp.241-246, 2009

Aliha, M.R.M., Ayatollahi, M.R., Smith, D.J., Pavier, M.J., "*Geometry and size effects on fracture trajectory in a limestone rock under mixed mode loading*", Engineering Fracture Mechanics, vol.77, pp. 2200-2212, 2010.

Aliha M.R.M. and Ayatollahi M.R., "*Mixed Mode I/II Fracture Evaluation of Marble Using SCB Specimen*", Procedia Engineering, Vol. 10, pp. 311-318, 2011.

Aliha M.R.M., Sistaninia M., Smith D.J., Pavier M.J. and Ayatollahi M.R., “*Geometry Effects and Statistical Analysis of Mode I Fracture In Guiting Limestone*”, Int. J. Rock. Mech. & Min. Sci., Vol. 51, pp. 128-135, 2012.

Anderson, T.L., “*Fracture Mechanics Fundamentals and Applications*”, CRC, Florida, 2005.

Arrea, M. and Ingraffea, A.R., “*Mixed Mode Crack Propagation in Mortar and Concrete*”, Report No.81-13, Cornell University, 1982.

Atkinson, C., Smelser, R.E. and Sanchez, J., “*Combined Mode Fracture via The Cracked Brazilian Disk Test*”, Int. J. Frac., Vol.18 (4), pp.279 – 291, 1982.

Ayatollahi M.R., Aliha M.R.M., and Hassani M.M., “*Mixed Mode Brittle Fracture in PMMA-An Experimental Study Using SCB Specimens*”, Mat. Sci. & Eng. A., Vol. 417, pp. 348-356, 2006.

Ayatollahi M.R. and Aliha M.R.M., “*Wide Range Data for Crack Tip Parameters in Two Disc-Type Specimens under Mixed Mode Loading*”, Compt. Mat. Sci., Vol. 38, pp. 660-670, 2007.

Ayatollahi, M.R., Aliha, M.R.M., “*On the use of an anti-symmetric four point bend specimen for mode II fracture experiments*” Fatigue & Fracture of Engineering Materials & Structures, DOI: 10.1111/j.1460-2695.2011.01583.x, vol.34, pp. 898-907, 2011.

Ayatollahi M.R. and Sistaninia M., “*Mode II Fracture Study of Rocks Using Brazilian Disk Specimens*”, Int. J. Rock. Mech. & Min.Sci., Vol.48, pp. 819 – 826, 2011.

Ayatollahi M.R. and Torabi A.R., “*Determination of Mode II Fracture Toughness for U-Shaped Notches Using Brazilian Disc Specimen*”, Int. J. Rock. Mech. & Min.Sci., Vol.47, pp. 454 – 465, 2010.

Ayatollahi, M.R., Dehghany, M., and Kaveh, Z., “*Computation of V-notch shape factors in four-point bend specimen for fracture tests on brittle materials*”, Arch. Appl. Mech. DOI 10.1007/s00419-012-0654-0, vol. 83, pp.345-356, 2012.

Ayatollahi, M.R., Akbardoost, J. “*Size Effects on Fracture Toughness of Quasi-Brittle Materials - A New Approach*”, Engineering Fracture Mechanics, Vol. 92, PP. 89-100, 2012.

Awaji, H. and Sato, S., “*Combined Mode Fracture Toughness Measurement by the Disk Test*”, J. Eng. Materials and Tech., Vol. 100, pp. 175 – 182, 1978.

Backers T et al., “*Fractography of rock from the new punchthrough shear test, in structural integrity and fracture*”, In: Dyskin AV, Hu X, Sahouryeh E (eds) The International Conference on structural integrity and fracture, Perth, Australia, 2002a.

Backers T, Stephansson O, Rybacki E., “*Rock fracture toughness testing in Mode II—punch-through shear test*”, Int. J. Rock. Mech. Min. Sci. 39(6):755–769, 2002b.

Backers T et al (2004) “*New data on Mode II fracture toughness of rock from the punch-through shear test*”, Int. J. Rock. Mech. Min. Sci. 41(3):351–352, 2004.

Backers T., “*Fracture toughness determination and micromechanics of rock under mode I and mode II loading*”, University of Potsdam, Potsdam, 2005.

Backers T., “*ISRM Suggested Method for the Determination of Mode II Fracture Toughness*”, Rock Mech. & Rock Eng., Vol. 45, pp. 1011-1022, 2012.

Barr, B., Derradj, M., “*Numerical Study of Shear (Mode II) Type Test Specimen Geometry*”, Engineering Fracture Mechanics, vol. 35 no1/2/3, pp.171-180, 1990.

Bazant, Z.P., “*Fracture in Concrete and Reinforced Concrete*”, Mechanics of Geomaterials, Rocks Concretes, Soils, Preprints, IUTAM Prager Symposium, Northwestern University, ed., Evanston, pp.281-317, 1983.

Bazant, Z.P., “*Size Effect in Blunt Fracture: Concrete, Rock, Metal*”, J. of Engng Mechanics, ASCE, vol.110, pp. 518-535, 1984.

Bazant, Z.P. and Pfeiffer P.A., “*Shear Fracture Tests of Concrete*”, Materiaux et Constructions, Vol. 19 No. 110, pp. 111-121, 1986.

Bazant, Z.P. and Pfeiffer P.A., “*Determination of Fracture Energy from Size Effect and Brittleness Number*”, ACI, Materials Journal, vol.84, pp. 463-480, 1987.

Bazant, Z.P., and Kazemi M.T., “*Size Effect of Fracture in Ceramics and Its Use to Determine Fracture Energy and Effective Process Zone Length*”, Journal of American Ceramic Society, vol. 77, no. 7, pp.1841-1853, 1990a.

Bazant, Z.P., and Kazemi M.T., “*Size Effect on Diagonal Shear Failure of Beams without Stirrups*” ACI Structural Journal vol.88, pp. 268-276, 1990b.

Bazant, Z.P., Daniel, I., and Li, Z., “*Size Effect and Fracture Characteristics of Fiber-Composite Laminates*”, Report Civil Engng Northwestern University, Evanston, 1995.

Bearman, R.A., Briggs, C.A., and Kojovic, T., “*The Application of Rock Mechanics Parameters to the Prediction of Comminution Behavior*”, Minerals Engineering vol.10, no.3, pp.255-264, 1997.

Bieniawski, Z.T., “*Mechanism of Brittle Rock Fracture: Part 1- Theory of the Fracture Process*”, International Journal of Rock Mechanics and Mining Sciences & Geomechanical Abstracts, Vol. 4, No: 4, pp. 395-406, 1967.

Callister, W.D., Jr., “*Materials Science and Engineering An Introduction*”, John Wiley and Sons, Inc., New York, 2007.

Chen, C.H., Wang, C.L., “*Application of Fracture Mechanics to Stability Analysis of Rock Slopes Subjected to Dynamics Excitations*” Proceedings of the ISRM International Symposium 3<sup>rd</sup>, pp.347-352, Rotterdam, 2004.

Chong, K.P. and Kuruppu, M. D., “*New Specimen for Fracture Toughness Determination of Rock and Other Materials*”, Int.J. Frac. Vol.26, pp. 59 – 62, 1984.

Cook, N.G.W., “*A note on rockburst considered as a problem of stability*”, J.S. Afr. Inst. Min. Metall., v. 66, pp. 435-528, 1965.

Cottrell, A. H., “*Theoretical Aspects of Radiation Damage and Brittle Fracture In Steel Pressure Vessels*”, Steels for Reactor Pressure Circuits, A Symposium of the Iron and Steel Inst., Special Report No. 69, Vol. Nov.-Dec., pp. 281, 1960.

Davies, A.J., “*The Finite Element Method, An Introduction with Partial Differential Equations*”, Second Edition, OXFORD University Press, 2011.

Deliac, E.P., “*Optimization Des Machines D’abattage a Pics*” PhD Thesis, University of Paris VI, Paris, 501 p., 1986.

Donovan, G. J., “*Fracture Toughness Based Models for the Prediction of Power Consumption, Product Size and the Capacity of Jaw Crushers*” PhD Thesis, Virginia Polytechnic Institute and State University, Blacksburg, 220 p., 2003.

Erdoğan, F., and Sih, G.H., “*On the Crack Extension in Plates Under Plane Loading and Transverse Shear*”, J. Basic Eng. Am. Soc. Mech. Engrs., Vol.85, pp. 519- 527, 1963.

ESDU, Data Item 96013 “*Fracture toughness ( $K_{Ic}$ ) values of some aluminium alloys*” 1996.

ESDU, Data Item 83023 “*Fracture toughness ( $K_{Ic}$ ) values of some steels*” 1995.

Fett, T., “*Stress Intensity Factors and Weight Functions for Special Crack Problems*”, Instut für Materialforschung, Forschungszentrum Karlsruhe GmbH, Karlsruhe, 1999.

Fischer-Cripps, A.C., “*Introduction to Contact Mechanics*”, Springer, Second Edition, pp. 31-48, New York, 2007.

Fowell, R.J. and Xu, C., “*The Cracked Chevron Notched Brazilian Disc Test – Geometrical Considerations for Practical Rock Fracture Toughness Measurement*”, Int.J.Rock.Mech. & Min.Sci., Vol.30, pp. 821 – 824, 1993.

Griffith, A.A., “*The Phenomena of Rapture and Flow in Solids*”, Phil. Trans. Roy. Soc. of London, Vol. A221, pp. 163-198, 1920/1921.

Griffith, A.A., “*The Theory of Rupture*”, Proc. of First Int. Cong. Appl. Mech., pp. 53-64, 1924.

Guo, H., “*Rock Cutting Studies Using Fracture Mechanics Principles*” PhD. Thesis, University of Wollongong, Australia, 225 p., 1990.

He MY, Hutchinson JW. “*Asymmetric four-point crack specimen*”, J. Appl. Mech. Trans. ASME, 67- pp. 207–9, 2000.

Heasley, K. A. and J. C. Zelanko, “*Pillar Design in Bump-Prone Ground Using Numerical Models with Energy Calculations*”, BuMines IC 9315, pp. 50-60, 1992.

Het, K., “*Shear Mode Fracture Toughness of Rock with Different Core-Based Specimen Geometries*”, PhD. Thesis, METU, Ankara, 294p., 2014.

Hood, M.C. and Roxborough, F.F., “*Rock Breakage: Mechanical*”, SME Mining Engineering Handbook, Second Edition, SME, H.L. Hartman (senior editor), Vol. 1, pp. 680-721, 1992.

Horiya T. And Kishi, T., “*Fracture Toughness of Titanium Alloys*”, Nippon Steel Technical Report, No: 62, 1994.

Huber, M.T. “*Czasopismo Techniczne*”, Lemberg, Austria, Vol. 22, pp. 181, 1904.

Hussain, M.A. and Pu, S.L., “*Strain Energy Release Rate for a Crack under Combined Mode I and Mode II*”, Fracture Analysis ASTM-STP, pp. 560-562, 1974.

Hydraulic Fracturing, <http://en.skifergas.dk/technical-guide/what-is-hydraulic-fracturing>, last visited on 16 July 2015.

Inglis, C.E., “*Stresses in A Plate Due to The Presence of Cracks and Sharp Corners*”, Trans. Inst. Naval Archit., Vol.55, pp.219-230, 1913.

Iannacchione, A. T. and J. C. Zelanko. “*Occurrence and Remediation of Coal Mine Bumps: A Historical Review. Proceedings: Mechanics and Mitigation of Violent Failure in Coal and Hard-Rock Mines*”, BuMines SP 01-95, pp. 27-67, 1995.

Irwin, G.R., “*Analysis of Stress and Strains Near the End of a Crack Traversing a Plate*”, J. of Applied Mechanics, A.S.M.E., New York, 1957.

ISRM “*The complete ISRM suggested methods for rock characterization, testing and monitoring*”: 1974–20014. In: Ulusay R, Hudson JA (eds) Suggested methods prepared by the commission on testing methods, International Society for Rock Mechanics, compilation arranged by the ISRM Turkish National Group. Kozan Ofset, Ankara (2014).

Karakaş, Ş. S., “*Shear Mode Rock Fracture Toughness Determination with a Circular Plate Type Specimen under Three-Point Bending*” PhD. Thesis, METU, Ankara, 127p., 2011.

Krishnan, G.R., Zhao, X.L., Zaman, M. and Roegiers, J.C., “*Fracture Toughness a Soft Sandstone*”, Int. J. of Rock Mech. Min. Sci., Vol. 35, pp. 695-710, 1998.

Krishnan, A., and Xu, L.R. “*A Short –Beam Shear Fracture Approach to Measure the Mode II Fracture Toughness of Materials with Preferred Interfaces*”, International Journal of Fracture, vol. 169, pp.15-25, 2011

Kumar, S., and Barai, S.V., “*Size-effect of fracture parameters for crack propagation in concrete: a comparative study*”, Computers and Concrete, vol. 9, no. 1, pp. 1-19, 2012.

Libatskii, L.L. and Kovichik, S.E., “*Fracture of Discs Containing Cracks*”, Soviet Materials Science, Vol. 3, pp. 334-339, 1967.

“Liberty Ships” <http://forum.worldwarships.com> last visited on 11 November, 2014.

Lim, I.L., Johnston, I.W., Choi, S.K., “*Stress Intensity Factors for Semi-circular Specimens Under Three-Point Bending*”, Eng. Fract. Mech., Vol.44 pp.363-382, 1993.

Lim, I.L., Johnston, I.W., Choi, S.K., Boland, J.N., “*Fracture Testing of A Soft Rock with Semi-circular Specimens under Three-point Bending*”, Part 1-2, Int. J. Rock Mech. & Min. Sci. and Geomech. Abstr., Vol.31, pp.185-212, 1994.

Liu, J. And Cao, P., “*Study on Rock Fracture with TBM Cutter Under Different Confining Stresses*”, Indian Geotech. J., DOI: 10.1007/s40098-015-0148-4, Springer, 2015.

Maleki, H., P. F. Wopat, R. C. Repsher and R. J. Tuchman, “*Proceedings: Mechanics and Mitigation of Violent Failure in Coal and Hard-Rock Mines*”, BuMines SP 01-95, 355 pp, 1995.

Martin R.H., Davidson, B.D., “*Mode II Fracture Toughness Evaluation Using Four Point Bend End Notched Flexure Test*”, *Plastics, Rubber and Composites*, vol 28 no. 8 pp. 401-406, 1999.

MTS System Catalogue, 1992.

Murakami, Y., et al., “*Stress intensity factors handbook*”, Pergamon Press, 1986.  
National Geographic Channel Documentary Series “*Air Crash Investigation*” Season, “3” Episode, “*Hanging by Thread*”; 2005.

Ouchterlony, F., “*ISRM Commission on Testing methods; Suggested Methods for determining fracture toughness of rock*”, Int. J. Rock Mech. Min. Sci. & Geomech. Abstr., Vol. 25, pp. 71-96, 1988.

Ouchterlony F. “*Suggested methods for determining the fracture toughness of rock*”. in: Ulusay R, Hudson JA, editors. *The complete ISRM suggested methods for rock characterization, testing and monitoring; 1974–2006*. Ankara, Turkey: ISRM Turkish National Group; 2007. pp. 231–258.

Quinn, G.D., Gettings, R.J. and Kubler, J.J., “*Indentation Studies on Y<sub>2</sub>O<sub>3</sub>- Stabilized ZrO<sub>2</sub>. II Toughness Determination from Stable Crack Growth of Indentation-Induced Cracks*”, Ceram. Eng. Sci. Proc. 15, pp. 252-257, 1994.

Rao, Q., Sun, Z., Stephansson, O., Li, C. and Stillborg, B., “*Shear Fracture (Mode II) of Brittle Rock*”, Int.J.Rock.Mech. & Min.Sci., Vol. 40, pp. 355 – 375, 2003.

Rice, J.R., “*A path independent integral and the approximate analysis of strain concentration by notches and cracks*”, J. App. Mech., Vol. 35, pp. 379-386, 1968.

Rooke, D.P. and D.J. Cartwright, “*Compendium of Stress Intensity Factors*”, H.M.S.O., London, 1976

Salamon, M.D.G., “*Elastic Analysis of Displacements and Stresses Induced by the Mining of Seam or Reef Deposits*”, J. S. Afr. Inst. Min. Metall., Part I, 64, pp. 128-149, 1963.

Saouma, V.E., “*Applications of Fracture Mechanics to Rock Slope Stability*”, Colorado School of Mines, 2010.

Shetty, D.K., Rosenfield, A.R. and Duckworth, W.H., “*Fracture Toughness of Ceramics Measured By A Chevron Notched Diametral Compression Test*”, J. Am. Ceram.Soc., Vol. 68, pp. c325-c443, 1985.

Shetty, D.K., Rosenfield, A.R. and Duckworth, W.H., “*Mixed-Mode Fracture of Ceramics in Diametral Compression*”, J. Am. Ceram. Soc., Vol. 69 (6), pp. 437-443, 1986.

Sih, G.C., “*Strain Energy Density Factor Applied to Mixed Mode Crack Problems*”, Int. J. Fract. Mech., Vol.10, pp.305-321, 1974.

Srawley, J.E., “*Wide Range Stress Intensity Factor Expressions for ASTM E399 Standard Fracture Toughness Specimens*”, Int. J. Fract., Vol.12, pp. 475 – 476, 1976.

Sun, C.T., Jin, Z.H., “*Fracture Mechanics*”, Academic Press, Elsevier, United States, 2012.

Suresh, S., Shih, C.F., Morrone, A, and O’Dowd, N.P., “*Mixed-Mode Fracture Toughness of Ceramic Materials*”, Journal of the American Ceramic Society vol. 75, no. 5, 1257-1267, 1990.

Tada H., Paris P.C., and Irwin G.R., “*The Stress Analysis of Cracks Handbook*”, Del Research Cooperation, Hellertown, 1973.

Tada, H., Paris, P.C. and George, R.I., “*The Stress Analysis of Cracks Handbook*”, ASME Press, New York, 2000.

Timoshenko, P.S., Gere, J.M., “*Theory of Elastic Stability*”, Second Edition, Dover, 560p., ISBN: 9780486472072, 2013.

Tutluoglu T and Keles C., “*Mode I Fracture Toughness Determination with Straight Notched Disk Bending Method*”, Int.J.Rock.Mech. & Min.Sci., Vol.48, pp. 1248 – 1261, 2011.

Von Mises, R. "Mechanik der Festen Korper im Plastisch Deformablen Zustand,"*Nachr. Ges. Wiss. Gottingen*", pp. 582, 1913.

Wang Ke Jen, Hsu Chi Lin and Kao Hua, “*Calculation Of Stress Intensity Factors For Combined Mode Bend Specimens*”, Advances in Research on the Strength and Fracture of Materials, Editor D:M.R. Taplin, vol 4 Fracture and Society, ICF4, Canada, Waterloo, 1977.

Watkins, J., “*Fracture Toughness Test For Soil-Cement Samples In Mode II*”, Int. J. Fracture, Vol. 23, pp. 135- 138, 1983.

Wells, A.A., “*Unstable Crack Propagation in Metals: Cleavage and Fast Fracture*”, Proceedings of the Crack Propagation Symposium, Vol 1, Paper 84, Cranfield, UK, 1961.

Westergaard. H.M., “*Stresses at a crack, size of the crack and the bending of reinforced concrete*”, Prov. American Concrete Institute, Vol.30, pp. 93-102, 1934.

Williams, M., “*On The Stress Distribution at The base of A Stationary Crack*”, Journal of Applied Mechanics, ASME 24(1), pp. 109-114, 1957.

Whittaker, B.N., Singh, R.N., Sun, G., “*Rock Fracture Mechanics-Principles, Design and Applications*”, Elsevier, Amsterdam, 1992.

Xu, C. “*Fracture Mechanics and Its Application in Rock Excavation Engineering*”, PhD. Thesis, The University of Leeds, 262p., Leeds, 1993.

Yoshihara, H., “*Mode II Fracture Mechanics Properties ff Wood Measured by the Asymmetric Four-Point Bending Test Using A Single-Edge-Notched Specimen*”, Engineering Fracture Mechanics, vol. 75 pp. 4727-4739, 2008.

Zipf, R. K. and K. A. Heasley. “*Decreasing Coal Bump Risk through Optimal Cut Sequencing with a Non-Linear Boundary Element Program. Rock Mechanics Contributions and Challenges*”, Proceedings of the 31st U.S. Symposium, Golden, Co, June 18-20, pp. 947-954, 1990.

Zhou, Y., and Lin, J., S., “*Modeling the Ductile–Brittle Failure Mode Transition In Rock Cutting*”, Engineering Fracture Mechanics, Article In Press, 2014.



## APPENDICES

### APPENDIX A: DIMENSIONLESS SHORT MOMENT ARM DISTANCE ANALYSIS

#### A.1 Beam Depth Group W= 40 mm graphs

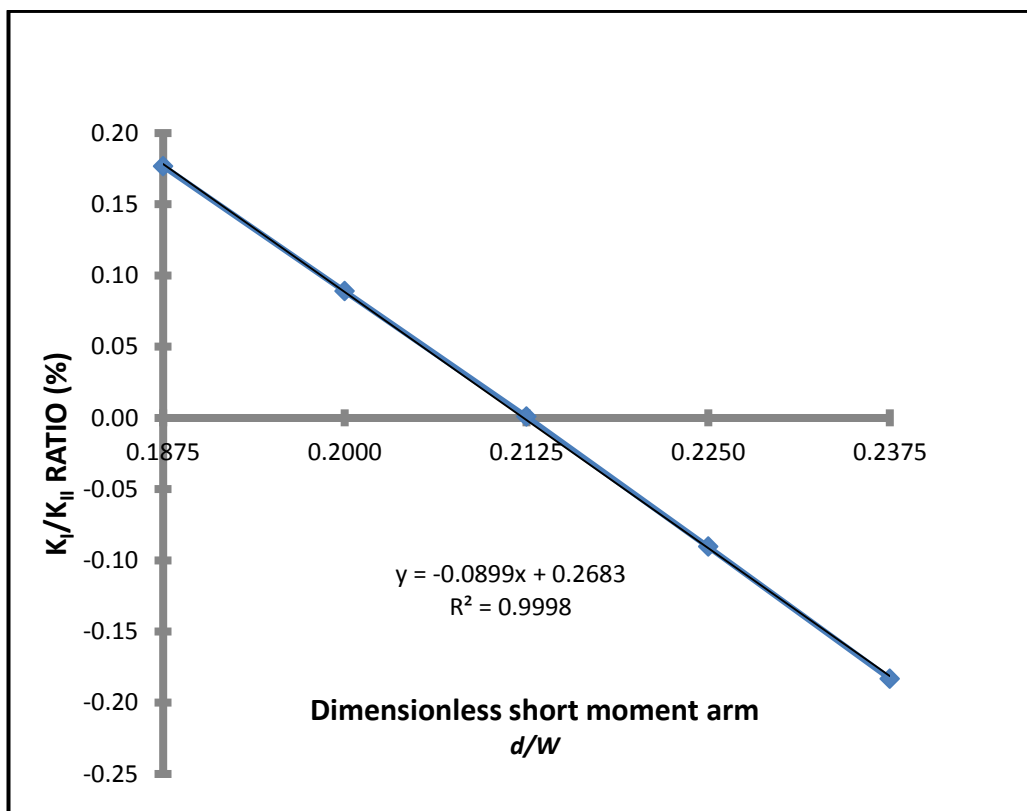


Figure A. 1 Dimensionless short moment distance for  $a/W = 0.15$  regarding pure shear SIF conditions

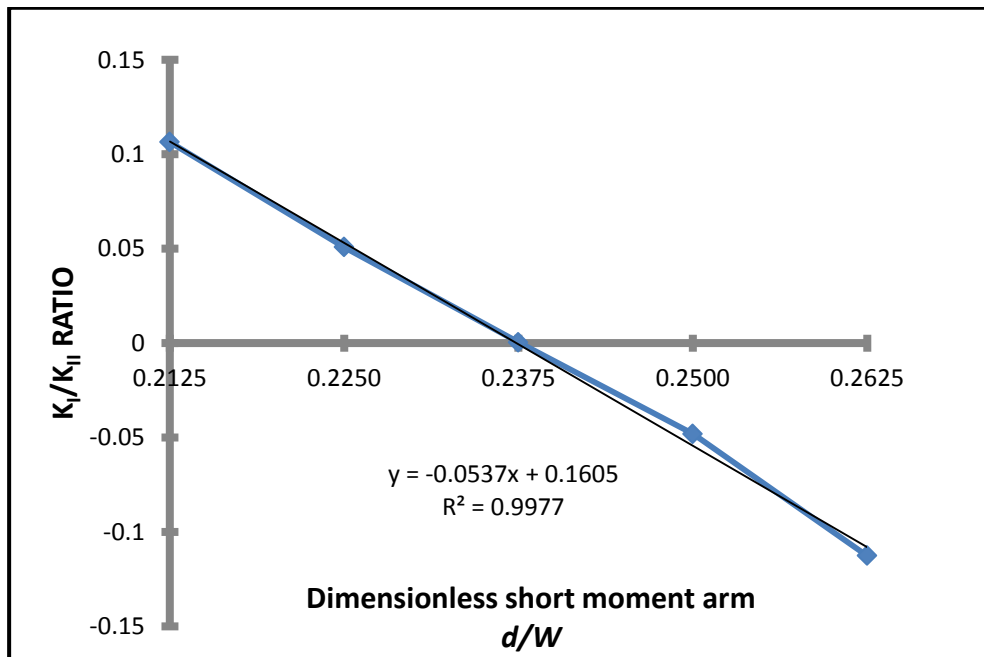


Figure A. 2 Dimensionless short moment distance for  $a/W = 0.20$  regarding pure shear SIF conditions

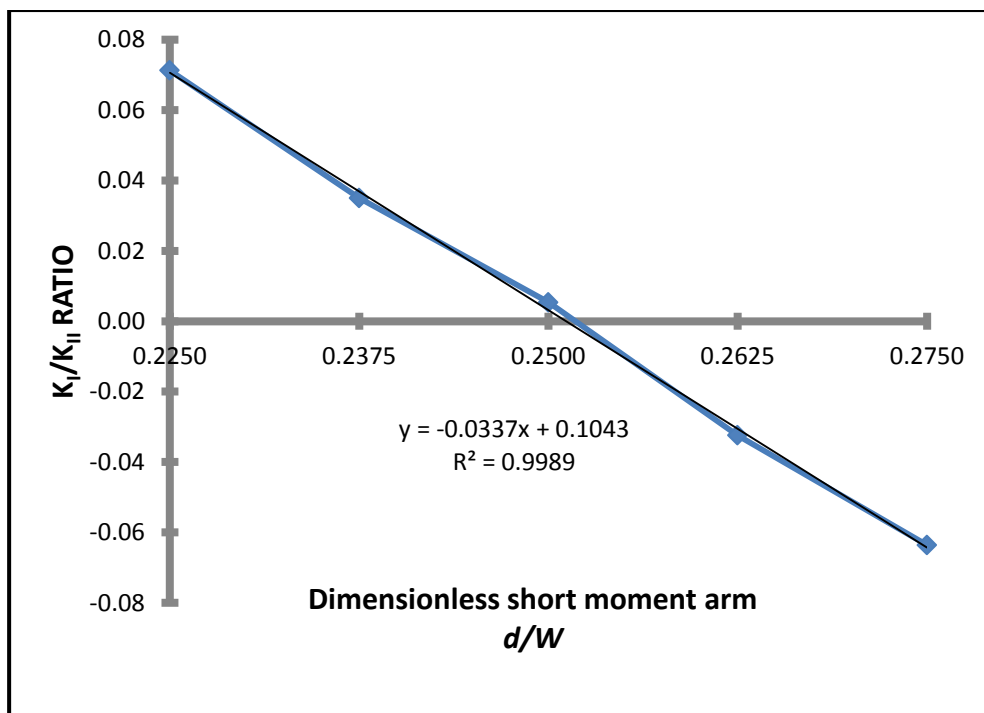


Figure A. 3 Dimensionless short moment distance for  $a/W = 0.25$  regarding pure shear SIF conditions

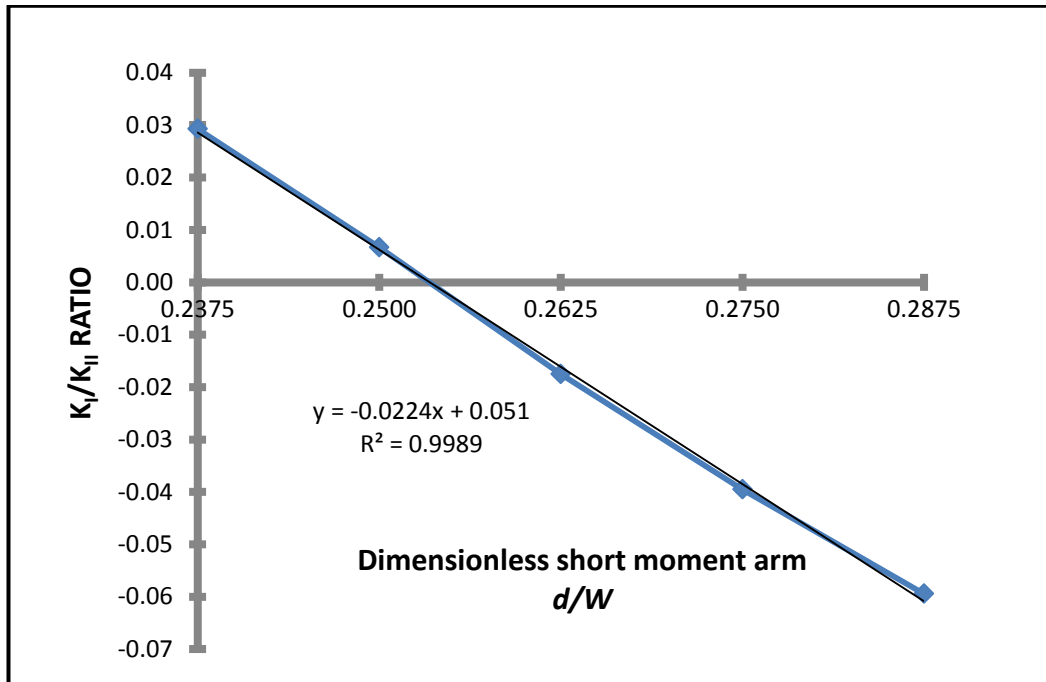


Figure A. 4 Dimensionless short moment distance for  $a/W = 0.30$  regarding pure shear SIF conditions

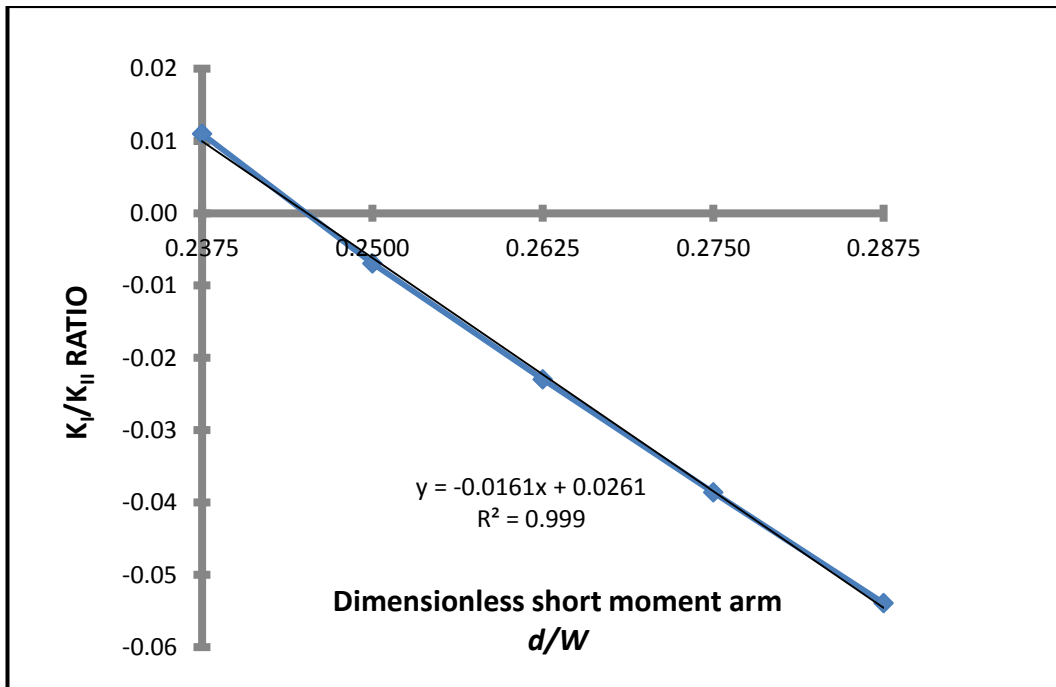


Figure A. 5 Dimensionless short moment distance for  $a/W = 0.35$  regarding pure shear SIF conditions

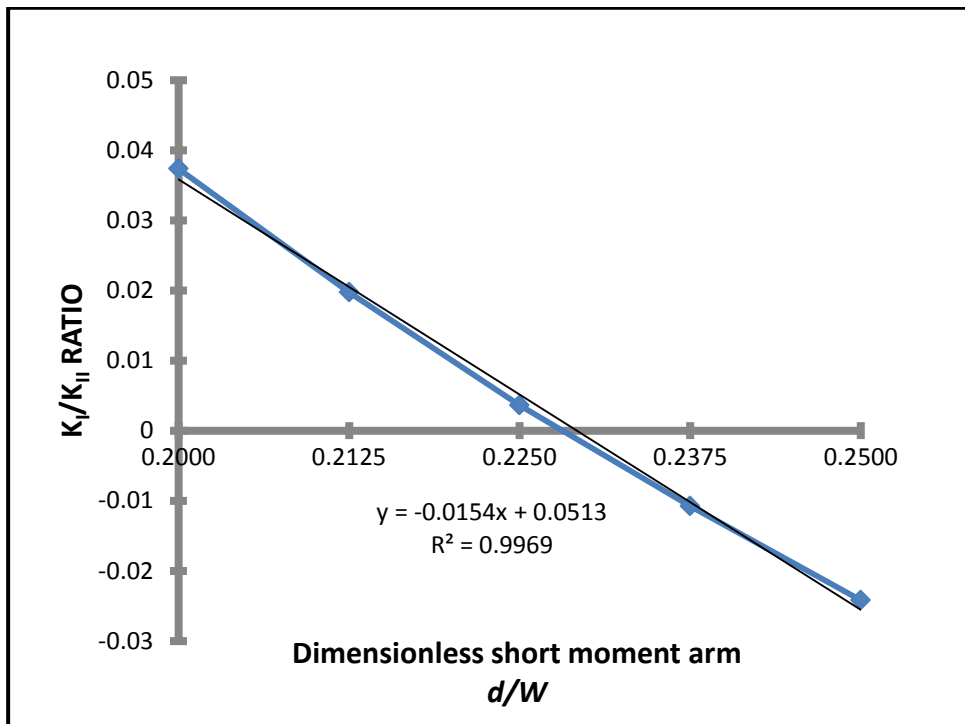


Figure A. 6 Dimensionless short moment distance for  $a/W = 0.40$  regarding pure shear SIF conditions

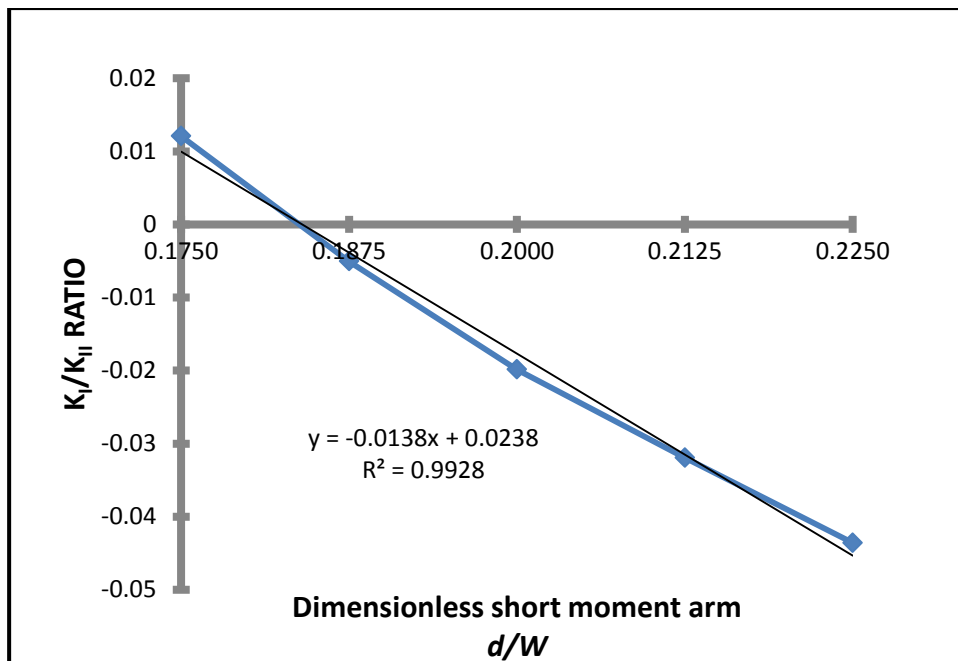


Figure A. 7 Dimensionless short moment distance for  $a/W = 0.50$  regarding pure shear SIF conditions

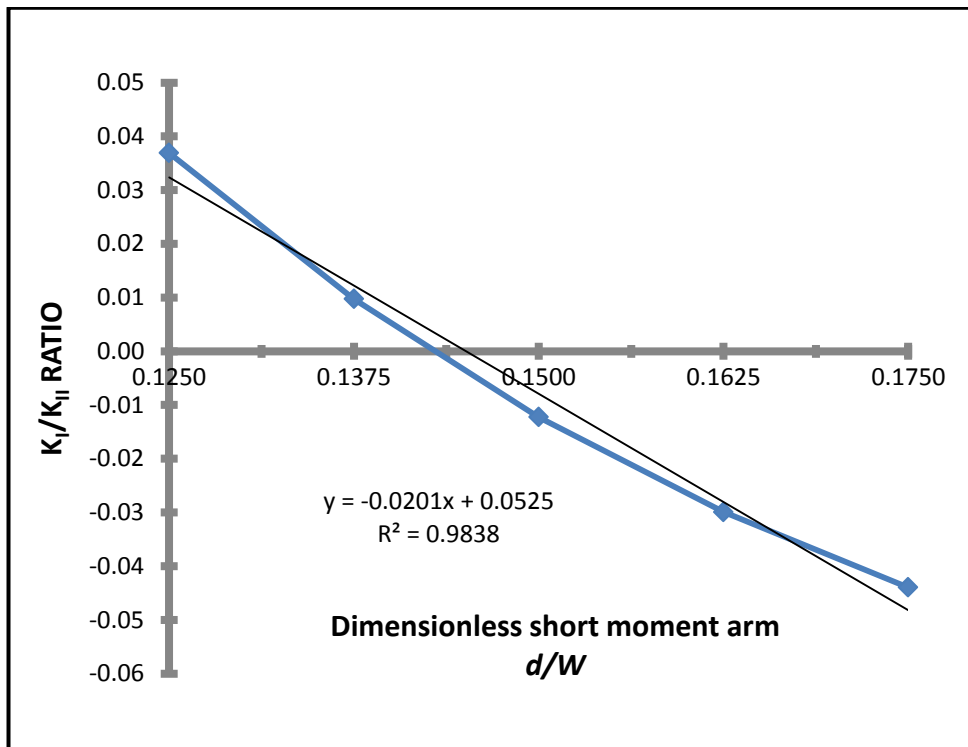


Figure A. 8 Dimensionless short moment distance for  $a/W = 0.60$  regarding pure shear SIF conditions

**A.2 Beam Depth Group W= 50 mm graphs**

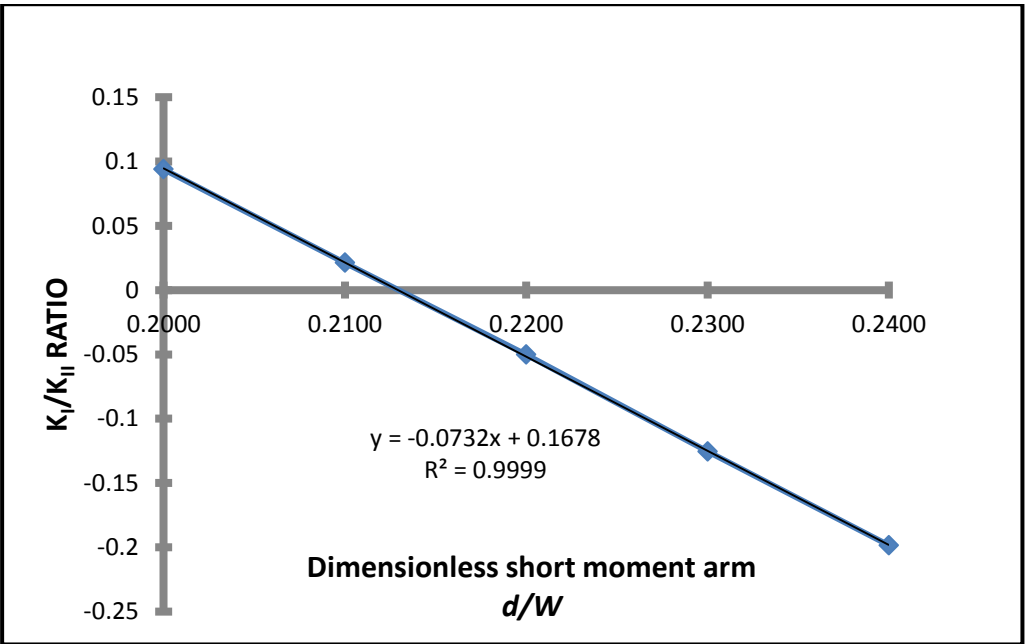


Figure A. 9 Dimensionless short moment distance for  $a/W= 0.15$  regarding pure shear SIF conditions

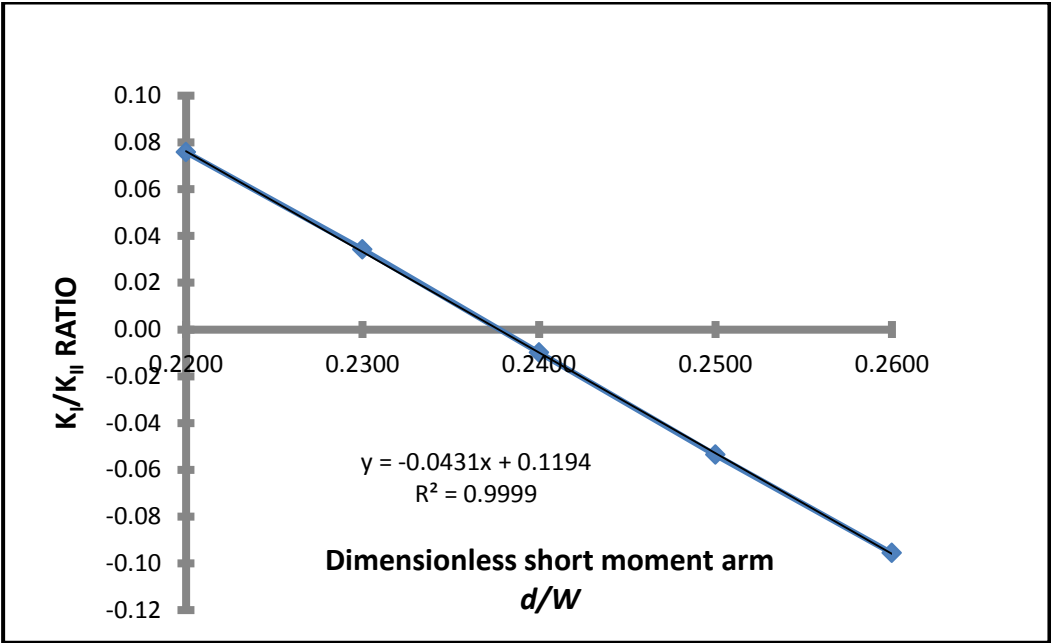


Figure A. 10 Dimensionless short moment distance for  $a/W= 0.20$  regarding pure shear SIF conditions

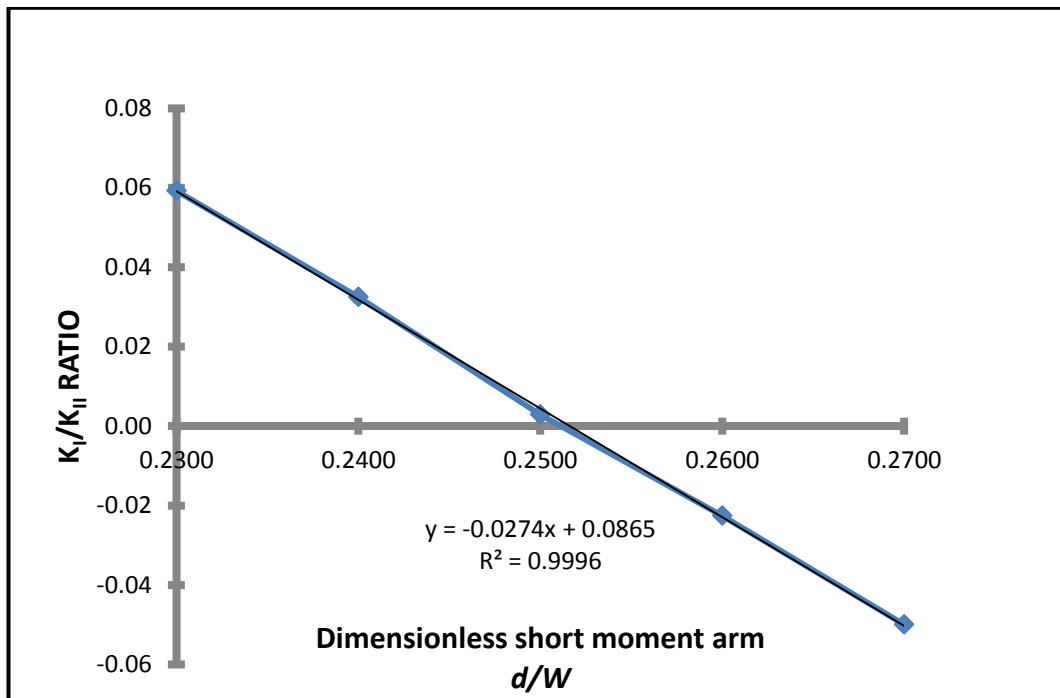


Figure A. 11 Dimensionless short moment distance for  $a/W = 0.25$  regarding pure shear SIF conditions

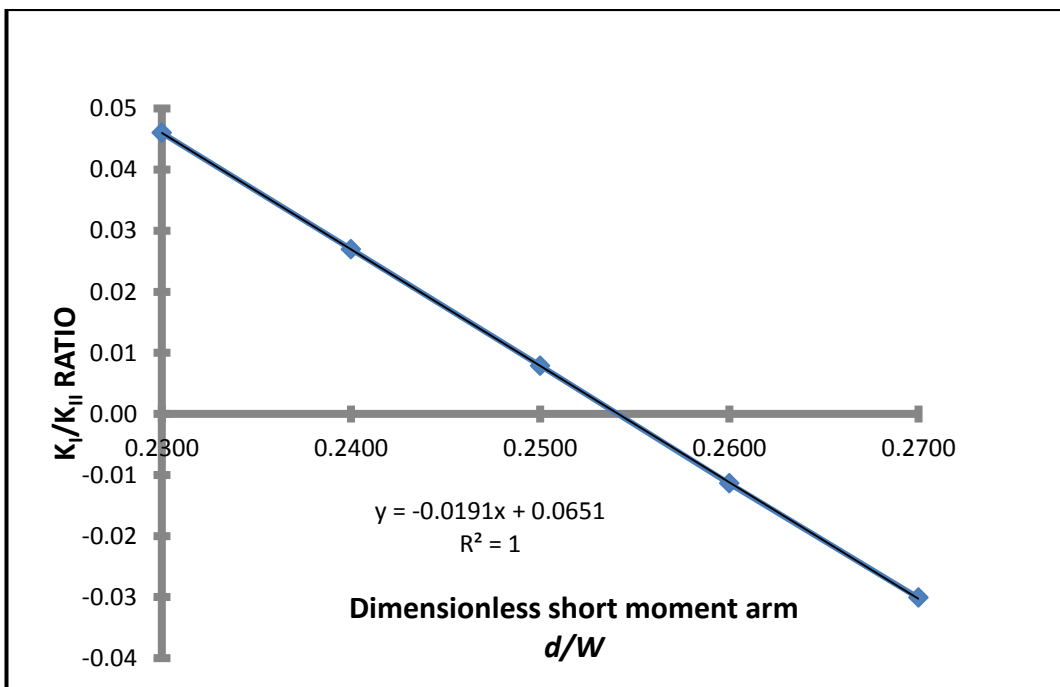


Figure A. 12 Dimensionless short moment distance for  $a/W = 0.30$  regarding pure shear SIF conditions

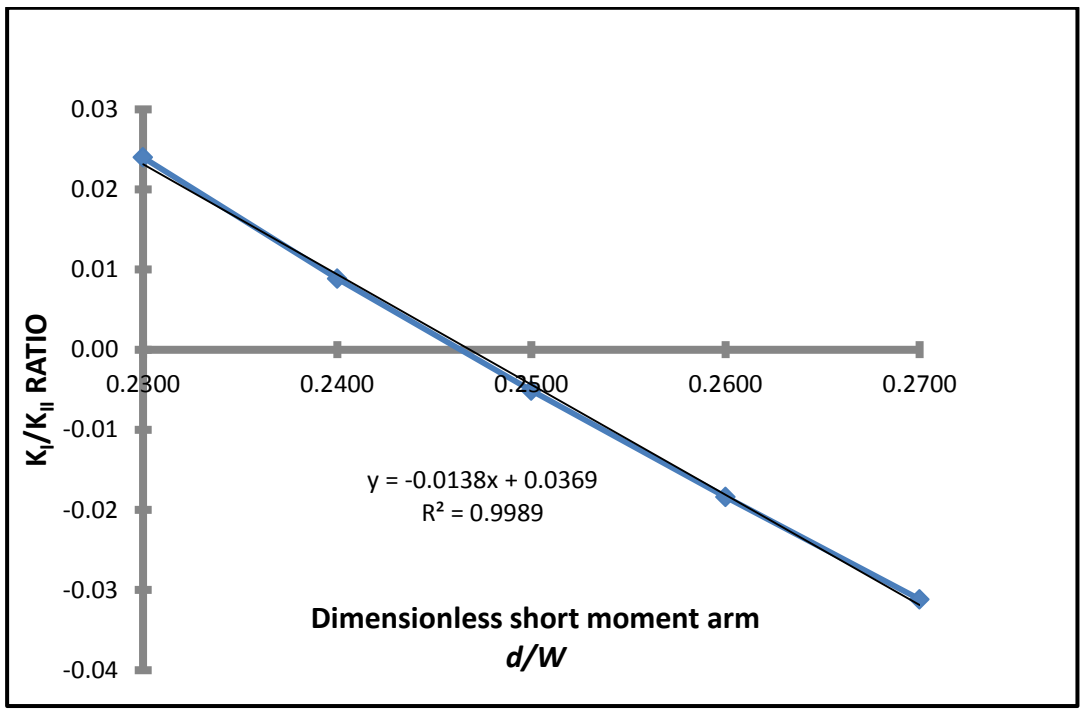


Figure A. 13 Dimensionless short moment distance for  $a/W = 0.35$  regarding pure shear SIF conditions

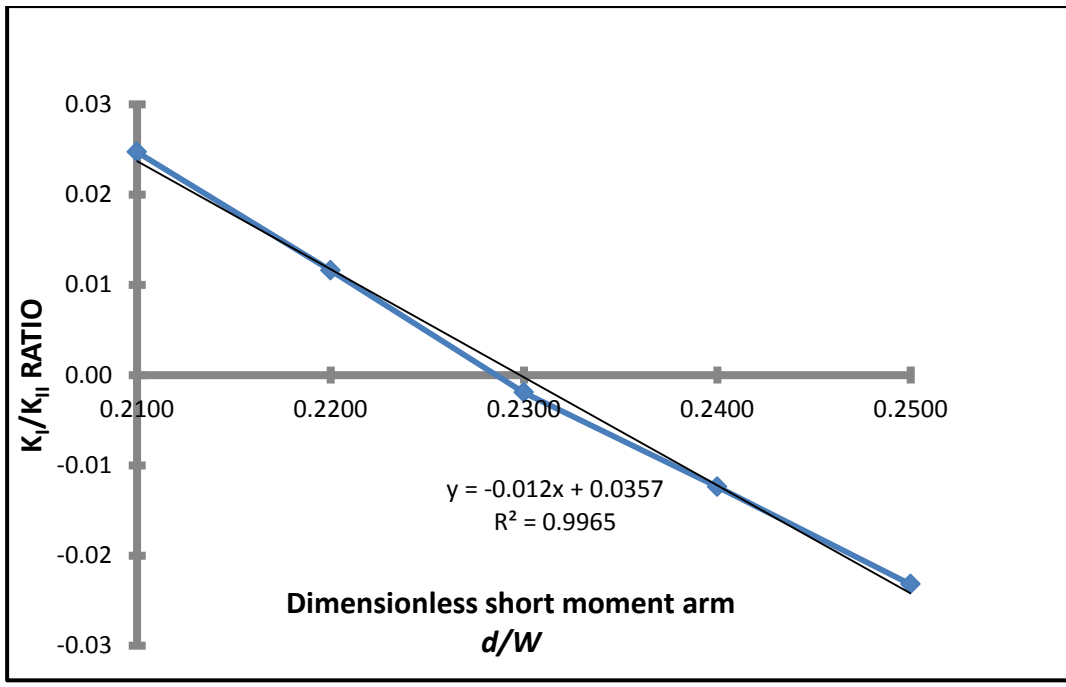


Figure A. 14 Dimensionless short moment distance for  $a/W = 0.40$  regarding pure shear SIF conditions

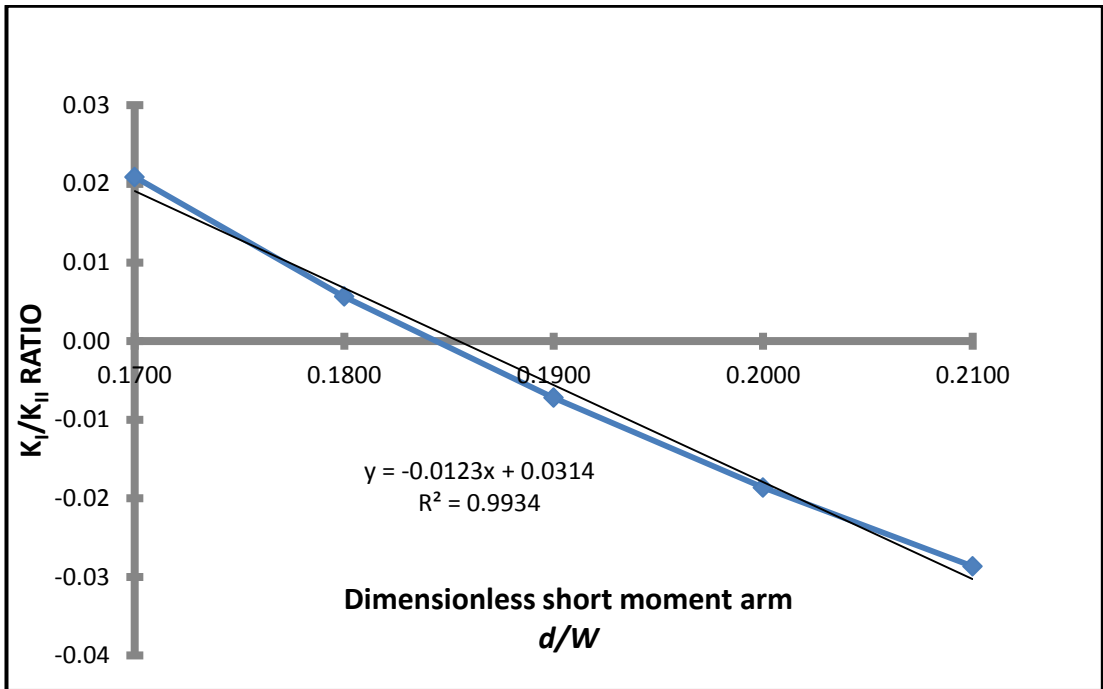


Figure A. 15 Dimensionless short moment distance for  $a/W = 0.50$  regarding pure shear SIF conditions

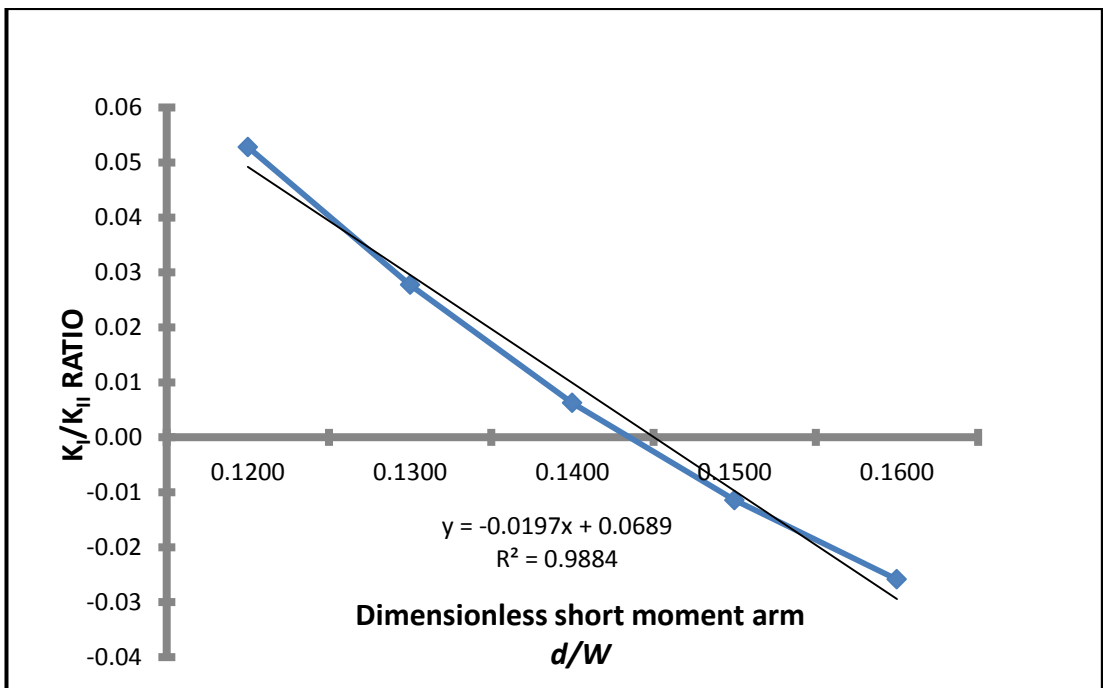


Figure A. 16 Dimensionless short moment distance for  $a/W = 0.60$  regarding pure shear SIF conditions

**A.3. Beam Depth Group W= 60 mm graphs**

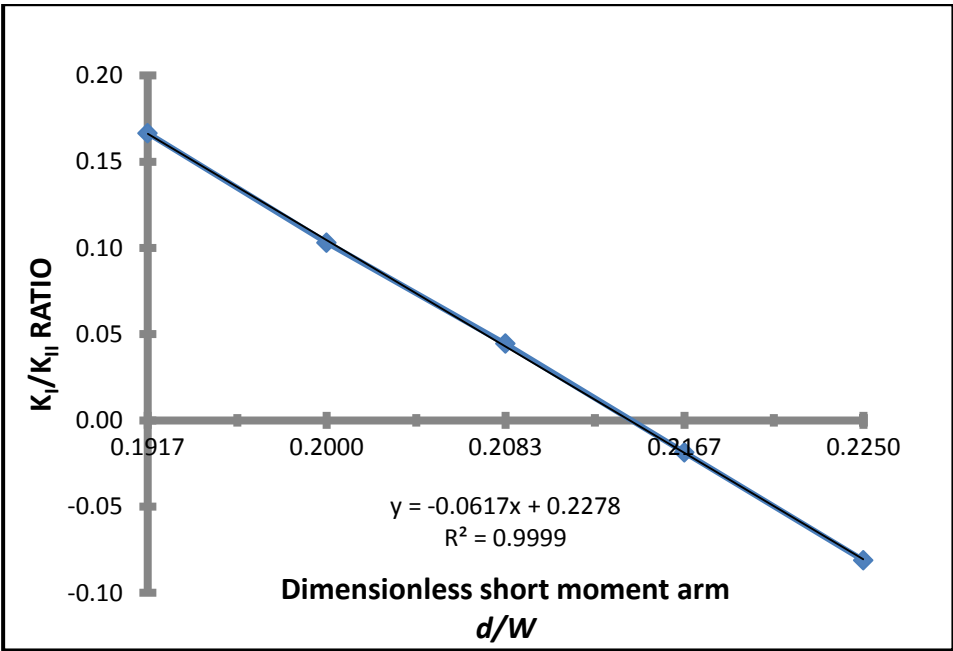


Figure A. 17 Dimensionless short moment distance for  $a/W = 0.15$  regarding pure shear SIF conditions

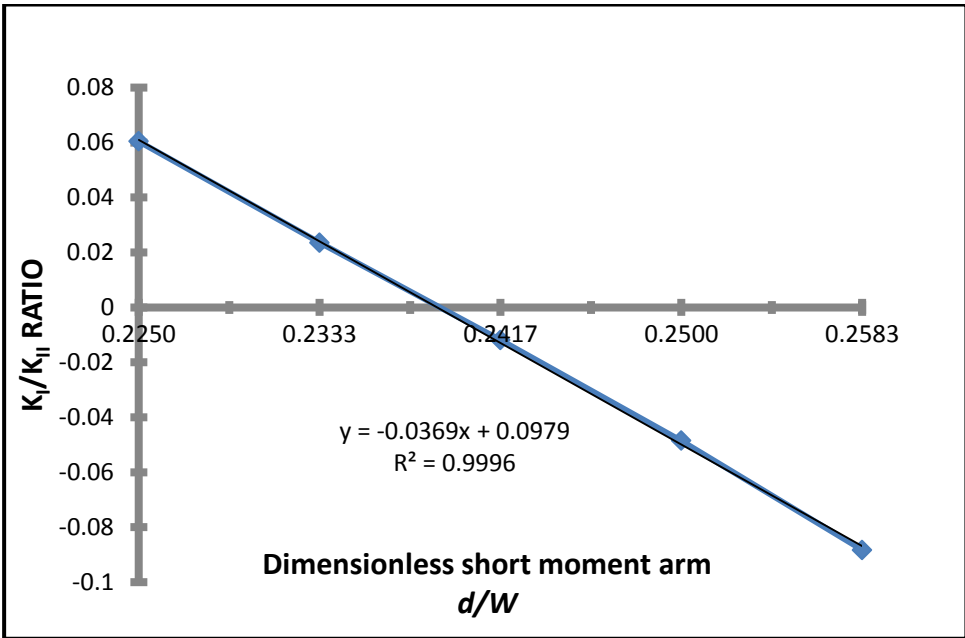


Figure A. 18 Dimensionless short moment distance for  $a/W = 0.20$  regarding pure shear SIF conditions

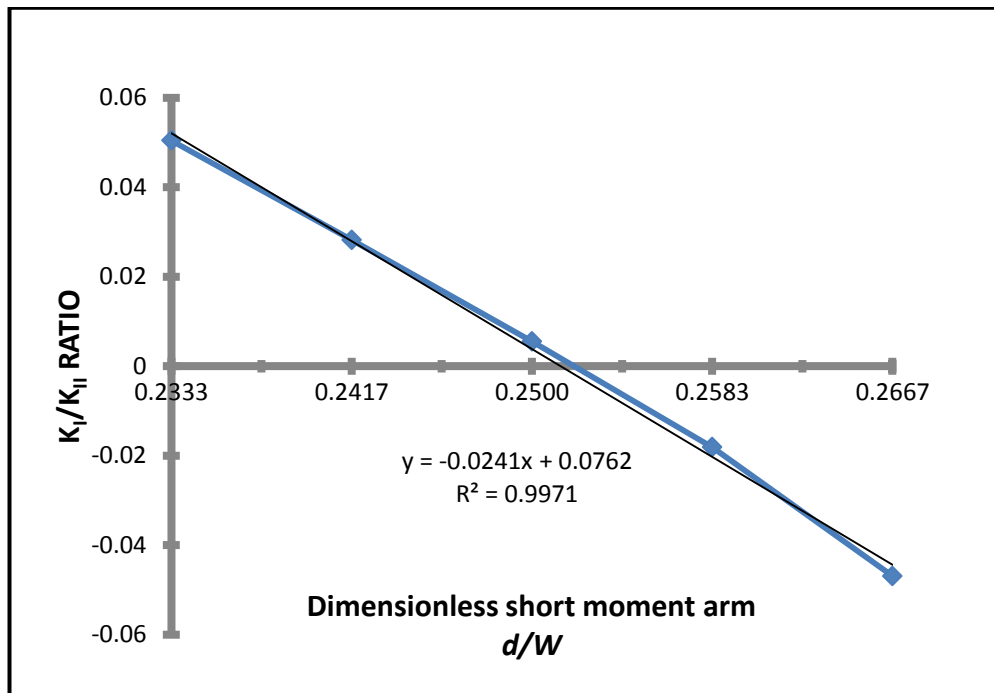


Figure A. 19 Dimensionless short moment distance for  $a/W = 0.25$  regarding pure shear SIF conditions

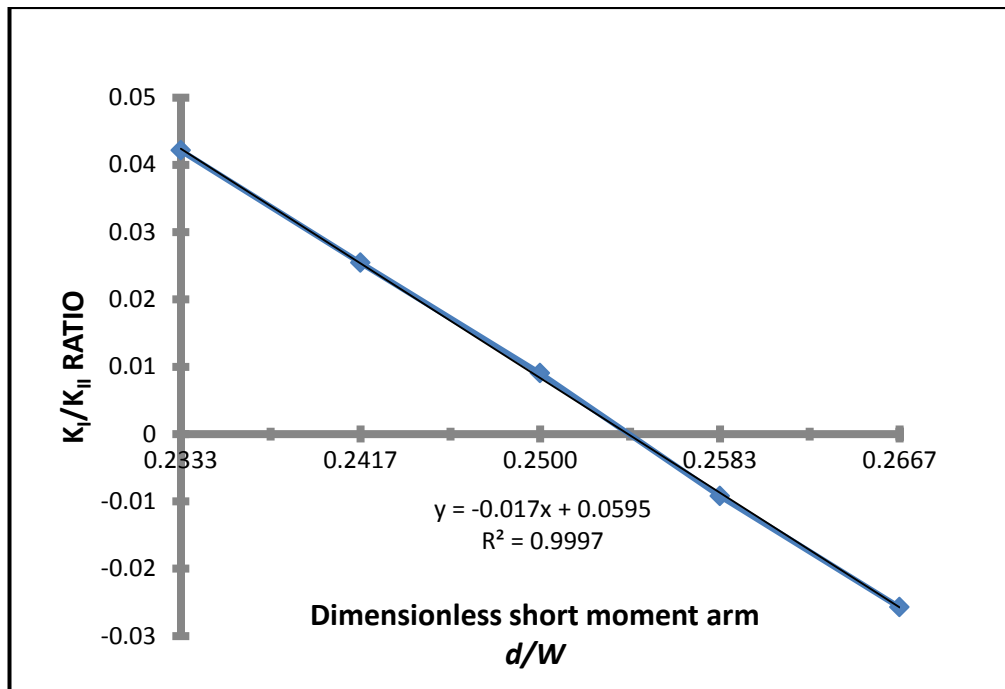


Figure A. 20 Dimensionless short moment distance for  $a/W = 0.30$  regarding pure shear SIF conditions

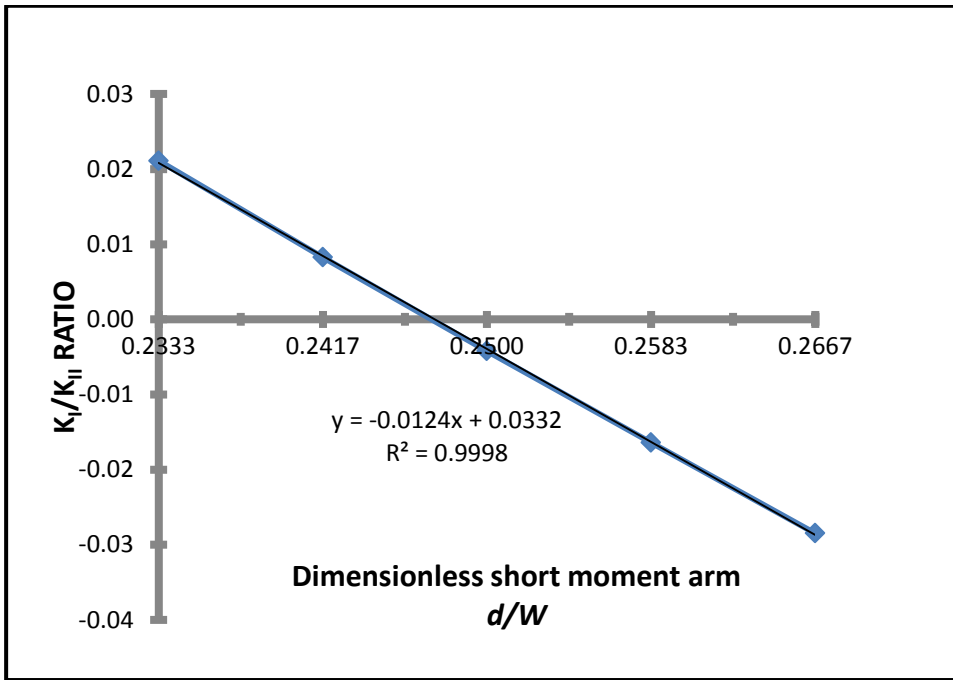


Figure A. 21 Dimensionless short moment distance for  $a/W = 0.35$  regarding pure shear SIF conditions

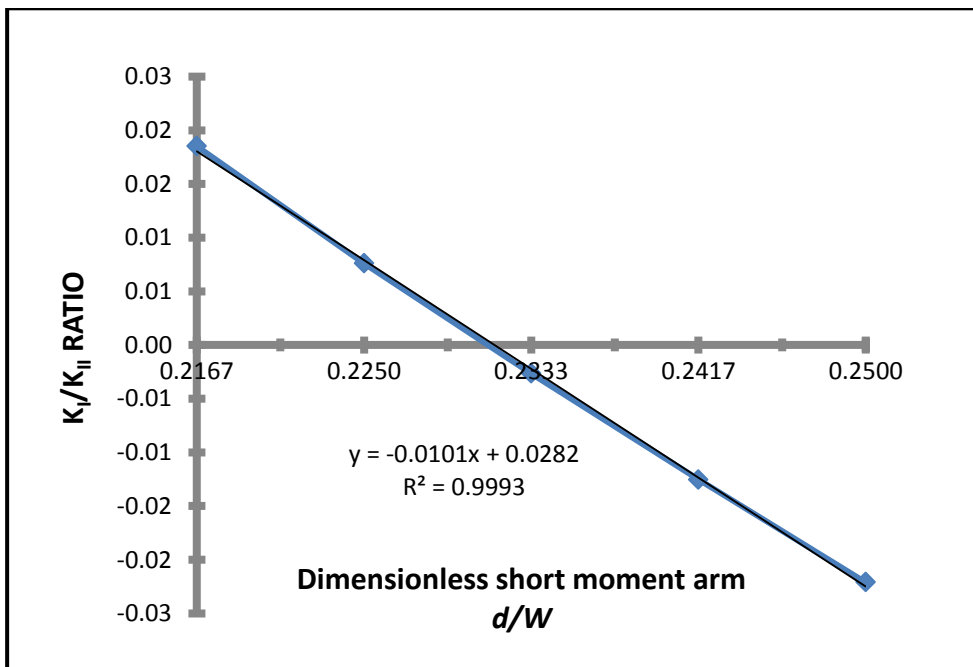


Figure A. 22 Dimensionless short moment distance for  $a/W = 0.40$  regarding pure shear SIF conditions

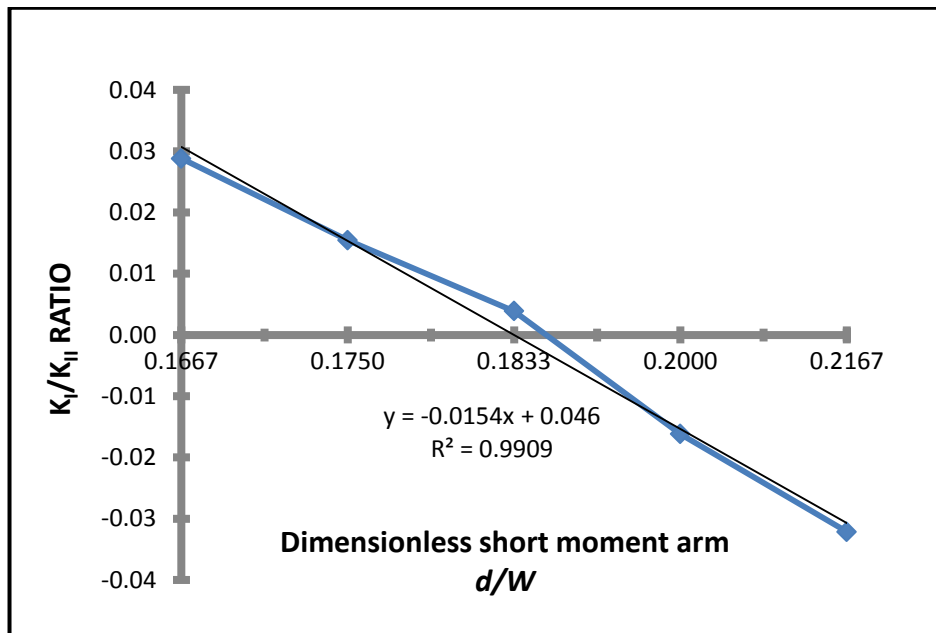


Figure A. 23 Dimensionless short moment distance for  $a/W = 0.50$  regarding pure shear SIF conditions

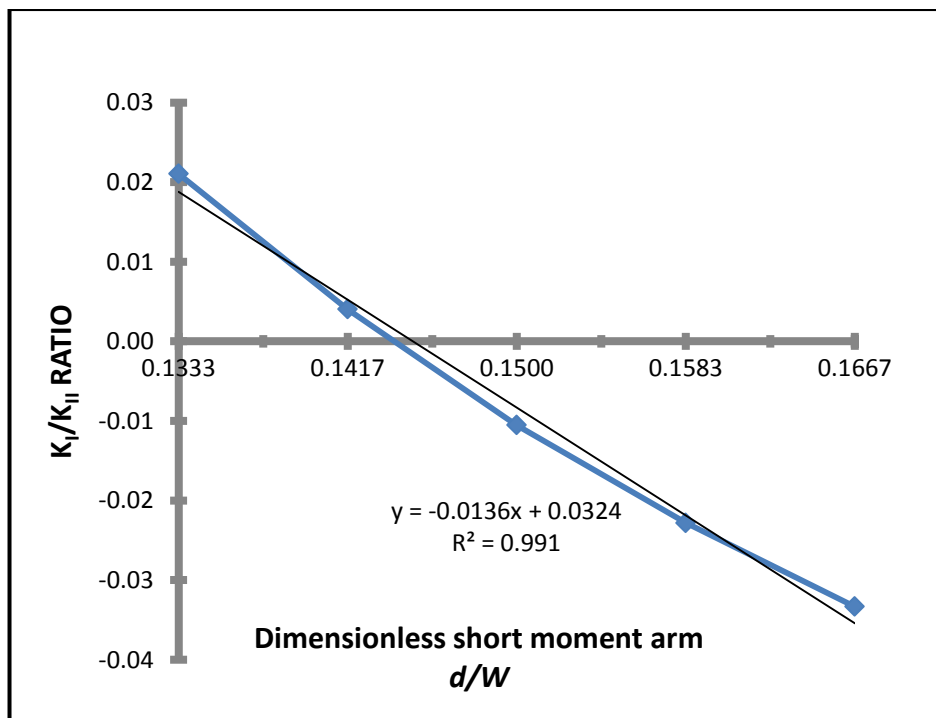


Figure A. 24 Dimensionless short moment distance for  $a/W = 0.60$  regarding pure shear SIF conditions

**APPENDIX B: SPECIMEN PHOTOGRAPHS AFTER EXPERIMENTAL STUDY**

**B.1 Beam Depth Group W= 40 mm photographs**



Figure B. 1 W= 40 mm a/W= 0.20 specimens after test

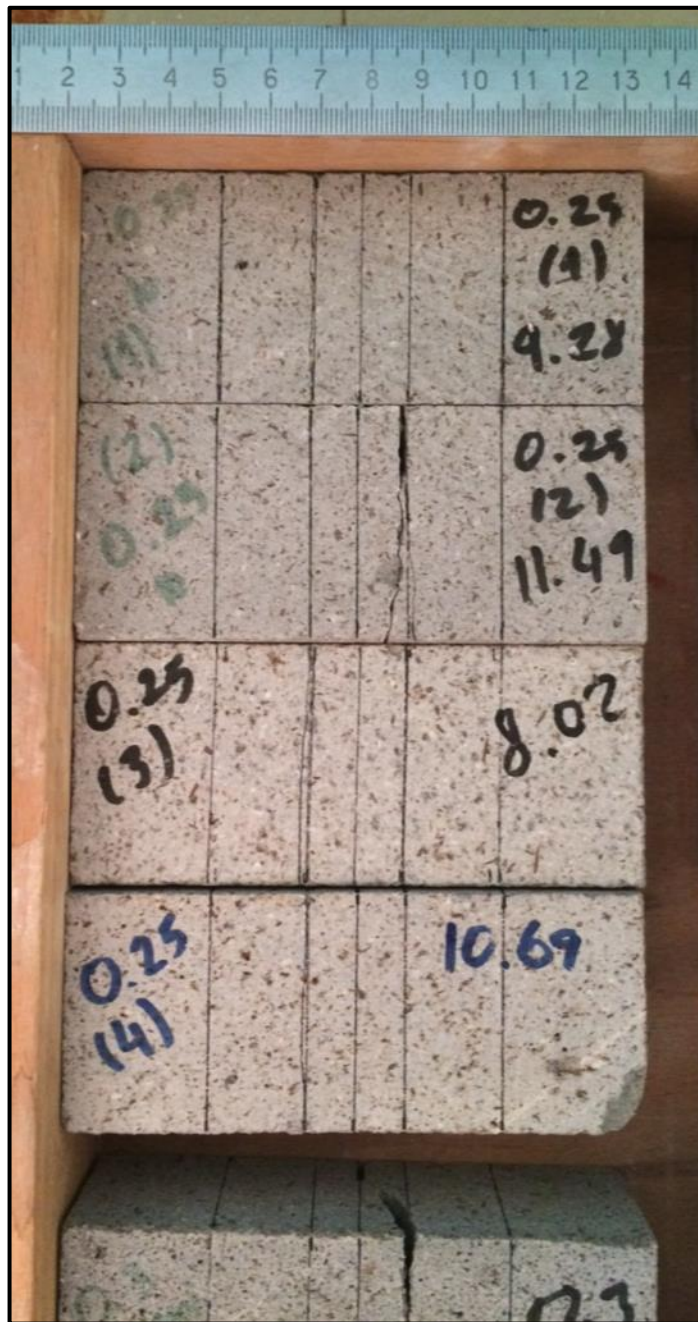


Figure B. 2  $W=40\text{ mm}$   $a/W=0.25$  specimens after test



Figure B. 3  $W = 40$  mm  $a/W = 0.30$  specimens after test



Figure B. 4  $W = 40$  mm  $a/W = 0.35$  specimens after test



Figure B. 5  $W=40\text{ mm}$   $a/W=0.40$  specimens after test



Figure B. 6  $W=40$  mm  $a/W=0.50$  specimens after test

B.2 Beam Depth Group W= 50 mm photographs



Figure B. 7 W= 50 mm a/W= 0.20 specimens after test



Figure B. 8  $W = 50$  mm  $a/W = 0.25$  specimens after test



Figure B. 9  $W = 50 \text{ mm}$   $a/W = 0.30$  specimens after test



Figure B. 10  $W= 50$  mm  $a/W= 0.35$  specimens after test



Figure B. 11  $W= 50$  mm  $a/W= 0.40$  specimens after test



Figure B. 12  $W=50\text{ mm}$   $a/W=0.50$  specimens after test



Figure B. 13  $W= 50 \text{ mm}$   $a/W= 0.60$  specimens after test

**B.3 Beam Depth Group W= 60 mm photographs**



Figure B. 14 W= 60 mm a/W= 0.20 specimens after test



Figure B. 15 W= 60 mm a/W= 0.25 specimens after test



Figure B. 16  $W=60\text{ mm}$   $a/W=0.30$  specimens after test

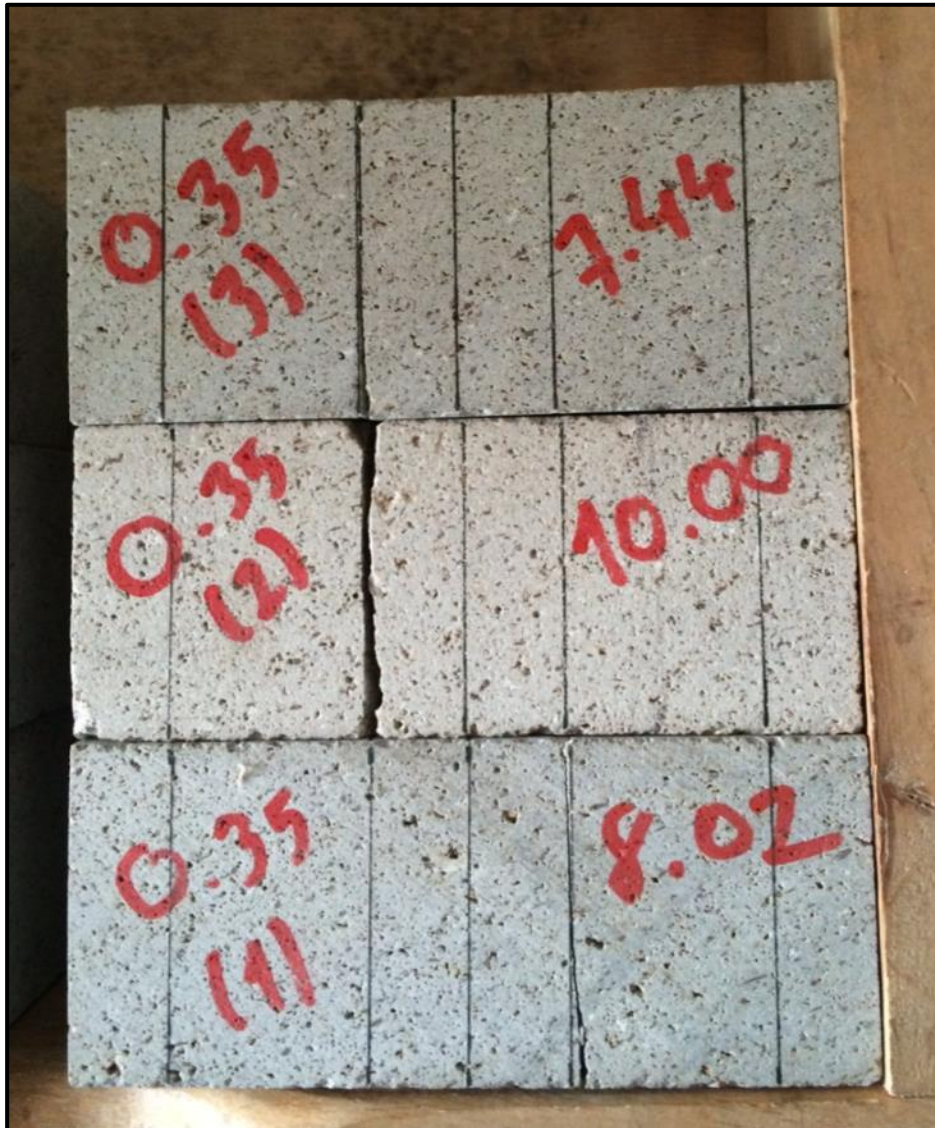


Figure B. 17  $W=60$  mm  $a/W=0.35$  specimens after test



Figure B. 18  $W=60\text{ mm}$   $a/W=0.40$  specimens after test



Figure B. 19  $W = 60$  mm  $a/W = 0.50$  specimens after test